On the Low Speed Longitudinal Stability of Hypersonic Waveriders

A Thesis submitted to the University of Sydney for
the Degree of Doctor of Philosophy,
from the School of Aerospace, Mechanical & Mechatronic Engineering

Jonathan J. Jeyaratnam

SID: [redacted]

May 2020

Abstract

The development of hypersonic civilian transport aircraft requires solutions to a number of challenging problems in the areas of aerothermodynamics, control, aeroelasticity, propulsion and many others encountered at high Mach number flight. The majority of research into hypersonic vehicle design has therefore rightly focused on solutions to these issues. The desire for good aerodynamic performance at high Mach numbers, most often defined by the lift to drag ratio, results in slender vehicle designs which minimise drag and take advantage of compression lift through attached shock waves along the leading edge. These so-called waverider designs show good promise for high aerodynamic efficiency and potential for long range transport applications. However a civilian transport aircraft that travels at hypersonic speeds requires satisfactory stability and handling qualities across the entire flight trajectory. The stability and handling of waverider shapes at the low speeds encountered at the take-off and landing phases of flight is not well studied.

The stability of an aircraft is characterised by the aerodynamic stability derivatives. Only a few existing studies have looked at these low speed derivatives for waverider designs and no research has been found on the dynamic damping derivatives even though these are important to characterising the handling qualities of a vehicle. The work presented here covers the use of various high fidelity methods to extract these derivatives for a particular vehicle, the Hexafly-Int hypersonic glider. This vehicle has been chosen as it represents a mature example of a waverider vehicle that has been designed for flight testing at Mach 7.2. It is therefore typical of waverider designs optimised for high speed performance. The highly separated flowfield which slender vehicle designs exhibit at low speeds and high angles of attack requires the use of higher fidelity Computational Fluid Dynamics (CFD) simulations.

The work covered in this thesis includes static and dynamic CFD simulations of the Hexafly glider which have been used to obtain longitudinal stability derivatives at low speeds. Complementary static and free-to-pitch dynamic wind tunnel testing, which has not been previously used to test hypersonic designs are used to validate the CFD computations. A final chapter on the optimisation of waverider designs incorporating low speed longitudinal stability as a criteria is presented to provide insight into the impacts of this additional requirement on the hypersonic design space.

The static wind tunnel testing has identified stability issues relating to the location of the centre of gravity. The design centre of gravity which is suitable for the Hexafly-Int vehicle at Mach 7.2 is found to be too far aft which results in instability at low speeds. This discrepancy between the centre of gravity location suitable for hypersonic cruise and the centre of gravity suitable for low speed operations with high angles of attack is found to be a significant issue for hypersonic waverider designs. In addition, the dynamic testing in the wind tunnel shows that the pitch damping is inadequate at low speeds. The CFD simulations agree well with the wind tunnel test results validating the use of CFD tools for determining dynamic stability derivatives of this class of slender vehicle in the design process. To alleviate the low speed stability issue of hypersonic vehicles, a waverider shape optimisation study has been carried out to understand what shapes will produce better low speed stability behaviour. These shapes are found to produce lower aerodynamic efficiency at high speeds which suggests that a design compromise between low speed stability and high speed performance is required at the outset of hypersonic waverider design.

Declaration

This thesis was completed between August of 2013 and July of 2019, under the supervision of Dr. Dries Verstraete from the School of Aerospace, Mechanical and Mechatronic Engineering (AMME) at the University of Sydney. The content contained within this thesis is the product of the work of Mr. Jonathan J. Jeyaratnam, with guidance provided by Dr. Dries Verstraete through discussions on research direction, interpretation of results and proofreading of the manuscript. No portion of the work referred to in this thesis has been submitted in support of an application for another degree or qualification at this or any other University or institution of learning.

....

Jonathan J. Jeyaratnam Dr. Dries Verstraete

Acknowledgements

I'll keep this as brief as I can.

Thanks to the University of Sydney for providing top notch high performance computing tools (USyd HPC), fabrication facilities, a wind tunnel and excellent support from workshop staff who were always ready to assist.

Thank you to Dr Johan Steelant of ESA and the rest of the Hexafly-Int project team for providing a highly refined hypersonic vehicle design for me to play with. It's taken years of work and I appreciate being a small part of it.

Thank you to Kai and Matt for teaching me the ways of dynamic wind tunnel testing, for letting me use your brilliant work and for being around for all my dumb questions. And Matt for teaching me how to solder and make a decent contact.

Thank you to Nick and Tamas who helped me get my head around CFD simulations and the joys of solving convergence errors. And Nick for being there in June 2019 when we stared into the abyss...well not really, but we did lose a lot of sleep and I'm grateful to have not been alone in the office during those weekends and late nights.

Thank you to Gareth for keeping us all sane with your wise counsel. You are the Gandalf of this school.

Thank you to my supervisor, Dries, for always being available to discuss ideas with and for always providing the resources I needed to get this thing done.

Thank you to my Aunty Sobhini for always seeing the possibilities and encouraging us all to excel.

To my brothers for being a constant source of confidence.

Thank you most of all to my mum, who has always been there for me, and has shown inconceivable patience, kindness and love at all times. I would not be much at all without her. She really is a picture of Jesus to me. And to dad, wish you were still with us, but know you are probably proud.

Contents

List of Figures

List of Tables

THIS PAGE HAS BEEN INTENTIONALLY LEFT BLANK

Chapter 1

Introduction

Flight technology has advanced at a tremendous rate over the course of the 20th century. Since the Wright Flyer first flew in 1903, aircraft designs have seen a number of leaps in capability from piston engines to jet power to high efficiency turbofans and from subsonic biplanes to supersonic fighter jets. Over the course of this development the desire to go faster has always been a driving goal. Advances in technology, often driven first by military investment, have allowed commercial flight to become commonplace, and reduced the cost, increasing accessibility and reducing the effective distance between people. Since the retirement of the Concorde, commercial aviation has been entirely subsonic, with supercritical aerofoils pushing the limits to which aircraft can enter the transonic region whilst maintaining a fully subsonic flow. Whilst military and research aerospace technology has extended well beyond the speed of sound, this regime remains elusive to civilian transportation applications. Commercial flight has mostly focused on increased efficiency, but there are compelling reasons for higher speeds, from reducing travel time, increasing range, and enabling cheaper access to space. The focus of this thesis is on the development of hypersonic vehicles for routine civilian transport, with the high-safety operations that civilian applications require. This requires good stability, control and performance across the whole flight range from conventional take-off to landing.

Section 1.1 will briefly outline the history of hypersonic research. The focus is on manned civilian endo-atmospheric missions, however some manned exo-atmospheric designs are also considered in order to establish what problems have been successfully solved. Section

1.2 will identify the gaps in knowledge required to achieve civilian hypersonic flight. The research topic and approach of this thesis is outlined in Section 1.3. Finally an outline of the chapters of this thesis is given in Section 1.4.

1.1 An incomplete history of high speed flight research

A number of major milestones are a result of American research projects led by the National Aeronautics and Space Administration (NASA). The selection presented here focuses on high speed designs that were intended to land horizontally on a runway, leaving out the many blunt, low lift to drag ratio reentry shapes, such as Mercury, Gemini and Apollo as well as ICBM payload designs.

Figure 1.1: X-15 on dry lake-bed [1]

The beginning of manned hypersonics was the North American X-15, flown in the 1960s, it achieved the fastest flight of a manned powered vehicle at Mach 6.7 (Figure 1.1). It was the first, and remains the only, endo-atmospheric hypersonic manned vehicle and the program is described in detail in references [2], [3], [4], [5]. The flight program ran from 1959 to 1968 and generated critical data for flight at extreme altitude and speed regimes. 199 flight tests were conducted and each test provided large amounts of aerodynamic, aerothermal, pilot-vehicle interaction and control data. These tests also allowed

verification of the methods of engineering calculations used to predict performance data. An example of novel technology tested was the Adaptive Flight Control System which was employed to provide stability augmentation across the very large flight envelop from high altitude control by small rocket motors to low speed un-powered deadstick landings [6]. The stability of the X-15 is outlined by Walker and Wolowicz in reference [7] from Mach 2 to Mach 6 from wind tunnel and flight measurements. The results show reasonable longitudinal performance which would be expected from the relatively conventional wing and tail layout. The lateral stability was a larger issue with unstable yaw and roll behaviour exacerbated by the lower portion of the split rudder. An assessment of the landing characteristics is provided in reference [8] which detailed good handling qualities at landing, though this was with pitch damping augmentation due to unstable oscillations identified in earlier glide tests.

Concurrently, from 1957 to 1962 the X-20 Dyna-Soar vehicle was under development. This spaceplane concept used high altitude and high speed such that centrifugal acceleration would produce a large portion of the required lift force. The air force project was envisioned for a variety of missions from reconnaissance and bombing to satellite repair or sabotage with flexibility of operation in atmosphere or in space for sub, single or multiple orbits flights [9]. As noted by Lesko [10] the maximum predicted subsonic lift to drag ratio was 4.5 which is high for a vehicle designed to withstand reentry trajectories. Contemporary reentry designs such as Gemini used high drag low lift trajectories. Although the project was cancelled in 1963, a significant amount of technical progress was made in structures, trajectory design, materials selection and novel areas such as maintaining communications whilst at hypersonic speeds [9]. As the project was cancelled, there was no experimental verification of the handling qualities of the vehicle at low speeds.

1.1.1 Horizontal Lifting Re-entry Design Flight Tests

A family of lifting reentry vehicles was also researched in the 1960s, designs that would suit reentry to horizontal landing. These lifting bodies are of interest as they were actually flight tested and large emphasis was placed on the low speed aerodynamic performance and also on pilot ratings of handling qualities. The first flight tested lifting body was the M2-F1 (Figure 1.2(a)), first flown in 1963, a teardrop shaped body designed

from a modified conical forebody and truncated aft body. This truncated aft body is characteristic of this family of vehicles and generates a large proportion of the base drag [11]. The M2-F1 lift and drag characteristics are outlined in reference [12] and results from tow tests and wind tunnel tests showed that the lift to drag characteristics were close to the maximum value of 2.8 over a wide range of angle of attack. Though low, the lift to drag ratio was shown to be sufficient for un-powered landing maneuvers. The lateral directional stability was outlined in reference [13], and deficiencies were mainly seen in the roll response, which was slow due to the large dihedral effect of the modified conical body.

(a) M2-F1(left) and M2-F2(right) [14]

(b) HL-10 at NASA's Flight Research Center [15]

Figure 1.2: NASA lifting bodies

The Northrop M2-F2 and HL-10 (Figure 1.2(b)), first flown in 1966, had very similar configurations with flights consisting of air drop from a modified B-52 as with the X-15 program, followed by a glide or powered test flight, and an un-powered approach and landing. The lift and drag characteristics obtained from flight data can be found in references [16] and [17]. This data was very important as significant differences between the flight obtained lift data and the wind tunnel obtained lift data were identified which Pyle attributed to the effect of the wind tunnel mount. These configurations had higher lift to drag ratios than the M2-F1 and were tested over a larger speed range. Multiple landing methods for the HL-10 were considered before the tricycle configuration was adopted [18]. The stability and control characteristics of the M2-F2 are outlined in reference [19] and showed good lateral and longitudinal stability and damping and good agreement for those values between flight data and wind tunnel data.

The fourth manned lifting body to be flight tested by NASA was the Martin Marietta X-24A (Figure 1.3(a)), part of a joint US Air Force NASA program. The design was the same as the unmanned X-23 PRIME, another reentry design which had been successfully flight tested in 1967 simulating a Low Earth Orbit descent and recovery. The flight tests were conducted similarly to the M2-F1, M2-F2 and HL-10 with a B-52 carrier air dropping the piloted test vehicle before it either performed a fully un-powered glide trajectory or a rocket powered maneuver followed by an un-powered landing. The lift and drag characteristics obtained from onboard accelerometer data during flight tests are correlated with wind tunnel data in [20]. The lift to drag ratio is highest, around 2.1, at the low speed subsonic region of landing.

The fifth and last lifting body considered here was the X-24B (Figure 1.3(b)). Despite the name the design was significant departure from the X-24A, featuring a flat bottom and sharp leading and trailing edges. This change in shape was intended to improve cruise performance on the assumption that improvements in materials would allow for higher temperatures on reentry [21]. An outline of the full test program can be found in reference [22], from simulator studies to tests of the XLR-11 rocket engine and the full powered test flights. The handling qualities were assessed in reference [23] and found to be good in all flight conditions, except for degraded directional stability in power on condition. The stability augmentation system prevented pilot induced oscillations in roll and yaw and these were only an issue in certain conditions with the system off. The longitudinal stability was less than the wind tunnel tests predicted with a 20-30% smaller static margin of 1 to 1.5 percent.

Saltzman et al [11] provide a comparison of the lift and drag characteristics of the five lifting body configurations alongside the X-15 and the space shuttle. The range of lift to drag for these is around 3 for the M2-F1 and M2-F2, 3.6 for the HL-10, 4.2 for the X-24A and the X-15, 4.5 for the X-24B and 4.7 for the space shuttle enterprise. These configurations are of particular interest as they are the only high Mach number configurations ever flight tested with pilots on board. They were designs that required good low speed handling, stability and performance and they provide an idea of what the requirements for horizontal landing hypersonic vehicles are. Significant challenges were identified due to the unconventional layout of the vehicles with a lack of roll control being a key issue as compared to conventional aircraft with larger aileron moment arms.

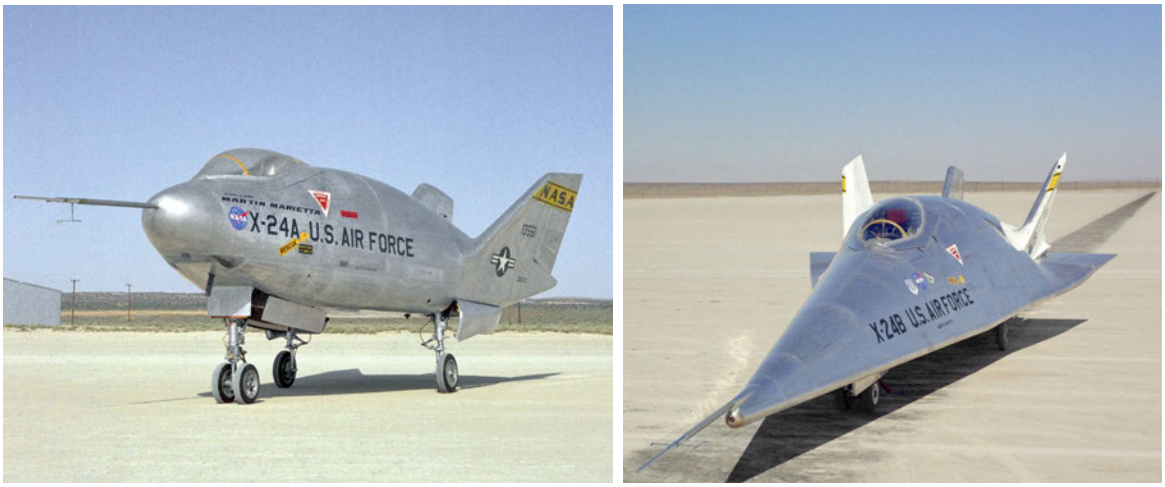

(a) X-24A [24] (b) X-24B [25]

Figure 1.3: NASA X-24 planes

1.1.2 High Supersonic USAF Designs

The XB-70 (Figure 1.4) was a proposed high altitude, high speed strategic nuclear bomber designed to fly at 70000 ft and Mach 3. Two test vehicles were built and flight tested from 1964 to 1969. It was one of the first examples of a vehicle designed to produce lift by capturing the shock wave on the underside of its lifting surfaces. Although it was only designed for Mach 3 flight this method of lift through compression is characteristic of hypersonic designs and the XB-70 flight program yielded a large amount of data in a range of fields including high altitude turbulence [26] and mountain wave effects [27], sonic boom effects [28], along with the aerodynamic performance, stability and control of a large flexible airframe in landing [29], takeoff [30] and cruise [31] conditions. The XB-70 is notable as it is the closest vehicle to a large hypersonic transport vehicle other than the Concorde to have flown. The experience gained in the high speed and high altitude environment with the size and configuration of the vehicle were unique. Wykes [31] outlines the structural modes that are excited during flight testing of the full scale flexible aircraft and correlates them to the wind tunnel data obtained with small scale rigid models with deformed shapes. The pilot ratings during landing outlined in [29] were a first of their kind for this type of vehicle which had previously only been studied using flight simulators. Longitudinal handling, control and damping of oscillations was rated highly with the control system on or off. The good speed stability was linked to the high level of static stability which leads to good control characteristics. Crosswind

landings were also found to be straightforward in the absence of turbulence [29].

Figure 1.4: XB-70 in cruise configuration [32]

The SR-71, a US air force reconnaissance aircraft in service for 3 decades from 1964, was the fastest and highest altitude air-breathing aircraft ever flown, reaching Mach 3.3 and an altitude record of 85000 ft. Although these speeds are below hypersonic, the aero-thermo-structural challenges were significant and the materials developed to overcome this were an important step towards higher speeds in a vehicle used for regular operations. The SR-71 exhibited low stability margins due to necessary compromise to reduce control trim at cruise which would have significantly impacted performance [33]. The large chines forward of the wings had a destabilising effect for longitudinal and lateral stability. As a result the vehicle required an active automatic flight control system including a Stability Augmentation System.

1.1.3 Hypersonic Airbreathing Vehicle Design Studies

Following these successful manned flight test and design programs, there was a period of lesser interest in atmospheric hypersonic flight. The lessons learned from the lifting body experiments, the X-15, the X-20 program and numerous manned space missions including Apollo were used to develop the space shuttle, the only reusable manned space plane [34]. The space shuttle program, beginning development work in 1968, flew from 1981 till 2011. From 1950 on-wards significant experience was gained in high speed hypersonic flows all the way up to the Mach 35 reentry of the Apollo. While these programs were highly successful and set performance records that are yet to be beaten, they were extremely expensive and occurred in an era where funding was high due to the cold war and the ensuing space race. These successful programs did not usher in an

age of commonplace hypersonic flight.

The quest for more regular atmospheric hypersonic flight requires advances in materials, propulsion and control among other things. The blunt shaped lifting bodies that had successfully flown had too much drag for the role of an air-breathing cruising or accelerating type vehicle. The desire for air breathing propulsion holds the promise of higher specific impulse and a larger payload delivered to space, in the case of an accelerator type vehicle, or faster and further travel around the world in the case of a cruise type vehicle. Air-breathing propulsion is desirable as it negates the need for on-board oxidiser to be carried, increasing payload fraction, although it can lead to heavier propulsion systems [35].

The US Air Force concept of the Aerospaceplane (Figure 1.5) studied in the 1960s was abandoned in 1963 as technologically unfeasible [34]. After a period of low interest in the 1970s, the 1980s saw renewed studies into low drag air-breathing hypersonic vehicles specifically for Single Stage to Orbit (SSTO) or Two Stage to Orbit (TSTO) type missions. The HOTOL study by British Aerospace Systems was one example of an air-breathing SSTO unmanned design, studied from 1981 to the early 1990s. It was to feature hydrogen fueled pre-cooled air turborocket engines which transitioned to full rocket operation [36]. It was one of a number of competing space launch designs being considered in Europe during the 1980s and early 1990s.

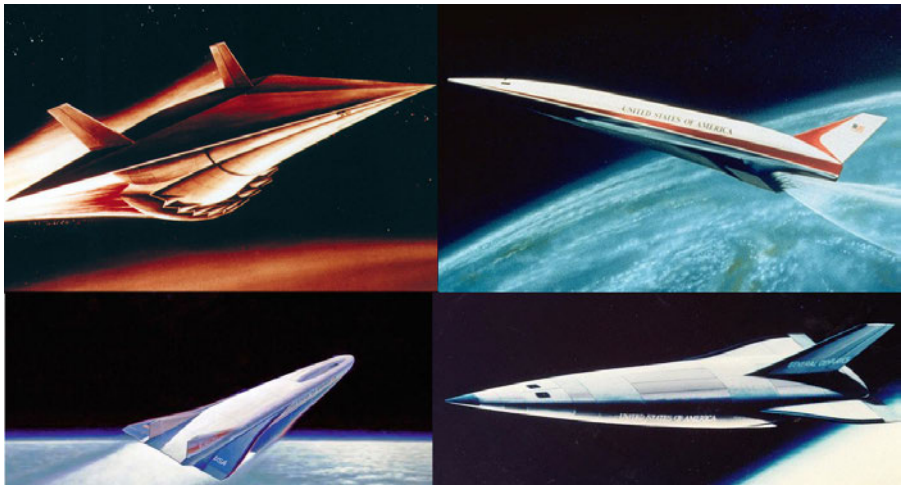

Figure 1.5: Concepts from USAF Aerospaceplane and NASP [37] [38]

A competing design was the TSTO German Sänger II design (Figure 1.6). The first stage named the EHTV (European Hypersonic Transport Vehicle) was to be powered by

a hydrogen fuelled turboramjet and reach speeds of Mach 6.8 before separation of the second stage, HORUS, a rocket propelled crewed vehicle or CARGUS, a cargo delivery system. The first stage EHTV was envisioned to be capable of operating as a hypersonic cruise vehicle with a capacity of 230 business class passengers at Mach 4.4 over a range of 10000 km [39]. Due to limited available funds from Britain for the HOTOL concept, and the likelihood that the Sänger II system would win ESA funding, interest was waning. Despite a radical proposal from the Soviet Union in 1989 to use the Antonov 225 as a first stage launcher for the HOTOL vehicle from Mach 0.8 and 30000 ft, the HOTOL concept was eventually abandoned. The Sänger II program was cancelled in 1994 due to the high cost required to complete development and more favoured competing space launch vehicles.

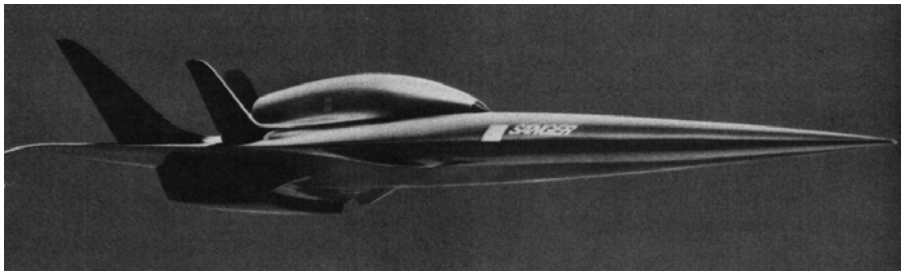

Figure 1.6: Sänger II TSTO [39]

In the meantime, in America, the National Aerospace Plane Program (NASP) was in progress. Begun in 1986, the program aimed to develop a SSTO vehicle capable of horizontal take off and landing. A number of different designs (Figure 1.5) including conical body, wing body, blended body and waverider shapes (Figure 1.7) were examined in the early stage [40]. The Rockwell X-30, a waverider based design, was chosen as a technology demonstrator for the program. The program facilitated investment in a number of key technology areas and generated a number of hardware testbeds.

The NASP was cancelled in 1993 for the same reasons as the Sänger II and the HOTOL concept, the technology requirements exceeded the current state of the art and the required budget for further work exceeded what was available [34]. A number of critical technologies were identified as limiting factors in the SSTO mission of the NASP X-30 design; boundary layer transition, propulsion performance, stability and controllability, structural and weight issues [41]. As a requirement for the X-30 was the full SSTO mission profile from launch to space and back down to a horizontal landing. Al-

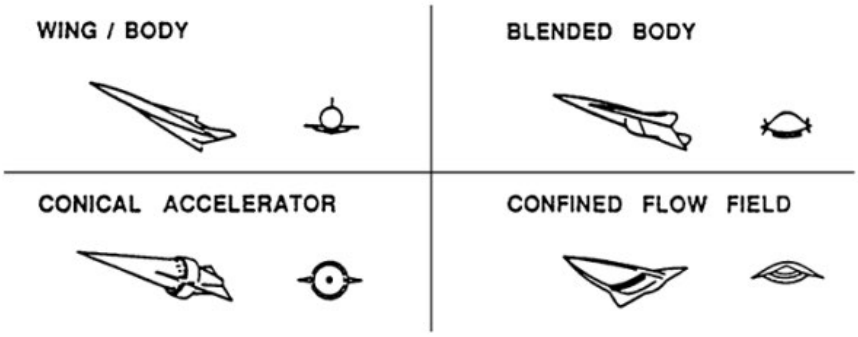

Figure 1.7: NASP vehicle designs [37]

though the low speed and high speed flight regimes could be demonstrated separately, the requirement for the X-30 to achieve both was deemed unfeasible.

The common thread with these cancelled Space launch programs is that the technological challenges were still too difficult to overcome for a full system at their time of development. Although NASA did also examine the X-33 and X-34 space launch vehicles [42], the hypersonics programs of the late 1990s and 2000s were much more focused on solving specific problems. The technology advances made in the NASP program were transferred to the Hyper-X program, which resulted in the successful X-43 scramjet tests [43].

1.1.4 Focused Hypersonic Technology Demostrators

The X-43 vehicle (Figure 1.8) was part of the NASA Hyper-X program. It was designed to fly at Mach 7 and Mach 10, rocket boosted by a first stage pegasus rocket after air drop from a B-52. The onboard scramjet propulsion system would then start and the vehicle would fly under scramjet power for 7 seconds, perform 15 seconds of parameter identification maneuvers before descending and decelerating to a subsonic splashdown [44]. The first flight, in 2001 was a failure. However the second and third flights in 2004 successfully set records for endoatmospheric air breathing vehicles at Mach 6.83 and Mach 9.68 respectively [45]. The X-43A instrumentation allowed for 3-axis acceleration and rate measurement, surface pressure measurements at 200 points, 100 temperature measurement locations both internally and surface as well as strain measurements at specific points within the vehicle. This data and the use of novel flight maneuver design [46] allowed for aerodynamic modelling and ground test data to be verified for the first

time in an airframe-integrated flight test.

Figure 1.8: NASA X-43A research vehicle [46]

The Hifire and Hyshot programs run in collaboration between Australian and US research organizations successfully flight tested scramjet technology over multiple tests [47] [48]. The test program used multiple rocket boosted vehicles to test different aspect of hypersonic scramjet propulsion. The Boeing X-51 was another air launched scramjet test which successfully flew in 2010 and set the record for the longest published scramjet powered flight at Mach 5 [49].

1.1.5 Hypersonic Civilian Transport Design Studies

The majority of the studies mentioned have focused on the high speed aspects of the hypersonic missions, with the exception of the early flight test programs for the M2-F1/F2 and HL-10 vehicles as these were designed to be piloted and landed horizontally. The military applications of hypersonic flight to weapons systems for prompt global strike capability only require performance in the high speed flight envelope. There is no need for consideration of transonic and subsonic flight. The following studies either completed or in progress by European, Japanese, Australian, Russian and US research organisations with other international partners are focused on developing hypersonic flight for civilian applications and therefore consider a wider range of flight conditions specific to transport or cheaper access to space.

The Japanese Aerospace Exploration Agency (JAXA) have researched pre-cooled turbojet powered lifting body configurations for Mach 4-5 high speed transports [50][51][52]. Some of these studies have been done in collaboration with European partners as part of the Zero Emissions High Speed Transport (ZEHST) vehicle design, a high supersonic transport vehicle designed for zero emissions using hydrogen fuel. In this case the environmental impact has been taken as a key design driver from the outset [53].

The concurrent ATLLAS I/II and LAPCAT I/II European Space Agency projects were design studies aimed toward producing civilian transportation capable of reducing flight times from Brussels to Sydney to 2-4 hrs. The Long-Term Advanced Propulsion Concepts and Technologies (LAPCAT) I project which began in 2005, ran for 3 years and was specifically focused on the hypersonic air-breathing propulsion problem and associated technologies. Examining the available advanced engine designs, such as rocket based combined cycle (RBCC) and turbine based combined cycle (TBCC) as well as different fuels such as kerosene and hydrogen, conceptual vehicle designs were created and focused experimental and numerical (CFD) studies of propulsion systems were undertaken [54]. The TBCC vehicle designs produced during the LAPCAT I program include the Reaction Engines Ltd A2 Mach 5 cruiser using a precooled hydrogen fueled tubojet and the DLR M4 blended wing body which used kerosene fueled turbo ramjets. The RBCC vehicle studies which incorporated the large fuel tank volume requirements resulted in the dorsal mounted engine design of the LAPCAT-MR1 (Figure 1.9) which exhibited higher aerodynamic efficiency than an equivalently sized vehicle with the engines mounted on the bottom surface [54].

The LAPCAT II project focused on the Mach 5 and Mach 8 designs as the most feasible, with the mission objective being a 300 passenger, or 60 ton equivalent payload carrying aircraft that can land and take-off from existing runways. As no Mach 8 design from LAPCAT I was sufficiently developed multiple designs were examined from different research groups, which were narrowed down to three, a TBCC lifting body and wing design from ONERA (Figure 1.10(b)), an axisymmetric design from MBDA Missile Systems (Figure 1.10(a)) utilising both RBCC and TBCC propulsion and a dorsal mounted TBCC design from ESTEC [56]. The Mach 5 A2 cruiser design was retained for more detailed numerical studies as it was further in the development cycle [57]. Wind tunnel tests of the A2 vehicle's scimitar engines were conducted as well as detailed analysis of

Figure 1.9: LAPCAT I MR1 design [55]

the vehicle structure and aero-elastic properties.

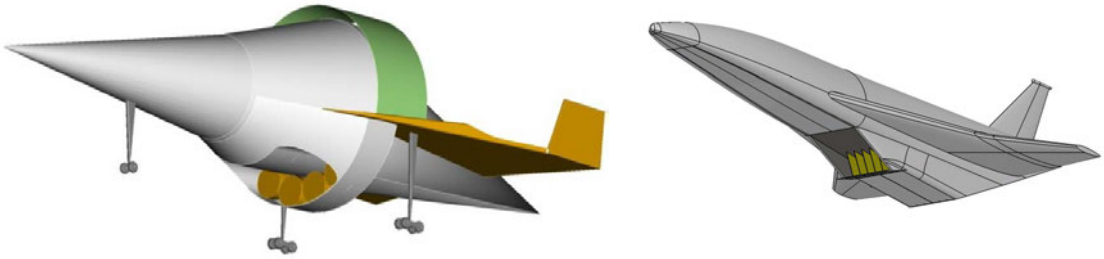

(a) MBDA axisymmetric design [57]

(b) Onera lifting body [58]

Figure 1.10: LAPCAT II designs

The unconventional MBDA axisymmetric design for the Mach 8 waverider is studied by Falempin et al [59], and while it exhibited good aerodynamic efficiency and propulsive performance, an analysis of the full integrated vehicle (nose-to-tail) performance indicated poor fuel efficiency and range, though there was some scope for improvement. The ONERA TBCC design, outlined by Serre and Defoort in [58], is built on the French Prepha design of the 1990s which was designed for a SSTO mission. Their design process resulted in a 900 ton vehicle with a 12500 km range. The ESTEC MR2.4 design (Figure 1.11), outlined by Steelant et al in [60] and [61], is an evolution of the LAPCAT I MR1 dorsal engine concept. The dorsal mounted engine allows the windward bottom surface to be purely designed for lift, maximising aerodynamic efficiency. The bottom surface is designed from waverider principles to obtain efficient compression lift at cruise and the intake to the dual mode ramjet engine was designed using the stream tracing method

from an inward turning elliptical generating body. Wind tunnel tests from Mach 3.5 to Mach 8 confirm the comparatively high aerodynamic performance of the shape with the L/D ratio greater than 4 across a wide range of Mach number, but also identified issues with the trim pitching moment and other stability and control issues requiring a shift in CG or re-sizing of canard shape [62].

Figure 1.11: LAPCAT MR2 vehicle [60]

The ATLLAS I (Aerodynamic and Thermal Load Interactions with Lightweight Advanced Materials for High Speed Flight) and ATLLAS II programs ran concurrently with the LAPCAT I and II projects and focused on the materials problem of high speed flight. The projects aim to develop new materials capable of withstanding the high temperatures and tight weight requirements of a high speed transport vehicle. Some of the advances in materials design obtained from these programs can be found in the following references [63] [64] [65] [66].

The LAPCAT and ATLLAS projects led to the HEXAFLY program, which aims to develop a small scale flight demonstrator of the Mach 8 cruise vehicle. The HEXAFLY (High Speed Experimental Fly Vehicles) project took the MR-2 LAPCAT design and modified it to produce a vehicle suitable for an experimental flight test. The modifications made are outlined by Steelant et al in [67], including changes to the internal engine flowpath, the undersurface from the pure waverider shape and the sizing of the control surfaces to achieve stable flight during the flight test. The purpose of this flight test is to validate the numerically predicted performance of the materials, propulsion system, aerodynamic databases and flight controllers from the preceding LAPCAT and ATLLAS

projects. The Experimental Flight Test Vehicle (EFTV) is instrumented with a large number of sensors including thermocouples, heat flux sensors, pressure sensors and high temperature strain gauges [67] which will allow the conditions during the test to be compared with the numerically predicted results outlined by Pezzella et al in reference [68].

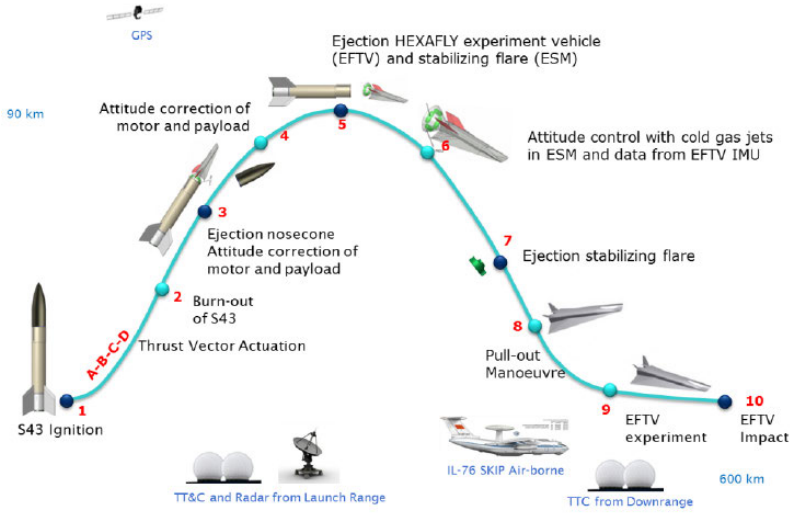

Figure 1.12: Hexafly test trajectory [68]

The follow-on HEXAFLY-International project continues the design process of the test vehicle and is intended to culminate with the flight test, the trajectory of which is shown in Figure 1.12. The scramjet flowpath was removed from the vehicle configuration to be tested under HEXAFLY-International and the specific material choices and structural design, internal component layouts and the design of the nose cap is outlined by Favaloro et al [69]. The work covered in this thesis forms part of the HEXAFLY-International project and the further details of the vehicle will be outlined in Chapter 2.

1.1.6 Off-Design and Low Speed Studies

Through this outline it is clear that high speed performance has been the key driver behind the designs that have been studied and tested. Though some studies, especially those that were intended for piloted flight tests which would land horizontally such as the X24, HL10 and M2, have focused on landing and general low speed handling qualities, these are the exception rather than the rule. There are a number of studies, however, which have quantified the low speed stability and control of hypersonic vehicle designs

of a number of different types.

Bowman and Grantham [70] used the 7 by 10 foot Langley wind tunnel to examine a X-15 like configuration at Mach 0.1 and 0.27. They tested a number of different combinations of horizontal and vertical tails to quantify the contribution of each to overall performance and stability. They found that the asymmetric flow off the forebody at high angles of attack resulted in large yawing moments resulting in unstable yaw stability. This is a common characteristic of slender vehicles at high angles of attack [71].

Freeman and Jones [72] examined two hypersonic cruise configurations, one with a distinct wing and body and the other with a blended body. Though the designs featured relatively large span to length ratios and therefore would only be considered for the lower end of the hypersonic range, they suffered from significant longitudinal stability problems. These were due to the ineffectiveness of the horizontal control surfaces due to main wing downwash and modifications to the position of the horizontal tail were required. The blended wing body featured no separate horizontal tail and also suffered from longitudinal instability.

Keating and Mayne [73] tested a number of waverider shapes at low speeds to determine the longitudinal and lateral static stability. They noted that the while the centre of pressure at high speeds for typical waverider shapes was towards the rear of the wings, the low speed centre of pressure was further forward. This results in a natural instability at low speeds, especially if the centre of gravity of the vehicle has been chosen to give low trim control deflections at the high speed flight condition. As a result, longitudinal stability was found to be an issue for many of the shapes tested, while lateral results showed adequate stability due to the vertical stabiliser.

Lamar and Fox [74] studied a highly swept delta wing at a range of speeds from subsonic to hypersonic speeds. They used both theoretical predictions and experiments to show the validity of potential flow methods with vortex corrections at subsonic speeds as well as hypersonic tangent cone methods at high Mach numbers for this class of slender vehicle.

Penland and Creel [75] examined a hypersonic lifting body configuration designed for a cruise or acceleration mission at low speeds and found that, due to high pitch stiffness, there was a design trade-off between shifting the CoG position rearward to achieve

trimmed flight with sufficient lift and lateral directional stability issues which were made worse by this shift. Their tests were conducted in the Langley 12 ft low speed wind tunnel and examined a number of different configurations of tail surfaces and canard designs. The canard was found to be ineffective at producing additional lift and also at alleviating the necessary trim deflections. This was due to the large static stability margin caused by the forward CG position. As expected, the vertical tail significantly improved the lateral stability, while the canards also caused an improvement in lateral stability at medium to high angles of attack, possibly due to vortex shedding impinging on the aft vehicle body.

Jackson et al [76] developed an aerodynamic model for simulation of the HL-20 lifting body configuration subsonic performance using data from wind tunnel experiments and aerodynamic calculations. Spencer et al [77] examined modifications to the HL-20 lifting body cross sectional shape as well as modifications to the camber of the body to improve the subsonic pitching moment characteristics. Changes to the vertical tail were also examined to improve the lateral stability characteristics. The addition of a forebody canard was also examined, and while it improved pitch moment characteristics, it limited the maximimum L/D ratio. Overall Spencer et al showed that improvements could be made by careful shaping of the body and vertical tails.

Gatlin [78] studied an axisymmetric body similar to the Mach 8 design of the LAPCAT project in a 14 by 22 foot subsonic wind tunnel using oil flow and force measurements. The conical body with engine intakes at the maximum thickness was also fitted with delta wings towards the rear of the vehicle. The vehicle was marginally stable in pitch but exhibited large lateral forces at high angles of attack due to asymmetric vortex shedding. It was found that these forces could be reduced by blunting the tip of the conical forebody or with the addition of a canard surface.

Hahne and Coe [79] studied a similar axisymmetric accelerator body along with a waverider and a wing body configuration similar to the Onera LAPCAT Mach 8 design. They highlighted the lateral directional issues that arise at low speeds due to the vortex systems caused by the slender forebodies and highly swept wings. They found that reducing the magnitude of these vortex systems by adding a canard surface improved the static stability as it ensured that lateral forces were within the control envelope, but that this reduced the dynamic stability. Low roll damping due to the small inertia

about the roll axis along with high lateral stiffness could also lead to wing rock problems which would require a stability augmentation system to control. The longitudinal stability of these configurations was very high due to the rearward locations of dedicated lifting surfaces. This large pitch stability results in a negative pitching moment requiring the trailing edge surfaces to be trimmed upward, significantly reducing lift. This was alleviated with the addition of the deployable canard surface.

There were also a number of test programs to flight test hypersonic vehicle designs. Pegg et al [80] examined the effect of modifications of the wing shape on a waverider configuration at low speeds. Two Mach 5.5 vehicles were designed using waverider principles, one with a cranked wing and the other straight. The straight wing design was the basis of the NASA LoFlyte test program which aimed to flight test a hypersonic cruise vehicle design at low speeds. The vehicle development is outlined by Lewis et al [81] including the design of the novel neural adaptive controller to be incorporated. Hahne [82] outlines the stability and control characteristics detailing the large impact of the vortex systems. The positioning of the vertical tails affects the burst position of the primary vortices which can cause a large pitch up moment at a much lower angle of attack than otherwise would occur. The test program of LoFlyte (Figure 1.13(a)) is detailed by Blankson et al [83] as well as the future use of the platform for further experiments on integrated hypersonic vehicle designs.

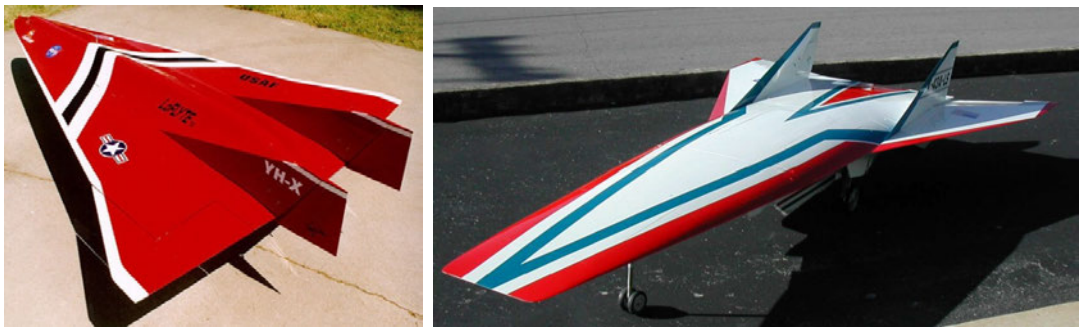

(a) LoFlyte Test Vehicle [84] (b) X-43A-LS UAV [85]

Figure 1.13: Low speed flight test vehicles

The X-43A-LS (Figure 1.13(b)) was a low speed version of the X-43A vehicle that was flown in 2003 [86]. The purpose was to examine the low speed handling of the X-43 as part of a long term goal to produce a vehicle that can land and take-off horizontally [85]. Some modification was required to the X-43A shape including a large increase in

the area of the horizontal stabilators. This shifted the centre of lift rearward, allowing the CoG to also be moved rearward, reducing the required ballast. The stabilators are all-moving on the X-43A, which would not work at subsonic speeds due to the shift forward in the aerodynamic centre, so the larger stabilators were fixed and trailing edge control surfaces were added. The flights were successful and showed good flying qualities after modification.

1.2 Towards a Hypersonic Civilian Transport

The complications of high-temperature flows on the form of the shock layer, the interactions with the boundary layer, temperature gradients and heat transfer to the surfaces, among many other issues have long presented significant challenges to the modelling of hypersonic flows and the subsequent design of hypersonic vehicles.

The highly integrated nature of the volume providing body, the lifting surfaces, compression and expansion surfaces of the propulsion system and the required size of hypersonic propulsion systems presents a challenge to traditional optimization schemes which allow these components to be improved in isolation. The interconnected nature of hypersonic vehicle designs causes any change to any particular component to result in performance changes in all the other components. A multi-disciplinary optimization approach as used by Bowcutt [87] is required in the hypersonic design process.

These challenges are the focus of most on-going hypersonic vehicle design research for good reason. However despite these challenges, as stated by Anderson in [34], "it is difficult to see a hypersonic civilian transport never becoming a reality". As hypersonic designs mature and civilian applications are developed further, the need to be able to land and take-off from a conventional runway will require low-speed performance and stability considerations to be incorporated into the overall design and optimisation process.

This work has endeavoured to characterise the aerodynamic stability of an actual hypersonic vehicle design. The results have been used to validate numerical analysis tools for use in the development of new hypersonic waverider designs. Current hypersonic vehicle design studies are mainly focused on the many significant challenges presented by the hypersonic flight regime. However for the most part these examine existing hypersonic vehicles which were designed only for cruise performance. Where off-design conditions

are considered, the focus is most often on the performance, characterised by the lift to drag ratio. A few studies have looked at stability of hypersonic vehicles however these have only tested the static stability, not the dynamic which has a large influence on the handling qualities of a design [88].

This work aims to introduce the necessary requirement of low speed stability to the hypersonic vehicle design process with the goal of regular civilian transport flights. The low speed regime presents the greatest departure from the aerodynamic flows that hypersonic vehicles will experience at the design cruise condition. As this is currently the dominant design point for most studies, the low speed aerodynamic regime will potentially present the greatest stability challenge to current hypersonic vehicle designs.

1.3 Research Proposal

This work aims to answer the following questions:

- What are the low speed static and dynamic stability characteristics of a typical hypersonic cruise vehicle?
- Are the current computational tools capable of providing valid answers for the aerodynamic static and dynamic stability coefficients of a hypersonic vehicle?
- Can rapid aerodynamic analysis tools be used in the vehicle design process to include low speed stability in the design of hypersonic waverider configurations?
- What impact will the low speed stability criteria have on resulting designs and their high speed performance?

These questions will be answered through the use of computational fluid dynamics tools for high fidelity numerical analysis, both static and dynamic, on an existing configuration, the Hexafly-Int EFTV vehicle. The results of this analysis will be verified by a wind tunnel testing campaign utilising low cost 3D printed models and novel small scale dynamic wind tunnel testing techniques. Finally, an optimisation routine will be developed using low fidelity vortex lattice method panel codes, validated against previous wind tunnel tests to produce waverider shapes with improved low speed stability characteristics.

1.4 Thesis Outline

The majority of the background literature and past studies have been given in the preceding sections. The work presented here is broken down into chapters by methodology used to obtain data. Although the majority of background research has already been presented, relevant studies and references are mentioned within each chapter in aid of analysis of results or justification for choices of methods and assumptions. While an attempt has been made to chronologically structure the chapters, some of the results from wind tunnel testing have impacted the numerical analysis and vice versa as these were largely done in tandem.

Thesis chapter outlines:

Chapter 1 has introduced the motivation for this work, a brief history of hypersonic research and development as well as the research proposal for the work conducted herein.

Chapter 2 outlines the design methodology of hypersonic vehicles, waverider principles and a detailed overview of the Hexafly vehicle design. The frames of reference, stability criteria and standard nomenclature are also described.

Chapter 3 describes the high fidelity numerical simulations conducted using the CFD code ANSYS Fluent, both static and dynamic.

Chapter 4 details the methods and results of the static wind tunnel testing that was carried out.

Chapter 5 covers the model design and construction of a free-to-pitch dynamic testing model. The system identification techniques and the results obtained are presented.

Chapter 6 outlines an initial optimisation study of a hypersonic waverider to maximise longitudinal static stability at low speeds while maintaining cruise lift to drag ratio. The compatibility of these two design objectives is also examined.

Chapter 2

Vehicle Design

This chapter introduces the general problem of hypersonic vehicle design. As established in Chapter 1, vehicles designed to fly at hypersonic speeds in the atmosphere are highly varied in shape and mission. The first section of this chapter will break these vehicles into general classes before homing in on the class of interest to civilian transport designs, the air-breathing cruise vehicle. The methods of designing hypersonic waveriders will then be discussed in Section 2.2 which will be used in Chapter 6. Section 2.2 will also outline a particular type of hypersonic cruise vehicle design of interest referred to as the dorsal engine waverider in this thesis. Finally, the Hexafly-Int vehicle will be described in detail as it is the subject of the CFD and wind tunnel tests carried out in Chapters 3, 4 and 5. The key results of this thesis will be the dynamic stability parameters of the Hexafly-Int vehicle at subsonic speeds from CFD and wind tunnel testing which have not been examined for a hypersonic vehicle previously. The reference system to be used and an outline of the stability parameters will be given at the end and used throughout the rest of the thesis.

2.1 Hypersonic Vehicles

The definition of hypersonic flow is dependent on what particular flow phenomenon we choose to focus on. For example this can be structural heating or the dissociation of the chemical components of air or others [89]. The definition of hypersonic can also be highly dependent on flight altitude due to dependence on the density, temperature and

composition of the surrounding air. The speed of Mach 5 is often used but significant temperature effects can be observed at lower or higher speeds depending on a number of factors, including the shape of the vehicle. As a result, the term hypersonic vehicle can be applied to a very broad range of vehicles. This includes blunt re-entry vehicles such as the Apollo command module, Vostok 1 and the Gemini reentry module, winged reentry vehicles such as the HL-10, M2-F1 and M2-F2 described in Chapter 1 and the Space Shuttle, and endo-atmospheric cruise vehicles such as the X-15 or the X-43 test vehicles. Hirschel and Weiland classify these vehicles into three broad classes [90]. First there is the Winged Re-entry Vehicles (RV-W), which includes the X-20 Dynasoar, the space shuttle orbiter, and the lifting bodies outlined in Chapter 1. Next is the Non-Winged Re-entry Vehicles (RV-NW) which covers the low lift, high drag, blunt bodies, used for high Mach number manned reentry from orbit such as the Apollo command module. Last, and of most importance for this thesis, are the Cruise and Acceleration Vehicles (CAV) covering designs with low drag and high lift which fly at hypersonic speeds within the atmosphere. The X-15 is the only example in this class of a manned vehicle which has flown. Design studies into hypersonic civilian transport often examine air-breathing vehicles in the CAV class as they offer the highest potential fuel efficiency for a hypersonic vehicle. The CAV class is also often proposed as part of designs for cheaper access to space forming the first stage of Two-Stage To Orbit (TSTO) platforms such as the Sänger described in Chapter 1. The rest of this thesis will focus on the CAV class of vehicle, and the cruise aspect in particular, as a solution to the high speed civilian transport challenge.

The defining characteristics of the CAV are a very slender planform, low angle of attack at cruise, low drag and high lift [90]. Figure 2.1 is reproduced from reference [91] and shows the typical slenderness ratios across the Mach number range for classical aircraft, with straight wings, swept wing types, and slender types with low span delta planforms or lifting bodies. The typical slenderness ratio (span/length, b_{ref}/L_{ref} in Figure 2.1) is less than 0.3 in the hypersonic regime.

No operational vehicles in the hypersonic CAV class currently exist, although a number of significant design studies of vehicles in this class have been conducted such as those mentioned in Chapter 1 (NASP, HOTOL, LAPCAT and Hexafly). This class of vehicle presents a number of unique challenges. The thermodynamic environment is particularly

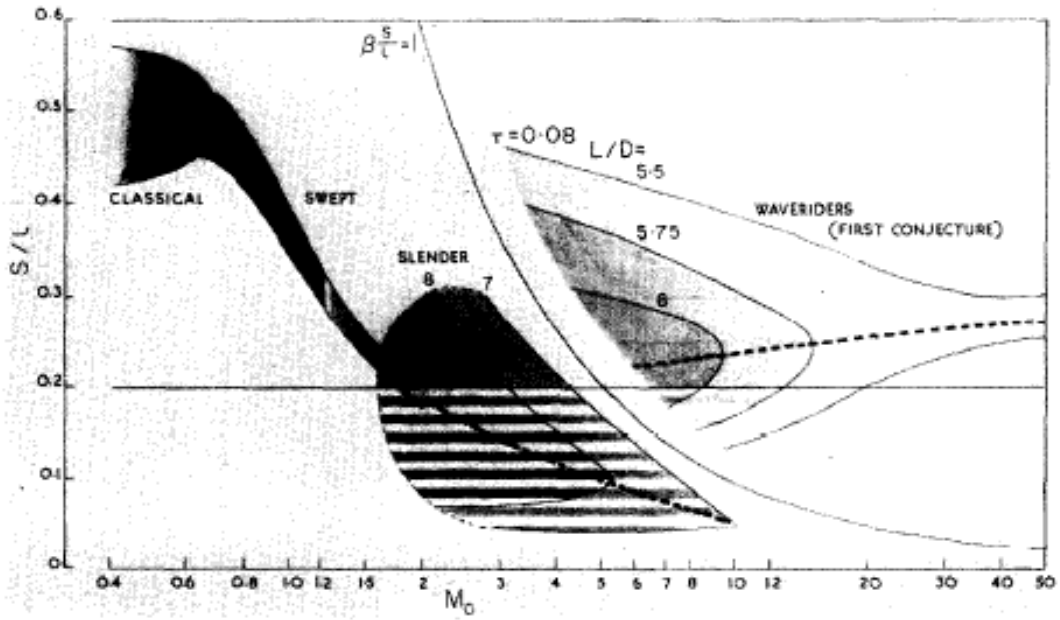

Figure 2.1: Slenderness ratios of typical aircraft designs [91]

difficult as, unlike the other classes, the requirement for low drag leads to sharp leading edged designs which fly at low angles of attack. This results in extremely high wall temperatures, in excess of 2000 K in the case of the Sänger II design [90]. One aspect of CAV type vehicles which is appealing to designers is the potential to use air-breathing propulsion systems to greatly improve fuel efficiency, as compared with rocket engines. This leads to a requirement for a full propulsive flowpath to be integrated into the airframe from intake to exhaust. In addition, the cruise Mach numbers go beyond the operating envelop of current propulsion systems such as turbojet engines and require Scramjet propulsion beyond Mach numbers of 5 as shown in Figure 2.2 reproduced from reference [92].

Scramjet engine designs remain the subject of experimental studies and only a few have ever flown such as the X-43, X-51 and the Hyshot experiments as covered in Chapter 1. Rocket Based Combined Cycle (RBCC), Turbine Based Combined Cycle (TBCC) engines and precooled turbojet engines are also propulsion systems that are under consideration [93] [64].

To add to these challenges, the maximum achievable lift to drag ratio decreases significantly as Mach number increases. This is due to the strong shocks and large viscous effects highlighted by the empirical relation developed by Kuchemann [94], using data

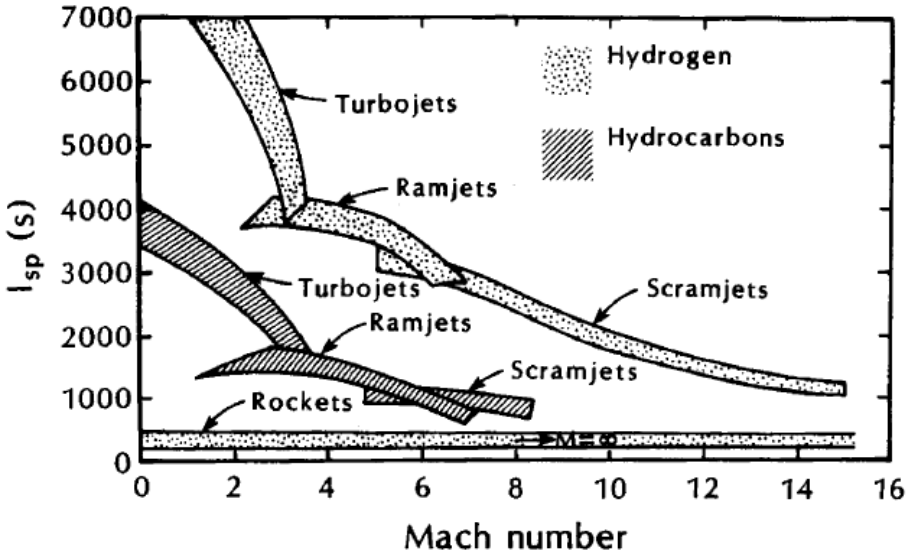

Figure 2.2: Operating Mach numbers and fuel efficiency of various engine types [92]

from flight tests and wind tunnel experiments, given in equation 2.1.

At Mach 10 this relation results in a lift to drag ratio of 5.2, which is significantly lower than subsonic and supersonic aircraft whose lift to drag ratios generally exceed 14 [95].

$$\frac{L}{D}_{max} = \frac{4(M_\infty + 3)}{M_\infty} \tag{2.1}$$

Each of these issues, and many others not covered here, will require novel solutions to produce the required performance to achieve a viable hypersonic CAV design. Structures will need to be developed that can endure the challenging thermal environment. Propulsion systems will need to be designed that can operate over the full range of flight from take-off to hypersonic cruise or acceleration. There are also significant flight control issues that are unique to hypersonic flight.

The waverider concept first proposed by Nonweiler in reference [96] has long been viewed as a possible solution to the problem of low aerodynamic efficiency. The concept, detailed in Section 2.2, is to design a vehicle shape based on the flow around a known shock generating body such that the leading edge of the vehicle contains the shock from the generating body under its bottom surface. Nonweiler proposed the use of a wedge shape to generate the shock and many other shapes have since been proposed.

Bowcutt optimised cone derived waverider shapes to gain performance improvements on Kuchemann's empirical relation (equation 2.1) obtaining a performance limit governed by equation 2.2. At Mach 10 this corresponds to a lift to drag ratio of 7.2. The relation is shown in Figure 2.3 reproduced from reference [97]. The waverider shape provides the potential for higher lift to drag ratios as the vehicle uses the shock generated from the leading edge to increase lift while reducing the wave drag by designing the top side as a freestream surface.

$$\frac{L}{D}_{max} = \frac{6(M_\infty + 2)}{M_\infty} \tag{2.2}$$

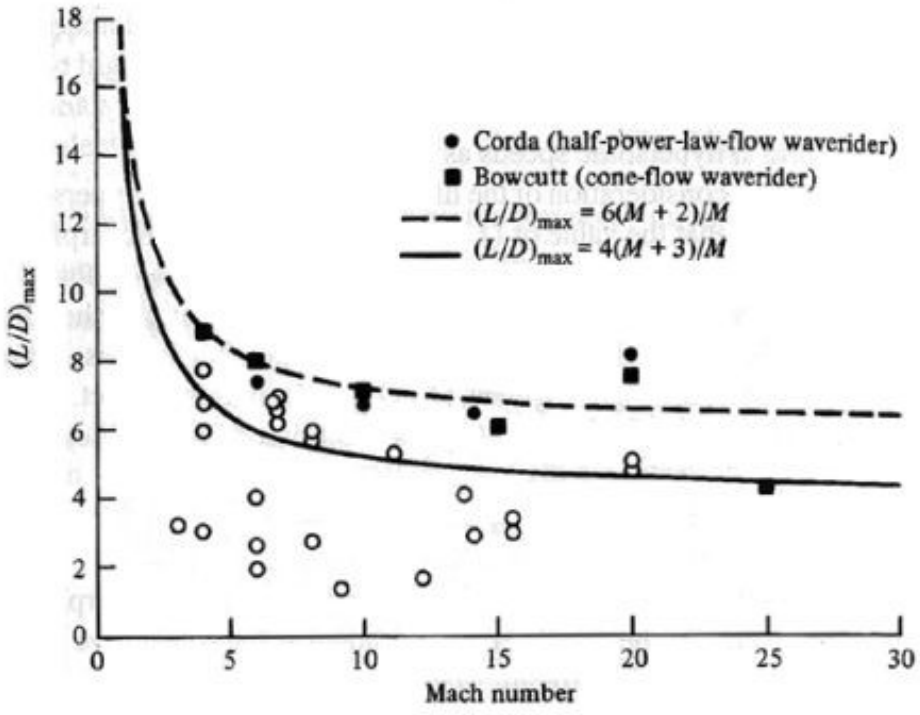

Figure 2.3: Empirical lift to drag ratio against Mach number of hypersonic designs [97]

At cruise speeds, the various issues outlined above present a highly integrated design challenge requiring a multi-disciplinary approach, such as that used by Bowcutt [87] and Tsuchiya et al [98].

The resulting designs are highly integrated by nature, generally with no distinguishable boundary between lifting surfaces, fuselage, and propulsion intake and exhaust components [87]. The focus of this thesis is on characterising and improving the low speed

stability of these hypersonic cruise type vehicles. A fully stable flight envelope from take-off to landing is a requirement of all civilian aircraft designs according to the US Federal Aviation Authority (FAA) regulations [99]. The following chapters focus on promising hypersonic design methods with high aerodynamic efficiency as a successful civilian transport vehicle will need to have. The waverider concept has shown good potential for producing good aerodynamic efficiency and this thesis will focus on the low speed aerodynamics of waverider designs. In particular the static and dynamic low speed stability of the Hexafly-Int vehicle, which is based on a modified waverider design, will be analysed. The penultimate chapter of this thesis will use waverider design methods to determine what waverider shapes lead to improved low speed stability properties.

2.2 Hypersonic Waveriders

A waverider is essentially any vehicle with an attached shock along the length of its leading edge. Nonweiler first proposed the waverider concept in 1959 [100]. His design used the shock generated by a 2D wedge shape in order to analyse the flow over a delta wing shape. The resulting shape is the so-called Caret wing waverider shown in Figure 2.4 reproduced from reference [96].

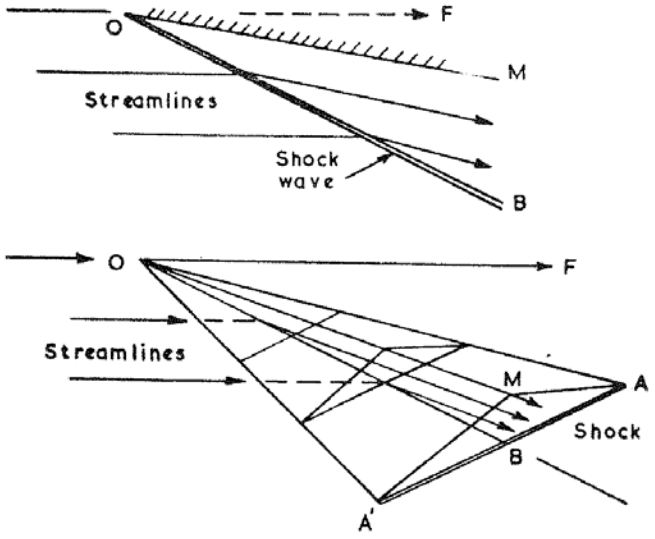

Figure 2.4: Inclined shock derived caret wing waverider [96]

The principal of the waverider uses the known flow behind a shock generating body and carves a body out of the flowfield. If the leading edge is coincident with the shock surfaces of the flowfield, and the lower surface is made from streamlines behind the shock, then

the resulting vehicle will contain the same shock surface on its lower side at the design Mach number. This results in high pressure on the lower surface with no leakage to the upper surface through the attached shock resulting in high lift to drag ratios [101]. For such designs, the upper surface is generally defined by a freestream surface projected from the leading edge to reduce wave drag. The simplest examples of this style of design are the caret wing waverider developed from the shock behind a two dimensional wedge shape and the cone derived waverider developed from the shock behind an axisymmetric cone. The shape that is chosen must have an analytically or numerically determined flowfield at the design Mach number.

In the case of the shock generating wedge shape, the flowfield is known analytically from the oblique shock relations. We define our reference system origin at the shock generating body leading edge, with the X axis pointing downstream, and the Y and Z axes in the spanwise and normal directions respectively. An upper surface shape is chosen at the proposed rear Y-Z plane of the vehicle to be designed and projected forward to the oblique shock plane. In the case of a caret wing waverider this shape is a simple delta meeting at an apex along the X axis. The projection of this shape forward in the freestream direction forms the upper (freestream) surface of the wings. The intersection of the projection with the oblique shock plane forms the leading edge curve of the wing. Streamlines are calculated from points on the leading edge chordwise to the rear Y-Z plane using the analytically known flow behind the oblique shock to obtain the lower (under) surface. The resulting upper and lower surfaces form a wing which will, under the same flow assumptions as the known flowfield, perfectly contain a shock wave generated from the leading edge on the bottom side of the vehicle at the design Mach number. This process is shown in Figure 2.5 reproduced from [102] for a general flowfield generating body (field-maker body).

The assumptions of the analytical relations used to generate the known flowfield will limit the extent to which such perfect shock containment can be achieved. For example, if inviscid flow is assumed in the flowfield calculations, then the resulting shape will behave differently in a real world viscous flow. The particular problem of the inviscid assumption in the generating flowfield was highlighted by Eggers and Sobieczky in reference [103] where the inviscid generated waverider shapes showed a significant 30% reduction in aerodynamic efficiency when viscous effects were accounted for. The work of Bowcutt

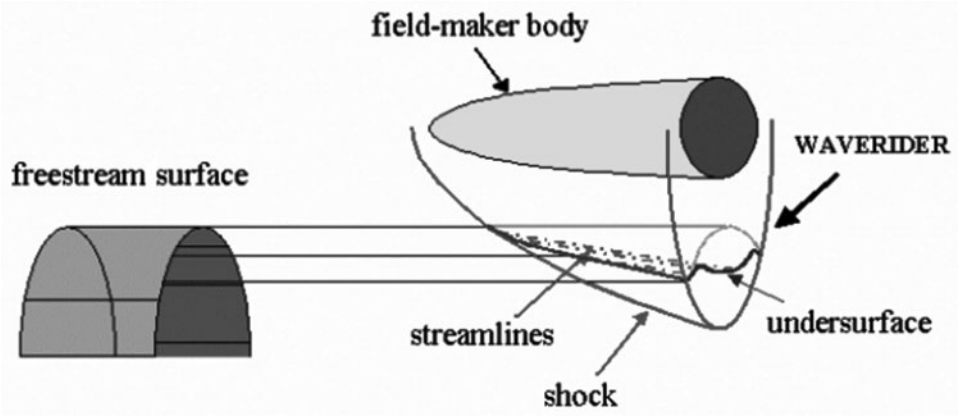

Figure 2.5: Waverider shape design method [102]

in [95] incorporated viscous effects into the shape optimisation procedure in order to produce waverider shapes with better performance in real world viscous flows.

2.2.1 Development of Waverider Designs

Since the introduction of the waverider concept, numerous additions have been made to the types of generating flowfields in an effort to extend the generality of the technique. The original caret wing type waveriders produce delta wing planforms with an anhedral droop to contain the shock. The next flow type to be added was the axisymmetric shock around a circular cone presented by Jones et al [104]. The flowfield behind the cone is determined from the Taylor-Maccoll equations which provide an inviscid solution or through a more general method of characteristics. Jones et al also proposed a flow drived from an Ogive body and outlined the use of expansion surfaces to improve the lift over the upper surface from the freestream condition. Using these methods Jones et al were able to produce more versatile shapes with better volumetric efficiencies and more control over the aerodynamic properties than the original wedge derived waverider.

Rasmussen further extended the conical method to include non-circular cones and inclined cones [105]. He developed the approximate relations that determined the flow field behind the generating bodies and the resulting shapes exhibited good lift to drag ratios. The caret waverider type was also used to add a vertical stabilising fin to the upper surface which contained shocks between its leading edge and the leading edge of the wings.

As mentioned, Bowcutt incorporated the effects of viscosity into an optimization of

conical waverider shapes based on aerodynamic and volumetric efficiency [95]. The work also considered the requirement for blunt leading edges based on temperature limits and accounts for the impact on the pressure distribution over the surface. Viscous effects are accounted for based on laminar and turbulent flow with a transition point determined by the local Reynolds number. The results showed that high lift to drag ratios could still be achieved with viscous effects accounted for, and also showed how the viscous effects impacted the resulting optimal shapes due to the impact of skin friction drag.

Cockrell examined two different Mach 4 optimised waverider configurations, one with straight wings and one with wing tips cranked upwards [101] from Mach 2.3 to Mach 4. He also examined the impact of various integration aspects such as canopy, control surfaces and propulsion intakes. The results of computational and experimental studies showed good aerodynamic performance with lift to drag ratios up to 6 for both configurations, and with integration of real aircraft components. However the results also showed lateral and longitudinal stability problems though the cranked model showed better lateral stability. The addition of a vertical tail surface improved the lateral stability for both designs. The longitudinal stability remained an issue to be solved.

Sobieczky et al [106] created a method of inverse design for conical derived waveriders that specifies the shock profile at the rear exit plane of the desired vehicle. This method, known as the osculating cones method, uses the specified shock shape, a specified upper surface shape and the freestream velocity to generate local conical flowfields in planes along the shock curve. At each point along the curve a tangential circle is produced in the rear Y-Z plane that is used to define a generating cone that produces the streamline in the plane normal to the tangential point that starts at the leading edge. This streamline is generated by solving the Taylor-Maccoll equations in that plane for that particular cone. A rear view of this procedure is shown in Figure 2.6, reproduced from [93]. The method assumes that the crossflow between osculating planes is small.

This method allows a large range of shapes to be designed which are amenable to shock flow containment. It can also be used to produce forebody shapes as part of a full integrated hypersonic waverider. By specifying the shock curve at the exit plane, the shock on lip condition at the engine inlet can be met for a range of inlet and vehicle shapes. The method also allows control of the span and length of the vehicle with appropriate selections of upper and shock surface curves. Selection of smooth curves

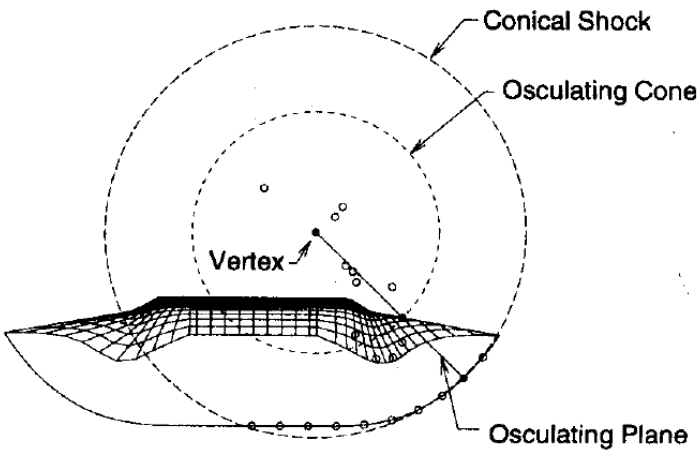

Figure 2.6: Osculating Cones waverider method [93]

to define the upper and shock curves in the exit plane will ensure that crossflow effects which could violate the osculating plane assumption are minimised.

Rasmussen and Duncan examined the use of power law bodies to overcome the problem of impractically thin conical waverider shapes at very high Mach numbers [107]. The method solves for the flowfield behind power law defined bodies using hypersonic small-disturbance theory.

Mangin et al [108] used higher fidelity computer codes to solve for the flowfields behind these power law derived waveriders and included viscous effects to compare the aerodynamic performance with conical flow waveriders derived from the Taylor-Maccoll solution. The results demonstrated the large impact of viscosity effects on the calculated lift to drag ratio. As the cone half angle decreased the difference grows exponentially with the effects of viscosity limiting the lift to drag ratio significantly.

Goonko et al [109] used the flowfield inside a converging duct to produce a generating flowfield. The resulting shapes demonstrated higher lift than comparable conical waveriders but a lower lift to drag ratio. The shape is also ideal for interfacing with converging inlets as part of a hypersonic vehicle forebody.

Rodi extended the osculating cones method to use the power law generating body [110], referred to as the osculating flowfield method. In the absence of an analytical solution to the flow behind a power law body, a computational Euler solver is used to compute the flowfield. This allows for convex or concave generating bodies which increases the flexibility in designing the vehicle, however care must be taken with variation of generating

bodies across the shock curve to ensure crossflow remains limited.

Rodi also developed a vortex lift waverider by modifying the upper surface design to produce vortex structures behind the leading edge [111]. This method uses the osculating flowfield generating method to design the lower surface of the waverider. A number of methods to induce vortex flow over the upper wing surface are examined including extended high sweep leading edges and via shock induced separation bubbles at increased AoA. The methods demonstrated improved lift performance and potential for use in modified boost glide reentry trajectories.

2.2.2 Off-design Performance of Waveriders

Waveriders are specifically designed for a particular cruise Mach number. The performance at off-design Mach numbers has been the subject of a number of studies, which have for the most part focused on the aerodynamic efficiency. These include studies by Eggers et al, on the off design performance of the WRE 12 vehicles shown in Figure 2.7 [112], Long, who examined Rasmussen's elliptical cone waverider type at a range of Mach numbers for a design Mach number of 4 [113], and Takashima and Lewis who optimised an integrated cruise waverider over a range of Mach numbers for a cruise Mach number of 10.

Eggers et al used an Euler code with viscous corrections to analyse the performance of two version of their WRE 12, a Mach 12 designed waverider, the pure base waverider, and a version modified to produce practical trailing edges [112]. They found that the lift to drag ratio for the pure waverider was invariant from Mach 6 up to the design Mach number of 12, but improved as the Mach number decreased below 6. This was due to expansion flow around the leading edge as the shock became detached below Mach 6. In inviscid simulations the lift to drag performance of the modified WRE 12 actually decreased with Mach number due to the expansion flow over the upper wing. The expansion flow increases lift but also increases drag, reducing the overall ratio. However, with viscous effects accounted for, both the pure and the modified waverider showed much lower lift to drag ratios, but in this case, the modified WRE aerodynamic performance actually improved as Mach number decreased. They also note the shift in the neutral point over the range of Mach numbers and a general shift to the rear as Mach number decreases to Mach 1. In addition, in the subsonic range, a comparison is made

of the stability compared to a pure delta wing with the same slenderness ratio and very similar pitching moment results are obtained to the waverider shape. Long observed a similar increase in aerodynamic performance as Mach number decreased [113].

In these studies, the key criteria was the aerodynamic performance measured by lift to drag ratio across a wide Mach number range. Some consideration was given to the low speed stability in reference [112] however, as noted by Hirschel and Weiland in reference [90] the low speed stability of hypersonic waveriders is not well understood in general.

A number of wind tunnel campaigns have been conducted at low speeds on waveriders which produced pitch moment curves against AoA. These include studies by Miller and Argrow on several osculating cones waverider shapes [114], the study by Pegg et al [80] mentioned in Chapter 1 and the Loflyte tests [79]. These studies have all produced information on the static stability characteristics of particular designs, but not on the dynamic behaviour.

2.2.3 Dorsal Engine Waveriders

The concept of the pure waverider offers the potential for high aerodynamic efficiency. However the need for propulsive flowpaths and the use of the waverider compression as pre-compression for a lower surface mounted engine can reduce the aerodynamic performance. While this bottom surface engine configuration is common among design studies, the dorsal mounted engine concept has good potential for higher aerodynamic efficiencies and less aero-propulsive coupling. By mounting the engine on the upper surface the vehicle lower surface can achieve the maximum possible compression lift for that waverider design. This concept was used by ESTEC to develop the MR-2 waverider design for the LAPCAT II project [115]. The aim of the design was to integrate a high performance propulsion unit within a high aerodynamic efficiency waverider design. According to Langener et al the mounting of the engine on the dorsal side allowed for better aerodynamic performance on the windward side and also allows the aerodynamic shape to be omptimised without need to consider the propulsion system [115]. The intake for the engine is inward turning which should have less impact on the aerodynamic lift of the configuration. This configuration is shown in Figure 1.11 in Chapter 1. The modifications to create a design that is flyable are similar to those applied by Eggers et al [112]. Eggers et al began with pure osculating cones waverider and modified the

flat base to produce a thin trailing edge which can accommodate control surfaces. The minimum volume requirement for a propulsive flowpath, from intake to nozzle, and fuel is calculated and this span of the base area is left at full thickness. The remaining portion of the span on either side of this is narrowed with a corresponding lowering of the upper surface to form two distinct wings on either side of a fuselage that can accommodate a dorsal mounted engine. This is shown in Figure 2.7 reproduced from reference [112]. With viscous effects accounted for, the two configurations show very similar lift to drag ratio performance with slightly lower values for the modified version.

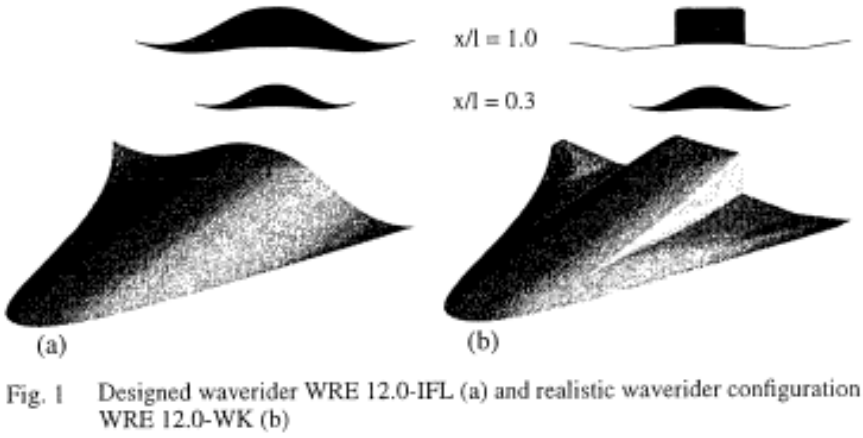

Fig. 1 Designed waverider WRE 12.0-IFL (a) and realistic waverider configuration WRE 12.0-WK (b)

Figure 2.7: Modified WRE 12.0 waverider [112]

The LAPCAT MR2 vehicle is the basis for the Hexafly vehicle that is the subject of CFD and wind tunnel tests in this thesis. The dorsal mounted waverider concept is a good waverider design concept for the optimisation of low speed performance as the majority of the aerodynamic shape is independent of the propulsion system. This will allow optimisation of the waverider shape for low speed stability and high speed aerodynamic efficiency without needing to account for the effect on the propulsion flowpath.

2.3 Hexafly-Int Hypersonic Glider

The majority of this thesis is concerned with characterising the low speed stability of the Hexafly-Int hypersonic glider which was introduced in Chapter 1. This work forms part of the University of Sydney contribution to the Hexafly-Int project. The vehicle is designed to perform a Mach 7.2 glide test whose trajectory is shown in Figure 1.12. The glider design, which will be flight tested and has been the subject of CFD and wind

tunnel tests in this thesis, is referred to as the Experimental Flight Test Vehicle (EFTV). The evolution of the Lapcat II MR2 design to the EFTV is outlined in reference [67] and reference [69]. In particular, the shape of the wings is altered to fit within the Hexafly launch vehicle faring, as are the vertical fins. The elevon surfaces are extended rearward to provide sufficient roll authority with the reduced lateral distance from the roll axis. The final layout of the vehicle with the Layout Reference Frame, which is used to define centre of gravity locations, is shown in Figure 2.8 reproduced from [68].

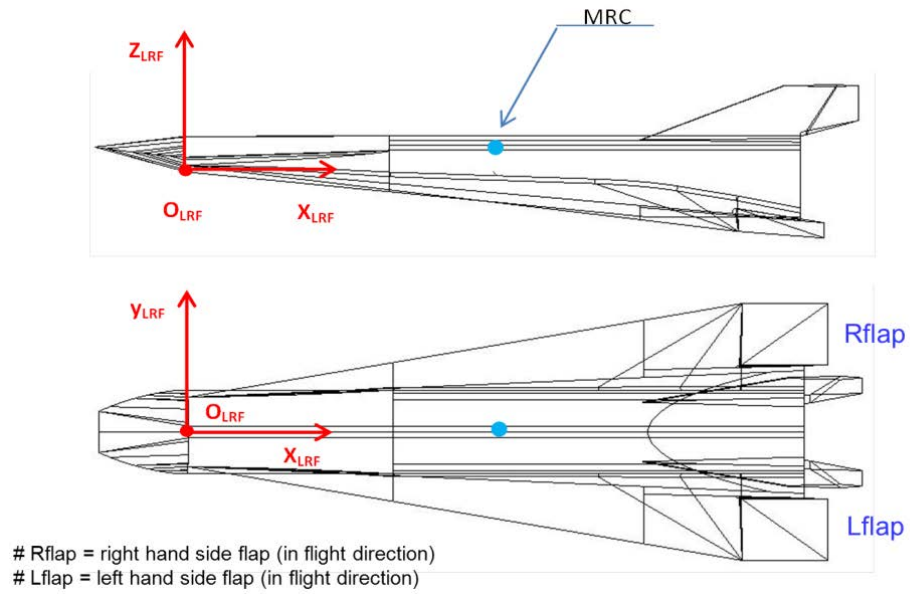

Figure 2.8: Hexafly vehicle showing Layout Reference Frame [68]

The vehicle has 80 degree swept wings with 14 degree anhedral droop [116]. The wings are designed such that the upper surface at the front is aligned with the flow at zero AoA for ideal cruise performance. Towards the rear, an expansion curve brings the upper wing surface down to the lower surface to provide a thin trailing edge for the control surfaces. The lower side of the wing is flat over its whole area. The leading edge of the wings features a 2mm leading edge radius on the nose and 1mm radius on the wings to provide acceptable thermal performance. The dimensions of the vehicle are shown in Figure 2.9. A powered option for the Hexafly-Int project has also been developed but is not intended for flight testing, and the remainder of this thesis is focused on the glider. More details on the powered version can be found outlined in reference [116].

The dimensions of the vehicle, mass, moments of inertia and centre of gravity location are given in Table 2.1.

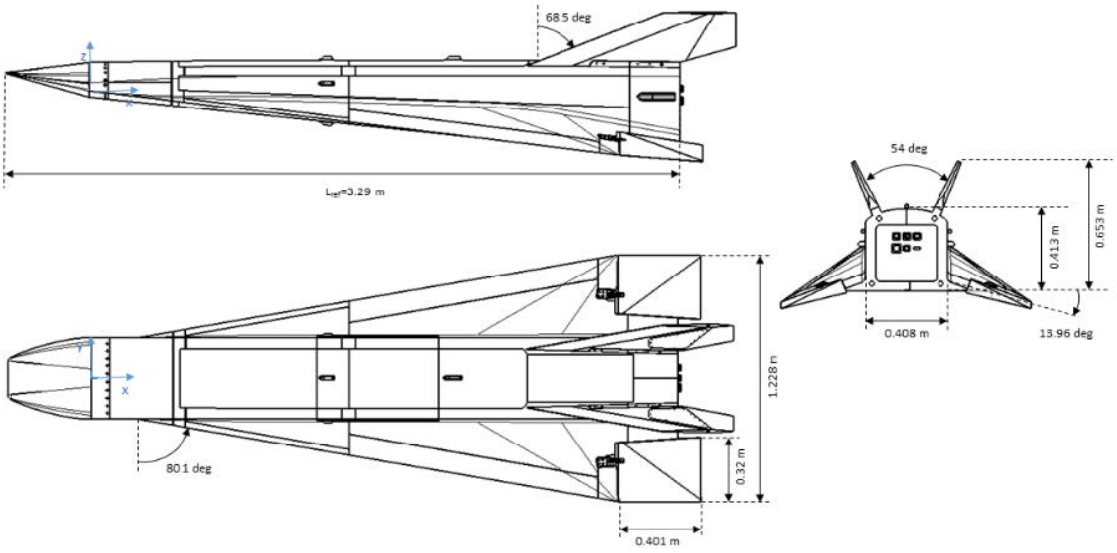

Figure 2.9: Three-view Hexafly EFTV drawing showing vehicle dimensions [116]

Table 2.1: Hexafly-Int glider vehicle details

L_{ref} (m)	3.29
S_{ref} (mˆ2)	2.52
B_{ref} (m)	1.23
$Mass$ (kg)	420
I_{xx} (kg.mˆ2)	24.04
I_{yy} (kg.mˆ2)	1417.9
I_{zz} (kg.mˆ2)	1426.2
CoG [m] (LRF x,y,z)	(1.555,0.0,0.0)

2.4 Reference Systems and Stability Criteria

The remainder of the thesis focuses on obtaining static and dynamic stability derivatives for the Hexafly-Int EFTV using both computational and wind tunnel testing methods. This will not only provide dynamic stability data for a waverider at low speeds, which is a gap in current knowledge, but will also allow the computational tools to be validated against the experimental results. This will allow extension of the use of computational tools for determining dynamic longitudinal stability parameters of slender hypersonic cruise vehicles in the design phase, in order to incorporate the low speed dynamic stability into hypersonic vehicle design for civilian transport use. Chapter 6 will give a preliminary design study into osculating cone waveriders to determine what changes in shape can

produce improvements in the low speed longitudinal stability.

The work presented herein will use the stability reference system defined by the Advisory Group for Aerospace Research and Development (AGARD) for defining positive directions of forces and moments as well as stability derivatives found in reference [117] and shown in Figure 2.10.

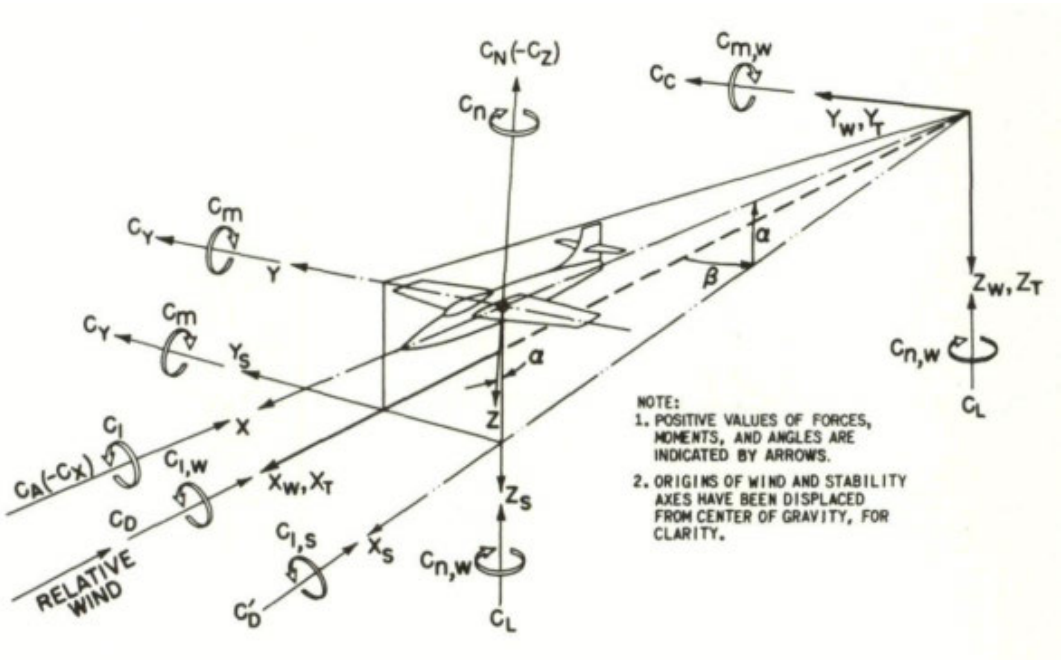

Figure 2.10: Stability reference axes and conventions [117]

The rotation rates are defined with the same sign convention as their corresponding moments shown in Figure 2.10. The non-dimensionalisation of general aerodynamic forces (F) and moments (M) are shown in equation 2.3 for reference length L_{ref}, reference area S_{ref}, freestream velocity V_∞ and density ρ. For longitudinal derivatives the reference length is the length of vehicle (L_{ref} in later chapters), and for lateral derivatives the reference length is the span (b_{ref}).

$$\begin{aligned} C_F &= \frac{F}{1/2\rho V_\infty^2 S_{ref}} \\ C_M &= \frac{M}{1/2\rho V_\infty^2 S_{ref} L_{ref}} \end{aligned} \tag{2.3}$$

The results of testing from wind tunnels and CFD are usually expressed as aerodynamic coefficient derivatives with respect to flightpath angles such as angle of attack (AoA α),

angle of sideslip (AoS, β), flightpath angular rates $\dot{\alpha}$, $\dot{\beta}$ and rotation rates about the body x, y and z axes, p, q and r. Examples of angle and rate derivatives are shown in equation 2.4. During processing, all angles are defined in radians and rates in radians per second.

$$\begin{aligned} C_{M_\alpha} &= \frac{\partial C_M}{\partial \alpha} \\ C_{M_q} &= \frac{\partial C_M}{\partial (qL_{ref}/2V_\infty)} \end{aligned} \tag{2.4}$$

2.4.1 Static Stability Criteria

Longitudinal static stability is primarily determined by the sign of the pitch stiffness, the derivative of pitching moment coefficient with respect to AoA, C_{m_α} for pitch moment m. A negative value of C_{m_α} indicates static stability as increases in AoA will result in a decrease in pitching moment which causes the nose to drop and reduces the AoA. Lateral static stability is dependent on AoS derivatives, C_{l_β}, C_{n_β} and C_{Y_β} for roll moment l, yaw moment n and sideforce Y. A negative value of C_{l_β} causes the aircraft to roll to the left under positive sideslip conditions. This alters the flight path towards the left resulting in a reduction in sideslip angle. A negative value of C_{Y_β} results in a sideforce to the left for a positive sideslip angle. This causes a reduction in y body axis velocity v, which reduces sideslip. A positive value of C_{n_β} results in a nose to the right rotation about the z body axis in response to a positive sideslip angle, reducing the sideslip. The static stability criteria are summarised below in Table 2.2

Table 2.2: Static stability criteria

$C_{m_\alpha} < 0$	$C_{l_\beta} < 0$	$C_{n_\beta} > 0$	$C_{Y_\beta} < 0$

The key dynamic stability criteria is that the pitch damping derivatives $C_{m_{\dot{\alpha}}}$ and C_{m_q} be negative. A negative value will oppose the motion of the vehicle and cause any oscillatory motion to subside. The exact handling qualities under dynamic motion depend on the magnitudes of both C_{m_q} and $C_{m_{\dot{\alpha}}}$ and the magnitude of C_{m_α} which in combination, determine the frequency and damping of the aircraft short period mode. The dynamic lateral behaviour is not covered in this work so is not described here.

2.5 Conclusion

This chapter has presented the basic principles of hypersonic vehicle design. The concept of the hypersonic waverider has also been described and is the focus of this thesis due to the potential for high aerodynamic efficiency at cruise. The waverider design concept will be used in Chapter 6 for a design optimisation study focusing on low speed stability. Static and dynamic Computational Fluid Dynamics (CFD) simulations and wind tunnel tests have been conducted on the Hexafly-Int hypersonic glider presented in Chapters 3 to 5. This chapter has presented details of the Hexafly design for reference in those chapters. In addition, the reference frames used, and definitions of stability criteria for aerodynamic derivatives has been presented as a guide for the rest of the thesis.

Chapter 3

Computational Results

The HEXAFLY-Int vehicle outlined in Chapter 2 is distinctly different from a conventional aircraft design. There are various engineering tools which allow designers to rapidly assess the aerodynamic performance of the common components of conventional aircraft with distinct wings, fuselage and tail surfaces. The predominantly two dimensional flow of high aspect ratio wing surfaces can be analysed using simplified analytical methods such as lifting line theory or vortex lattice methods, which, with appropriate efficiency factors, will yield reasonably accurate results for stability and control derivatives. The effect of most streamlined fuselage bodies is on the drag of the vehicle and is less significant for the stability.

This is not the case with the highly swept wings and control surfaces of the Hexafly vehicle. The added factor of the blended lifting surface of the fuselage further complicates analysis. Wing surfaces with sweep angles of 80 degrees experience separated flows from the leading edge at even moderate angles of attack. The sharp leading edges will experience a "flow off" type vortex separation [118] where the boundary layers of the upper and lower surfaces flow from the edge and interact with the external inviscid flow resulting in large vortex structures on the lee-surface of the wings. Although the vortex itself is mainly inviscid, the boundary layer separation is necessary in order to model the vortices. The general vortex structure which is expected is shown in Figure 3.1 reproduced from Lee et al in [119], showing the primary and secondary vortices as well as the flow and attachment lines that run chord-wise along typical delta wings at moderate to high AoA.

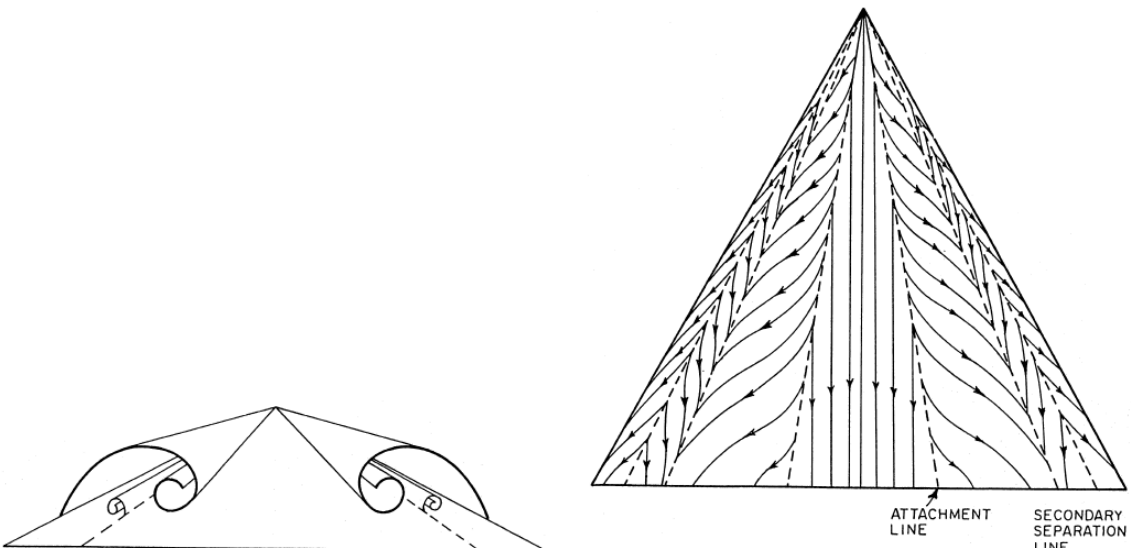

(a) Vortex Structure (b) Surface Flow

Figure 3.1: Vortex structure diagrams from reference [119]

The potential flow solver, Tranair was used for initial calculations. The Tranair results are presented in Appendix A. Tranair was used in reference [98] to model a hypersonic vehicle due to the ability to give good results from low subsonic to hypersonic flow speeds. The limitation is the reliance on coupled two dimensional boundary layer approximations which do not handle separated flows. Although the unsteady formulation of Tranair made obtaining dynamic stability parameters quick and simple, it was found after initial CFD and wind tunnel testing that the inability to model the vortex flows severely reduced the accuracy of the results. The vortex lift and its effect on the pitching moment in particular, are critical to correctly estimating the longitudinal stability characteristics. The effect of the vortices on the fins and fuselage at high angles of attack and sideslip is also an important consideration for lateral stability.

There are corrections to simplified potential flow methods such as vortex lattice method, which allow for the estimation of the vortex lift and distribution, and these will be used in Chapter 6 for estimation of aerodynamic performance and stability in an optimization routine. These methods are not considered accurate enough for the complex Hexafly design so a full Computational Fluid Dynamics approach has been adopted. CFD solvers using the Euler and full Navier Stokes equations have been compared with regard to modelling of vortices and it was found that both can simulate vortex formation over highly swept wings. However the inviscid Euler calculations cannot properly model the

vortex structure on the wing surface, the pressure distribution and secondary vortices [120], so a full Reynolds Averaged Navier Stokes (RANS) solver has been opted for here.

This chapter will outline the numerical solver used, the vehicle size and Reynolds number, the computational mesh, followed by results of calculations in steady and unsteady dynamic pitching conditions.

3.1 Numerical Solver, Domain and Conditions

This section outlines the numerical solver used, the computational domain, the vehicle specifications of the simulations and the computational resources involved.

3.1.1 ANSYS Fluent

High fidelity numerical solutions are obtained using the commercial Reynolds Averaged Navier-Stokes (RANS) solver, ANSYS Fluent R19.0, a cell-centred finite volume code. A Pressure-Based Coupled Algorithm is applied which solves a system of equations based on the momentum and pressure based continuity equations simultaneously [121]. Although the coupled algorithm requires up to twice the memory it achieves convergence at a much faster rate than the alternative segregated method. Second order upwinding methods are used to spatially discretize the momentum, turbulent kinetic energy and the specific dissipation rate to improve accuracy. Scalar gradients across cells are computed using a Least-Squares Cell-Based Gradient Evaluation method. Interpolation of the cell centred pressure values to the faces between is achieved using a Second Order method which should achieve higher accuracy than the alternative Linear and Standard methods available.

The flowfield is initialised using the ANSYS Fluent Full Multi-Grid (FMG) technology which solves the inviscid Euler equations beginning on a coarsened version of the input mesh. The FMG process uses the density-based explicit formulation with first order discretization of the governing equations but switches back to the pressure based formulation once complete [121]. FMG initialisation does not compute the turbulence equations.

Viscous effects in the boundary layer must be accounted for in order to model the flow

off leading edge separation which interacts with the external inviscid flow to create the main vortex structure. The Reynolds Averaged formulation of the Navier Stokes (NS) equations, in contrast to the Large Eddy formulation, decomposes the NS equations into time averaged and fluctuating components. This decomposition results in a Reynolds stress term which must be solved via some turbulence model, in order to close the system of equations. The k-ω SST turbulence model has been chosen to close the RANS equations. The k-ω SST model developed by Menter [122] blends the accurate near-wall capability of the Wilcox k-ω model with the far field accuracy of the k-ϵ which assumes a fully turbulent flow [121]. The k-ω SST model shows good accuracy where adverse pressure gradients are encountered as shown in reference [122], which due to the likely leading edge separation is necessary to model. As the key results to be obtained are the global forces and moments, this turbulence model is deemed appropriate for the numerical simulations. Although the Spallart Almaras model relaxes the requirements on resolving the near-wall conditions with a highly refined mesh, it was not deemed necessary as the flow is low Mach number and incompressible. Instead, appropriate inflation layers have been used to refine the mesh around the Hexafly-Int vehicle near the wall to achieve y^+ values below 1 over the whole surface as recommended in reference [123].

3.1.2 Simulation Conditions

The aim of the CFD calculations presented in this chapter is to match the results obtained in the wind tunnel test campaign, outlined in Chapters 4 and 5. The length scale of the vehicle and the freestream airspeed of the CFD calculations are chosen to give results representative of the Reynolds numbers achievable in the University of Sydney 3x4 Wind tunnel facility (outlined in Chapter 4). The expected flow-speeds of the test are between 15 and 30 m/s, while the model lengths that could be tested in that facility range from 0.5 to 1 m. This is specific to the Hexafly Vehicle which has a high length to span ratio. A summary of the flowspeed (V_{ref}), reference length (L_{ref}) and Reynolds number (Re) for the full scale vehicle, the CFD simulations and the eventual wind tunnel model are given in Table 3.1. There is a small difference between the CFD Reynolds number and the wind tunnel number as the simulations were set up while the wind tunnel model was still in the process of being designed. The difference is small enough that it should

have no impact. The Reynolds number is an important measure of flow similarity and is defined in Eq. 3.1 for dynamic viscosity (μ) and density (ρ) using the sea level values from the US Standard Atmosphere model [124] [125]. The speed of the full scale vehicle has been assumed at 80 m/s. As the Hexafly EFTV is not specifically designed to land on a runway, this assumption is based on the typical landing speeds of civilian aircraft on the basis that a civilian transport based on the Hexafly-Int design would be constrained by the same regulations [126].

$$\begin{aligned} Re =& \frac{\rho V_{ref} L_{ref}}{\mu} \\ \mu = 1.789 \times 10^{-5} \quad & \rho = 1.225 kg/m^3 \end{aligned} \tag{3.1}$$

Table 3.1: CFD and Full scale vehicle parameters

Scale	L_{ref} (m)	V_{ref} (m/s)	Re
Hexafly EFTV	3.29	80 m/s	1.8×10^7
CFD simulation	0.72	25 m/s	1.23×10^6
Wind Tunnel Model	0.95	20 m/s	1.3×10^6

There is an order of magnitude difference between the Reynolds number at full size and the CFD and wind tunnel size. The impact of this difference will be assessed by running a CFD simulation of the full size vehicle at selected AoA to see what difference there is in the resulting forces and moments.

Initial wind tunnel tests on a 0.56 m model outlined in Appendix A had shown that the vehicle is unstable in pitch at the design centre of gravity CG_{des}. Dynamic wind tunnel testing of the method used in Chapter 5 requires static longitudinal stability. Chapters 4 and 5 explain in detail, the process and reasoning behind selection of an alternative centre of gravity referred to as CG_{test}. As the goal of the CFD calculations is to match the results from the wind tunnel testing, CG_{test} is also used as the centre of rotation in these calculations. The selection of moment reference centre is not critical to steady calculations as the results can be shifted to any location as long as the forces and moments are known. However, the unsteady pitching calculations do require the centre of rotation of the applied motion to be the same as the centre of gravity which is being simulated. The dynamic damping characteristics cannot be translated in post processing as they are a function of local flow angles that are dependent on the centre of

rotation that is simulated. The design and dynamic testing centres of gravity are given in Table 3.2 for the CFD length scale using the reference system introduced in Chapter 2 alongside the full scale locations.

Table 3.2: Full Scale and CFD CG locations

Scale	L_{ref} (m)	CG_{des} (x,y,z) (m)	CG_{test} (x,y,z) (m)
Hexafly EFTV	3.29	(1.555,0,0)	(1.247,0,0.052)
CFD simulation	0.72	(0.342,0,0)	(0.274,0,0.002)

The remainder of this chapter presents the results at the dynamic wind tunnel testing Centre of Gravity CG_{test}.

3.1.3 Computational Mesh

The focus of this thesis is primarily on the longitudinal characteristics, and the CFD simulations have been run to obtain lift, pitching moment and to a lesser extent, drag. As such a half mesh of the vehicle is used and symmetry applied at the X-Z plane to reduce the computational time required. As no Angle of Sideslip (AoS) would be modelled, this symmetry assumption is adequate to obtain longitudinal force and moment characteristics.

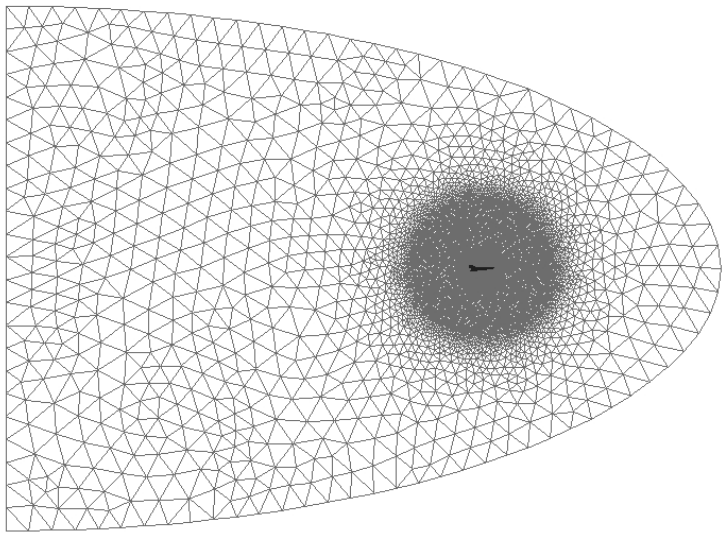

Figure 3.2: CFD Mesh Domain

The computational mesh domain is shown in Figure 3.2. The Hexafly vehicle design does not easily lend itself to a structured meshing approach. An unstructured meshing method has been used here which has yielded good results validated by wind tunnel testing in a similar study on the powered Hexafly-Int vehicle [127] as well as high speed studies on the Hexafly-Int EFTV [68]. The mesh is comprised of a majority 4 node tetrahedral cells and 6 node prisms in the inflation layer. The far-field of the mesh extends 10 vehicle reference lengths upstream and 20 lengths downstream of the vehicle centre of gravity. The flowfield is divided into a coarse main section between the far-field boundary and a spherical inner section with a finer mesh. The unsteady dynamic CFD calculations rotate this inner fluid region relative to the inlet and main fluid section to simulate pitching motion. The mesh interface between the inner and main fluid regions allows matching between the two regions during steady and unsteady pitching calculations. The internal boundary between these inner and outer regions is shown in Figure 3.3(a) where the mesh interface is the spherical mesh surface. The Hexafly-Int model is placed such that the moment reference centre, CG_{test} is at the centre of the rotating fluid region as this is required to obtain the damping characteristics.

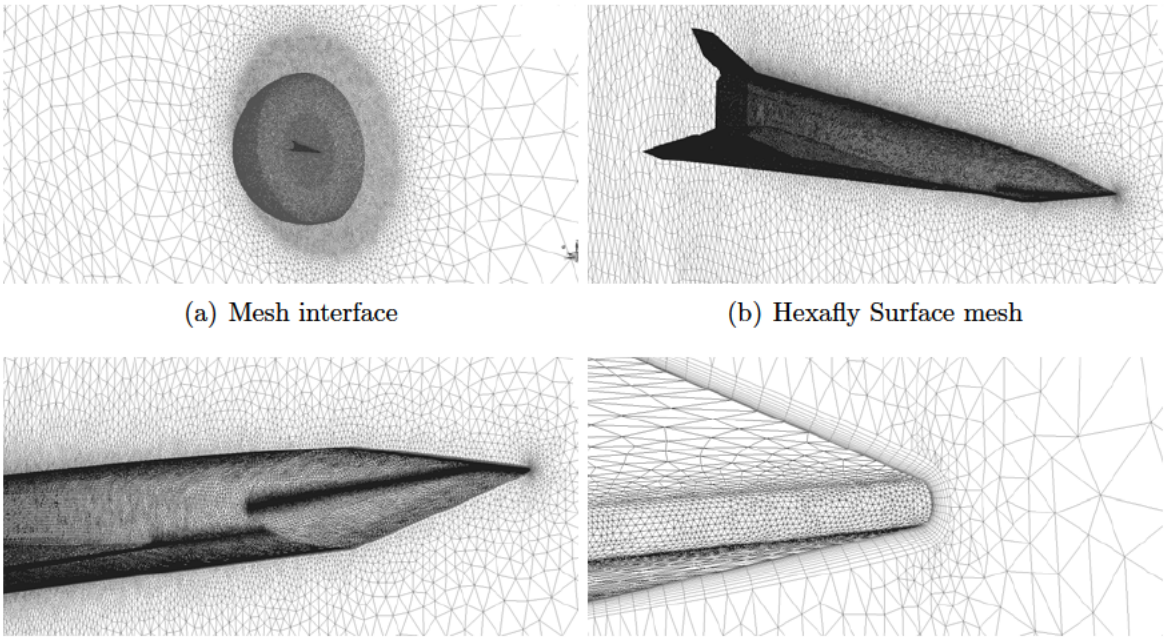

(a) Mesh interface

(b) Hexafly Surface mesh

(c) Nose and Wing LE refinement

(d) Nose and Inflation layer

Figure 3.3: Computational mesh, detailed views

The vehicle wall is refined to less than 0.002m element size over most of the surface shown in Figure 3.3(b), and is refined further in certain key regions such as the leading edge

of the wing at the root where the vortex generation begins, and on the leading edge of the nose and vertical tail as seen in Figure 3.3(c). As mentioned in the previous section the chosen k-ω SST turbulence model requires good resolution of the boundary layer so a first cell layer height of $4.5 \times 10^{-5}m$ was used. Figure 3.3(d) shows the symmetry plane and the Hexafly vehicle nose refinement and the inflation layer that resolves the boundary flow.

3.1.4 Computing Tools

The University of Sydney High Performance Computing facility, Artemis, was used to perform these CFD simulations. The computing cluster features 56 Standard Haswell nodes with 24 cores and 128 GB of RAM, and 80 Standard Broadwell nodes with 32 cores and 128GB of RAM each. Steady calculations were run for up to 40 hours, using 48 CPUs using 4GB of RAM each for a total of 192GB. Unsteady calculations were run for up to 120 hours using the same number of CPU's and total RAM [128].

3.2 Steady Simulations

The steady CFD simulations were used to evaluate the lift, pitch moment and drag characteristics of the scaled Hexafly-Int vehicle at AoA of -5, 0, 5, 10, 15, 20 and 25 degrees with an airspeed of 25m/s. Simulations were also run of the full scale vehicle at 80m/s at the same AoA to analyse the impact of Reynolds number on the results.

Initial wind tunnel tests had shown a distinct change in the pitching moment curve at around 20 degrees AoA. This was assumed to be due to some change in the vortex structure over the wing at this angle. The pitching moment abruptly jumped at this critical AoA indicating that there was a potential crossing of the vortex breakdown point over the trailing edge. This causes a previously low pressure region on the rear of the top surface of the wing to have higher pressure, inducing a positive change in the pitching moment. Research on this vortex breakdown phenomenon is reviewed by Nelson in reference [71]. The steady simulations may not be sufficient to model this inherently unsteady phenomenon so it is unclear how accurate the steady solutions will be beyond 15 degrees AoA. This is investigated by carrying out unsteady calculations at 10 degrees, where the solution is expected to be steady and at 25 degrees where the

solution is expected to be unsteady.

3.2.1 Post Processing

The CFD calculations will output the lift (C_L), drag (C_D), moment (C_m) and pitch stiffness (C_{m_α}) coefficients which will be compared with the results from the wind tunnel testing in Chapter 5. An advantage of CFD calculations is the ability to visualise the flow features of the results using a post-processing tool. Tecplot has been used to visualise the pressure coefficient contours on the surface and the vortex system on the wing.

There are numerous methods for defining a vortex and there is no commonly agreed upon one [129]. The lambda-2 criterion of Jeong and Hussain [130] has been used here, however, no claim is made that this is the best method, and it has been used as it successfully extracts the vortex features on the Hexafly-Int vehicle.

The λ-2 criteria uses the symmetrical, $\mathbf{S}$, and anti-symmetrical, Ω, components of the velocity gradient tensor ∇u. The tensor, $S^2+\Omega^2$ is constructed and the second eigenvalue, λ-2 is calculated from it. A vortex is identified in the regions where λ-2 is negative [130]. This is referred to as EgnVal2 in the visualisation figures.

3.2.2 Grid convergence

The baseline mesh shown in Figures 3.2 and 3.3 has a cell count of 18 million. The most computationally challenging steady state was assumed to be the 20 degree AoA condition. Meshes were generated with 23 and 28 million cells in order to compare the resulting lift, drag and moment results and convergence to determine whether the 18 million cell grid sufficiently resolves the flow. The convergence criteria for the residuals between solution iterations of C_m, C_L and C_D force and moment coefficients is set to 1×10^{-7} which is a stricter requirement than the 1×10^{-6} level recommended by Tu et al in [123]. As the convergence criteria are applied to the surface force and moment data, there could be unsteady flow in other parts of the flowfield but as long as it does not affect the vehicle surface significantly, a steady state solution can still be achieved.

The convergence of the three different meshes for C_L and for C_m as a function of computation step is shown in Figure 3.4. There is generally good convergence for all three meshes, although the difference in the final answer for C_m does warrant an increase in

mesh density to ensure accuracy in the answer. The results indicate an expected accuracy for the moment calculations of the order ±0.0005 which was considered acceptable. The steady calculations were done using both the 18 million cell grid and the 28 million cell grid and the agreement between the two was better over the rest of the AoA range, with the results at 20 degrees AoA representing the maximum deviation. For unsteady calculations, in order to limit the simulation computational resources, the 18 million cell mesh was used as it was determined to be sufficiently accurate for the purpose of comparison to wind tunnel data, which has similar or larger uncertainties.

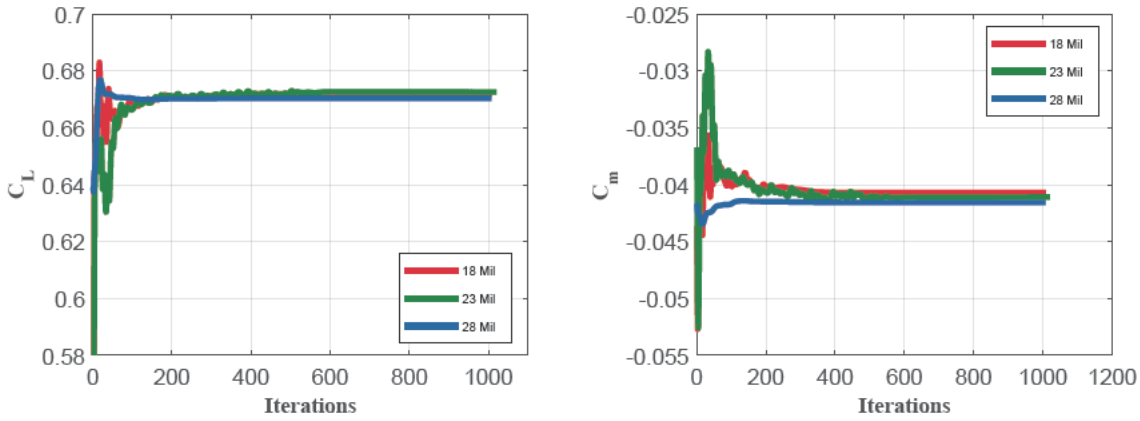

(a) C_L Convergence

(b) C_m Convergence

Figure 3.4: Grid convergence tests at 20 degrees AoA

3.2.3 Steady Results

The results for lift, moment and drag are shown in Figures 3.5 and 3.6 for the 18 million cell mesh, the 28 million cell mesh and the full scale 80m/s simulations. The results from the Tranair calculations are included in Figure 3.5(a) to highlight the impact of vortex lift which the Tranair potential flow solver does not adequately model, although there is good agreement in the low AoA range where vortex lift is small or non-existent.

The lift and drag results show that there is very good agreement between the two different grid densities and the full scale 80m/s results. The results at 20 degree AoA are the exception with the largest deviation suggesting that Reynolds effects are more significant above 15 degrees AoA. This is also the range where changes in moment trend were observed in the wind tunnel data from initial testing, suggesting some change in the vortex behaviour that may be Reynolds number dependent.

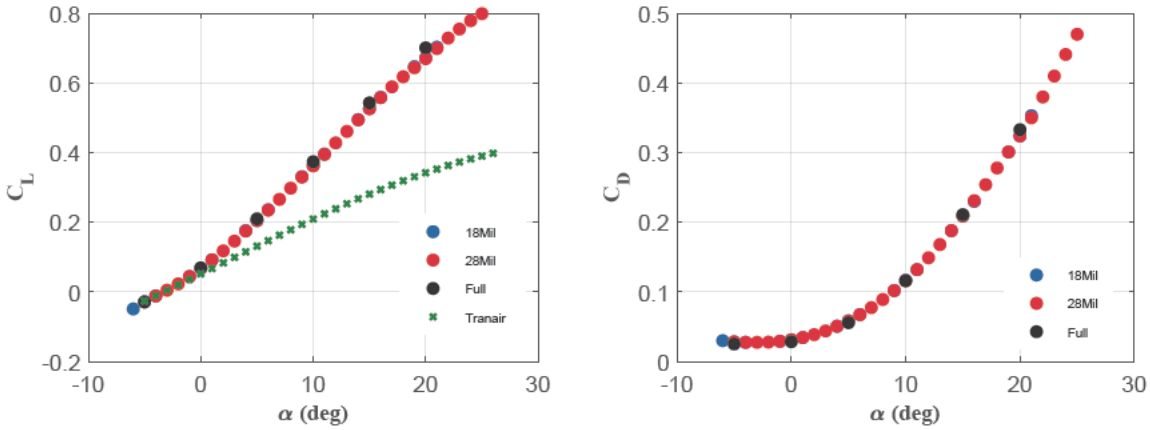

(a) C_L vs AoA

(b) C_D vs AoA

Figure 3.5: C_L and C_D vs AoA for 18 million, 28 million and full size simulations

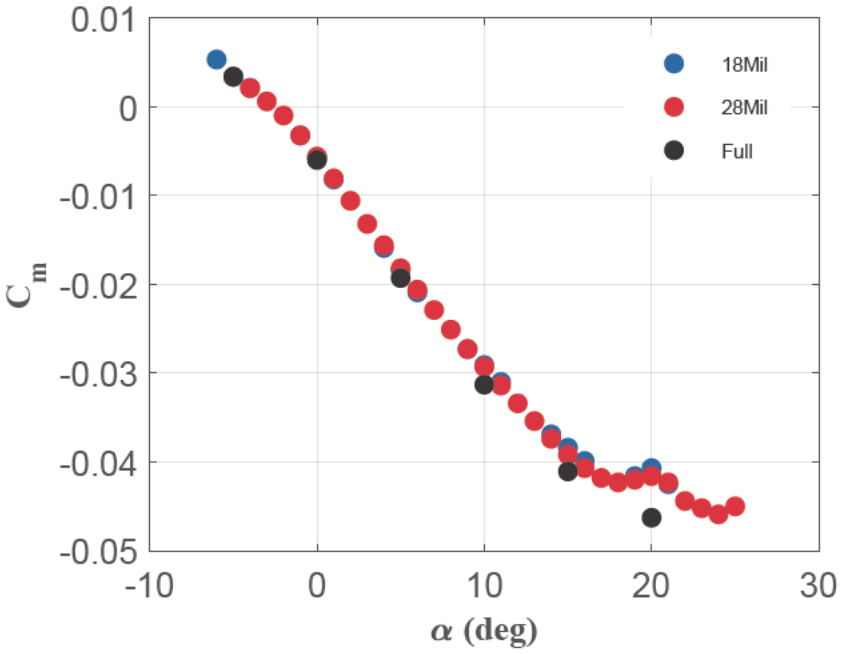

Figure 3.6: C_m vs AoA

The pitching moment results show stable behaviour, indicated by the negative gradient, across the majority of the AoA range. There is good agreement over the majority of the AoA range up until 15 degrees AoA between the 18 million and 28 million cell meshes. At 14 to 16 degrees there is some divergence and again at 19 to 20 degrees. The results from the full scale vehicle show an average 4% deviation from -5 to 15 degrees AoA, but a large difference is observed at 20 degrees AoA, again in the region of abrupt change in pitch behaviour observed in wind tunnel data. This suggests that if the wind tunnel

data is consistent with the CFD in the AoA range from -5 to 15 degrees then we can infer that the wind tunnel results will also be consistent with the behaviour of the full scale vehicle despite the order of magnitude difference in Reynolds number.

Longitudinal stability requires that pitch stiffness, C_{m_α}, is negative. This is one of the most important factors in determining whether an aircraft is statically stable. The pitch stiffness results from the static CFD simulations are shown in Figure 3.7. The results show that vehicle is statically stable from -5 up to 15 degrees AoA and is unstable at 20 degrees AoA. This will constrain the low speed flight envelop to below 15 degrees AoA as civilian aircraft are required to be statically stable.

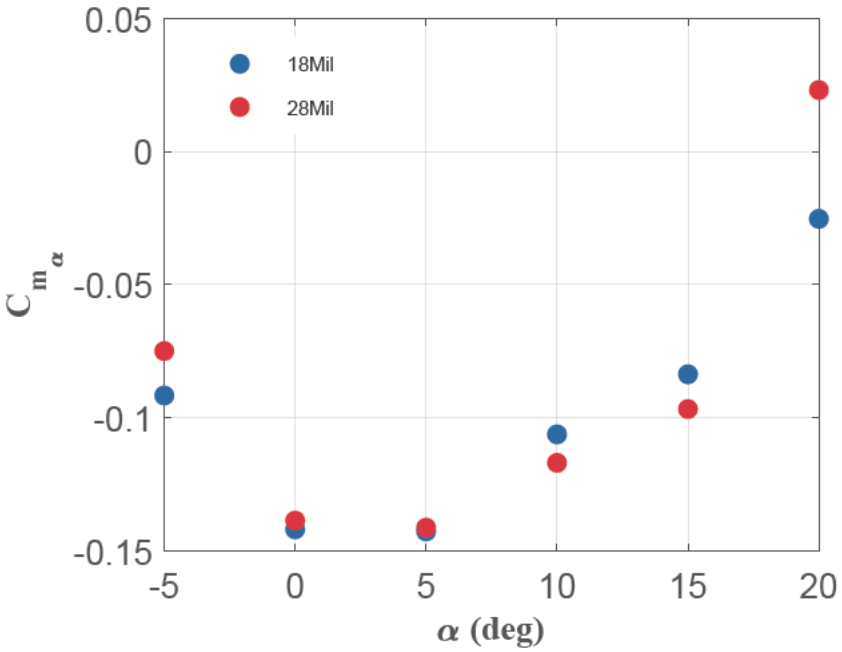

Figure 3.7: C_{m_α} vs AoA

The evolution of the computed flowfield with AoA is shown in Figures 3.8 to 3.11 where the Hexafly surface of the half mesh has been reflected about the X-Z symmetry plane. The figures show pressure coefficient contours over the surface of the vehicle and cutoff contours of the $\lambda 2$ (labelled as EgnVal2 in Tecplot) at five Y-Z planes along the Hexafly wing to visualise the vortex location. At -5 degrees AoA, there are no vortices present as the wings are not inclined to the flow. This is the region where the potential flow solution of Tranair is consistent with the CFD results. At 0 degrees AoA a primary vortex has formed as seen by the circular regions of the $\lambda 2$ value. The shear layer from the leading edge that feeds the vortex is also visible.

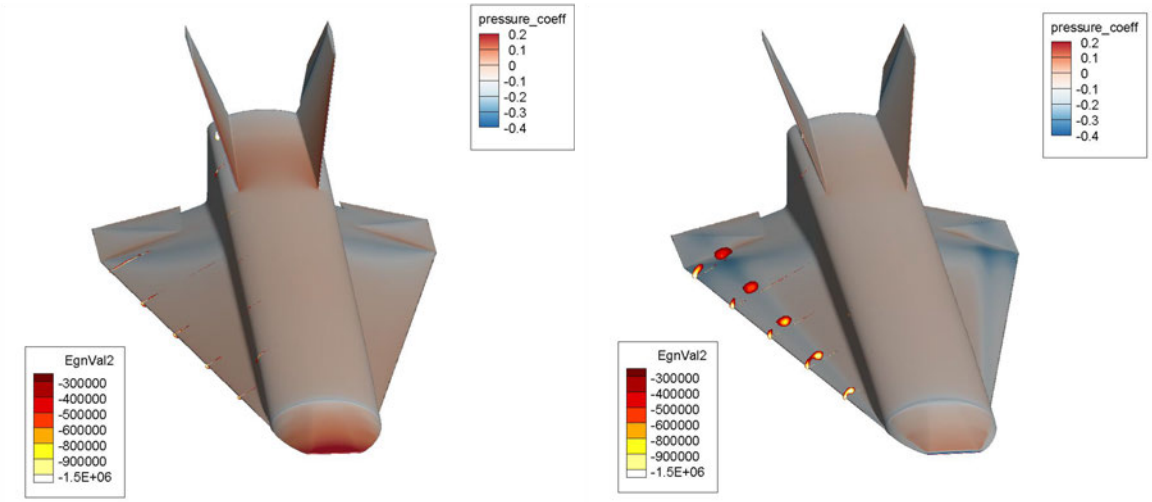

(a) -5 degrees AoA

(b) 0 degrees AoA

Figure 3.8: Surface pressure coefficient and vortices at -5 and 0 degrees AoA

At 5 degrees AoA a secondary vortex has begun to form, seen as the smaller circle formed closer to the leading edge which is caused by secondary separation shown in Figure 3.1 and described in reference [119]. In addition, a vortex has begun to form off the swept edge of the nose cone and is running along the top corner of the fuselage. There is also a noticeable shift of the vortex inboard.

The increasingly negative pitching moment observed in Figure 3.6 is due to the increasing vortex strength which can be observed in Figures 3.9(a) to 3.11(a). This increasing vortex strength is observed in the pressure coefficient over the top surface of the wings. The increasing vortex strength causes an area of the surface to have low pressure with a larger low pressure area towards the rear of the wing behind the centre of gravity. At 10 and 15 degrees AoA the secondary vortex persists and grows, as does the primary vortex and the nose vortex.

At 10 degrees AoA a vortex is observed forming off the vertical tail in Figure 3.9(b). As the vortex is forming off the outside surface, this suggests that the flow is moving in an outward (towards the wing) direction along the top surface of the fuselage. This is visualised in Figure 3.10(a) using streamlines which show the impact of the nose vortex causing the flow over the top of the fuselage to be pulled in an outward direction, effectively giving the vertical tail a sideslip angle. As the vertical tail is also a highly swept wing surface this leads to the vortex formation on the outer surface. The effect this has on the yaw stability under sideslip would be of interest but as these simulations

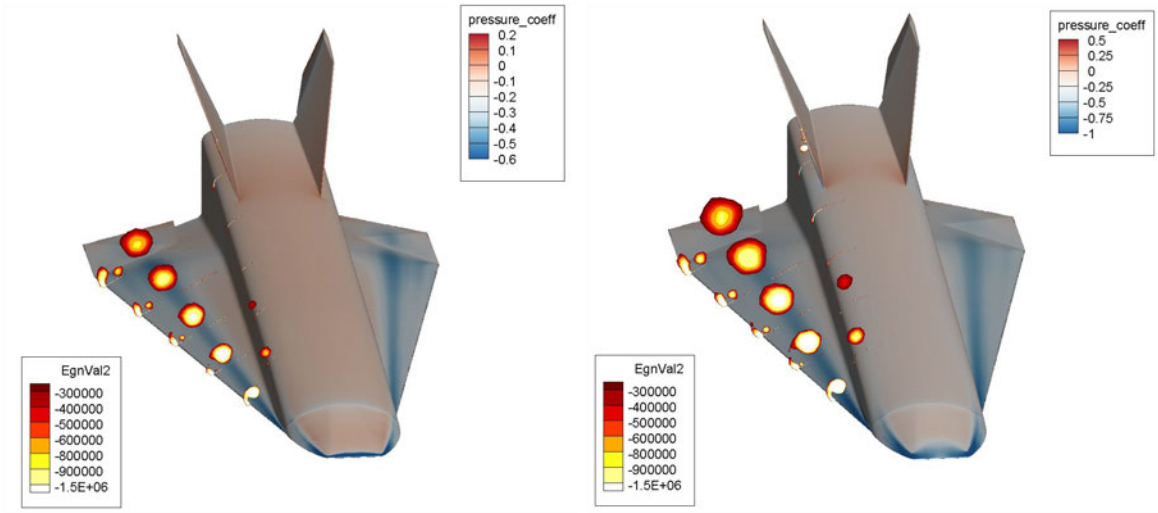

(a) 5 degrees AoA (b) 10 degrees AoA

Figure 3.9: Surface pressure coefficient and vortices at 5 and 10 degrees AoA

are symmetrical using a half mesh, no sideslip has been applied in this study.

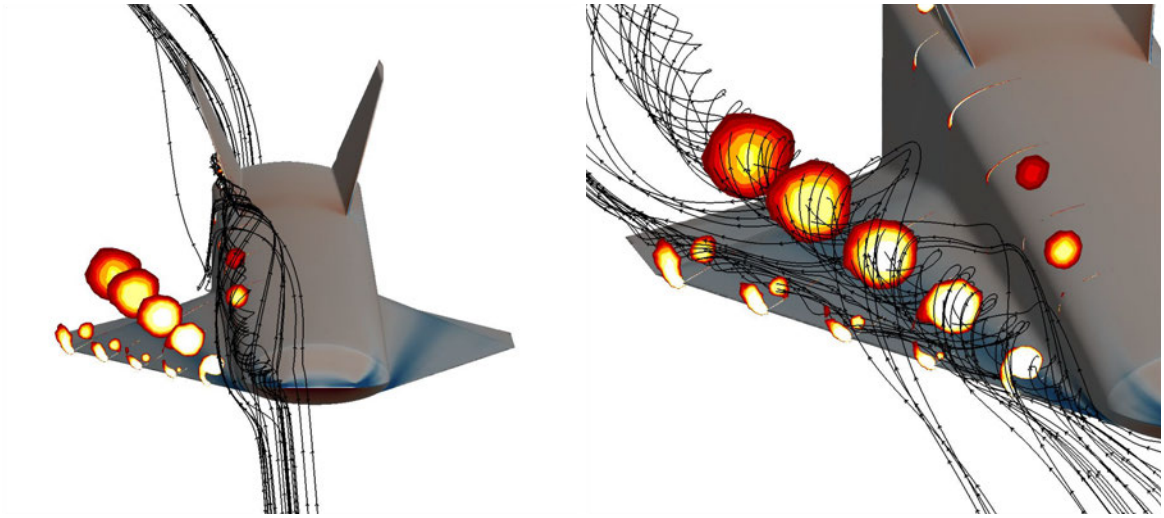

(a) Streamline at Vertical Tail (b) Streamlines over wing

Figure 3.10: Streamlines over vertical tail and wing at 10 degrees AoA

The primary and secondary vortex formation over the wing results in the flows shown in Figure 3.10(b). The primary vortex pulls airflow rising from the leading edge back down onto the surface resulting in an outward surface flow. This flow then separates again resulting in the smaller secondary vortex flow closer to the leading edge.

From 15 to 20 degrees AoA the pitching moment data shown in Figure 3.6 shows a local minimum at 18 degrees AoA. Figures 3.11(a) and 3.11(b) show that the vortex at the rear of the wing at 20 degrees has become more diffuse relative to the vortex near the

front of the wing. The pressure contours suggest that the relative suction on the rear of the wing is not as strong leading to an increase in pitching moment from 18 degrees AoA.

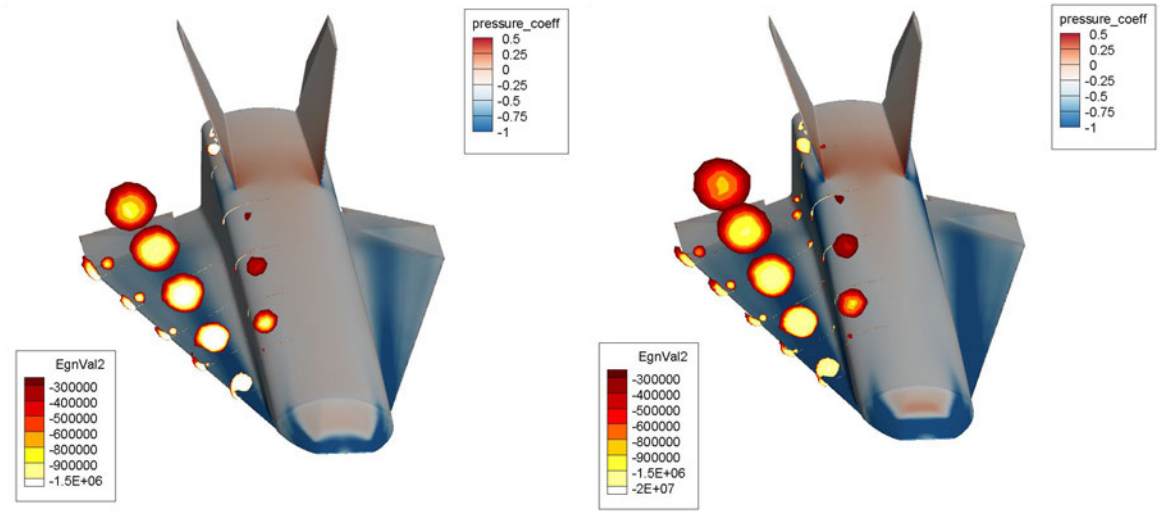

(a) 15 degrees AoA (b) 20 degrees AoA

Figure 3.11: Surface pressure coefficient and vortices at 15 and 20 degrees AoA

This is illustrated in Figure 3.12 which shows the pressure coefficient on the top surface of the wing against the spanwise location for axial locations, x/L_{ref} (ξ), of 0.3, 0.59 and 0.87. The span-wise coordinate is the Y-coordinate on the wing scaled by the local semi-span, η. Increasing AoA for ξ=0.3 and 0.59 causes an increase in the magnitude of the pressure minimum while the shape of the pressure distribution remains largely the same. At ξ=0.87, there is only a small decrease in pressure from an AoA of 15 to 20 degrees. This smaller relative decrease changes the lift distribution of the wing leading to a tendency to increase pitching moment. This matches the pitch increase seen in the wind tunnel data at a similar AoA. It is also clear that the pressure minimum moves towards lower values of η as the AoA increases. This suggests the main vortex is shifting inboard with increasing AoA as observed in the flow visualisation in Figures 3.8 to 3.11.

An additional consideration is the height of the vortex core above the wing surface. A side view of the vortices at 15, 20 and 25 degrees AoA is shown in Figure 3.13 which distinctly shows the vortex core moving up off the wing surface at higher AoA. This leads to a more diffuse low pressure region as well as impacting on the flow at the vertical tails to a greater degree.

This is further shown by observing the change in the λ-2 value through the core of the

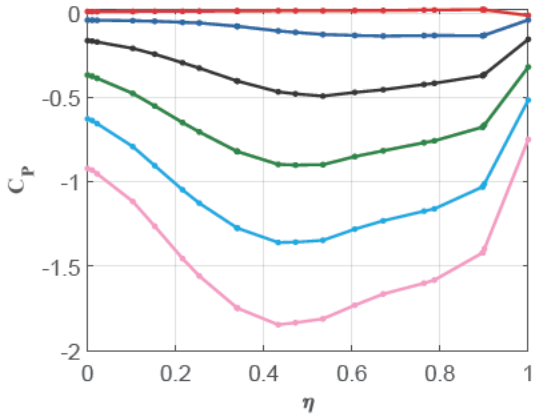

(a) $\xi = 0.3$

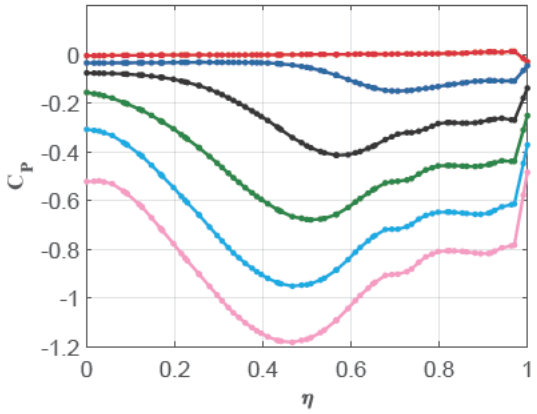

(b) $\xi = 0.59$

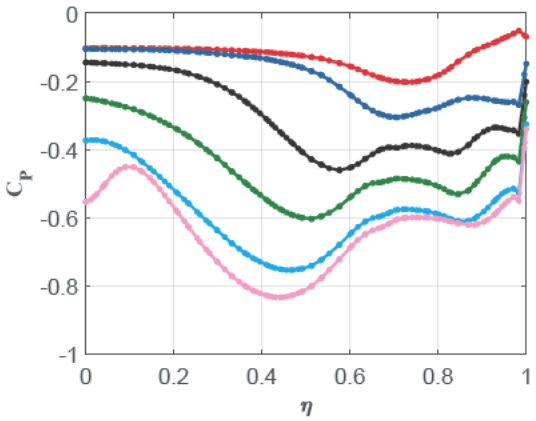

(c) $\xi = 0.87$

Figure 3.12: C_P vs Y/Span at each ξ for AoA = -5, 0, 5, 10, 15, 20

(a) 15 degrees AoA

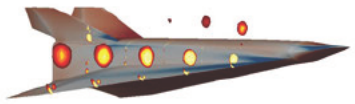

(b) 20 degrees AoA

(c) 25 degrees AoA

Figure 3.13: Vortices at 15, 20 and 25 degrees AoA

vortex as it changes with height above the wing. Figure 3.14 shows the variation of λ-2 on the figure x-axis against the vertical distance from the wing upper surface scaled by local semi-span (z/span) on the y-axis at the same three ξ slices used in Figure 3.12. The AoA of -5 degrees has been ignored as no vortex is observed at this condition. At $\xi = 0.3$ and $\xi = 0.59$ the front and mid section of the wing show a trend of the vortex system increasing in strength with AoA and rising off the wing surface. $\xi = 0.87$ shows

the same rising trend but beyond 5 degrees AoA the peak value does not increase.

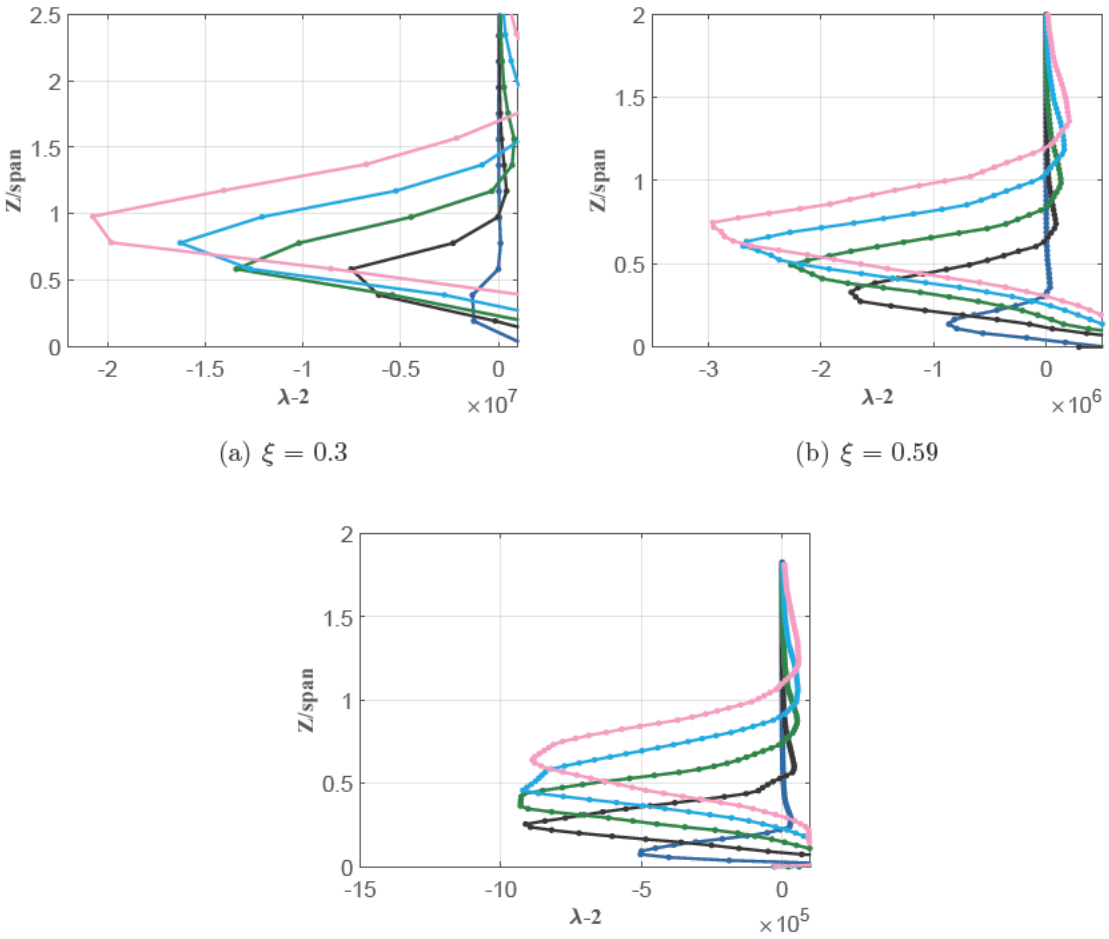

(a) $\xi = 0.3$

(b) $\xi = 0.59$

(c) $\xi = 0.87$

Figure 3.14: λ-2 vs Z/Span at each ξ for AoA = 0, 5, 10, 15, 20

The axial velocity profiles shown in Figures 3.15(a) and 3.15(b) show good agreement with experiments conducted by Pagan and Solignac detailed in reference [131]. The increase in AoA is matched by an increase in the vortex core axial flow velocity. The magnitude of scaled axial flow that they observed over a 75 degree swept delta wing is higher, although the different sweep angle, thickness distribution and anhedral angle of the wings will lead to differences in vortex magnitude. The upward shift of the vortex core with AoA is clearly visible in Figure 3.15(c) as well as the significantly reduced axial flow magnitude indicating that the vortex is losing strength.

Finally we examine the swirl (Y-Z plane component) velocity through the vortex shown in Figure 3.16. As the data is sampled on a line which goes vertically through the vortex core, we can use the side velocity scaled by freestream velocity (V/U_∞) for the swirl

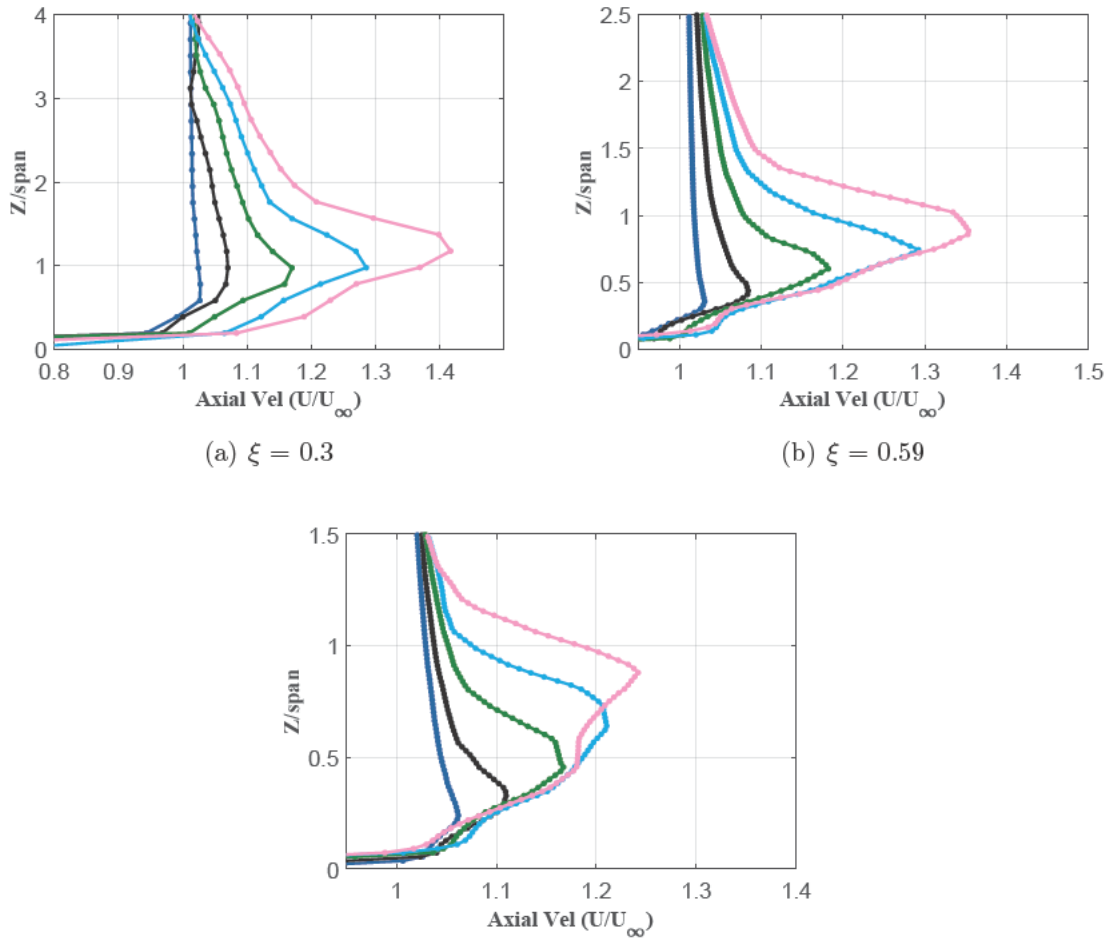

(a) $\xi = 0.3$

(b) $\xi = 0.59$

(c) $\xi = 0.87$

Figure 3.15: U/U_∞ vs Z/Span at each ξ for AoA = 0, 5, 10, 15, 20

velocity component. We might expect to observe an anti-symmetrical distribution of side velocity with a positive peak as the sample moves up to the vortex, corresponding to the outwards spanwise flow below the vortex core followed by a negative peak of equal magnitude above the vortex as the flow is pulled back inwards over the top of the vortex. Instead we observe a shift towards the positive side indicating that the vortex flow is superimposed on a net outward flow which, as observed in Figure 3.10, is likely due to the outward flow over the top of the fuselage instigated by the nose vortices being pulled down the side of the fuselage into the main wing vortices.

The overall flow structure is highly complex with four separate vortex structures observed at high AoA which all have some impact on the vehicle forces and moments. The effect of the nose vortex on the sideslip stabilisation effect of the vertical tails will require additional simulations of a full vehicle under non-zero AoS. The results for the full scale

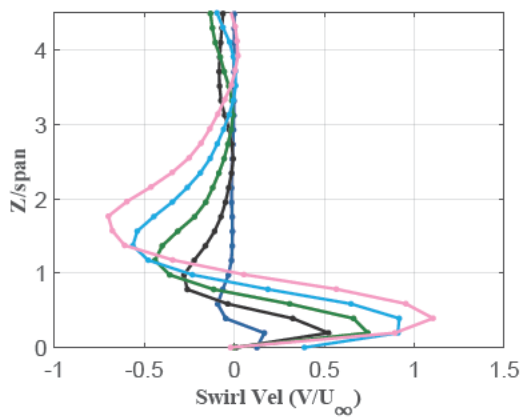

(a) $\xi = 0.3$

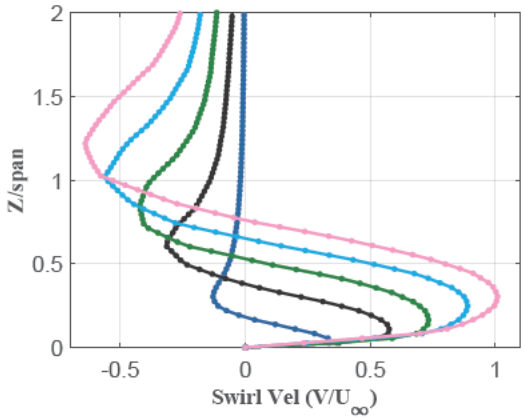

(b) $\xi = 0.59$

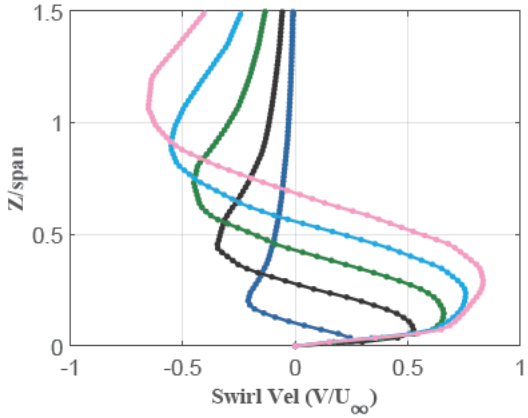

(c) $\xi = 0.87$

Figure 3.16: V/U_∞ vs Z/Span at each ξ for AoA = 0, 5, 10, 15, 20

Reynolds number simulations produce good agreement with the lower Reynolds wind tunnel scale simulations except at 20 degrees AoA. The results show that at the shifted centre of gravity, the pitch behaviour is stable up till 18 degrees AoA, and becomes stable again between 20 and 24 degrees. It is unclear whether the results beyond 18 degrees are fully reliable due to the likelihood of unsteady effects, which are investigated further in Section 3.3.3 by comparison to transient simulations.

3.3 Dynamic Simulations

This section describes the unsteady simulations of the Hexafly both under sinusoidal pitch oscillations and with a constant pitch angle to determine the damping characteristics of the vehicle and the impact of flow transients at selected AoA. The oscillating

simulations work on the same principles as a forced oscillation experiment in a wind tunnel. The sinusoidal motion results in a change in the forces (C_L and C_D) and moments (C_m) acting on the vehicle through each cycle of AoA. The single-point method for data reduction in forced oscillation testing outlined in reference [132] is used to analyse the pitching moment data for damping and stiffness characteristics (C'_{m_q} and C_{m_α}). This is carried out at AoA of -5, 0, 5, 10, 15 and 20 degrees and the results will be validated using the data collected from the concurrent wind tunnel test campaign.

Unsteady fixed pitch tests have been conducted at 10 and 25 degrees AoA. The results are analysed to determine the time dependent fluctuations of moment coefficient and are compared with the results of the steady calculations.

3.3.1 Transient CFD calculations

Sinusoidal pitch oscillations are implemented using the ANSYS Fluent User Defined Functions capability to specify the rotational rate of the spherical inner mesh region about the Y-Axis. This definition of pitch rate ($\dot{\theta}$) is implemented as in Eq. 3.2 where ω is the rotational frequency in rad/s, AOA_{max} is the oscillation amplitude in radians and t is the time in seconds. This is used to define the internal mesh rotational rate in rad/s.

$$\dot{\theta} = -AoA_{max}\omega cos(\omega t) \tag{3.2}$$

The mesh itself is the same 18 million cell mesh used for the steady calculations as it was determined to be sufficiently accurate and more likely to converge in a reasonable time during the dynamic simulations. The transient Fluent calculations are run for a specified number of iterations at each time step and for a specified time step length and each calculation is initialised using the steady state solution at the AoA under investigation. The determination of a sufficiently small time step length was done by setting the number of iterations at each time step, to 40, adjusting the time step length and comparing the results. The simulations were run for time steps of 0.01s and 0.005s at 20 degrees AoA which was again used as the benchmark condition on the assumption that the flowfield would be the most complex. The time step of 0.01 was considered

sufficient as the results in Figure 3.17 shows good agreement between the two.

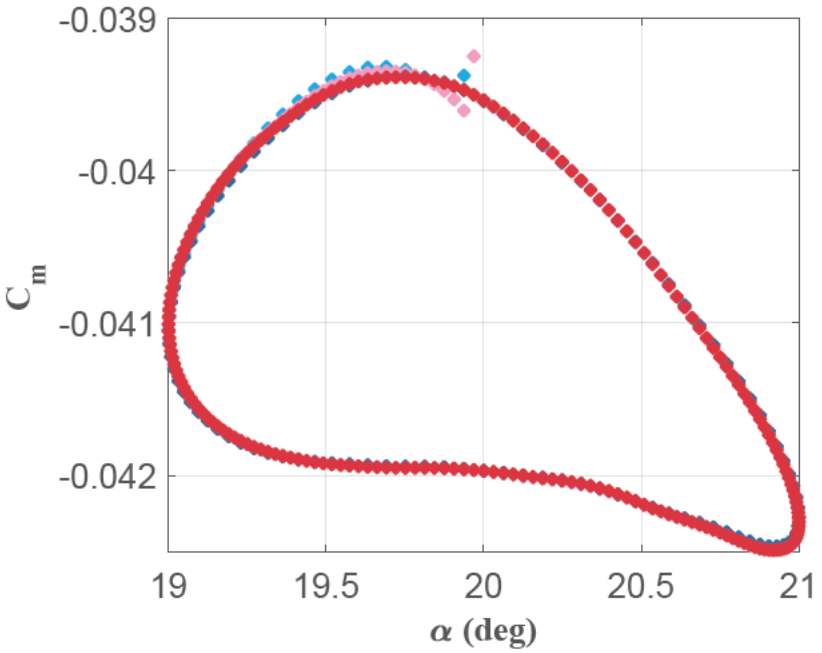

Figure 3.17: C_m vs AoA time step convergence, 0.01s 1st cycle, 0.005s 1st cycle, 0.01s 3rd cycle, 0.005s 3rd cycle

It is noted that the first cycle does show a significant difference between the two time steps however by the 3rd cycle these differences have become negligible and the difference in the resulting moment coefficients are 0.2% and 5% for pitch damping C'_{m_q} and pitch stiffness C_{m_α} respectively. This difference in C_{m_α} is particular to the 20 degree AoA case due to the small magnitude of C_{m_α} at this condition and at 10 degrees AoA the difference in the calculated pitch stiffness between the 0.005s and 0.01s time step calculations was found to be 0.3%. In subsequent figures, only the last full cycle that was run will be shown, as this provides the most converged results.

3.3.2 Data Reduction Methods

The key results to be obtained from this testing is the C'_{m_q} and C_{m_α} where C'_{m_q} is a combination of C_{m_q} and $C_{m_{\dot{\alpha}}}$. The method of forced oscillation of a model fixed at the moment centre (CG_{test} in this case) does not allow for the separation of the contributions to pitch moment from pitch rate q (C_{m_q}) and AoA rate $\dot{\alpha}$ ($C_{m_{\dot{\alpha}}}$) as both occur simultaneously at equal magnitudes. A separate forced plunging motion or forced flapping motion as investigated by Liu et al in reference [133] would be required to

isolate the q and $\dot{\alpha}$ components. The dynamic wind tunnel testing conducted in Chapter 5 is also similarly constrained to combined C'_{m_q}, therefore a comparison between the two to validate the CFD results can still be undertaken. The C_L and C_D components will also be analysed and compared to the steady results. The dependence of C_D on q and $\dot{\alpha}$ is usually negligible and not considered here [88]. However the derivative of C_L with respect to q and $\dot{\alpha}$, C'_{L_q} is presented as it is important to capturing plunge response to dynamic motion. The wind tunnel techniques used in Chapter 5 however, are not capable of independently verifying this result as lift force is not directly measured during the dynamic experiments.

Extracting the dynamic aerodynamic properties from the pitch oscillation data can be accomplished by a number of methods. As the motion is constrained to the specified sinusoidal motion, the pitch angle and rate are known. The general linearised aerodynamic model for a given aerodynamic coefficient about a particular steady state AoA is given in reference [134] and is repeated here, in Eq. 3.3 for freestream velocity U_∞, reference length c (=L_{ref}) and perturbation from steady state AoA, $\Delta\alpha$.

$$\Delta C_m = C_{m_\alpha}\Delta\alpha + C_{m_{\dot{\alpha}}}\frac{c}{2U_\infty}\dot{\alpha} + C_{m_q}\frac{c}{2U_\infty}q + C_{m_{\dot{q}}}\frac{c}{2U_\infty}\dot{q} \tag{3.3}$$

Using the combined pitch damping coefficient C'_{m_q}, this becomes Eq. 3.4.

$$\Delta C_m = C_{m_\alpha}\Delta\alpha + C'_{m_q}\frac{c}{2U_\infty}q + C_{m_{\dot{q}}}\frac{c}{2U_\infty}\dot{q} \tag{3.4}$$

Following a transient pitching simulation, the known AoA, pitch rate, q, and pitch acceleration, $\dot{q}$, and the calculated moment data C_m can be used to perform a least squares evaluation of the data to estimate the aerodynamic parameters. Alternatively a frequency domain analysis could be conducted which can also be used to determine the damping and stiffness characteristics. Both of these methods are described by Ronch et al in reference [134]. In both cases the resulting data is an average damping characteristic estimated over the whole range of the oscillation motion. For this work it is simpler, and preferable, to obtain the pitch and damping characteristics at the particular steady state

condition about which the oscillatory motion is applied. This allows the specific aerodynamic parameters to be directly correlated with a particular flight condition provided the dynamic response remains linear.

As such the single-point method described by Hoe et al in reference [132] is used to extract damping information. In order to compute the derivatives, the In-phase components ($\overline{C_{m_\alpha}} = C_{m_\alpha} - k^2 C_{m_{\dot{q}}}$ where $k = \frac{\omega c}{2U_\infty}$, the non-dimensional frequency) and Out-of-phase component (C'_{m_q} only) are calculated by taking the difference between the values of C_m at the specific points. The In-phase components are calculated from the difference in C_m at the maximum (point 1) and minimum (point 2) AoA as in Eq. 3.5, and the Out-of-phase component is determined from the difference between C_m at the nominal AoA at the descending (point 3) and ascending (point 4) nodal points as in Eq. 3.6.

$$\overline{C_{m_\alpha}} = \frac{C_{m_1} - C_{m_2}}{\alpha_1 - \alpha_2} \tag{3.5}$$

$$C'_{m_q} = \frac{C_{m_3} - C_{m_4}}{\frac{c}{2U_\infty}\dot{\alpha}_3 - \frac{c}{2U_\infty}\dot{\alpha}_4} \tag{3.6}$$

The contribution of $C_{m_{\dot{q}}}$ to the In-phase component will be determined by varying the frequency of the pitch oscillation and comparing the resulting trend in $\overline{C_{m_\alpha}}$. The value of C'_{L_q} will be determined by an analogous procedure.

3.3.3 Comparison of Unsteady and Steady Results

The unsteady simulations at 10 and 25 degrees AoA are compared to the steady results to determine the impact of transient effects on the resulting moment coefficient. 25 degrees AoA was chosen as it is likely that any transient effects will be most significant at a higher AoA. 10 degrees AoA was chosen as it should be indicative of the majority of the AoA range as it exhibits the full vortex structure development.

Figure 3.18(a) shows that the unsteady moment coefficient at 10 degrees diverges from the steady state solution within 0.05 seconds and settles into a steady cycle with an amplitude of 1×10^{-5}. The unsteady solution average is 0.1% lower than the steady

solution which is a negligible difference. The unsteady solution for 25 degrees AoA shown in Figure 3.18(b) similarly diverges from the steady solution, in this case increasing in 0.3s to a steady cycle with an amplitude smaller than the data resolution. The average unsteady pitching moment coefficient is 0.3% higher than the steady solution. In both cases the difference is not significant and we can conclude that the steady solutions are representing the flowfield over the surface sufficiently well when compared to the transient simulations.

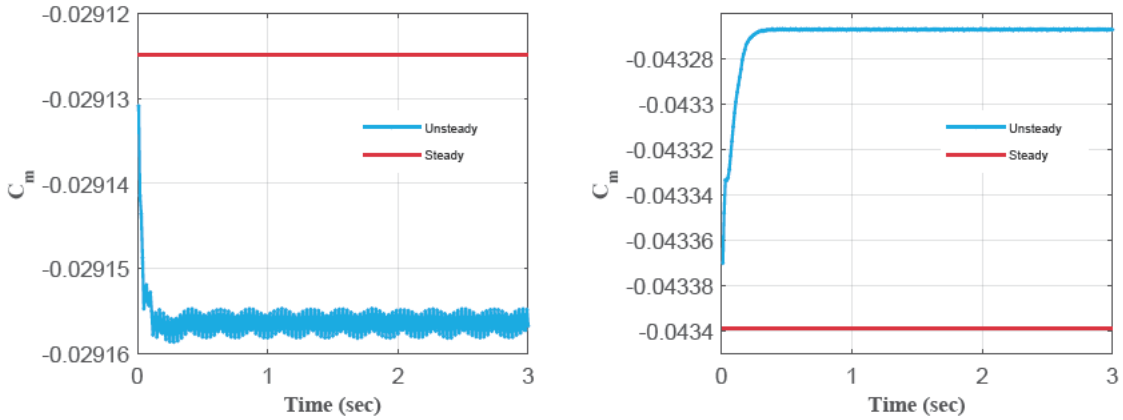

(a) 10 deg AoA

(b) 25 deg AoA

Figure 3.18: Unsteady and steady C_m vs time (s)

3.3.4 Dynamic Pitching Results

Pitching moment coefficient C_m for a 4 degree amplitude, 1 Hz oscillation at 5 degrees AoA is shown in Figure 3.19. The direction of change of C_m through the oscillation cycle is marked with black arrows. This anti-clockwise direction is important as it determines the stability of the damping characteristics. As the pitch oscillation drops through the descending node, Point 3, C_m is greater than the static value, and as it rises through the ascending node, Point 4, C_m is less than the static result which shows that the damping coefficient is opposing the moment. As the nose is rising the change in moment is negative which opposes the motion, and vice versa.

This stable pitch damping behaviour is observed across the entire AoA range from -5 to 20 degrees, and for each subsequent pitch cycle figure herein, the direction of motion around moment cycles is anti-clockwise and not annotated.

Pitch oscillations tests are run with amplitudes of 1, 2 and 4 degrees at 1 Hz and

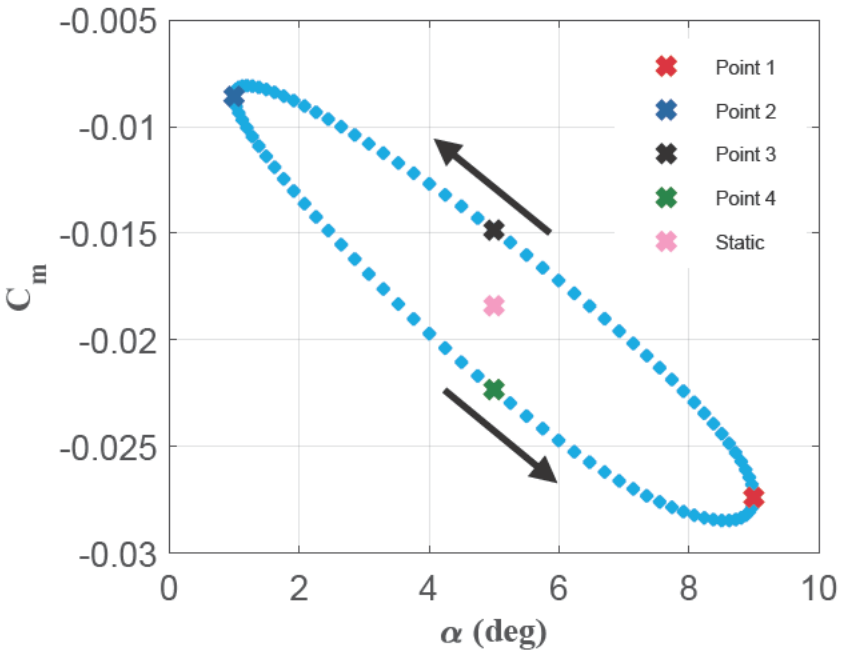

Figure 3.19: C_m vs AoA oscillation example

frequencies of 0.5 and 0.75 Hz at 4 degrees amplitude. These frequencies were chosen on the basis of initial wind tunnel tests outlined in Appendix B which suggested a short period frequency in the range 0.1-0.9Hz. The impact of frequency on the measured pitch damping was yet to be established but the frequencies chosen would allow this to be determined independently and the importance of $C_{m_{\dot{q}}}$ to be assessed in the relevant range of short period motion.

The pitch cycles for each AoA are shown in Figures 3.20 and 3.21. The static results at each AoA from the 18 million cell simulations are included in red on each figure. The static and dynamic results can only be compared at the extrema of the oscillation where the pitch rate is zero. At these points the static and dynamic results match very well. The moment cycles show adherence to the static trend shown in Figure 3.6 which increases our confidence that the linear model is applicable.

The cycles at 15 and 20 degrees AoA are more complex than the largely elliptical shapes at lower AoA, especially at 20 degrees shown in Figure 3.21(b). However, this complexity in the cycles is due to the underlying complexity of the static C_m curve at these AoA, and the shape of each cycle is largely due to the pitch moment response to pitch rate superimposed on the pitch moment at the instantaneous AoA.

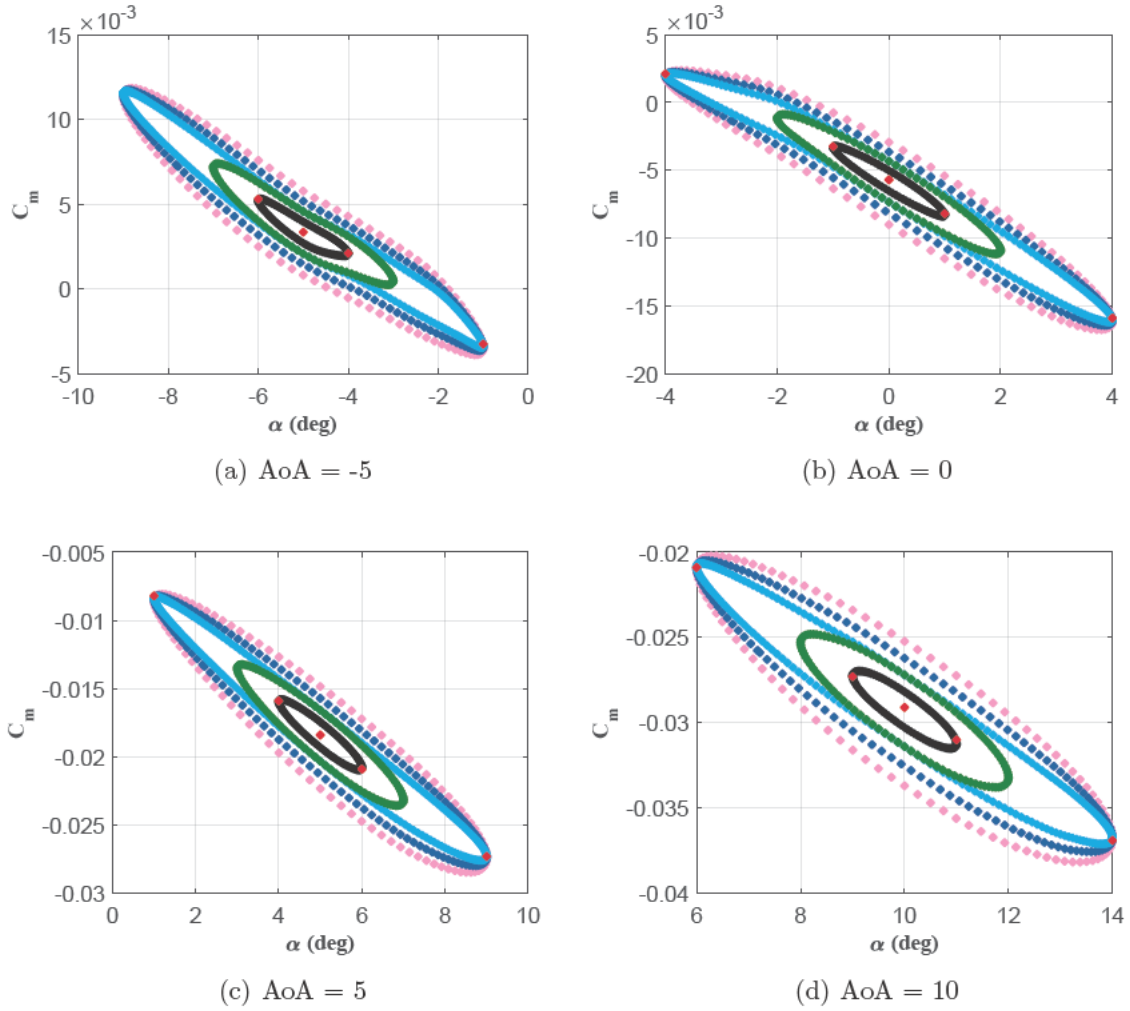

(a) AoA = -5

(b) AoA = 0

(c) AoA = 5

(d) AoA = 10

Figure 3.20: C_m cycles from -5 to 10 degrees AoA for amplitudes and frequencies: 4 deg 0.75 Hz, 1 deg 1 Hz, 2 deg 1 Hz, 4 deg 0.5 Hz, 4 deg 1 Hz and static results

The shape of each cycle seems invariant with amplitude and frequency. Different amplitudes and frequencies of oscillation scale the response along the static C_m curve and perpendicular to it respectively. The amplitude scaling along the C_m curve is highlighted in Figure 3.22 which shows the moment cycles superimposed on the static pitch curve over the whole AoA range. The width of the each curve in the direction perpendicular to the C_m curve is due to the maximum pitch rate of the specified oscillation. This depends on both the amplitude of oscillation and the frequency. This is highlighted in Figures 3.20 and 3.21 by the fact that the width of the curves for 2 deg, 1 Hz oscillations, shown in green, are the same as the width of the 4 deg, 0.5 Hz oscillations shown in cyan. The maximum pitch rate of the oscillations is given by Eq. 3.2 where the cosine term equals 1, $\dot{\theta}_{max} = AoA_{max}\omega$. Doubling the amplitude and halving the frequency results in the

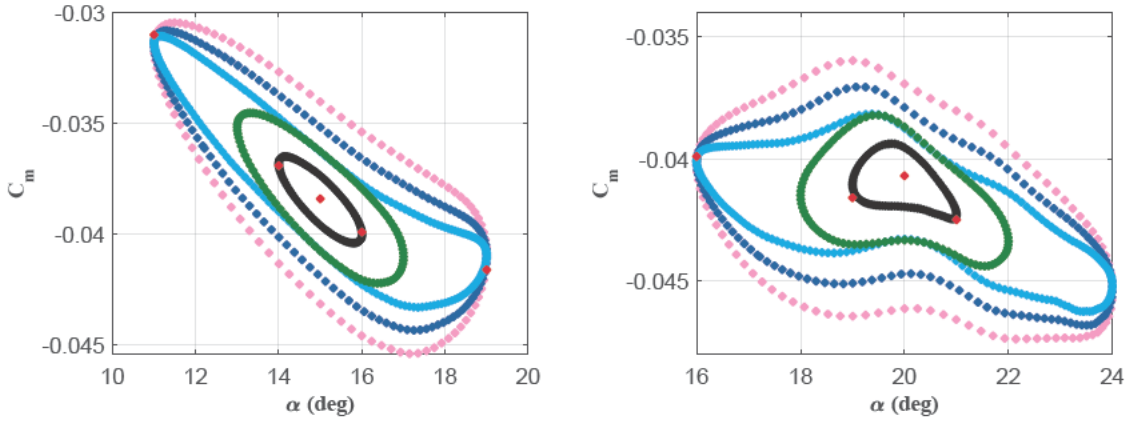

(a) AoA = 15 (b) AoA = 20

Figure 3.21: C_m cycles at 15 and 20 degrees AoA for amplitudes and frequencies: 4 deg 0.75 Hz, 1 deg 1 Hz, 2 deg 1 Hz, 4 deg 0.5 Hz, 4 deg 1 Hz and static results

same maximum pitch rate and these curves match at nodal Points 3 and 4 at all AoA presented.

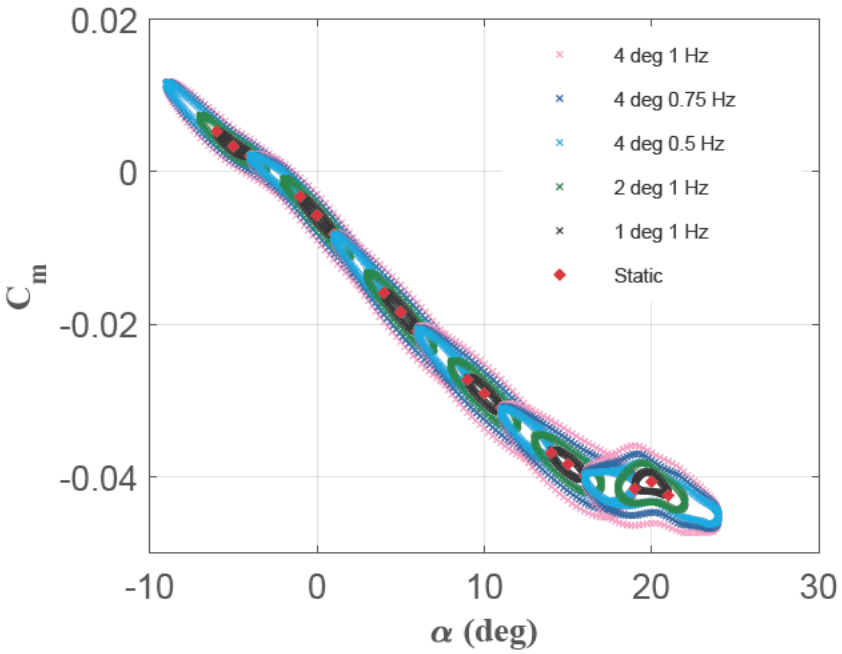

Figure 3.22: C_m across AoA range

The In-phase components ($\overline{C_{m_\alpha}} = C_{m_\alpha} - k^2 C_{m_{\dot{q}}}$) are computed using the single-point method at Points 1 and 2 as described earlier. By comparing the three 4 deg amplitude oscillations which only differ in frequency we can estimate the magnitude of the $C_{m_{\dot{q}}}$ term. Figures 3.20 and 3.21 show these curves overlapping at the extreme AoA Points 1

and 2 which suggests the magnitude of $C_{m_{\dot{q}}}$ is small. Using the assumption that the pitch stiffness term C_{m_α} and $C_{m_{\dot{q}}}$ are the same for the three 4 degree oscillation amplitude cases, $C_{m_{\dot{q}}}$ can be calculated from any two of the data sets, 1 and 2 using Eq. 3.7.

$$C_{m_{\dot{q}}} = \frac{\overline{C_{m_\alpha 2}} - \overline{C_{m_\alpha 1}}}{k_1^2 - k_2^2} \tag{3.7}$$

The actual differences between the calculated C_{m_α} terms for 0.5 and 1 Hz oscillations are of the order 0.001 which is approaching the limits of the accuracy of the CFD simulations. The data from the 0.5Hz and 1Hz 4 degree amplitude cases is used to calculate $C_{m_{\dot{q}}}$ in order to maximise the difference. The resulting $C_{m_{\dot{q}}}$, C_{m_α} and C'_{m_q} calculated at each AoA and for each input oscillation condition are presented in Figures 3.23 and 3.24 and Table 3.3.

Figure 3.23 shows very good agreement between oscillation conditions in the resulting calculated C'_{m_q} with the exception of the 4 deg, 0.75 Hz simulation which deviates over the whole AoA range by around 2%. The 1 deg, 1 Hz result deviates from the other results by 6% at 20 degrees AoA. This AoA is also where the static simulations showed larger sensitivity to grid density and this could be an effect of not fully resolving the flow adequately. The 2% deviation between the 4 deg, 0.75 Hz simulation and the other results is likely due to the lack of a data point exactly at the descending node, Point 3, which therefore relies on an estimate based on the adjacent points.

Figure 3.24 shows the results for C_{m_α} against AoA. There is significant variation in the calculated C_{m_α} between the different oscillation conditions. Differences between the oscillation amplitude are the cause of this variation. The single-point method used here calculates C_{m_α} across a larger range of AoA for larger amplitude oscillations. The amplitude dependence is reflective of the non-linear relationship between C_m and AoA evident in Figure 3.6. As oscillation amplitude increases, the resulting C_{m_α} is averaged over a wider portion of the C_m curve. The close agreement between C_{m_α} results for the three 4 deg oscillation simulations highlights this effect. Further adding to this is the generally good agreement between the static results for C_{m_α}, which were based on a 2 point gradient estimation spaced 1 deg AoA apart, and the smaller oscillation amplitude simulations. The difference between $\overline{C_{m_\alpha}}$ and C_{m_α} was found to be negligible due to the

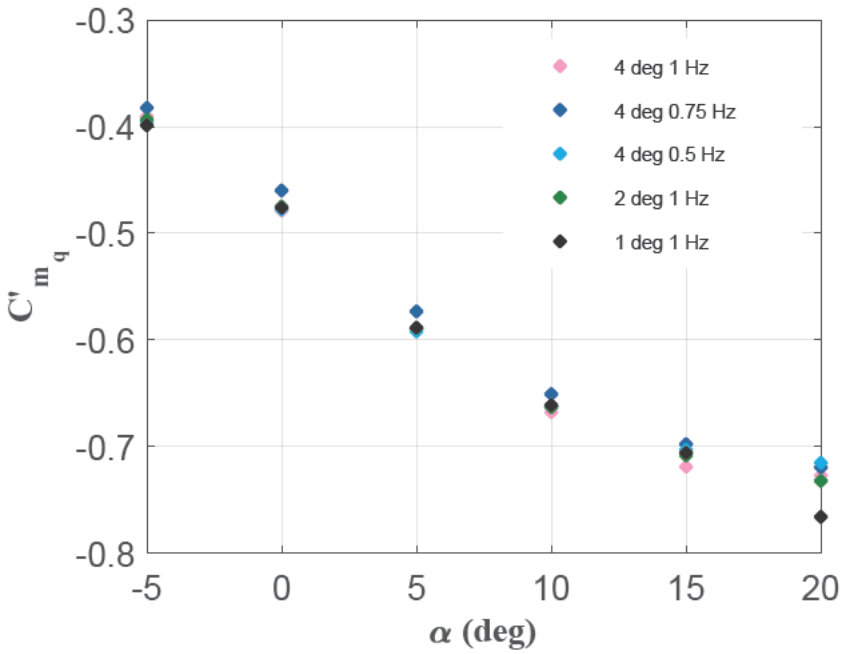

Figure 3.23: C'_{m_q} vs AoA from dynamic CFD simulations

small value of non-dimensional frequency k (0.04 - 0.09) so the result is referred to as C_{m_α} from here on.

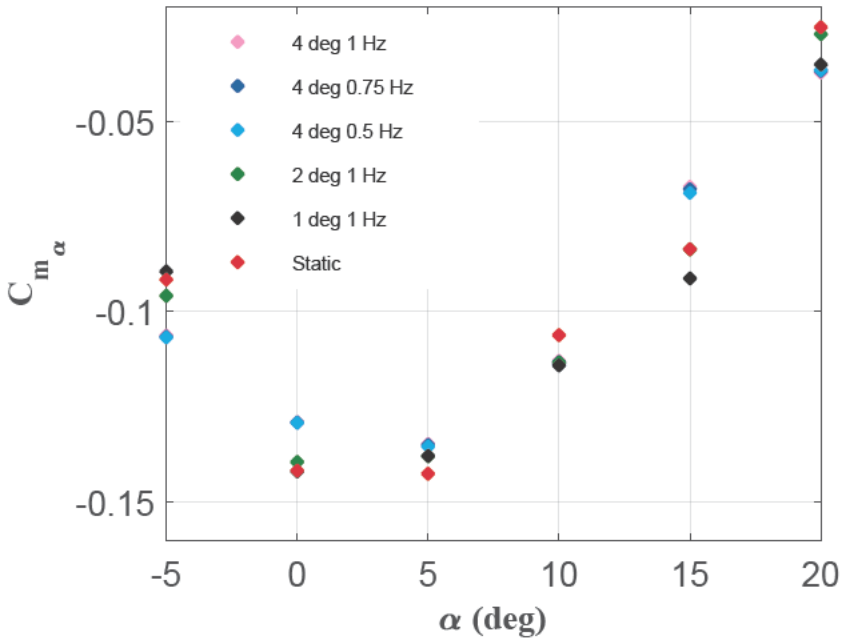

Figure 3.24: C_{m_α} vs AoA from dynamic CFD simulations

The results for $C_{m_{\dot{q}}}$ are shown in Table 3.3 and suggest that there is a measurable

influence of pitch rate acceleration on the resulting pitching moment, however, this dependence would only have a significant impact at much higher frequencies. Analysis presented in Chapter 5 in relation to the dynamic wind tunnel testing uses the calculated values of C_{m_α} from this static and dynamic CFD as well as static wind tunnel testing to find the estimated short period mode frequency. The results lie between 0.15 and 0.88 Hz for the AoA range of -5 to 20 degrees. This suggests that the $C_{m_{\dot{q}}}$ can be safely ignored for this vehicle as the results of this dynamic CFD suggest that the impact on in-phase motion in this frequency range is negligible.

Table 3.3: $C_{m_{\dot{q}}}$ Results

AoA (deg)	-5	0	5	10	15	20
$C_{m_{\dot{q}}}$	-0.085	-0.024	-0.11	-0.16	-0.26	0.11

Lift coefficient results across the AoA range are shown in Figure 3.25. The responses match the static results across the whole AoA range and the shape of each cycle show the characteristic elliptical shape of a linear response.

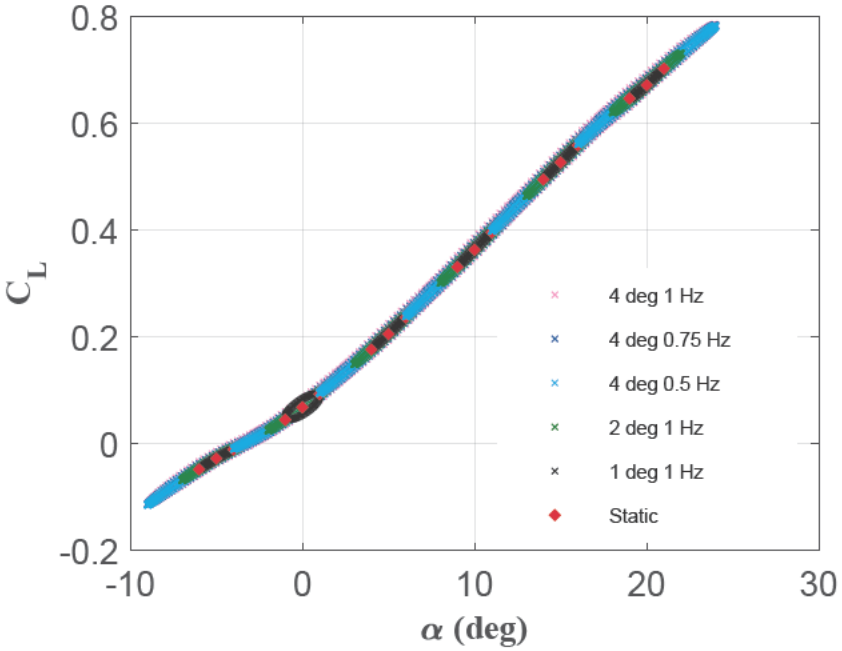

Figure 3.25: C_L vs AoA from dynamic CFD simulations

The C'_{L_q} results are shown in Figure 3.26. The positive values and increasing trend are typical of aircraft with more lifting surface behind the centre of rotation than in front. As the vehicle pitches up the relative flow angle at the rear of the vehicle is increased

and the the angle is decreased at the front. This results in increased lift towards the rear and decreased lift at the front due to the pitch rotation. In the case of conventional aircraft this is due to the increased lift at the horizontal stabiliser which opposes the pitching moment and increases overall lift. Roskam in reference [88] gives typical values of around 25 for C'_{m_q} in the case of large civilian transport aircraft. In the case of the Hexafly-Int the values of C'_{m_q} are two orders of magnitude smaller, partly due to the much larger reference length than typically used (vehicle length versus wing mean aerodynamic chord), and also due to the lack of a separate tail surface with a large moment arm to the centre of gravity. The Hexafly-Int values for C'_{L_q} are in the order of 2 to 3 which is again smaller than a typical aircraft which Roskam states are roughly 8-10 at low subsonic speeds. Again, this is likely due to the lack of a separate tail surface. The results from the 4 deg, 0.75 Hz simulation are again, significantly different from the other values due to the lack of a data point at the descending node of the cycle.

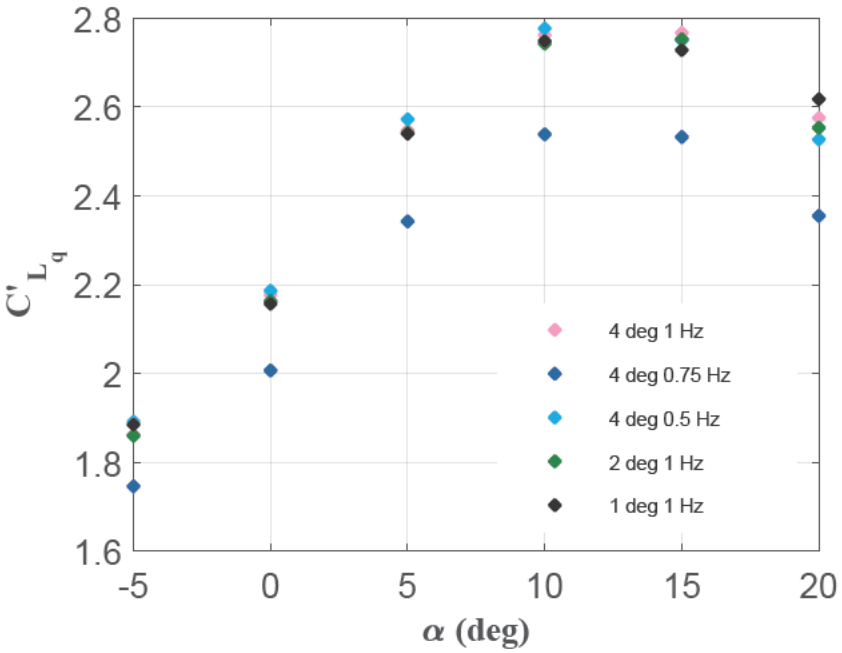

Figure 3.26: C'_{L_q} vs AoA from dynamic CFD simulations

For completeness the drag coefficient data across the AoA range for the dynamic simulations is shown in Figure 3.27. The results show agreement between the static CFD simulations and the dynamic oscillating results. There is very little effect from pitch rate on the drag coefficient reflected in the small width of the oscillation cycles.

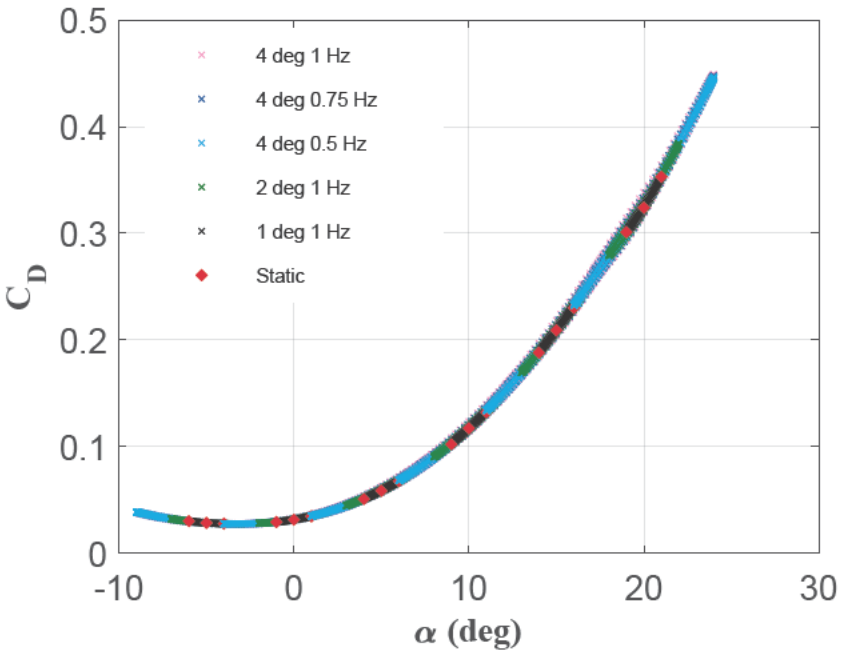

Figure 3.27: C_D vs AoA from dynamic CFD simulations

3.4 Conclusions

The static and dynamic CFD simulations which have been presented in this chapter show good agreement with each other. The numerical methods used are robust and are expected to provide accurate results. The results of the static and dynamic CFD testing are compared to the results from the wind tunnel tests in Chapter 5. In the case of the dynamic CFD testing the result of most importance is the combined pitch damping coefficient, C'_{m_q}. This value has the greatest impact on the handling qualities of the aircraft of all the dynamic stability derivatives and will be directly compared to the results from the dynamic wind tunnel tests. The dynamic results are taken from the 4 deg amplitude, 1 Hz oscillation as this matches the conditions of the dynamic wind tunnel testing best. If the CFD calculations presented here show good agreement with the wind tunnel tests then this will validate the use of these numerical tools on similar hypersonic waverider type vehicles to calculate dynamic stability derivatives at low speeds. This reduces the need for costly and time consuming flight tests or wind tunnel testing.

Chapter 4

Static Wind Tunnel Testing

Wind tunnel testing is vital to confirming the performance of computational aerodynamic tools such as the CFD analysis used in Chapter 3. It provides a method of generating data from flows that, ideally, are similar to the free air flows that aircraft will actually encounter. Although CFD and other numerical methods have improved over the years, there is still a need to confirm their results against data from practical experiments. Static force and moment measurements, such as lift, drag, side-force and moments about the three axes, cannot be directly measured from flight test data. Mounting an aerodynamic model of the vehicle in question in a wind tunnel through a force sensor is the only practical means of directly observing this data.

This chapter details the static testing results for the Hexafly vehicle and the model, wind tunnel and mounting method used. The wind tunnel facilities at the University of Sydney are outlined, as are the sensors used for force measurements. The design of the experiments is discussed with ranges of angle of attack, angles of side-slip and velocity ranges used also detailed. The results are presented for the longitudinal static force, moments and stability derivatives, followed by the lateral results. The elevon control derivatives are also determined.

4.1 Wind Tunnel Facilities

Experiments were conducted in the 4x3 foot wind tunnel at the University of Sydney. This tunnel has low turbulence levels (critical Reynolds Number of 3.6×10^5) and was

calibrated recently by Anderson [135]. The high speed test section is capable of flow speeds up to 60m/s but limitations of the model structure, the wind tunnel mount and the limits of the load balance capped the tested speeds to 25m/s. Limited test runs up to 30m/s did not produce a significant change in the results. The layout of the closed loop tunnel is shown in Figure 4.1.

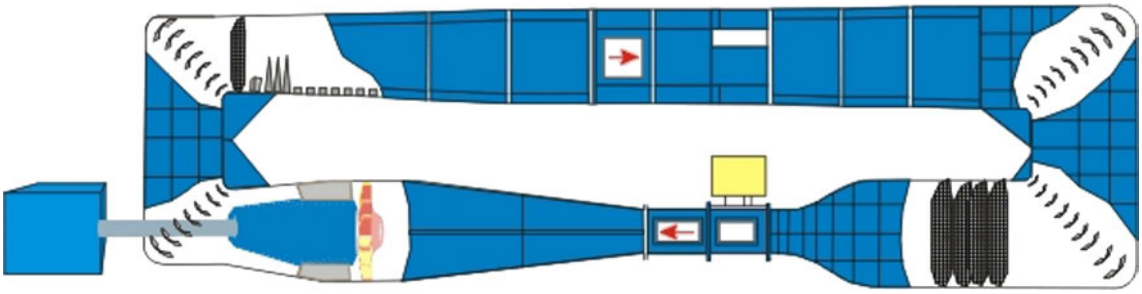

Figure 4.1: Diagram of the University of Sydney 3x4 wind tunnel from reference [135]

The mount used in the wind tunnel was developed by Anderson [135] specifically to test small models with minimal interference. The mount shown in Figure 4.2 is specifically designed to be small. This allows small scale models to be designed such that as much of the force sensor and AoA rotation mechanism shown in Figure 4.2(b) are within the model as possible to reduce interference with the flow. The load balance is attached to the end of the mount and forms the link between the mount and the model. This isolates the force measurements to the aerodynamic forces on the model itself. The mount is capable of a large range of angles of attack, well beyond the capabilities required for the Hexafly testing conducted here. Angle of attack is controlled by a linear actuator with angle feedback provided by an accelerometer on the head of the mount.

Forces are measured using an ATI Mini-45 6 component Force Transducer shown attached to the wind tunnel mount rotation mechanism via adaptor plates in Figure 4.2(b). The load cell has a small profile and is capable of measuring XYZ moments and forces up to 10 Nm and 290 N respectively. The ATI load cell is ideal for the application as its small profile allows it to be housed within the model reducing flow interference. The load cells are individually factory calibrated so no further calibration is needed, though the validity of the calibration has been checked using known weights [135]. The signals from the load cell and the accelerometer are read by a National Instruments Data Acquisition (NIDAQ) device which handles converting the analogue voltages to digital signals for the computer to process.

(a) 3x4 mount in wind tunnel test section

(b) Close-up of mount rotation mechanism and load cell

Figure 4.2: 3x4 wind tunnel mount with load cell attached

Wind tunnel speed is measured by two static pressure ports upstream of the model, one before the contraction region and one in the contraction region. The ratio of these pressures is used to calculated the flow speed in the test section and has been previously calibrated against pitot static readings in the test section [135]. As this system is directly measuring dynamic pressure as a function of the two static port readings, no assumptions need to be made about air density, pressure and temperature on the day as dynamic pressure is the data which is used to non-dimensionalise the force and moment data.

Matlab software has been developed in references [136] and [135] to read in the data from the airspeed sensors and the NIDAQ which is receiving the load cell and AoA measurements. It sends signals to the linear actuator of the mount which controls the angle of attack. The software also handles the calibration of the load cell signals to forces and moments in Newtons (N) and Newton-Meters (Nm). This allows automation of the process to run angle of attack data collection sweeps and allows control over the data sampling rate and duration of measurements from the NIDAQ. For this work the sample rate for the load cell was set to 2kHz and each AoA was sampled for 2 seconds resulting in 4000 samples. A delay in measurement at each AoA is applied to allow the model motion vibration to settle before the load cell measurements are taken. The dynamic pressure measurements were sampled at a frequency of 10Hz.

The software also allows a sequence of tare measurements to be taken at a range of AoA settings. This is run before the wind tunnel is switched on to account for the weight of the model and this AoA dependent value is removed from all subsequent measurements

taken after.

4.2 Wind Tunnel Model

The model used during the static testing is the same shell as that used for the dynamic testing. The model itself is made of 22 3D printed parts split to accommodate the size limitations of the Upbox 3D printers used. The model is 0.95m long, or 0.289 scale to the Hexafly EFTV. Model sizing was a trade-off between a number of factors. These include allowing for a minimum separation between the nose of the model and the wind tunnel walls at large angles of attack, not having the nose of the model in the contraction zone of the wind tunnel at zero angle of attack, and having less than 50% area blockage at the maximum angle of attack. This blockage limit is in line with the recommendations for low speed testing used for the NASA Ames Unitary Plan Wind Tunnel [137]. Another consideration was the requirements of the dynamic test campaign outlined in Chapter 5. In the end the size of the electronic components, and the pitch gimbal with attached sensor required to fit within the body of the model became the limiting factor. The resulting area ratio of the model cross section to the wind tunnel section area was only 8% at 25 degrees AoA.

The parts are fastened to each other by bolts and are attached to two laser cut 3mm thick wood struts which run along the sides of the main cavity within the fuselage and brace the whole structure. The laser cut struts allow precise positioning of the holes used to fasten the external 3D printed parts and the internal mounting points for the load cell. The wind tunnel model configured for static testing is shown in Figure 4.3(a).

The internal gimbal mount and UAVMainframe boards (detailed in Chapter 5) are removed and replaced with a perspex mount attached to the structural laser cut ribs that connect the 3D printed body parts to the internal components and each other. The perspex mount is designed such that the load cell origin is at the centre of gravity for the vehicle used for dynamic testing as shown in Figure 4.3(b). Shifting the moment reference centre in post processing requires a combination of the moment and force data at each AoA. This introduces additional error as a result of combining the errors in the force and moment measurements. Therefore the point at which the load cell is measuring the forces and moments will yield the most accurate results possible.

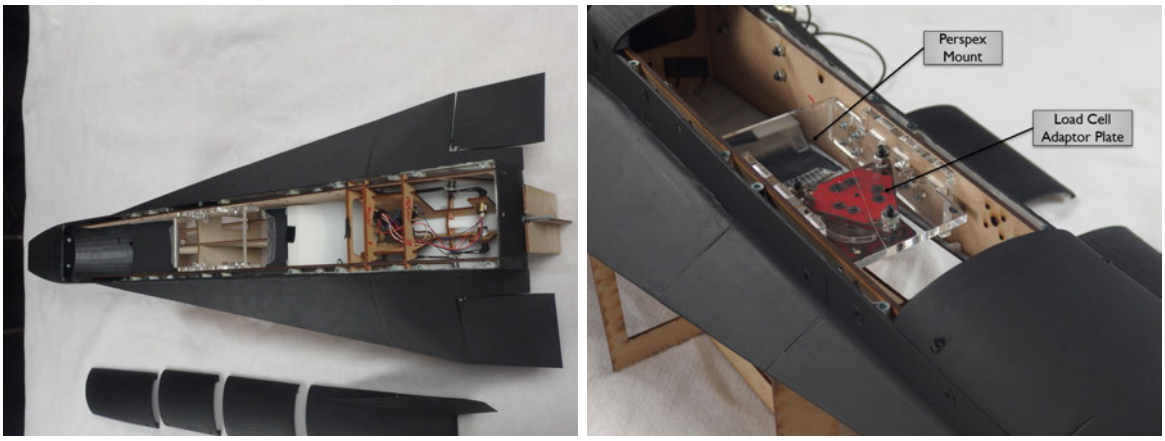

(a) Model configured for static testing (b) Perspex mount with load cell attached

Figure 4.3: Wind tunnel model static testing configuration

The centre of gravity used during the static testing CG_{test} and the expected centre of gravity of the full Hexafly EFTV CG_{des} are given in Table 4.1 relative to the reference frame outlined in Chapter 2. These are also shown in Figure 4.4.

Table 4.1: Wind tunnel and Full scale vehicle parameters

Scale	L_{ref} (m)	CG_{des} (x,y,z) (m)	CG_{test} (x,y,z) (m)
Hexafly EFTV	3.29	(1.555,0,0)	(1.247,0,0.052)
Wind Tunnel Model	0.95	(0.449,0,0)	(0.360,0,0.003)

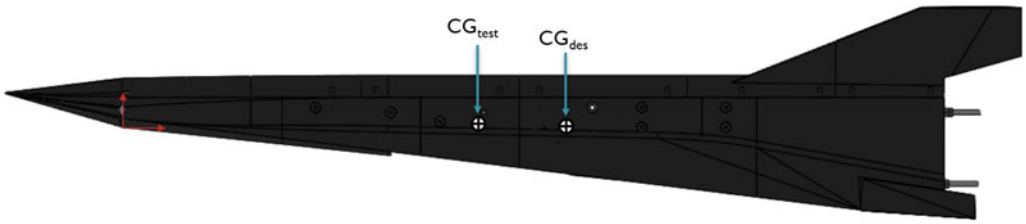

Figure 4.4: CG_{des} and CG_{test} superimposed on sideview of WT model in CAD software

The model mounted within the wind tunnel for static testing is shown in Figure 4.5 from a side angle. Note that the model is mounted upside down and is shown at a positive angle of attack. This makes no difference to the outcome of the measurements although care must be taken to ensure the directions of forces and moments are converted to the appropriate reference frame.

Figure 4.5: Model mounted in 3x4 wind tunnel for static testing at positive AoA

4.3 Test Conditions

The static testing was conducted at 15, 20 and 25m/s. The speed was limited to this range to reduce the loads on the model itself, which had unknown structural limits, and to limit the forces and moments measured by the load cell. Smaller loads allows a more precise calibration mode (accuracy given in Table 4.2) to be used on the Mini45 6 component load cell.

The Reynolds number is the key similarity parameter for static testing. The full scale vehicle is expected to land at speeds below Mach 0.3 so compressibility effects are not an issue [138]. The compromises required for model sizing and the available test facilities make testing at the same Reynolds number impossible. The key issue is then, how well are the results at this Reynolds number going to match the full vehicle at full speed? CFD testing presented in Chapter 3 was used to guide this question. The comparison of the forces and moments showed very good agreement between the full scale higher speed and small scale lower speed results. This gives us confidence that the Reynolds effects at these speeds will not greatly impact the applicability of the wind tunnel results, provided good agreement is observed between the lower Reynolds number CFD and wind tunnel test results. Initial wind tunnel testing at different speeds also suggested little effect from the Reynolds number over the range tested. This matches the results observed in

previous studies on vehicles with high sweep angle delta wings with sharp leading edges which showed smaller flow variance with Reynolds number compared with more blunt leading edges [71]. Most results for the static testing are presented in this chapter are for a 20m/s flow speed. Given the model reference length of 0.95m, this corresponds to a Reynolds number of 1.3×10^6 at 20m/s. The full scale vehicle landing at 80m/s with a length of 3.29m has a Reynolds number of 1.8×10^7 which is an order of magnitude larger.

The Angle of Attack (AoA) was varied between -5 and 23 degrees. Larger angles would have moved the nose of the model too close to the walls for the results to be reliable. Ideally a smaller model would have allowed larger angles of attack to be tested, but as mentioned above, the use of the same model for dynamic testing forced a minimum model size to fit the dynamic testing components. The angle of sideslip (AoS) was set to 0, 1, 5, 6, 10 and 11 degrees to allow gradients to be calculated at 3 sideslip conditions. These sideslip conditions match those tested by Pegg et al [80] to simulate a worst case scenario landing at 151kts with a 30kt crosswind. Non-zero manufacturing tolerances in model construction results in small asymmetry, so side force, roll and yaw moments are not zero at zero angle of sideslip as would be ideally expected. This is unavoidable, however, the key stability derivatives are obtained using a gradient based calculation so this data offset is not a significant issue.

4.4 Uncertainty, Corrections and Calibration

This section deals with the process of obtaining accurate data from wind tunnel experiments. Sensor calibration, wind tunnel corrections and characterising uncertainty are outlined in order to clarify how well the resulting force and moment results are unlikely to match the true vehicle forces and moments.

4.4.1 Sensor Calibrations

As outlined above, the load cell and the airspeed measurements were not re-calibrated in this work due to recent calibration and good agreement between data collected during this work and previous tests. However the AoA data in the wind tunnel calibration did require calibration. An offset is expected due to differences in the wind tunnel model

reference axis and the wind tunnel mount. Calibration was done using an iGagin Angle Cube, a digital angle measurement device which is accurate to 0.2 degrees [139], using the rear surface of the model as the reference z-y plane of the model.

In addition, limitation in the AoA tracking meant that the exact AoA sequence could not be replicated exactly between runs. The wind tunnel software developed by Anderson and Lehmküler [135] [136] and mount developed by Anderson require precise calibration as the linear actuator which drives AoA position uses fixed inputs to produce specific AoA. Over time, and likely with temperature change, this calibration has drifted. Although the measured AoA from the software was calibrated directly, the commanded AoA was not re-calibrated in this work. This meant that although repeated runs could be done in order to establish the level of repeatability and quantify error, the data between runs required interpolation to align the AoA range. The added uncertainty of this process was accounted for as outlined in Section 4.4.3.

4.4.2 Wind Tunnel Corrections

The correction method outlined in reference [140] has been used here. This method is a simplified equation which corrects for solid and wake blockage. The correction factor is given in Eq. 4.1 where AR_{GEO} is the geometric aspect ratio of the model, A_{WT} is the wind tunnel section cross sectional area, C_D and C_L are the uncorrected lift and drag coefficients, S is the reference area of the model and δ_w is a downwash correction constant obtained from reference [138]. The correction factor is used to obtain a corrected dynamic pressure (q_c) which accounts for solid and wake blockage effects. In practice the difference was found to be very small due to the small blockage area of the model.

$$\begin{aligned} \epsilon &= (S/A_{WT})(C_D - C_L^2[(1/\pi AR_G EO) - \delta_w(S/A_{WT})]) \\ q_c &= q(1+\epsilon)^2 \end{aligned} \tag{4.1}$$

4.4.3 Measurement Uncertainty

Measurement uncertainty is an inevitable factor in experimental work. The sources of systematic errors in this work have been minimized where possible, such as calibrating

AoA measurements against an external sensor, and then characterized to allow the uncertainty to be measured. The sources of uncertainty during static wind tunnel testing are the AoA measurement, the dynamic pressure sensor measurement, and the load cell resolution.

The various measurements are treated in two different ways. Where they represent single measurements they are treated using the method outlined by Kline and McClintock [141] for combining individual measurement uncertainties. Where multiple measurements have been taken, with a resulting standard deviation, they are treated as independent with an assumed normal distribution, which are combined using the confidence interval method outlined by Pope [138]. In both cases the 95% confidence level has been chosen.

The dynamic pressure measurement uncertainty is directly measured by the wind tunnel software during each sample of 40 measurements. The standard deviation of the data can be calculated and with 40 measurements, the 95% confidence interval is 32% of the standard deviation [138].

The AoA measurements are limited by the accuracy of the iGagin Angle Cube used to calibrate the accelerometer readings which is accurate to ± 0.2 degrees [139]. The angle calibration is carried out over the full AoA range from -5 to 25 degrees and a linear fit is applied. The spread of the resulting gradients based on the ± 0.2 degree uncertainty results in an AoA uncertainty over a 2 degree interval of 0.03 degrees. This is the uncertainty in AoA measurement that has been applied to C_{m_α} calculations which use 2 degree AoA intervals to calculate gradient.

The Load cell measurement resolutions in each axis are shown in Table 4.2 for the selected calibration [142]. As the load cell measurements are taken 4000 times each sample, this can be treated as multiple individual measurements and the 95% confidence interval is 0.031 of the standard deviation [138].

Table 4.2: ATI Mini-45 Resolution

Calibration	Fx,Fy	Fz	Tx,Ty	Tz
SI-290-10	1/8 N	1/8 N	1/376 Nm	1/752 Nm

For most measurements of concern here, the bias errors likely introduced with calibration errors are not a problem as the stability derivatives are the key data examined. This is a gradient based analysis for lateral and longitudinal stability that removes the effect of

bias. Where gradients have been calculated, the uncertainty of the results is calculated by combining the uncertainties of the coefficient and the angle of sideslip or attack using the Kline and McClintock method [141].

4.5 Results

Results are presented for the two key centres of gravity shown in Figure 4.4. The vehicle design centre of gravity for Hexafly and the centre of gravity used for the dynamic tests. The design CG is referred to as CG_{des}, and the shifted CG used for the dynamic testing is referred to as CG_{test}.

The effect of varied airspeed was examined by running tests at 15, 20 and 25 m/s. The key result of interest is the effect on the pitching moment, though the other forces and moments are also examined. The coefficient of moment at 20 and 25 m/s is compared in Figure 4.6. The closeness of the shape at 20 and 25m/s gives confidence that the Reynolds effects are small in the range that is being tested and that the flowfield is the same between the two speeds. The fact that the pitch break occurs at the same angle of attack suggests the vortex strength and breakdown characteristics are also invariant with Reynolds number. Studies summarised by Nelson and Pelletier [71] suggest that delta wings without centerbodies are usually insensitive to Reynolds number, although the presence of the fuselage on the Hexafly design may introduce a Reynolds dependent effect on the flowfield. The differences in magnitude could be due to uncertainties in the velocity measurement or inadequate correction factors being applied. The speed variance was tested at zero sideslip so the effect on the lateral coefficients is not determined here, however, the drag and lift are shown in Figure 4.7. The results confirm the small dependence on Reynolds number in the range tested. The results from here on are presented for 20m/s.

4.5.1 Longitudinal Results

The lift to drag (L/D) ratio curve shown in Figure 4.8 shows a peak L/D of 3.3 at approximately 7 degrees AoA. This is very low compared to conventional subsonic aircraft but is consistent with the L/D range of the Space Shuttle (4.5 [11]) and the X-15 (4 [5]). The Concorde had an L/D ratio of 4 at takeoff and landing [143]. The L/D ratio decreases

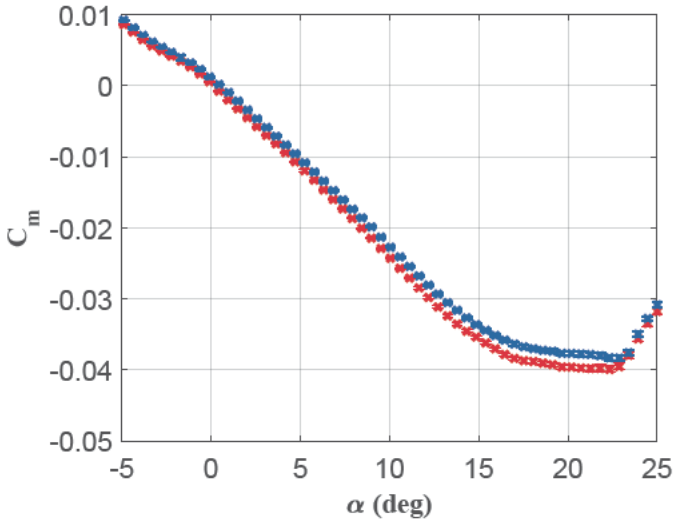

Figure 4.6: Pitching moment vs AoA, ● - 20m/s, ● - 25m/s

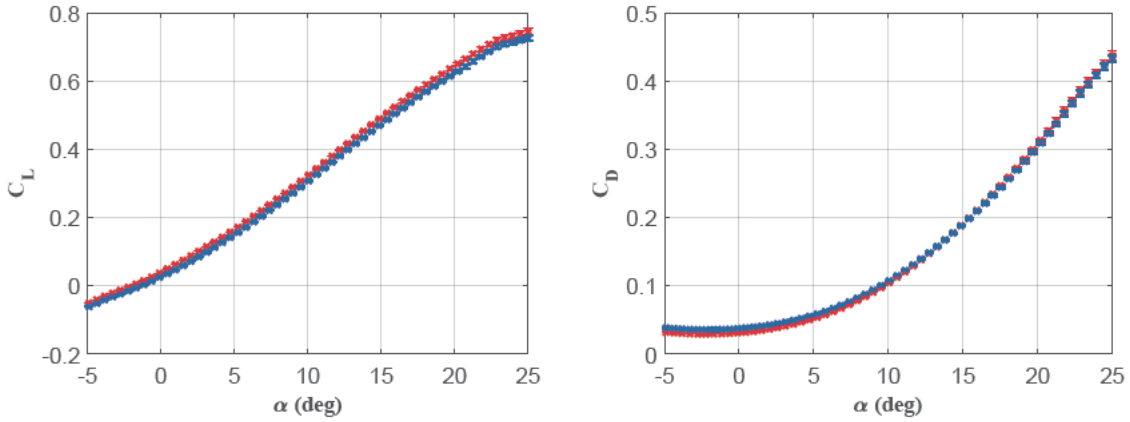

(a) Lift coefficient at 20 and 25 m/s

(b) Drag coefficient at 20 and 25 m/s

Figure 4.7: Lift and Drag coefficient vs AoA, ● - 20m/s, ● - 25m/s

beyond 7 degrees AoA which may be of concern if the required lift pushes the landing trim AoA to higher values.

The lift curve slope shown in Figure 4.7 exhibits the strong non-linearity which is a feature of low aspect ratio, highly swept planform vehicles due to the vortex systems which develop on the upper wing surface. The lift curve slope is only linear in the region between -5 and 1 degrees AoA. A linear fit has been applied to this region and extrapolated to clearly show the non-linear vortex lift contribution in Figure 4.9. The calculated linear lift gradient is 1.1 per Radian which is far below that of conventional subsonic, higher aspect ratio wings. Tranair was used to provide initial predictions of the

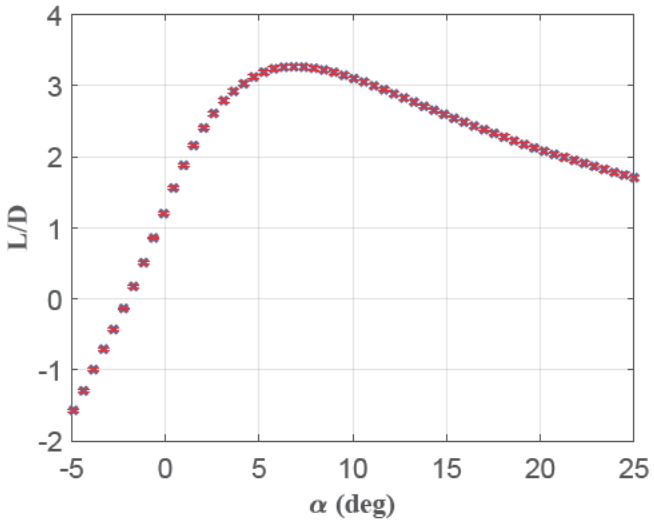

Figure 4.8: L/D at 20 m/s

aerodynamic coefficients as outlined in Appendix A. As a potential flow solver, Tranair does not predict the vortex behaviour that occurs over slender wing vehicles such as Hexafly. This is shown in Figure 4.9 where the predicted lift matches reasonably well for the low AoA region but is much lower as the AoA increases.

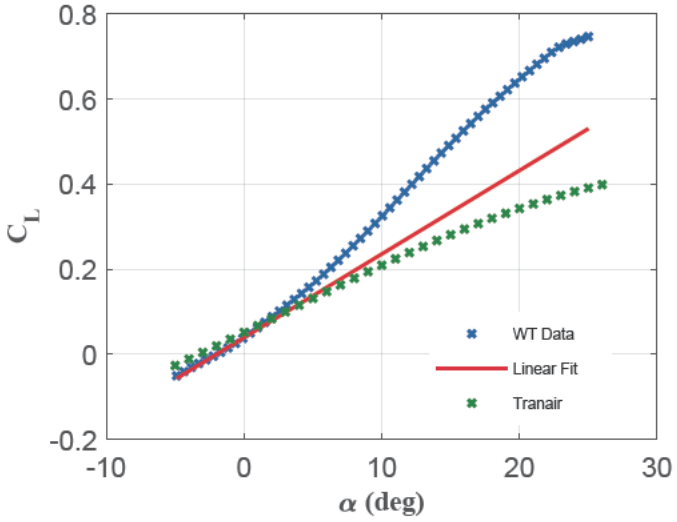

Figure 4.9: Lift coefficient from wind tunnel data and Tranair

The moment curve at CG_{test} and CG_{des} in Figure 4.10 with error bars included. A large uncertainty in the data point at -1.7 degrees AoA for CG_{des} is noted. Shifting the raw wind tunnel data to other CG locations requires both the measured moments and forces. This particular AoA has the smallest recorded force in the Z body axis. The uncertainty

of the force in the z direction at this zero lift AoA is therefore large from the Kline and McClintock method of calculation as the standard deviation of load cell measurements is fairly constant regardless of the measured force. This only impacts the data for the shifted CG location as the unshifted moment calculation does not depend on the other forces and moments. The uncertainty in the AoA is 0.2 degrees but has been omitted from the graph to prevent clutter. There are three main regions of the pitch moment curve for CG_{test}, the decreasing trend from -5 to 17 degrees indicating stability followed by a flatter portion up to the so called 'pitch-break' phenomenon at 22 degrees AoA. The stable range is reflective of the increasing vortex strength producing a strong suction force on the top surface of the wing which is larger towards the rear of the wing. This produces an increasingly negative moment as the AoA increases (stable pitch stiffness).

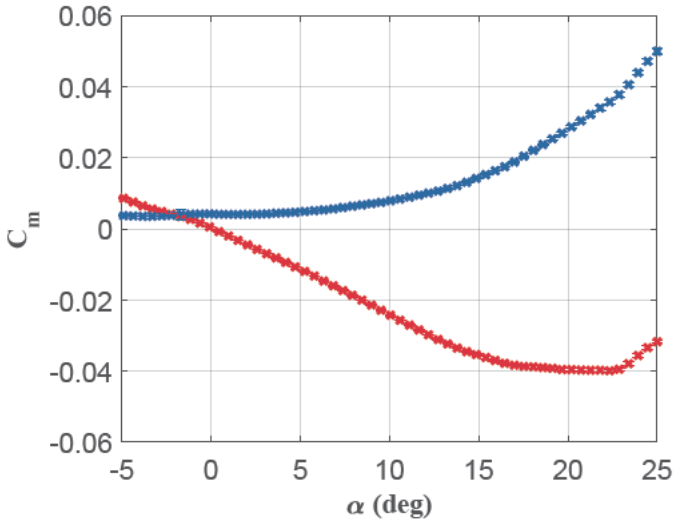

Figure 4.10: C_m at 20m/s, CG_{des}, CG_{test}

For a given AoA the vortex bursts at some point downstream from the wing [71]. As the AoA is increased the vortex strength increases and the burst point moves upstream. At large AoA the vortex begins to lift off the top surface, reducing the rear top surface suction. As the AoA increases to the point at which the burst crosses the trailing edge the high pressure behind the burst causes an increase in the pressure on the top rear wing surface, increasing the pitching moment.

The gradient of the pitching moment, C_{m_α} is the key indicator of pitch stability, negative values indicating static pitch stability, shown in Figure 4.11. The calculation of the gradient compounds the uncertainties in the pitch moment derivative and the AoA,

leading to large uncertainties. The smooth trend of the C_m data in Figure 4.10 suggests that the results are more accurate than the conservative uncertainties would suggest and the stable trend (negative C_m gradient) up to 17 degrees is clear.

The results indicate marginal stability up to 22 degrees, followed by instability beyond the point where the vortex breakdown crosses the trailing edge. The frequency of the short period mode for the vehicle is determined by the pitch stiffness scaled by the moment of inertia about the pitch axis and this is used in the next chapter to estimate the expected frequency of the short period mode for the purpose of manoeuvre design.

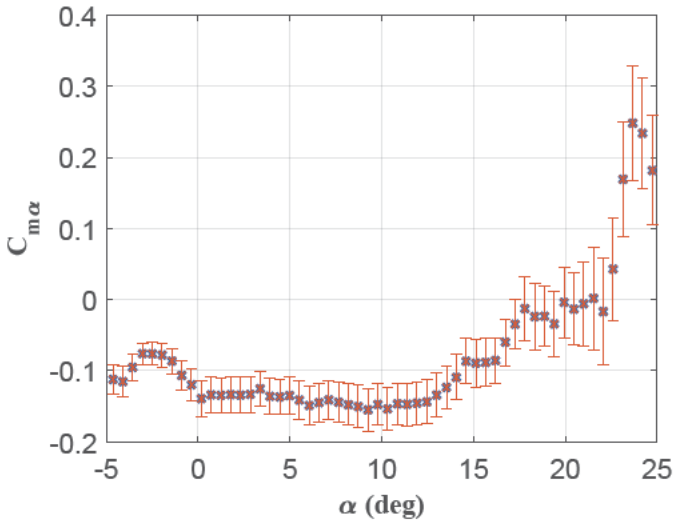

Figure 4.11: Pitch stiffness at 20m/s, CG_{test}

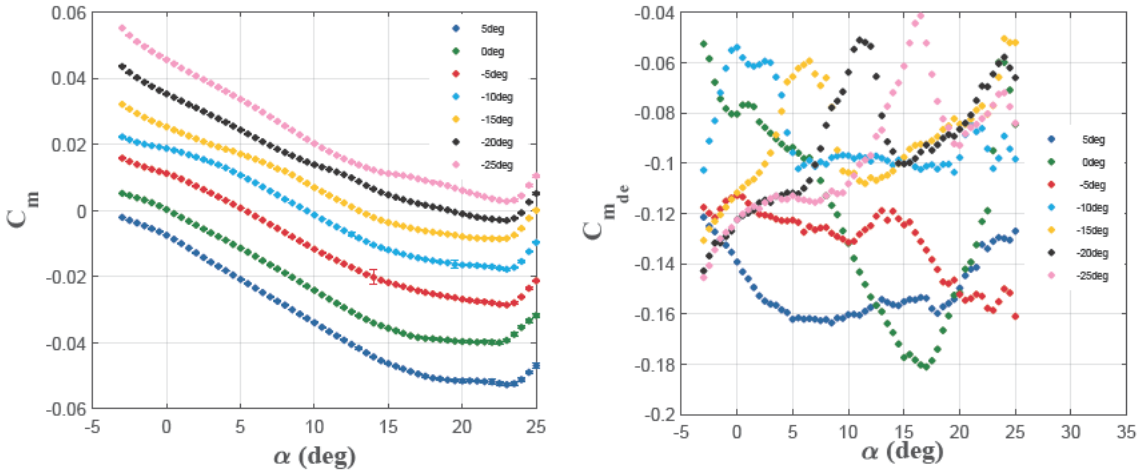

(a) Pitching moment at varying elevon deflections (b) Elevon control authority at varying elevon deflections

Figure 4.12: Pitching moment and elevon control authority at various δe

Figure 4.12(a) shows the pitching moment for a range of elevon deflection angles (δ_e) from -25 to 5 degrees. This range covers trim deflections over the range of stable flight with positive lift coefficients. The control moment authority of the elevon is shown in Figure 4.12(b). There is a large variation in this authority across the angle of attack range with sharp minimima and maxima exhibited, depending on both δ_e and AoA. This variation in the control authority $C_{m_{\delta e}}$ across the stable range has not been examined in detail here as that would require correlation with surface pressure data. The model was tested at δ_e deflections from -25 to 5 degrees in 5 degree increments and -27 to 3 degrees in 5 degree increments and the linear gradient calculated by taking the difference between the 2 degree shifted results and the nominal results. The error bars have not been shown in this case as the graph is already difficult to decipher but are in the range of 0.01 to 0.02. The main takeaway is the highly nonlinear behaviour with pitch authority varying significantly with elevon deflection and with angle of attack.

The vortex burst crosses the trailing edge of the wing at the AoA where the pitching moment gradient becomes positive. This point is shown to shift to slightly more positive AoA with decreasing elevon deflections. This could be due to the dependence of the vortex burst phenomenon on the streamwise pressure gradient as shown by Pagan [131] and Delery [144] although the effect is not large.

4.5.2 Lateral Results

The non-zero lateral coefficients at zero sideslip are indicative of asymmetries in the model itself and uncertainties in the sideslip setting. However, the key lateral results are the gradients with respect to sideslip which indicate stability about the lateral stability axes. AoA sweeps were run at 0, 1, 5, 6, 10 and 11 degrees AoS. Gradients are calculated by taking the difference of the 1 degree separated runs divided by the angle shift in radians. The gradient calculation results in large uncertainties using the Kline and McClintock method and have not been included in the beta coefficient figures for clarity.

The yaw moment derivative and gradient are presented for CG_{test} in Figure 4.13. The uncertainty in C_{n_β} is of the order $\pm 0.1 - 0.2$. A positive value of yaw stiffness (C_{n_β}) indicates stability as an increasing sideslip causes a positive yawing moment that realigns the nose of the aircraft with the flow. The primary source of stability is the vertical tail surfaces, which provide a strong restoring force behind the centre of gravity.

Another factor is the highly swept wings. The windward side of the vehicle effectively has a lower sweep angle than the leeward side. Lower sweep is associated with a stronger vortex and earlier breakdown as the angle of attack increases [71]. If the vortex burst were to happen at the same time on both sides then the effect on the lateral coefficients would be small. Figure 4.13(a) shows that a large shift in the yaw moment behaviour occurs between 15 and 20 degrees, which is likely due to asymmetric vortex bursting. Asymmetric vortex burst occurs due to the difference in the effective sweep angle between the two wings under non-zero AoS conditions. The effect of this asymmetry on the yawing moment is not consistent across the AoS range. At 5 deg AoS the shift in yaw moment happens at 21 degrees AoA and causes the yawing moment to increase. At 10 deg AoS the shift begins at 18 degrees and causes an initial increase in yawing moment followed by a sharp decrease beyond 20 degrees AoA. The asymmetric vortex bursting occurs at lower AoA for higher AoS as the effective difference between the sweep of the windward (right side for positive AoS) and leeward wings is higher and wing sweep is the main determining factor in the occurrence of vortex burst.

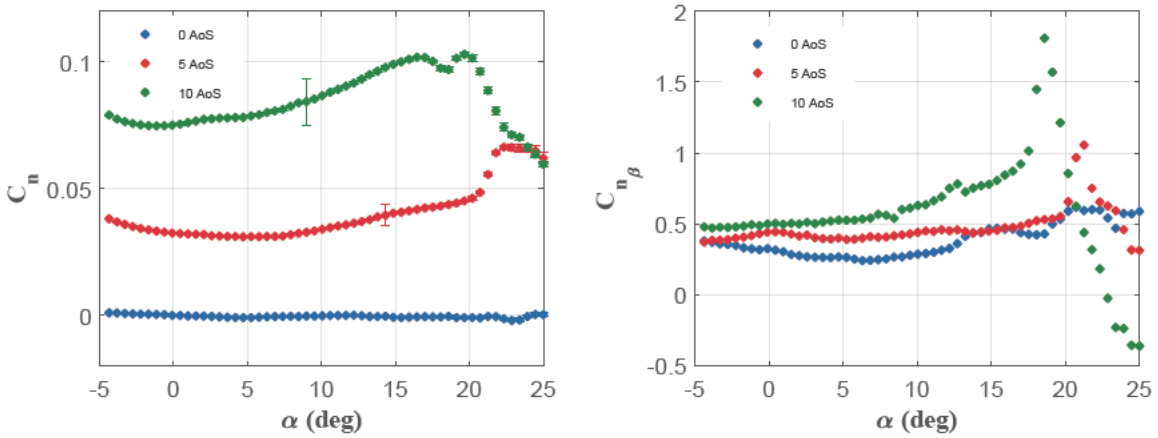

(a) C_n at CG_{test}

(b) C_{n_β} at varying elevon deflections

Figure 4.13: C_n and C_{n_β} at CG_{test}

The initial increase in yawing moment at both AoS indicates that the windward vortex has burst first, and the resulting increased pressure on the rear of the fuselage, behind the CoG, has increased the positive yawing moment. The subsequent decrease in yawing moment at 10 degrees AoS that starts at 19.5 degrees AoA, could be caused by the leeward vortex system also bursting. As AoA increases with high sideslip, the vertical tail surfaces become less effective as the wake of the burst vortex system impinges on

them. At 5 degrees AoS this effect is less pronounced and the bursting of the leeward side vortex causes the gradient of yawing moment to flatten out. Yaw coefficient is still at an elevated level as compared with the value before 20 degrees AoA, as the windward vortex will be bursting further upstream than the leeward vortex. Overall, the yaw stiffness (C_{n_β}) only becomes negative at AoA similar to where the pitching moment becomes unstable as seen in Figure 4.13(b). The yaw moment is only slightly lower in magnitude at CG_{des} with the same stability characteristics due to the reduced moment arm to the vertical tail.

The rolling moment coefficient, C_l, and roll stability coefficient, C_{l_β}, are shown in Figure 4.14. The uncertainty in C_{l_β} is of the order ± 0.1. Figure 4.14(a) shows an increasingly negative trend in C_l which corresponds to the negative values of C_{l_β} observed in Figure 4.14(b) observed from 0 up to 20 degrees AoA. Roll behaviour is defined as stable when an increase in sideslip causes a reduction in roll moment. A negative roll moment causes the direction of flight to change in a way that reduces the sideslip angle. Therefore, C_{l_β} should be negative for static roll stability. The key factors in roll response to sideslip are the wing design, dihedral and sweep angles, and the vertical tail surface. Upward dihedral angle on the wing tends to increase the magnitude of C_{l_β}, increasing stability, by effectively producing a higher angle of attack on the windward side under sideslip conditions. This leads to an increase in lift on that side and a decrease in lift on the leeward side which results in a negative roll moment. The Hexafly wing has negative dihedral which causes the opposite effect.

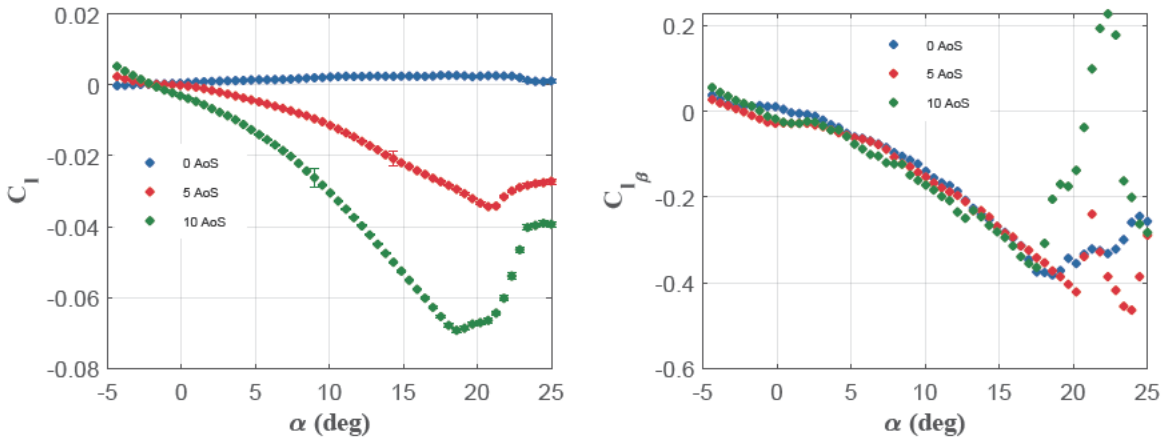

(a) C_l at CG_{test}

(b) C_{l_β} at varying elevon deflections

Figure 4.14: C_l and C_{l_β} at CG_{test}

Wing sweep causes a negative roll moment in response to positive sideslip as the windward side has an effectively lower sweep angle, and the leeward side has a higher sweep angle. The higher the sweep the lower the lift coefficient leading to higher lift on the windward side and lower on the leeward side. This produces a negative roll moment if the combination of wing dihedral and AoA results in a positive effective AoA for the windward wing. The negative dihedral of the Hexafly wing means that at low AoA, the wing sweep does not have a roll stabilising effect. The vertical tail surface placed on the upper side of the vehicle causes a negative moment during positive sideslip. At negative angles of attack the roll behaviour is unstable as the impact of the negative dihedral angle is larger than the stabilising effect of the vertical tails. As the AoA increases the sweep effect becomes stabilising and grows in magnitude which, along with the vertical tails, leads to stable behaviour for the rest of the tested AoA range.

Under sideslip the breakdown point of the vortex system on the windward side will cross the wing trailing edge first as the windward side has higher vortex strength and breaks down earlier [71] [144] [131]. At higher AoS this asymmetric breakdown occurs earlier indicated by a positive break from the trend of increasingly negative C_{l_β} with increasing AoA. At 17 degs AoA and 10 degs AoS Figure 4.14(b) shows a sharp break from the negative trend which does not occur until 21 degs AoA at 5 degs AoS. These match the locations of sharp changes in gradient in the C_{n_β} graphs. At 0 deg AoS, the vortex breakdown occurs symmetrically and the reduction in the C_{l_β} magnitude is likely due to the flow from the burst vortex impinging on the vertical tail surface, and blockage due to the rest of the model at high AoA, reducing the effectiveness of the vertical tails. At 5 and 10 degrees AoS the asymmetric vortex breakdown causes a rapid reduction in the magnitude of C_{l_β} until the leeward vortex breaks down as well. This is due to the high surface pressure after the breakdown point producing a reduction in lift on the windward side. After the vortex has broken down on the leeward side the value of C_{l_β} at 5 and 10 degrees AoS converge to the value at 0 degrees AoS with increasing AoA. This leeward vortex breakdown is observed at 22 degrees AoA for 5 degrees AoS and 23.5 degrees for 10 degrees AoA.

The sideforce coefficient (C_Y) and sideslip derivative (C_{Y_β}) are shown in Figure 4.15. The uncertainty in the C_Y measurement is very large at 22 degrees AoA as the measured sideforce is close to zero. The uncertainty of the C_{Y_β} is in the range of ± 0.1. The stability

requirements on sideforce response to sideslip is similar to the roll moment behaviour. A positive sideslip should produce a negative sideforce which accelerates the aircraft to the left side, reducing the sideslip. This leads to a requirement that C_{Y_β} be negative for static stability. The C_{Y_β} coefficient is negative and stable over most of the AoA range until breakdown occurs. Before breakdown, the sideforce is dominated by the vertical tail and the fuselage. As vortex breakdown crosses the trailing edge on the windward side, there is an initial increase in the sideforce coefficient due to the higher surface pressure on the windward side. As the breakdown occurs on the leeward side this asymmetric pressure is countered and C_{Y_β} reduces in magnitude again. The C_{Y_β} then reduces again beyond this range as the vertical tail surfaces becomes blocked by the rest of the vehicle and the flow from the burst vortex on the windward side reduce their effectiveness.

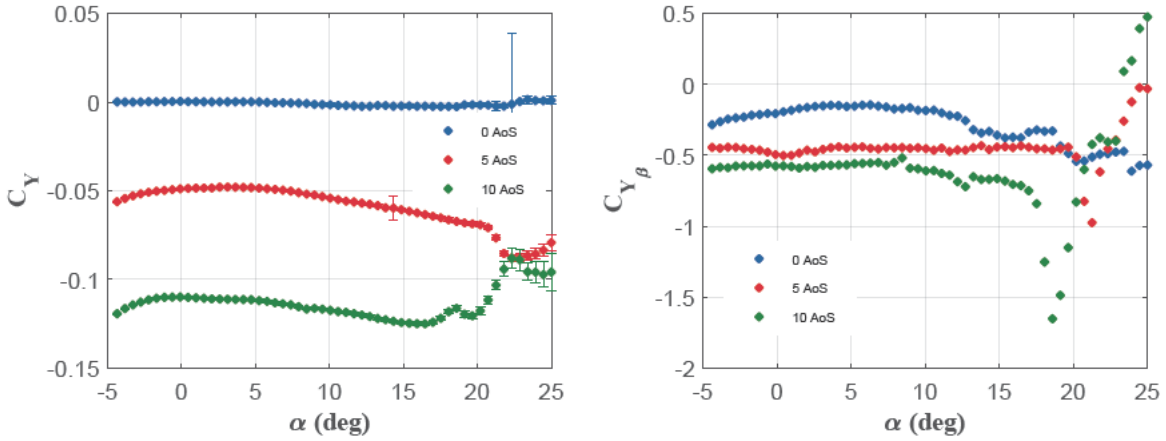

(a) C_Y at CG_{test}

(b) C_{Y_β} at varying elevon deflections

Figure 4.15: C_Y and C_{Y_β} at CG_{test}

4.6 Conclusions

In summary, the key longitudinal stability result is that the design centre of gravity is unstable across the entire AoA range (Figure 4.10). The results indicate that the centre of gravity must be shifted further forward for stable low speed flight to be achieved without active control systems. This reflects the forward position of the centre of pressure which is characteristic of waverider wing design which runs the length of the vehicle. Whereas studies of hypersonic shapes with more conventional wings set further to the rear of the vehicle tend to be stable in pitch [78] [75] experiments on similar waverider shapes have

shown pitch instability due to the forward location of centre of pressure at high angles of attack and low speeds [80] [73].

In addition, the highly nonlinear nature of the elevon control effectiveness will make the design of a flight controller that could stabilize the vehicle at the design CG challenging. The static results suggest that the vehicle is longitudinally stable at the forward shifted CG location, CG_{test}, until vortex breakdown crosses the trailing edge.

The vehicle is laterally stable except in roll at low AoA and at very high AoA. This is consistent with results observed by Penland and Creel on a similarly slender hypersonic vehicle [75]. The lateral behaviour is highly nonlinear at AoA above 17 degrees depending on the AoS due to the effect of asymmetric vortex bursting which matches the expected behaviour described in reference [71] for highly swept wings at high AoA. This also matches experimental results obtained by Keating and Mayne [73].

The static wind tunnel testing results showed good agreement across the repeat tests run at each condition, however the gradient methods used to calculate stability derivatives result in relatively large confidence intervals. Comparison with other sources of data such as the dynamic wind tunnel tests and CFD results will allow an assessment of the accuracy of these results. These will be compared at the end of Chapter 5.

Chapter 5

Dynamic Wind Tunnel Testing

The dynamic wind tunnel testing outlined in this chapter aims to experimentally characterise the low speed dynamic pitching derivatives of a dorsal engine type hypersonic waverider design turned glider. The dynamic stability of these models in low speed subsonic conditions is not well understood and has not been experimentally tested in any previous studies found. The technique used to dynamically test the wind tunnel model has also not been used for hypersonic designed aircraft in subsonic testing and it is hoped that the results from this testing can validate the results of dynamic CFD presented in Chapter 3. This would not only characterise the pitch damping behaviour of this class of vehicle in the low speed flight phase but also give confidence to the use of CFD methods outlined in Chapter 3 on slender hypersonic cruise vehicle designs in general.

Fixed attitude wind tunnel testing can be used to determine the static aerodynamic coefficients of a design, however some form of dynamic testing is required to experimentally obtain the dynamic aerodynamic derivatives. These dynamic derivatives are key to simulating how the aircraft will behave during manoeuvres and to assess the handling qualities of the aircraft-pilot system [145]. The ability to produce high fidelity flight simulation is the standard used by Anderson [135] and has been adopted here. The FAA guidelines outlined in reference [145] lay out tolerances for each variable during a particular type of motion. For the short period mode, the tolerances are ± 2 deg/s for pitch rate and ± 1.5 deg for pitch attitude. This standard will be used here to assess the accuracy of the pitch damping and pitch stiffness estimates obtained.

Obtaining data on the dynamic response either requires flight testing, which is a long pro-

cess and carries high risk, or dynamic wind tunnel testing, which is capable of obtaining a significant amount of dynamic data with less risk and expense involved. Dynamic wind tunnel testing is often used to bridge the gap in data between sub-scale and full flight testing. In this chapter, the methodology and results of dynamic wind tunnel testing of the Hexafly-Int vehicle are presented. The methodology includes the test apparatus used, the conditions of the test, the construction of the model, the data acquisition system, and the manoeuvre design of the test itself. The reasoning behind the type of dynamic testing that was selected, the methods used to process the data, and the test conditions used are also described.

5.1 Dynamic Wind Tunnel Testing Methods

Dynamic wind tunnel testing falls broadly under free-flight or forced oscillation tests. There are other types of tests such as free-fall and free-spin that test extreme flight conditions but these are not as applicable here. A good overview of the various types is given by Owens et al [146] but the trade-off between free-flight and forced oscillation is given here. The Hexafly test vehicle has no rudder surfaces and is designed to be stable without them for the short duration of the hypersonic glide test. To fly stably about the lateral axes at low speeds would require rudder control with significant authority. The high angles of attack, low inertia about the roll axis (I_{xx}), and non-zero off diagonal inertial components will lead to coupling between pitching motion and the lateral motion. This complex interaction has been avoided in the present work by limiting the analysis of the dynamics to purely pitching motion as an initial study into subsonic stability of this unconventional hypersonic waverider design. The static analysis has shown good static stability properties in the lateral axes though dynamic behaviour in a real vehicle will likely be a challenging control problem for the reasons mentioned. Therefore, the type of free-flight testing considered here is the free-to-pitch only type. The model has one degree of freedom about the pitch axis and the control problem is then limited to elevon control of the pitch attitude only.

A key part of designing the test and model is the scaling parameters which allow the sub-scale results to be applied to full-scale flight predictions. The main scaling parameter for static testing is the Reynolds number which is defined for density (ρ), freestream

velocity (V_∞), reference length (L_{ref}), and dynamic viscosity (μ) as $\rho V_\infty L_{ref}/\mu$ [138]. Dynamic testing must also consider the Strouhal number, also known as the reduced oscillation frequency ($\omega L_{ref}/V$), the reduced linear acceleration (aL_{ref}/V^2), the reduced angular acceleration ($\dot{\Omega}L_{ref}^2/V^2$), the Froude number ($V^2/L_{ref}g$), the relative density factor ($m/\rho L_{ref}^3$) and the relative mass moment of inertia ($I/\rho L_{ref}^5$) [146]. Where compressibility factors are considered Mach scaling is also required, however this is not the case here. It is clear that matching all of these scaling parameters simultaneously between the sub-scale model and the full size vehicle is not possible as they conflict with each other. The reduced linear acceleration does not apply here as for both free-to-pitch and forced oscillation, the model translation is fixed and it does not linearly accelerate. The Froude number is also considered less important as it is used to balance flow forces to gravitational force and in order to obtain the same trim angle of attack during test manoeuvres as at full flight. This is important for free flight tests but not as much for wind tunnel tests where the angle of attack can be varied without the requirement that lift be equal to weight. Dynamic tests of the F-16XL at high AoA have shown that the Strouhal number is important [146], as it enforces similitude of flow angles over the model surface during dynamic oscillatory manoeuvres [147]. The scaling factors that are focused on here are the Reynold's number and the Strouhal number as they impact the aerodynamics of the test vehicles to the greatest degree.

Forced oscillation testing, as used in references [132], [148], [149] and [150], requires a wind tunnel mount that is capable of oscillating the test vehicle about the expected centre of rotation. The model must rotate about this point as the dynamics of the system cannot be transferred to a different point after the test has been completed as can be done with static forces and moments. The key aerodynamic feature to capture is the specific rate of change of the flow angles at different points on the vehicle during the rotational motion. The key difficulty for this work was accessing or developing this type of mount for the University of Sydney 3x4 wind tunnel. The main advantages of this type of test is that the manoeuvre frequency and amplitude can be directly selected allowing for matching of the Strouhal number to the full scale more easily. This allows the effect of the frequency and amplitude to be assessed independently. The model itself is also less complex without need for internal components and sensors. The mount interfaces to the model via a force measuring load cell similar to the static testing conducted in

Chapter 4. Most importantly, unstable flight states can be tested independent of any control system in the loop, allowing for the pure aerodynamic forces to be assessed. Free flight and free-to-rotate tests cannot assess the aerodynamics of unstable configurations without the flight control system active and although it is possible to do parameter estimation of the aerodynamic model from closed loop testing, it is much more difficult.

The limitations of forced oscillation testing are that it relies on numerical predictions of important frequencies such as that of the short period mode and the dutch roll mode to select test frequencies that are representative of the vehicle motion. The shape of the oscillatory motion is also constrained to the oscillation mechanism, usually sinusoidal in nature, on the assumption that the motion of the actual aircraft can be linearised about some trim condition. This may not be the case with highly non-linear flows and some element of the feel of the vehicle and behaviour under free flight is lost.

The free-to-pitch method requires a far more complicated wind tunnel model with actuated control surfaces connected to a flight controller and on board sensors to measure the attitude and control surface states. The requirements are much closer to a full flight model although the availability of affordable high accuracy small scale components has made conducting this type of testing easier in recent years [151]. A gimbal system must be designed to attach the free-to-pitch model to the static mount in the wind tunnel. Internal sensors are required to measure the angle of the gimbal and the control surfaces simultaneously, and the data must be stored to allow post processing of the damping characteristics. The model must, as far as possible, be scaled and weighted to be balanced around the centre of gravity and to have an inertia as close as possible as that required by the dynamic scaling factors to give a similar oscillation characteristic to the full vehicle. Linear regression techniques used here cannot separate the dynamics of a control system from the vehicle aerodynamics effectively as the controller would always be actively suppressing motion during a manoeuvre. Therefore the tests must be done of the open-loop response and cannot be done if the model is unstable in pitch. This forces the centre of gravity of the Hexafly-Int vehicle to be moved forward from the design centre of gravity referred to as CG_{des} in Chapter 4.

Despite the aforementioned limitations, the main advantage of free-to-pitch includes testing using the same mounting system as used for the static testing without the need for complex oscillation systems. If the inertial characteristics are similar then the observed

response to a control surface input will also be similar to that of the full vehicle including the actual shape of the rotational response over time. The use of the free-to-pitch method also allows a qualitative assessment of the ease of control in both open loop (pilot inputs only) and closed loop (controller active) modes. A controller can also be tuned to assess the requirements for controlling the closed loop response with software. Control sequence inputs can be automated to give step, doublet and 3-2-1-1 type manoeuvres among others. These are all broadband inputs and with a reasonable estimate of the short period frequency based on static testing results, can ensure that the short period mode is excited.

A free-to-pitch model as shown in Figure 5.1 has been developed for this work. The model freely rotates about the gimbal shown in blue, which is attached to the wind tunnel mount. Attempts to balance the geometric constraints with the various scaling requirements are described below. The data obtained from this model will be used to calculate a pitch damping derivative.

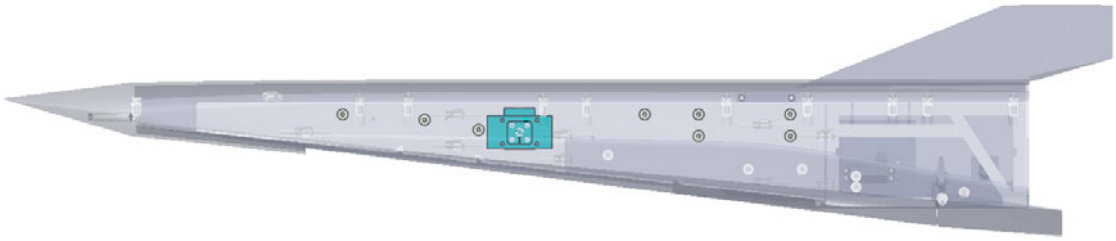

Figure 5.1: Free-to-pitch model (gimbal shown in blue)

5.2 Data Processing methods

The main outcome of dynamic wind tunnel testing is obtaining the dynamic stability derivatives of the model. The pitch damping derivatives, C_{m_q} and $C_{m_{\dot{\alpha}}}$ are the key result of the pitch only testing conducted here, as they cannot be ascertained from static tests.

The short period mode is characterised by oscillations in pitch rate (out-of-phase component) and angle of attack (in-phase component) [132]. The full motion involves both pitch rotation and plunge motion; However as the model is fixed in the z axis the degrees of freedom can be reduced to one. This means that the $C_{m_{\dot{\alpha}}}$ term cannot be separated

from the C_{m_q} term and the pitch damping term obtained here will be the sum of the two. As the model speed does not vary, the phugoid mode is not present in the wind tunnel motion. As covered by Carnduff et al [151] this is not considered a problem as the long term phugoid motion tends to be dominated by the much faster short period mode response and is therefore much less important in flight control design and handling qualities considerations.

The short period model is developed from the full 6 DoF linearised model by removing all the forces that are balanced by the wind tunnel mount. The following reduced model is used in Carnduff et al [151], Lehmküler [136] and Anderson [135] and is given in Eq. 5.1 and 5.2:

$$C_m = M\frac{I_{yy}}{\bar{q}Sc} = C_{m_\alpha}\alpha + C_{m_{\delta_e}}\delta_e + C'_{m_q}\frac{qc}{2V_\infty} + C_{m_0} \tag{5.1}$$

For pitch moment of inertia I_{yy}, dynamic pressure $\bar{q}$, reference area S, reference length $c = L_{ref}$, pitch rate q, and $C'_{m_q} = C_{m_q} + C_{m_{\dot{\alpha}}}$

In state space form, $\dot{x} = Ax + Bu$, this is presented as:

$$\begin{bmatrix} \dot{\alpha} \\ \dot{q} \end{bmatrix} = \begin{bmatrix} 0 & 1 \\ \frac{\bar{q}Sc}{I_{yy}}C_{m_\alpha} & \frac{\bar{q}Sc^2}{2VI_{yy}}C'_{m_q} \end{bmatrix} \begin{bmatrix} \alpha \\ q \end{bmatrix} + \begin{bmatrix} 0 \\ \frac{\bar{q}Sc}{I_{yy}}C_{m_{\delta_e}} \end{bmatrix} \delta_e \tag{5.2}$$

These equations represent a second order harmonic oscillator with an angular frequency and damping ratio given by Eq. 5.3:

$$\begin{aligned} \omega_{n,SP} &= \sqrt{-\frac{\bar{q}Sc}{I_{yy}}C_{m_\alpha}} \\ \zeta_{SP} &= -\frac{\frac{\bar{q}Sc^2}{2VI_{yy}}C'_{m_q}}{2\omega_n} \end{aligned} \tag{5.3}$$

As the model proposed for the short period mode motion is linear, the linear least squares regression technique has been utilised here to estimate the pitch damping and stiffness

coefficients, C_{m_α} and C'_{m_q}. SIDPAC functions developed by Klein and Morelli [152] were used in this process.

The linear least squares regression algorithm is one of the easiest parameter estimation methods to implement. If X is the measured states, Y is the measured rate data and $\hat{\theta}$ is the vector of model parameters then Eq. 5.4 relates the three parameters.

$$\hat{\theta} = (X^T X)^{-1} \times X^T \times Y \tag{5.4}$$

The model parameters are the elements of the A and B matrices defined in Eq. 5.2, which can be divided by their dimensional scaling factors to give the aerodynamic derivatives of interest, C_{m_α}, C'_{m_q} and $C_{m_{\delta_e}}$.

More complex data regression techniques such as Output Error Method and Filter Error Method could be used [153]. These are however, more suited to system identification of non-linear models, though they do allow noise and bias factors to be better accounted for than linear least squares regression. The results of the linear regression are analyzed later in this chapter and the need for more complex processing is assessed.

Wind tunnel correction factors based on the method used in Chapter 4 were also applied here. In this case, as no direct force measurements are made during dynamic testing, the correction factors calculated in Chapter 4 using the Shindo method [140] were correlated with the angle of attack and applied here to adjust the dynamic pressure.

The collected data was passed through the frequency domain filter, *fdfilt()*, a component of SIDPAC [152]. The expected frequencies of the short period mode based on the static testing results were lower than 1 Hz so a cutoff frequency of 4 Hz was applied to the filter. Several other types of time domain filtering outlined in reference [153] such as Spencer and Henderson were tested in combination with higher order Lanczos and Pavel differentiators, however, the best performance (judged by the closeness of the resulting curve to the collected data) was the five point smoothed differentiation scheme found in SIDPAC (*deriv()*) in combination with the *fdfilt()* function. The SIDPAC Least Squares formulation has also been used here for the parameter estimation step, which also outputs the Cramer-Rao bounds used to quantify the minimum achievable error

that can be obtained from the data set.

5.3 Model Design

This section details the design of the wind tunnel model. The details and justification of the model sizing are outlined and a comparison of the relevant scaling factors and geometric parameters between the wind tunnel model and full scale vehicle are given. The construction of the model is outlined and the methods used to balance the models mass about the chosen centre of gravity are described.

5.3.1 Centre of Gravity and Mass Distribution

The results from initial static testing on a small wooden model, detailed in Appendix B, showed that the vehicle is pitch unstable at the design Centre of Gravity (CG_{des}). Current regulations require civilian transport aircraft to be open-loop stable, or stable with the stick fixed (FAA regulation 25.181 [99]) in the event of a flight computer failure. The initial static test results were used to find the CG shift required to give stability up to 20 degrees AoA (CG_{test}) detailed in Chapter 4 in Table 4.1 and shown in Figure 4.4.

The mass of the model must be equally distributed about the centre of rotation along both the x and z axes. Any difference in the x or z direction between the actual centre of gravity of the vehicle and the centre of rotation of the gimbal will generate a restoring or destabilising moment that will affect the pitch dynamics. A large amount of the usable volume is distributed towards the rear of the model due to the nature of the waverider shaped body. As a result, all of the sensors and micro controllers used to run the data acquisition and flight controller are placed behind the chosen centre of rotation and the centre of gravity of the vehicle is naturally quite far to the rear. Balancing the weight along the x axis is achieved through the use of weights placed at the nose of the vehicle mounted to the main support struts. The required weight needed was estimated using a detailed CAD (Computer Aided Design) model of the existing parts outlined below using the Dassault Systèmes software, Solidworks. The weights were machined on a lathe out of 1010 mild steel as the required weight was around 1.3kg. The Centre of Rotation was placed at a position that would give pitch stability up to 20 degrees AoA, and would also allow for weight balancing along the z axis, which was much harder to achieve due

to the smaller z height of the model.

5.3.2 Model Sizing

The sizing of the model initially attempted to take into account the similitude constraints for dynamic testing outlined previously. As the Strouhal number is the key scaling parameter for dynamic testing the aim is to match the wind tunnel model with the full scale vehicle. The definition of the Strouhal number is given in Eq. 5.5.

$$St = \frac{\omega L_{ref}}{V_{ref}} \tag{5.5}$$

The aerodynamic pitch stiffness (C_{m_α}) is assumed to be the same between the two vehicle scales. Using a postulated landing speed of 80m/s as used in Chapter 4, and the formula for $\omega_{n,SP}$ from Eq. 5.3 the Strouhal number for the full scale vehicle divided by the square root of the pitch stiffness was found to be 0.20. The requirement to fit the various PCBs (Printed Circuit Boards), control servos and the pitch gimbal especially, described in Section 5.4, meant that the model length needed to be at least 0.95m. The desire to increase the Reynolds number also meant a longer model was favoured. The model construction method of using 3D printed parts attached to a laser cut frame placed limitations on the structural strength of the model. In addition, the data collection requirements of the regression technique mean that at higher speeds the increased damping and frequency and decreased settling time will reduce the information available to achieve parameter estimation. In the end a model length of 0.95m and test speeds of 15, 20 and 25m/s were used. This lead to a Strouhal number divided by the square root of pitch stiffness of 0.63, 3 times greater than the expected value for the full scale vehicle.

Using the estimate for ω_n from 5.3, the expression for the Strouhal number from Eq. 5.5 can be expressed in terms of aerodynamic coefficients shown in Eq. 5.6.

$$\frac{St}{\sqrt{C_{m_\alpha}}} = \frac{\sqrt{\frac{\bar{q}S_{ref}L_{ref}}{I_{yy}}}L_{ref}}{V_{ref}} \tag{5.6}$$

Or, removing the V_{ref} term in the numerator and denominator to obtain Eq. 5.7.

$$\frac{St}{\sqrt{C_{m_\alpha}}} = \sqrt{\frac{0.5\rho S_{ref} L_{ref}}{I_{yy}}} L_{ref} \tag{5.7}$$

Due to the influence of velocity on the oscillation frequency and on the flow angle, its effect on Strouhal number is nil. The Strouhal scaling therefore depends only on the characteristic length and ratio of the moments of inertia given that the atmospheric density is the same between the wind tunnel tests and the full scale model at landing conditions. The requirement simplifies to.

$$\frac{I_{yy_{WT}}}{I_{yy_{Full}}} = \left[\frac{L_{ref_{WT}}}{L_{ref_{Full}}}\right]^5 \tag{5.8}$$

The target model moment of inertia is therefore 2.86 kg.m^2, about ten times larger than the actual model inertia. Unfortunately due to the limitations already outlined, it was simply not possible to add the required weight (approx 10 kg) in the existing volume. The 3D printed parts alone are quite lightweight. The weights placed at the front to balance the model about CG_{test} are already on the limits of what the model forward fuselage can physically accommodate.

The final size, weight and moment of inertia about the pitch axis for the full vehicle and the wind tunnel model are shown in Table 5.1.

Table 5.1: Wind tunnel and Full Vehicle Size Comparison

Model	Full Scale	W/T Model
Scaling factor (n)	1	0.288
L_{ref} (m)	3.29	0.95
S_{ref} (m^2)	2.52	0.21
B_{ref} (m)	1.24	0.359
$Mass$ (kg)	420	3.71
I_{yy} (kg.m^2)	1417.9	0.281
V_{ref} (m/s)	80	20

From the static CFD results presented in Chapter 4, we expect the moment coefficient between the full scale and wind tunnel scale models to be similar. C_{m_α} also varies over the range of AoA so the Strouhal number is presented in terms of C_{m_α} for comparison.

Table 5.2 compares the wind tunnel model scaling factors against the full scale model factors.

Table 5.2: Wind tunnel model scaling factors

Model	Full Scale	W/T Model
Reynolds Number	2.26×10^7	1.3×10^6
Strouhal Number	$0.20\sqrt{C_{m_\alpha}}$	$0.63\sqrt{C_{m_\alpha}}$

5.3.3 Model Construction and Internal Components

The design of the vehicle is relatively complex and the integrated fuselage and wing shapes are difficult to construct out of simple extruded shapes as conventional aircraft can be. The highly integrated wings with upper surfaces curved in both surface axes means that the construction techniques were limited to multi-axis machining or additive techniques. The first static model was constructed out of layers of wood using a 3 axis CNC machine but this technique was limited due to the complexity of the wing body interface. The resulting model produced results which did not match well with CFD calculations. The cost of 5 axis CNC machining from solid aluminium meant that using multiple 3D printed parts was the most effective method available for producing the model. In the end, the outer shell, nose, vertical stabilisers, elevons and wings of the model were split into 21 different components to be printed individually due to the build volume constraint of the UpBox printers. These parts are shown within the CAD assembly in Figure 5.2 in exploded layout alongside all the other model components. The parts are designed to be fastened to each other using bolts and nuts as well as threaded inserts that can be glued into the components.

The 3D printing process produces significant surface roughness as well as a tendency for warping, especially in the larger components with significant material and large protrusions, such as the wing components. It was found that the wing tips tended to curve upward due to contraction of the ABS (Acrylonitrile Butadiene Styrene) material as it cooled. This resulted in parts that did not fit tightly together and required sanding and

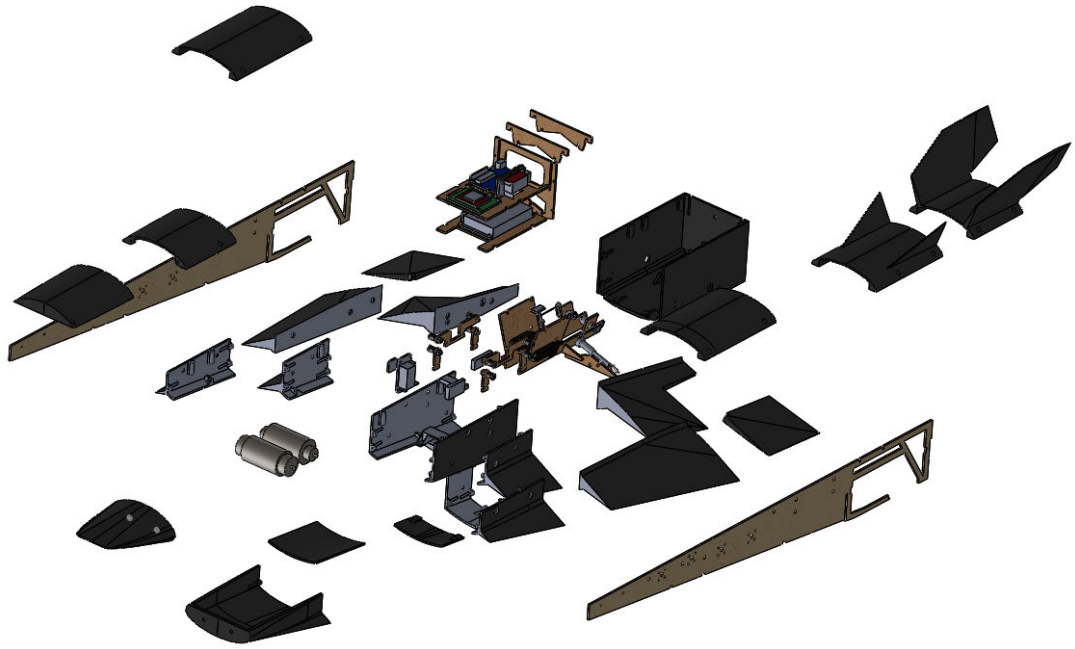

Figure 5.2: Exploded view of complete CAD model (fasteners hidden for clarity)

gap filling during assembly. The estimation method for the moment of inertia involves weighing each part individually before assembly and the requirement to gap fill added uncertainty to this estimate as detailed later, so lightweight filler is used to reduce the uncertainty.

As the model will undergo pitching motion and require fairly heavy internal components that are required to be precisely and securely placed, the internal components are mounted on laser cut struts that run along the length of either side of the internal bay. These are fastened securely to the outer shell and provide a strong load path for the aerodynamic and inertial forces to transfer to the gimbal and wind tunnel mount. The laser cut struts also allow the internal components to be positioned accurately and securely. Additional laser cut components are used to mount the PCBs and servo motors. The internal components, laser cut mounts and 3D printed components are laid out in Figure 5.3.

The aerodynamic and inertial loads must all be transferred through the single axis gimbal with as little friction as possible. The gimbal has been designed using layers of laser cut pieces glued together. The design is shown in Figure 5.4. A small adjustable 3D printed clasp is used to ensure the steel axle stays centred on the gimbal and model does not

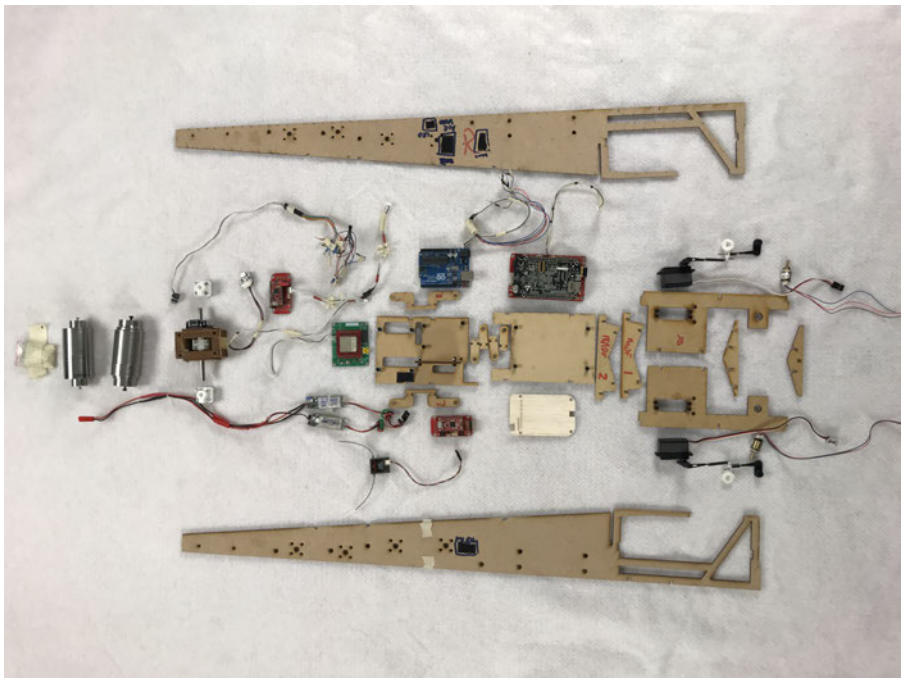

Figure 5.3: Wind tunnel model internal components

translate in the sideways (y-axis) direction. Roller bearings are used to limit rotational friction which would effect the model dynamics. The AMT-20V rotary encoder, used to obtain the pitch angle, is mounted on the side of the gimbal and press fit onto the steel axle.

Figure 5.4: Close view of assembled gimbal

The internal electronic components are a Beaglebone Black(BBB), a VN100 IMU (Inertial Measurement Unit), two SAMD21-mini breakout, and an Arduino Uno which are attached to laser cut wood mounting boards. There are also two servos, three rotary encoders, a radio receiver and two UBECs (Ultimate Battery Eliminator Circuit). The internal circuit boards, sensors, servos and gimbal are shown in the annotated image, Figure 5.5.

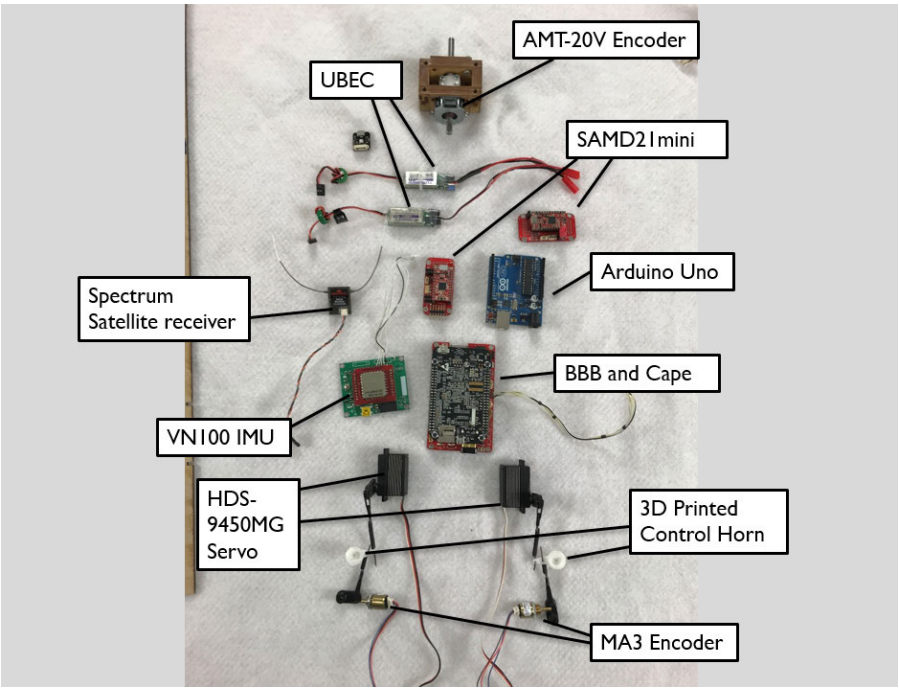

Figure 5.5: Internal electronic components annotated layout

The airspeed board, the radio receiver and status LED board are mounted directly on the main struts. One difficulty with the design of the Hexafly is the angle of the elevon surfaces. Their axis of rotation is angled downwards from the X-Y plane due to the anhedral angle of the wings and is also slightly swept back. This presents alignment challenges for designing a servo mount and control linkage to the elevon shaft assembly. After several iterations a system has been designed using a machined steel elevon shaft, standard push rods and angled mountings made from laser cut parts as shown in Figure 5.6.

The MA3 encoders used to measure control deflections are mounted behind the elevon shafts with additional control linkages providing the rotational connection to a 3D printed shaft control horn. It is important to limit the deadband (freeplay) between the control surface angle and the rotary encoder angles to ensure the fidelity of the control surface

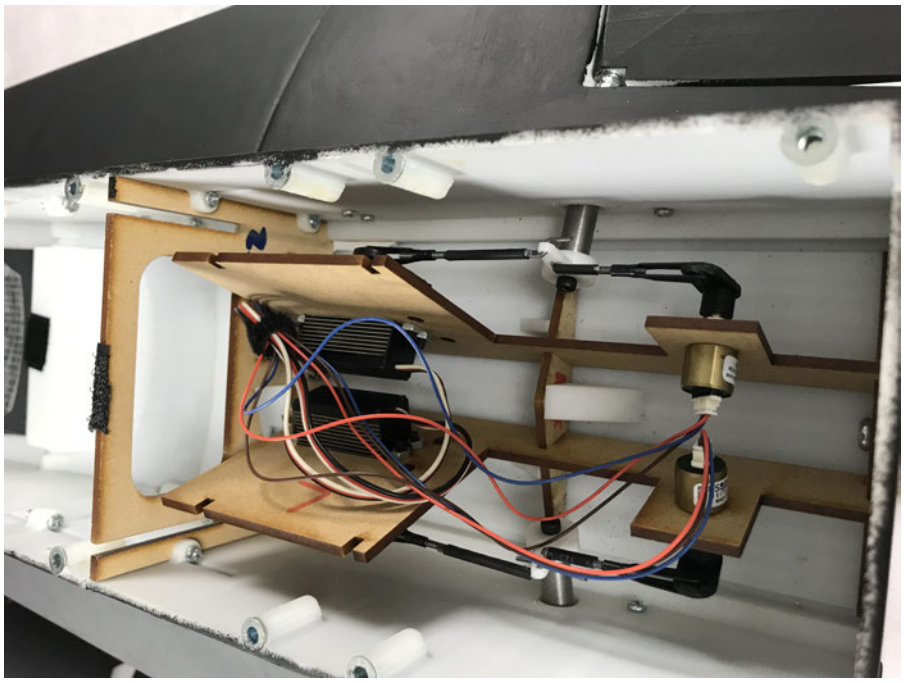

Figure 5.6: Elevon control actuation and position sensing assembly

deflections. This has been largely achieved with a tight fit for the elevon shaft within the 3D printed body part and the low rotational friction of the encoder itself.

Once all the parts had been constructed and weighed, it was found that approximately 1.3kg of counter weight would be required at the front of the vehicle to achieve the desired centre of gravity. This needed to be attached directly to the laser cut struts as the 3D printed parts were not sufficient to bear the load. The large weight requirement and limited volume at the front of the vehicle fuselage resulted in steel weights being machined down to the required mass. Two weights were made as shown in Figure 5.7.

Balancing the model and estimating the mass moment of inertia

The moment of inertia is estimated using the detailed CAD model. The CAD model includes every 3D printed part, the laser cut components, the electronic components and the weights added to balance the Centre of Gravity. The only components not modelled in the CAD assembly are the wiring (which is not insignificant) and the gimbal assembly as this does not contribute to the moment of inertia of the model. All the components are individually weighed and added from the actual model. The real model is then balanced about the test centre of gravity using lead ball bearings fastened to the front of the fuselage cavity (see Figure 5.7), on the rear surface of the nose, and adjustable

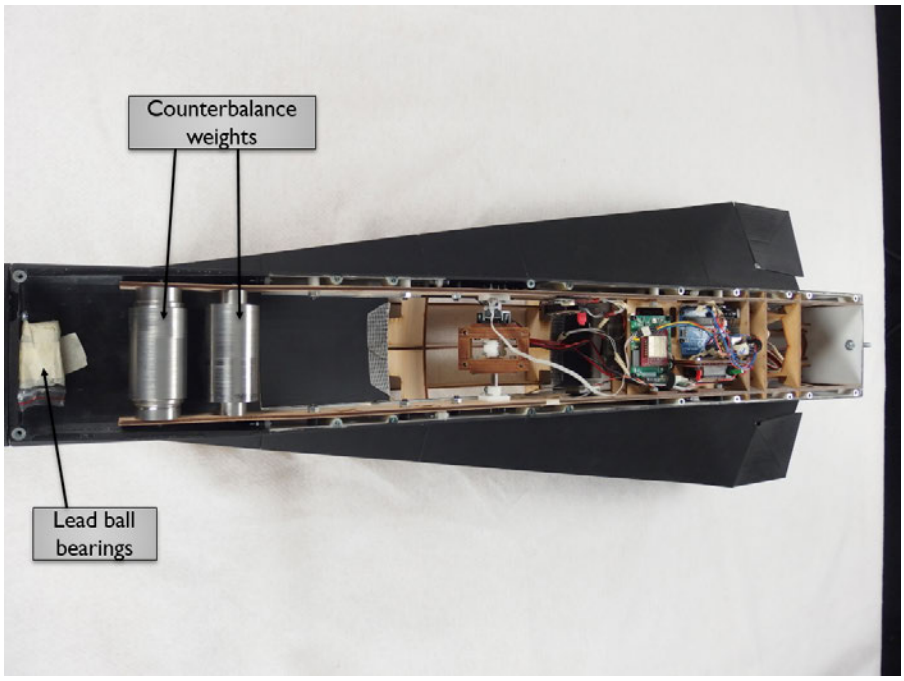

Figure 5.7: Model showing fully installed internal components

nuts at the rear of the vehicle for fine balancing in the x and z directions. Balance is assessed using a custom mount that allows the model to turn on the gimbal. The model is considered balanced when it exhibits no clear restoring moment toward a particular attitude as shown in Figure 5.8. This method assumes that there is little friction in the gimbal, which is the case due to the use of roller bearings.

The mass of the lead balls and the position of the nuts is added to the CAD model, and using the assumptions that the model is balanced and the only non-modelled components are the wires, a dummy component is added with the mass required to ensure the CAD model total mass matches the actual model's total mass. This mass is then moved within the CAD model to shift the CG in the CAD model to the known CG of the actual model. The total mass of the model was 3712g and the estimated mass from the CAD model was 3704g, which is a very small difference, giving us confidence in the CAD modelling of the components. The final CAD model with all components is shown in Figure 5.9 with the computed centre of gravity marked.

A number of assumptions are made at this step which, while necessary, do reduce the accuracy of the resulting moment of Inertia. The main source of error here is the assumptions that the model is perfectly balanced and that the unaccounted for mass can be accounted for with a small component in the correct location. As some of the un-

Figure 5.8: Wind tunnel model on balancing stand

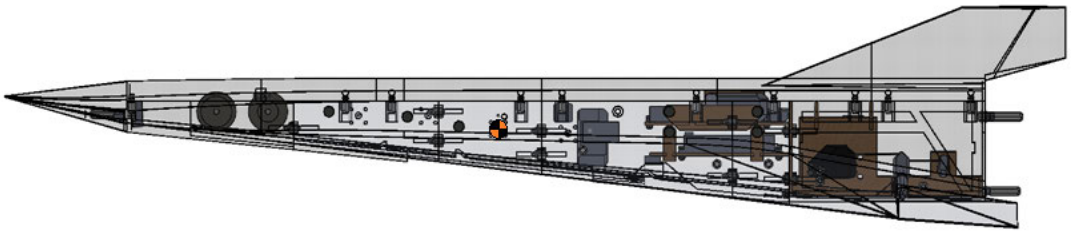

Figure 5.9: CAD assembly with computed centre of gravity

accounted for mass is gap filling material and the wires which are not a concentrated mass, this approach will slightly underestimate the model moment of inertia. The 3D printed parts could not obviously be measured individually after assembly and gap filling without destroying the model. It is estimated that the uncertainty introduced from this assumption is in the order of $\pm 0.001 \text{kg.m}^2$, or 0.3% after experimentation with differing wire masses and locations in the CAD model.

5.4 Data Acquisition System

UAVMainframe was developed by Lehmküler, described in detail in reference [136], and further developed by Anderson [135]. It is a sophisticated real time flight control and

data acquisition system. It is capable of providing an interface with ground control software to control flight tests whilst obtaining high quality synchronised data from many sensors, fusing the resulting data and providing highly accurate data for immediate real time use by the flight controller, and for post flight analysis and system identification routines. It consists of a BeagleBone Black (BBB) single board computer with a wifi adapter to provide a UDP (User Datagram Protocol) link to open source ground control software, QGroundcontrol. The BBB features several I2C and standard serial interfaces that connect to the various sensor boards. The full capability of the system allows for many such boards collecting data from multiple angle sensors, pitot sensors, Global Positioning System (GPS), Inertial Measurment Unit (IMU), Radio Frequency (RF) communications, power management and flight control. In the present work, a very limited subset of these functions is needed, with only 3 rotary encoders, airspeed, IMU, RF communications and flight control required for the 1 degree of freedom wind tunnel tests. A high level diagram of the data flow between components is shown in Figure 5.10.

The BBB board runs a Linux like operating system and handles all communications between UAVMainframe and peripheral sensor boards and to the users computer. The in-built wifi capability is used to connect the BBB Linux operating system to an SSH shell on the remote laptop to allow the user to transfer files onto the BBB and to start and stop the UAVMainframe executable. The files on the BBB include the compiled UAVMainframe executable as well as configuration and input files. The configuration files contain information specific to the model being tested such as the type, either fixed wing or rotary, as well as the mode of the data processing among other things. The input files contain control deflection sequences stored as pairs of control surface angle and time. These input files are used during system identification tests where UAVMainframe steps the control surface between the specified angles at the prescribed time steps. A custom cape has been developed by Lehmküler [136] and Anderson [135] to support various connectors to all of the boards. The cape also converts I2C voltages for use by the peripheral sensor boards.

UAVMainframe uses individual boards with hardware interrupt capabilities to directly interface with sensors. In this application an Arduino Uno board, referred to as the sensor board, interfaces with the 3 rotary encoders used for attitude and control surface

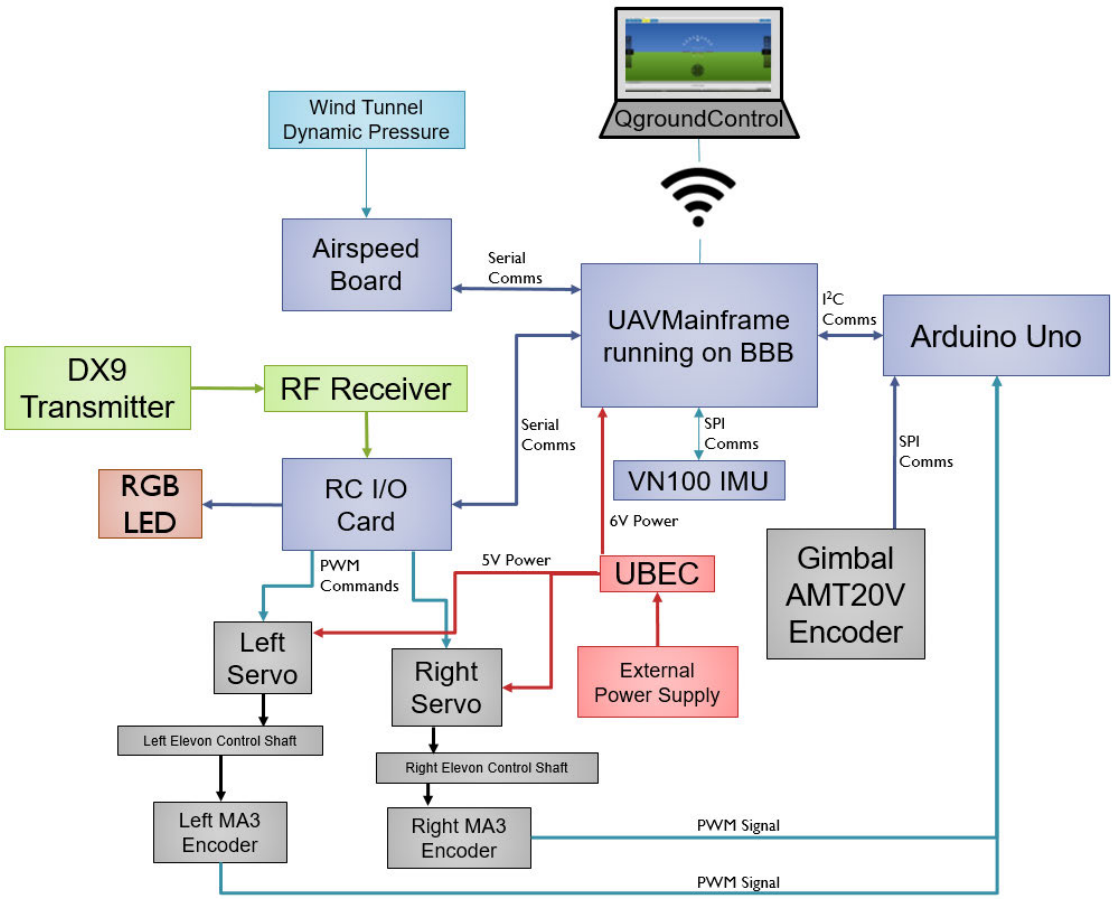

Figure 5.10: UAVMainframe high-level control and data flow

angle sensing. The sensor board has 3 hardware interrupts which collect from the rotary encoders as soon as it is available. UAVMainframe sends a sync signal to every peripheral board to collect data from the sensors. UAVMainframe then requests this data from the remote sensor boards, so although there is a delay in UAVMainframe collecting the data from each board, every reading is taken at the same time. This is very important for the system identification application as any time delays require more complex processing techniques [153].

RF communications are passed via a Spektrum satellite receiver, which communicates with a SAMD21-mini board (referred to as RC I/O board) and breakout board developed by Anderson [135]. The RC I/O board also controls the two servos used to drive the elevons using its native Pulse Width Modulation (PWM) output capability. This board communicates to the BBB using SPI protocol in addition to separate digital sync and reset lines controlled from the BBB. A second SAMD21 board (Airspeed board) is used to interface with the wind tunnel pressure readings to obtain dynamic pressure readings

synchronized with the other sensor data.

The two rotary position sensors used are the AMT-20V and the MA3-P12-125-B. The AMT-20V is accurate to 0.2 degree resolution [154] while the MA3 sensor resolution is 0.1 degrees [155]. The AMT-20V is specifically designed for measuring rotational position of the shaft and is ideally suited to sensing the gimbal rotation position. 3D printed horns were created for the MA3 to connect to the elevon control shaft. There is no measurable play between the elevon control shaft and the elevon surface, so by custom designing the elevon and MA3 3D printed horns, the measured control surface deflection matches the actual control surface deflection. The AMT-20V sends data to the sensor board using SPI (Serial Peripheral Interface) communications. The MA3 encoders output PWM signls which are read by the sensor board using the native hardware interupts to catch the PWM frames.

The control surfaces are actuated by two HDS-9450MG servos from Scanner RC which are capable of producing 4.1kg-cm of torque which is more than sufficient for Elevon control. These servo motors receive PWM commands from the RC I/O board. There is play between the servo motors, and the elevon control shafts, however this does not have an impact on the system identification process. Deadband between the elevon surfaces and servo motors does cause issues returning the control surface to the trim location during test manoeuvres.

Two UBECS provide power to the BBB and the servo motors at 6V and 5V respectively from a power supply located outside of the model. A power line runs along the wind tunnel mount and into the model to power these UBECs. This power line is attached to the mount in such a way that the lower portion which enters the model is slack, to prevent any impact on the model motion.

Custom QGroundcontrol software widgets allow for tuning of the PID flight controller gains and setting of maximum rotation rates during testing by passing these parameters over a standard MAVlink communication protocol. System identification sequences are also controlled via the custom Qgroundcontrol interface with another widget. This interface allows the pre-loaded input sequences on the BBB to be modified using amplitude and frequency controls. This greatly speeds up the process of testing as tuning the amplitudes and frequency of the inputs can be done without needing to stop the test

and transfer new input files onto the BBB. The system can run in either an armed or disarmed mode. When disarmed the vehicle is entirely controlled via a remote transmitter, the Spektrum DX9 SPMR9900 was used during these tests. When armed the flight controller maintains a trim angle of attack specified by a combination of the transmitter pitch command and the QGroundcontrol pitch trim parameter. During system identification tests, the input sequence, and frequency and amplitude adjustments are selected and sent to UAVMainframe. During the period of the control input and a short settling time afterwards, the control surface deflection is the sum of the deflection that was used to trim the vehicle and the input sequence deflection. The flight controller is not actively controlling the vehicle during this period to maximise the vehicle response signal in the measured data.

5.5 Manoeuvre Design and Test Conditions

The aim of designing a flight test manoeuvre is to maximise the magnitude of aerodynamic response in the measured data. As the model is constrained in the wind tunnel, the risks are limited to the model nose or elevons striking the wind tunnel walls. This was alleviated by using guide lines attached to the wind tunnel to limit the angle excursions of the model. This allowed experimentation of different sized control inputs to determine how large the response would be at varying speeds.

The shaping of the control surface inputs is based on the methodology outlined by Jategaonkar [153]. The only mode we expect to be active during this testing is the short period mode. Jategaonkar shows that the optimal input to stimulate this mode will contain frequencies above and below the expected short period mode natural frequency. This frequency can be estimated from Eq. 5.3 using the C_{m_α} results from static wind tunnel testing and static CFD. This is given in Table 5.3 for AoA from -5 to 20 degrees.

A second criterion is to maintain the trim AoA. The linearised model that is applied here (Eq. 5.2) assumes that the motion of the model remains near a trim angle of attack. This criteria corresponds to minimising the energy input at zero frequency. Energy at zero frequency will result in a deviation of the flight state from the trim angle of attack.

The three common multi-step inputs are the step(impulse), doublet and 3-2-1-1. Another common sequence is the modified 3-2-1-1 which adjusts the amplitudes of each step to

Table 5.3: C_{m_α} and ΔT_{3211} for each airspeed

	Static WT Testing				Static CFD			
AoA (deg)	C_{m_α}	ΔT_{3211} 15m/s	ΔT_{3211} 20m/s	ΔT_{3211} 25m/s	C_{m_α}	ΔT_{3211} 15m/s	ΔT_{3211} 20m/s	ΔT_{3211} 25m/s
-5	-0.112	0.48	0.36	0.29	-0.092	0.53	0.40	0.32
0	-0.139	0.43	0.32	0.26	-0.142	0.43	0.32	0.26
5	-0.135	0.44	0.33	0.26	-0.143	0.43	0.32	0.26
10	-0.147	0.42	0.32	0.25	-0.106	0.50	0.37	0.30
15	-0.089	0.54	0.41	0.33	-0.084	0.56	0.42	0.34
20	-0.004	2.66	2.00	1.60	-0.025	1.02	0.76	0.61

reduce the energy input at zero frequency. These inputs are shown in Figure 5.11.

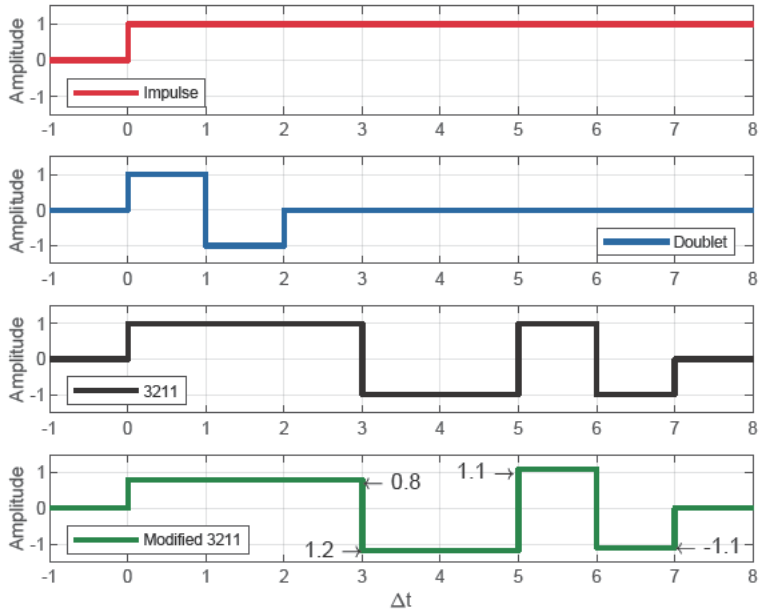

Figure 5.11: Multi-step inputs

The method for estimating the frequency distribution of the energy in a multi-step input is found in reference [153] and reproduced in Figure 5.12. It is clear from this that the Modified 3-2-1-1 input provides the best spread of input frequency content and lowest excitation energy at zero frequency. Therefore the modified 3-2-1-1 sequence has been used in this work. Figure 5.12 shows the frequency content normalised by the time step length of the input. The choice of this time step length is determined by the estimated natural frequency of the short period mode. The main frequencies excited by this input lie in a band from 0.31 to $2.7\omega\Delta t$ with the main peak at approximately 1.6 $\omega\Delta t$. The required step length for the modified 3-2-1-1 input is therefore given by Eq. 5.9.

$$\Delta T_{3211} = \frac{1.6}{\omega_{nSP}} \tag{5.9}$$

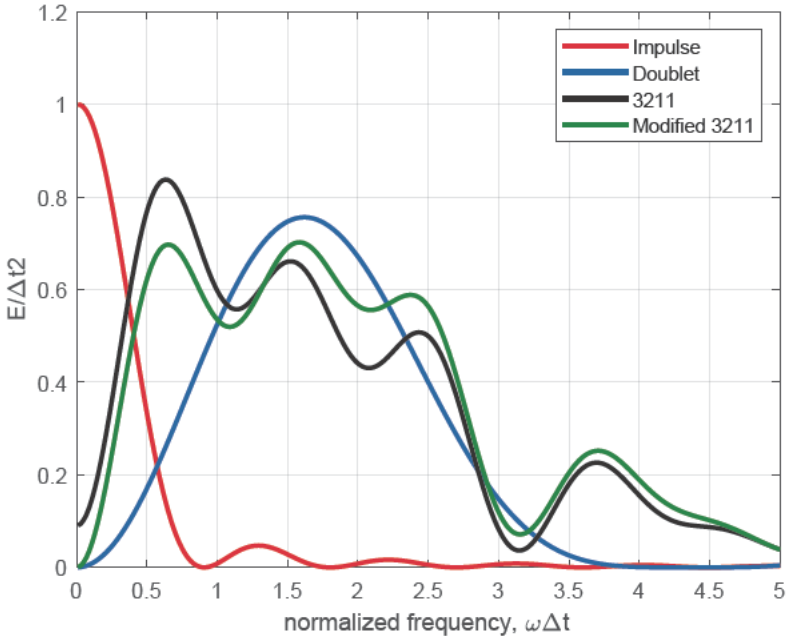

Figure 5.12: Frequency domain representation of multi-step inputs [153]

The first estimate of the model moment of inertia was 57% bigger due to an error in the CAD software used. The estimated natural frequency varies inversely with the moment of inertia. The resulting time step estimate therefore increases with increasing moment of inertia. Therefore the input sequences that were tested used time steps of 0.5, 0.65 and 1 second to cover the range of AoA and airspeeds. During testing it was found that the time step of 0.5s performed best. However, the wide band of energy input of the 3211 still ensured that the short period mode was adequately excited.

As the angle of attack increases towards the unstable pitch break at around 20 degrees, the pitch stiffness reduces in magnitude, lowering the estimated natural frequency of the short period mode. The required time step to excite the short period mode becomes quite long at this flight condition (Table 5.3), and was found during testing to be impractical to implement. The length of time of each control deflection becomes too large to keep the model near the trim AoA, or, if the amplitude is reduced to remain at the trim AoA, then the response is too small to measure with the resolution of the AMT-20V

rotary encoder. The main issue during testing at 20 degrees AoA was found to be the proximity to the edge of the stable flight envelope. Any input large enough to produce good data for system identification pushed the model into the unstable range during the test, causing the model to push into the protective guide wires. The trim angles for which data is obtained during the dynamic testing is -5, 0, 5, 10, 15 and 18 degrees.

The model was tested at 15, 20 and 25 m/s at all trim AoA. The aim of the testing is to produce aerodynamic responses from the model that are large enough to be clear in the recorded data, without deviating by too much from the trim AoA (to maintain linearity). In this case the definition of 'too much' is vague and the criteria was largely based on whether the model returned to the trim angle and whether the data was not limited by the resolution of the sensor. As mentioned previously, the Strouhal number scaling is invariant with airspeed but Reynolds scaling could be improved with higher airspeeds. From Eq. 5.3 we can see that the damping ratio is proportional to the freestream velocity. During a test run, the oscillations of the model after a control surface deflection contain the most information on the damping of the system. If the airspeed, and therefore the damping, is increased then this motion post control deflections subsides rapidly, and the resolution limit of the sensors reduces the useful information available from small oscillations to the system identification process.

As the model moment of inertia had been initially estimated as bigger there were very large discrepancies between the dynamic CFD results and the wind tunnel results when the data was first processed. As a result, a number of retests were conducted experimenting with different input sequence amplitudes and step lengths. During these retests it was found that each AoA had slightly differing results, depending on the amplitude used, as well the time step length, which was to be expected from the differing pitch stiffness at each AoA. The different trim AoA are therefore treated independently and the manoeuvre amplitude and time step length for each AoA are chosen on the basis of the various error measurements and validity tests described in the next section. The combination of airspeed, amplitude and time step length which perform best at each AoA are chosen to provide the final estimate of the pitch damping.

In the end, with the accurate moment of inertia estimate, even the data that was collected during initial tests was found to yield good results. This validates the robustness of the modified 3-2-1-1 as it gave good results without a precisely accurate time step

length. Given that the time step length estimate is dependent on estimates of aerodynamic parameters, the broad energy input of the modified 3-2-1-1 manoeuvre relaxes the accuracy requirements of pitch stiffness estimates before testing is conducted.

5.6 Experimental Procedure

The results presented here are evaluated against a number of different criteria. In isolation, the quality of the estimated aerodynamic coefficients are measured against the dynamic testing data using the previously mentioned FAA standard for flight simulation, ± 2 deg/s pitch rate and ± 1.5 deg for pitch attitude. Ten repetitions of each flight condition and input amplitude were carried out so the error of the data itself is measured by the spread of the resulting aerodynamic coefficient estimates, as well as the Cramer-Rao bounds, which describe the minimum error achievable from each dataset, or in effect, the maximum available information from the data [153]. Finally, the average estimated aerodynamic coefficients are used to simulate the model response for the recorded elevon deflections over the ten data sets at each flight condition, and the maximum deviations for pitch rate and attitude are found to check against the FAA simulation limits.

The resulting data is then evaluated against the estimates for C_{m_α} and $C_{m_{\delta_e}}$ from the static testing using the trim AoA and elevon deflections (interpolating the static testing results where necessary). This data is then used as a validation for the static and dynamic CFD estimates for C_{m_α} and C'_{m_q} described in Chapter 3. In this regard, the effect of the wind tunnel walls and support cannot be independently accounted for, so some difference between the wind tunnel testing and CFD results is to be expected, even in the ideal case where both methods are perfectly accurate. The following sections outline the procedures for calibrating the data and initial testing conducted to assess the input manoeuvres and test conditions.

5.6.1 Calibration

The calibrations outlined in Chapter 4 were again used in the dynamic testing process. The Angle Cube was used to calibrate the IMU and gimbal sensor by fixing the model at the desired angle of attack step and recording the IMU and gimbal sensor data. The control surfaces were calibrated using laser cut custom compass tools to directly measure

the control surface deflection and compare against the recorded data from the control surface sensors. This tool is shown in Figure 5.13.

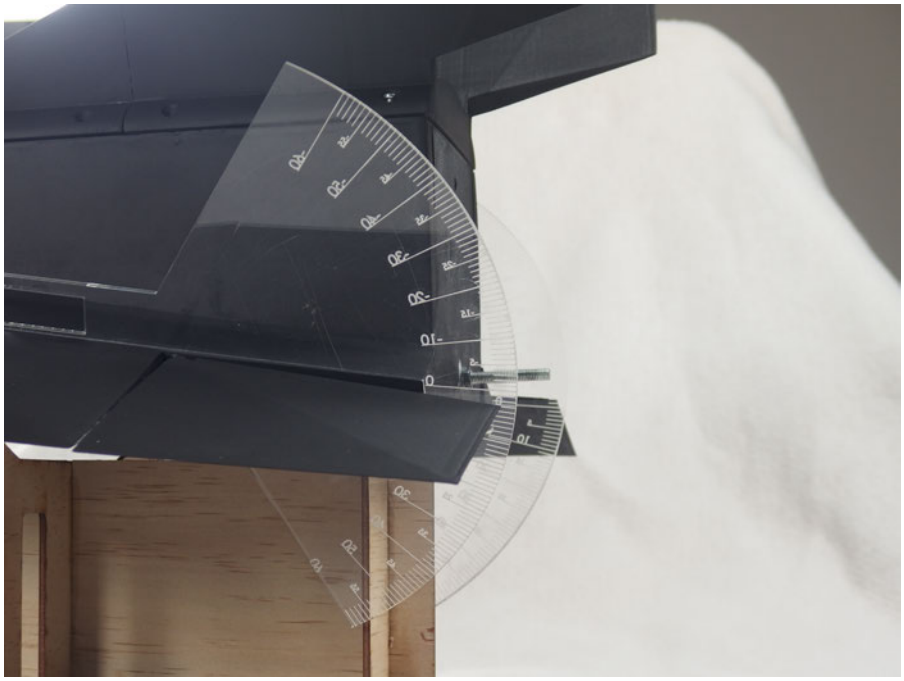

Figure 5.13: Elevon angle calibration tool

The airspeed sensor card was connected to the same wind tunnel pressure ports as during the static testing, and used the same calibration scheme as verified by Anderson [135]. During processing of the test results, it was found that the filtered derivatives of the gimbal pitch angle did not perform as well as the output pitch rate and pitch rotational acceleration from the IMU. This is due to the numerical differentiation scheme used on the gimbal pitch sensor data which introduced significant noise. Although filtering was applied the output rates from the IMU were found to be a better match to the measured pitch data. The least squares regression produced lower Cramer-Rao bounds when using the IMU rate and acceleration data. The gimbal sensor however, performed better for the pitch angle measurement. The regression process was therefore carried out using the gimbal sensor data for the pitch angle, and the IMU sensor data for the pitch rate and acceleration.

5.6.2 Initial Testing

The wind tunnel testing was conducted over a number of different days. The initial tests had used a guide string attached to the model itself to limit the maximum and minimum

AoA to prevent damage to the model when experimenting with control surface deflection amplitudes. When the initial results were found to differ by a large margin from the expected results, the influence of this string was identified as a possible source of error, resulting in the change to a set of ropes arranged around the model to prevent large AoA excursions, without being in physical contact with the model during testing.

As mentioned previously, each airspeed, input sequence amplitude and time step length were tested at each trim AoA resulting in a test matrix of 72 combinations to test. Where it was clear that the combination of input amplitude, airspeed and time step length were not appropriate for that trim condition (for example, large amplitude at high airspeed), that test was not repeated, resulting in a much lower number of tests run. In the end, 250 individual tests were run, at 25 of the test condition combinations. The two best performing input sequences of 1.5 and 2.5 degrees amplitude are shown in Figure 5.14. The measured data represents the actual control surface deflection, and the command data is the angle requested from the motor servos. The difference between the two shows the play between the servos and the elevons. This highlights the advantage of directly measuring the control surface deflection rather than the command. Experiments showed good results from these two amplitude settings, with too small a response with lower amplitudes and too large a deviation at higher amplitudes. As can be seen, the actual surface deflections do not match the ideal modified 3-2-1-1 sequence that is commanded, however the inputs still succeed in stimulating the short period mode, with only minimal departure from the trim pitch angle. The frequency distribution of the measured elevon input energy is shown in Figure 5.15. The experimental manoeuvre has less energy input at the higher frequencies than the ideal modified 3-2-1-1 but retains the low energy input at zero frequency that helps maintain trim conditions.

Typical test runs begin by assessing the manoeuvres to determine suitability of amplitude and time step length for a given airspeed. For an AoA of -5 degrees, and an airspeed of 15m/s Figure 5.16 shows the sequence of amplitudes tested, and Figure 5.17 shows the different time step lengths. The suitability of the input was assessed on the basis of the final deviation from the trim attitude (to ensure linearity) and the Cramer-Rao bounds of the identified parameters, expressed as a minimum possible variance in estimated C_{m_α}, C'_{m_q} and to a lesser extent, $C_{m_{\delta_e}}$. For this flight condition it was found that the 2.5 degree amplitude input with a 0.65s time step achieved the best results and returned

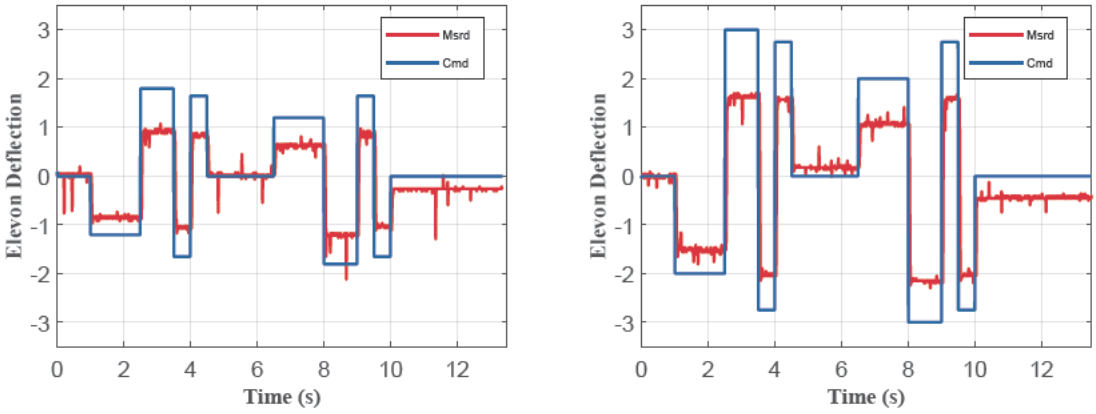

(a) 1.5 degree sequence

(b) 2.5 degree sequence

Figure 5.14: Two input sizes used

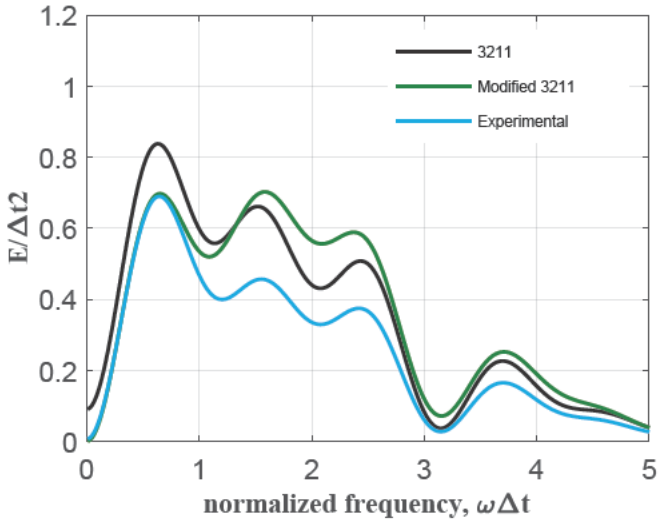

Figure 5.15: Frequency domain representation of experimental multi-step inputs [153]

to the trim pitch. This process was repeated for each AoA and airspeed to determine appropriate input sequences at each flight condition, and it was found that the 0.65s time step was more suited to the 15m/s input, whereas the 0.5s sequence was more effective at 20 and 25 m/s.

The repeatability of tests is also considered an important criteria, as it ensures that good quality data can be obtained through multiple samples at each condition. Figure 5.18 shows five of the ten tests conducted at 0 AoA, 20m/s with 2.5 degree amplitude input. The results show that the response in each case is very similar and gives a high degree of confidence in the repeatability of testing, and the ability to get good results

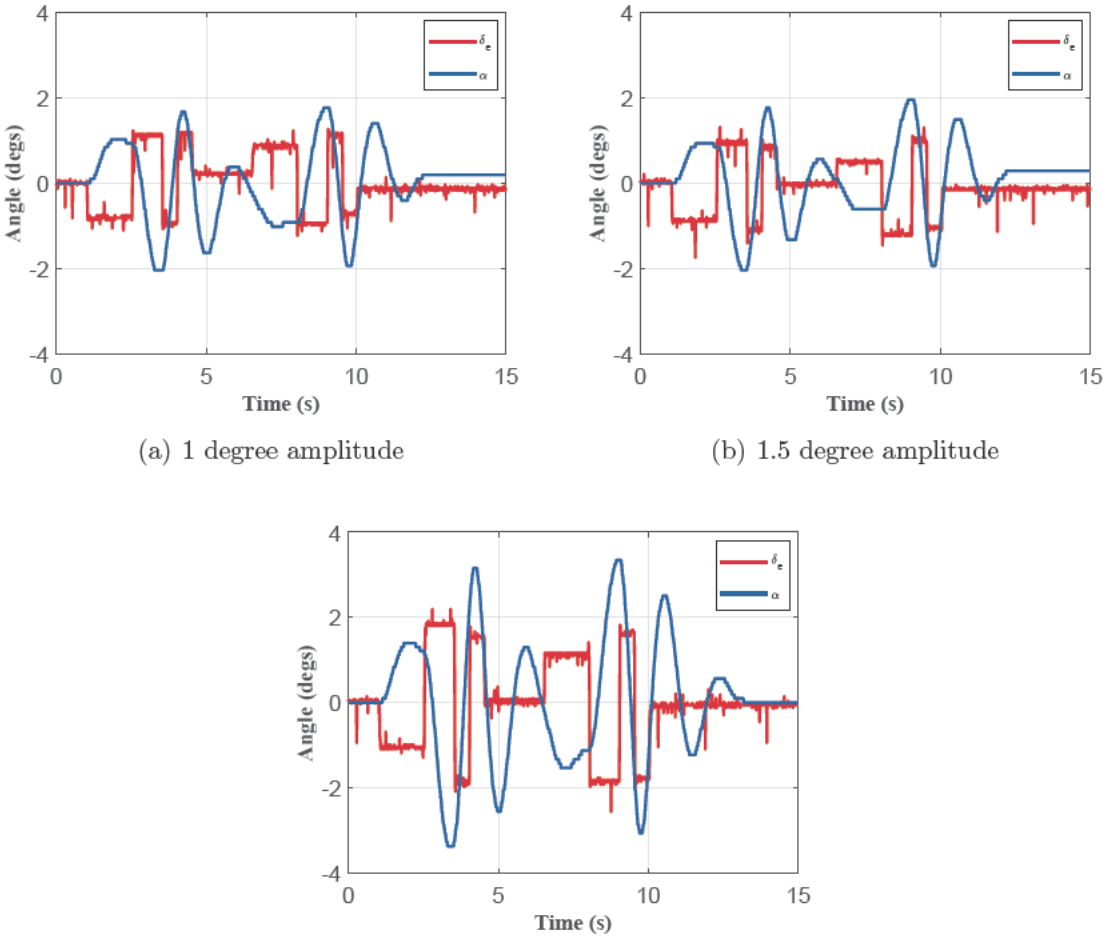

(a) 1 degree amplitude

(b) 1.5 degree amplitude

(c) 2.5 degree amplitude

Figure 5.16: Initial Amplitude Tests at 15m/s, 0.5s time step

from multiple tests at each flight condition.

5.7 Results

The results are presented in Figure 5.19 for each AoA. Testing was not conducted at 25m/s for all AoA but where that data was obtained, it has been included. The estimated parameters are presented for each run to show the spread of the results. The error bars are the square roots of the corresponding Cramer-Rao bound and represent the best possible variance obtainable from the data.

Whereas the results for 15 and 20 m/s were generally close to each other, there was some deviation for the data obtained at 25m/s at 5 degrees AoA. Although there is no consistent trend in velocity dependence across all flight conditions, it is clear that there

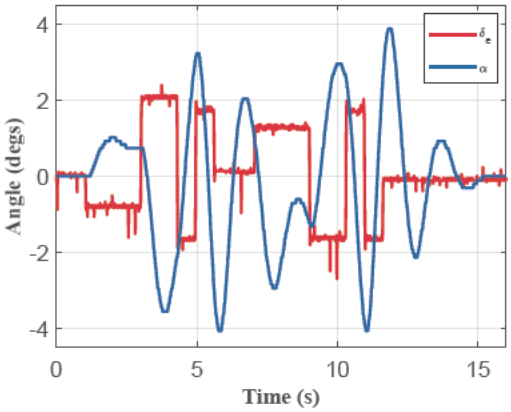

(a) 0.65s Timestep

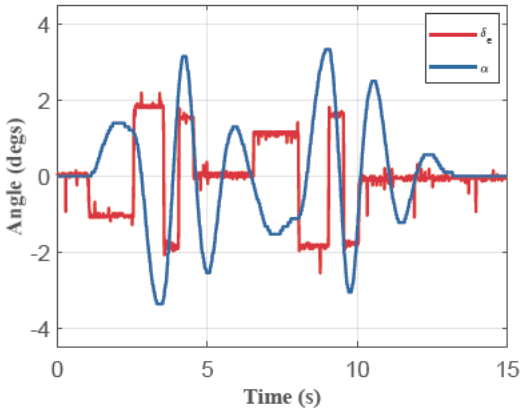

(b) 0.5s Timestep

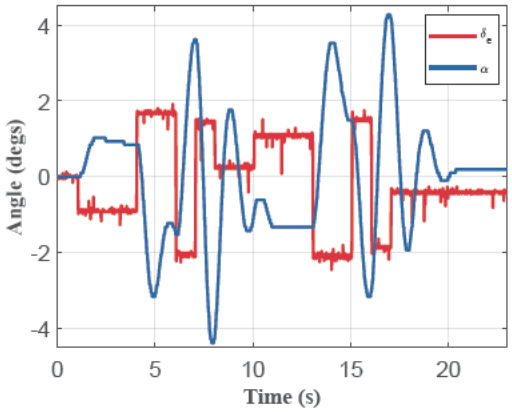

(c) 1s Timestep

Figure 5.17: Initial Time Step Tests at 15m/s, 2.5 degree amplitude

is some velocity correlation in the data. As the wind tunnel wall correction factors are only approximate and based off static testing, we do expect some velocity dependence to be observed in the data. As mentioned in Chapter 4, it is difficult to account for the effects the walls will have on the vortex systems which dominate the longitudinal stability of this vehicle. It is expected that at larger angles of attack where the vortex system is bursting at some point downstream, the wake blockage will likely be different from that predicted by the Shindo method [140] used here. In addition, the effect of the walls on the vortex may effect where the vortex system begins to lift off from the upper surface at higher AoA, and even when the vortex burst crossed the trailing edge, which could lead to large discrepancies beyond 15 degrees AoA.

The accuracy of the results are further assessed by utilising the Matlab state space modelling tools. The *ss* command is used to create a generalised state space model whose

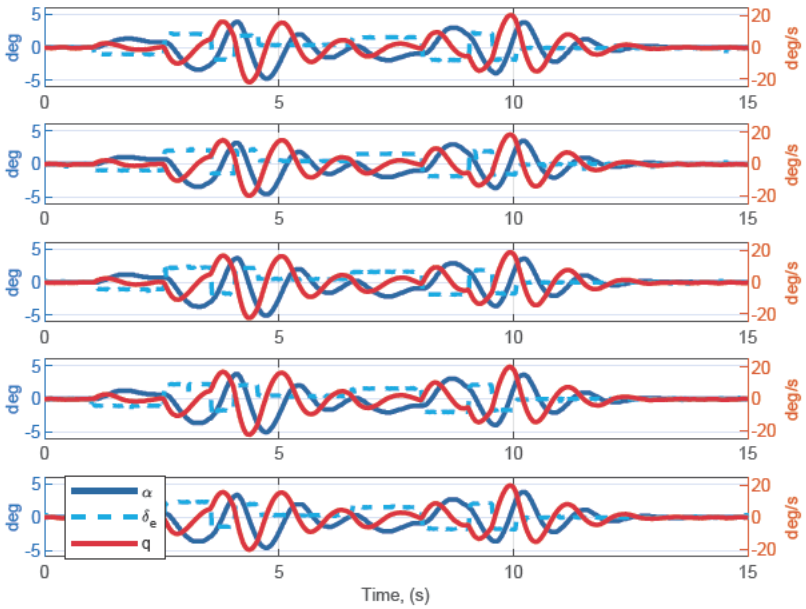

Figure 5.18: Repetition of tests at 0 AoA, 20m/s

A and B matrices are formed using the model in Eq. 5.3, populated with the estimated aerodynamic parameters. The response of this system to the recorded control sequence is then simulated using the *lsim* function. The results of this simulation represent the modeled response, which is subject to the FAA limits of ±2 deg/s pitch rate and ±1.5 deg for pitch attitude for matching the measured model response. The error in this response for pitch and pitch rate shall be defined as:

$$\begin{aligned} e_q &= |q_{modelled} - q_{measured}| \\ e_\alpha &= |\alpha_{modelled} - \alpha_{measured}| \end{aligned} \tag{5.10}$$

The modelled pitch and pitch rate responses for a particular test run at five degrees AoA and 20m/s are shown in Figure 5.20. The limiting lines are the measured response shifted by the FAA limits for pitch and pitch rate. The modelled pitch response is well within the limits laid out over the whole manoeuvre. The modelled q response is on or outside the limits of pitch rate between 5 and 5.5s and between 10s and 10.5s, when the rotational acceleration, $\dot{q}$ is at its maximum. This could indicate that the model used to fit the data is insufficient, and that higher order or nonlinear terms are significant when

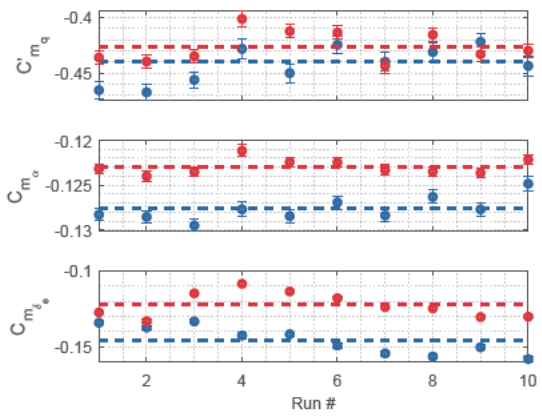

(a) -5 degrees AoA

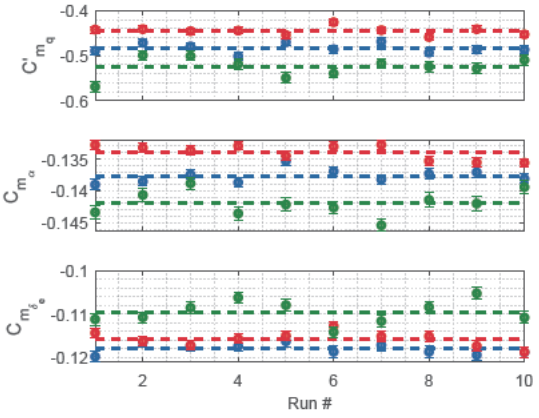

(b) 0 degrees AoA

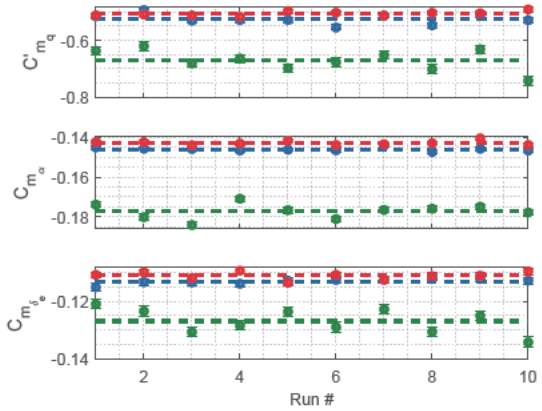

(c) 5 degrees AoA

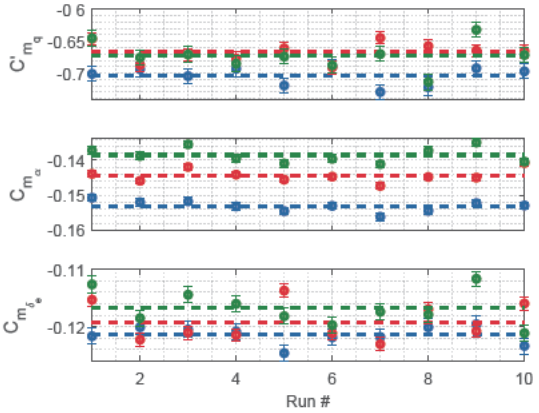

(d) 10 degrees AoA

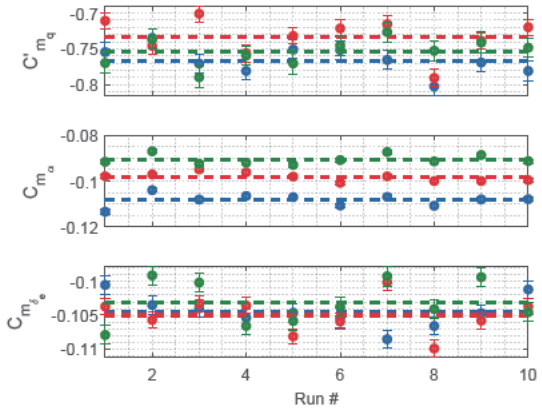

(e) 15 degrees AoA

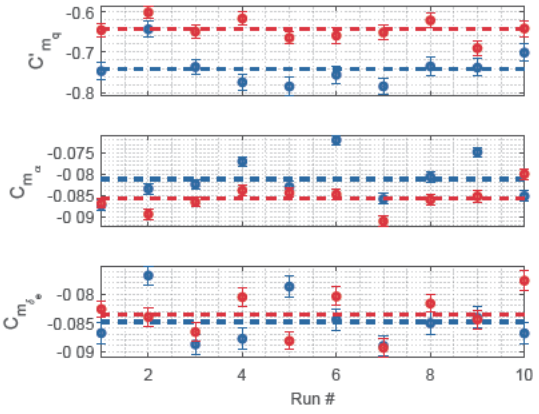

(f) 18 degrees AoA

Figure 5.19: Dynamic test results ● - 15m/s, ● - 20m/s, ● - 25m/s, dashed lines indicate mean value

the model motion is faster. As the wind tunnel model has a significantly lower moment of inertia than desired for matching the dynamic response of the full scale vehicle, it is

likely that the model will exhibit a faster response than the full scale vehicle, and such nonlinear or higher order effects would be less apparent at larger scales for the same amplitude motion.

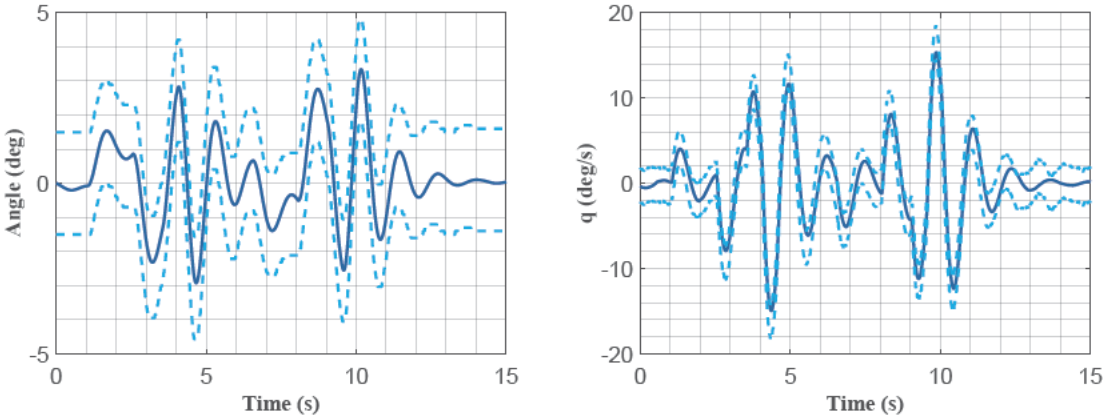

(a) AoA response

(b) q response

Figure 5.20: Sample modelled aerodynamic response at 5 degrees AoA, 20m/s

Figure 5.21 shows the mean fitted parameters at each AoA and airspeed for the multiple amplitudes tested for C'_{m_q} and C_{m_α}. Each test was repeated ten times to produce the average and standard deviation values, so the 95% confidence interval according to reference [138] is $\bar{x} - 0.7154\sigma < \mu < \bar{x} + 0.7154\sigma$ assuming a normal distribution of noise across the test runs. Tables 5.4, 5.5 and 5.6 show the average estimated parameters at each flight condition and for each amplitude of input. The amplitudes varied for higher AoA as the lower natural frequencies meant that a slower input was used, with a 1 second time step, and the amplitude was tuned for best results.

Table 5.4: Estimated mean $\overline{C'_{m_q}}$ and standard deviation $\sigma_{C'_{m_q}}$ for each AoA, Airspeed and Input Amplitude

	15m/s				20m/s				25m/s	
	1.5 deg		2.5 deg		1.5 deg		2.0/2.5 deg		1.0/2.0 deg	
AoA (deg)	$\overline{C'_{m_q}}$	$\sigma_{C'_{m_q}}$	$\overline{C'_{m_q}}$	$\sigma_{C'_{m_q}}$	$\overline{C'_{m_q}}$	$\sigma_{C'_{m_q}}$	$\overline{C'_{m_q}}$	$\sigma_{C'_{m_q}}$	$\overline{C'_{m_q}}$	$\sigma_{C'_{m_q}}$
-5	-0.370	0.036	-0.440	0.018	-0.460	0.011	-0.426	0.014		
0	-0.569	0.012	-0.483	0.011	-0.505	0.012	-0.445	0.009	-0.526	0.022
5	-0.618	0.018	-0.526	0.018	-0.560	0.025	-0.507	0.008	-0.670	0.037
10	-0.799	0.036	-0.704	0.014	-0.706	0.033	-0.667	0.015	-0.673	0.022
15			-0.766	0.019			-0.733	0.026	-0.754	0.019
18			-0.740	0.043			-0.644	0.026		

Parameter estimation has been run on each set of data, and the results of modelling using

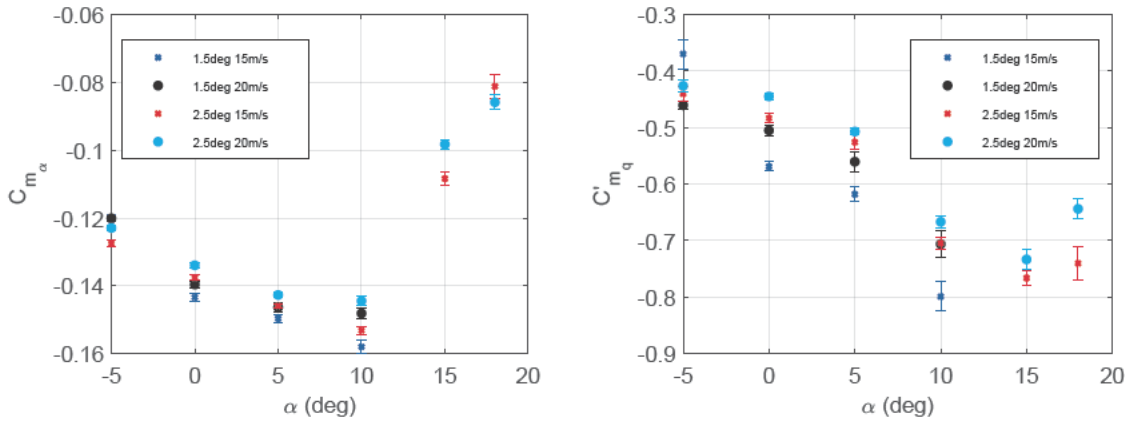

(a) C_{m_α} against AoA

(b) C'_{m_q} against AoA

Figure 5.21: Estimated Parameters at each AoA for 15m/s and 20m/s

Table 5.5: Estimated mean $\overline{C_{m_\alpha}}$ and standard deviation $\sigma_{C_{m_\alpha}}$ for each AoA, Airspeed and Input Amplitude

	15m/s				20m/s				25m/s	
	1.5 deg		2.5 deg		1.5 deg		2.0/2.5 deg		1.0/2.0 deg	
AoA (deg)	$\overline{C_{m_\alpha}}$	$\sigma_{C_{m_\alpha}}$	$\overline{C_{m_\alpha}}$	$\sigma_{C_{m_\alpha}}$	$\overline{C_{m_\alpha}}$	$\sigma_{C_{m_\alpha}}$	$\overline{C_{m_\alpha}}$	$\sigma_{C_{m_\alpha}}$	$\overline{C_{m_\alpha}}$	$\sigma_{C_{m_\alpha}}$
-5	-0.121	0.002	-0.128	0.001	-0.120	0.001	-0.123	0.001		
0	-0.143	0.002	-0.138	0.001	-0.140	0.002	-0.134	0.001	-0.142	0.002
5	-0.150	0.002	-0.146	0.001	-0.146	0.002	-0.143	0.001	-0.178	0.004
10	-0.158	0.003	-0.153	0.002	-0.148	0.002	-0.144	0.002	-0.139	0.002
15			-0.108	0.003			-0.098	0.002	-0.091	0.002
18			-0.081	0.005			-0.086	0.003		

Table 5.6: Estimated mean $\overline{C_{m_{\delta_e}}}$ and standard deviation $\sigma_{C_{m_{\delta_e}}}$ for each AoA, Airspeed and Input Amplitude

	15m/s				20m/s				25m/s	
	1.5 deg		2.5 deg		1.5 deg		2.0/2.5 deg		1.0/2.0 deg	
AoA (deg)	$\overline{C_{m_{\delta_e}}}$	$\sigma_{C_{m_{\delta_e}}}$	$\overline{C_{m_{\delta_e}}}$	$\sigma_{C_{m_{\delta_e}}}$	$\overline{C_{m_{\delta_e}}}$	$\sigma_{C_{m_{\delta_e}}}$	$\overline{C_{m_{\delta_e}}}$	$\sigma_{C_{m_{\delta_e}}}$	$\overline{C_{m_{\delta_e}}}$	$\sigma_{C_{m_{\delta_e}}}$
-5	-0.151	0.011	-0.146	0.009	-0.133	0.003	-0.123	0.008		
0	-0.117	0.003	-0.118	0.001	-0.111	0.003	-0.116	0.002	-0.110	0.003
5	-0.106	0.004	-0.113	0.001	-0.105	0.002	-0.111	0.001	-0.127	0.004
10	-0.122	0.004	-0.123	0.002	-0.119	0.002	-0.119	0.003	-0.117	0.003
15			-0.104	0.002			-0.105	0.003	-0.103	0.003
18			-0.085	0.004			-0.084	0.004		

the estimated parameters produce good results. However, the aim of repeating the tests is to produce one average parameter estimation result for the whole set of data. To test the robustness of this set of averaged estimated parameters, these parameters are used to model the response to each sequence of ten recorded control inputs and the results

are measured against the recorded data of each run. Table 5.7 shows the maximum error across all samples at each flight condition and input amplitude alongside the average maximum deviation from the measured data over all samples. It is noted that in some instances, the maximum error of the modelled response using the average parameters to the individual sample results is smaller than the modelling error using the parameters estimated from that sample only. This is a result of using the linear least squares regression which may allow short, large excursions from the measured data for a better fit over the whole sample. A nonlinear system identification method such as output error method may yield better performance if minimising this maximum deviation is the key requirement. Table 5.7 shows that the worst case errors in the pitch rate q are outside the FAA ±2 deg/s pitch rate limit for a number of test condition combinations. This criteria may lead us to surmise that the small amplitude input is achieving better system identification performance. However modelling that used the identified parameters from the larger input amplitude tests also achieved better results when simulating the smaller amplitude samples. Examination of the data shows two issues. The response size to the 1.5 degree amplitude inputs is smaller, and therefore the error in absolute terms from the modelled response will also be smaller. The second issue is that the larger amplitude input is likely resulting in motion that is beyond the capacity of the linearised system to model. This is made clearer by the fact that the pitch rate errors only occur for very short periods of time at the maximum or minimum points in the pitch oscillation. The short length of the pitch rate deviations results in the modelled pitch remaining within the FAA ±1.5 deg limits over all samples.

Table 5.7: Largest pitch rate error ($max(e_q)$ deg/s) and pitch error ($max(e_\alpha)$) deg) across all samples at each flight condition and input size

	15m/s				20m/s				25m/s	
	1.5 deg		2.5 deg		1.5 deg		2.0/2.5 deg		1.0/2.0 deg	
AoA (deg)	e_q	e_α	e_q	e_α	e_q	e_α	e_q	e_α	e_q	e_α
-5	3.59	1.38	4.72	1.47	2.49	0.51	4.83	0.96		
0	1.87	0.61	3.50	1.11	2.79	0.70	5.16	1.11	2.83	0.49
5	1.85	0.48	2.88	0.78	2.57	0.51	3.82	0.73	3.31	0.60
10	1.49	0.42	1.93	0.58	2.18	0.52	2.62	0.67	3.33	0.53
15			2.40	0.64			2.42	0.59	3.13	0.55
18			2.89	1.28			3.40	0.96		

The main outlier among the flight condition input amplitude combinations is the 1.5 degree input at 15m/s. This is apparent from Tables 5.4, 5.5 and 5.6 and from Figure

5.21(b). Examination of individual test run data for this combination found that the model response is small enough that the sensor resolution becomes a problem. Figure 5.22(a) shows a 1.5 degree amplitude input at 10 degrees AoA and 15m/s. The peaks of pitch oscillations are truncated while the settling oscillations are noticeably stepped and this results in poor quality data for the system identification. When performance of the identified parameters is assessed by the maximum absolute deviation of the modelled response from the measured response it does perform well, however this is due to the small response magnitude rather than good model performance. The percentage deviation shows poor performance at this condition. A better response shape is shown for a 2.5 degree amplitude input at 20m/s showing the smoother peaks and the greater information content in the settling period from 10 to 15 seconds.

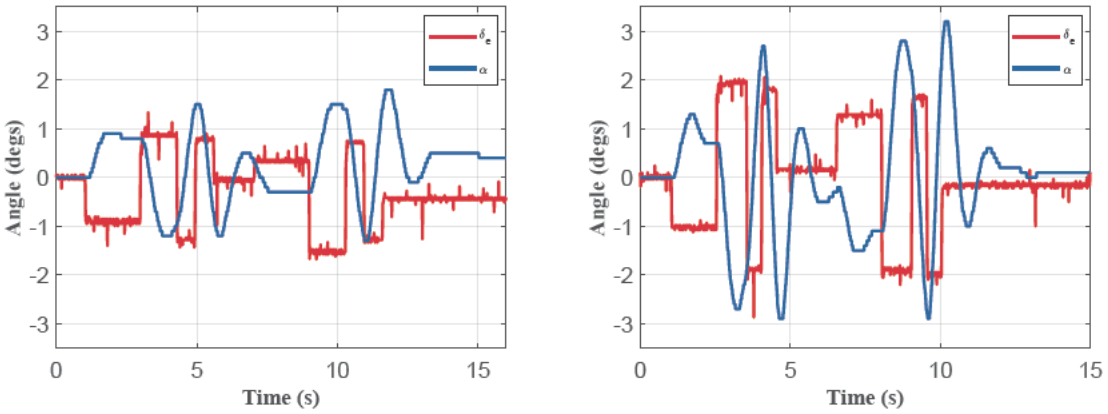

(a) Model response for 1.5deg amplitude at 15m/s (b) Model response for 2.5deg amplitude at 20m/s

Figure 5.22: Good and poor responses for system identification

As a result of the preceding analysis of the errors for the different combinations of input amplitudes and flight conditions, the results from the 2.5 degree input amplitude at 20m/s have been chosen as the best results from the dynamic testing and are shown in Figure 5.23.

Table 5.8 and Figure 5.24 compare the dynamic wind tunnel results for C_{m_α} and $C_{m_{\delta_e}}$ against the results from the static wind tunnel testing. As the two methods work on different principles, system identification of the model motion for dynamic and direct force and moment measurement for static, this comparison provides an additional validation method for the two sets of data. The static $C_{m_{\delta_e}}$ estimate at the AoA and trim elevon deflections of the dynamic tests are estimated by linearly interpolating the static

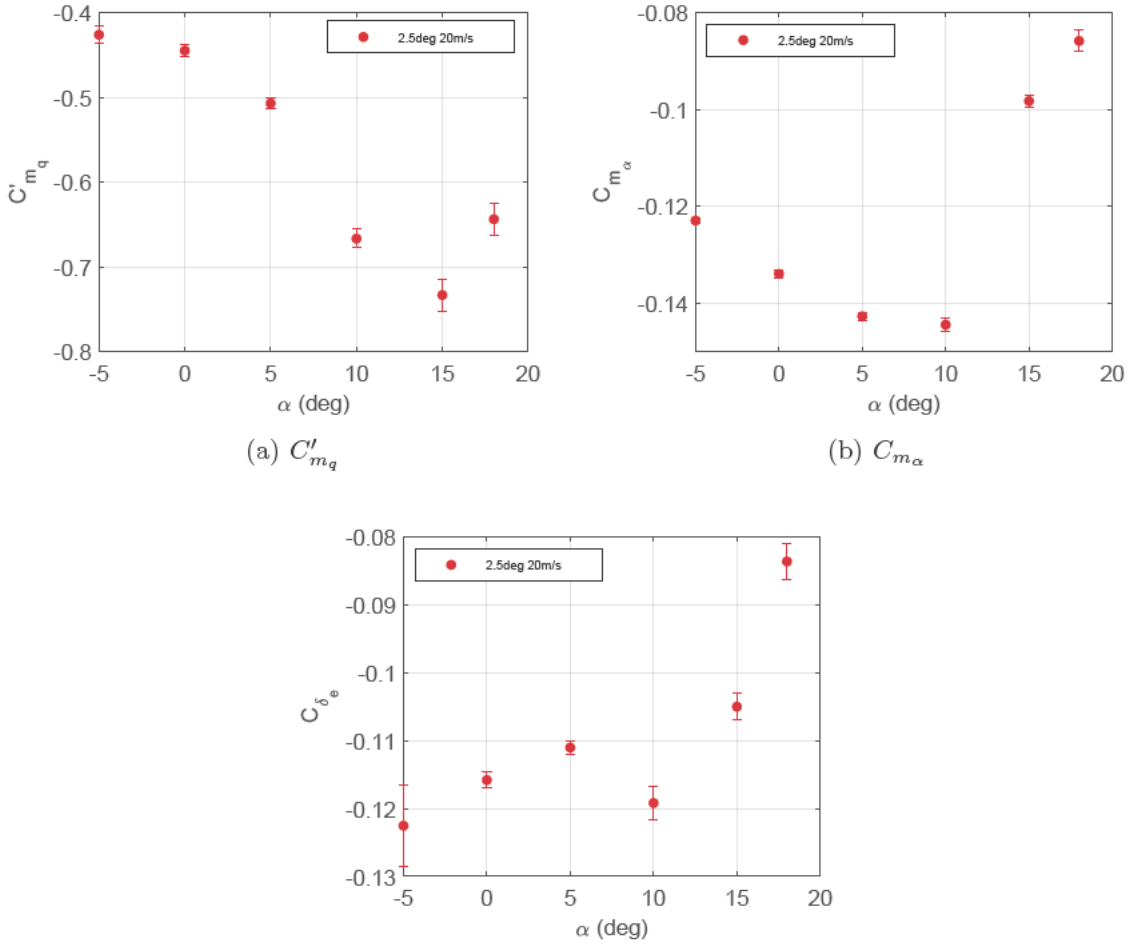

Figure 5.23: Final aerodynamic parameters from dynamic wind tunnel tests

$C_{m_{\delta_e}}$ estimates for each fixed elevon deflection tested. The combination of 7 degree trim elevon deflection and -5 degrees AoA is outside the range of the static testing so no data is included there for $C_{m_{\delta_e}}$. The rigorous approach to error accounting outlined in Chapter 4 resulted in large 95% confidence intervals for C_{m_α} due to the conservative approach to dealing with uncertainty in AoA for the gradient calculations. The comparison with the dynamic testing data shows very good agreement and the small 95% confidence interval for the dynamic data gives us good confidence in the accuracy of the static data. There is a discrepancy at 18 degrees AoA at the edge of the stable envelope, which is likely due to reduced accuracy in the dynamic testing at this region and potentially from differences in the elevon deflection angle when testing was conducted. In addition, the transient development of the vortex system during oscillation where burst is beginning to cross the trailing edge could be different from the steady state behaviour.

The stability requirement for the full vehicle suggests that this region would ideally not be encountered at any point during a flight profile and therefore is of less relevance. The static $C_{m_{\delta_e}}$ results again show large uncertainty due to the gradient based method of calculation, however the confidence interval calculated shows good agreement with the dynamic testing data.

Table 5.8: Comparison of dynamic and static test results for each AoA

	C_{m_α}		$C_{m_{\delta_e}}$	
AoA (deg)	static	dynamic	static	dynamic
-5	-0.112 ± 0.022	-0.123 ± 0.0006		-0.123 ± 0.006
0	-0.139 ± 0.026	-0.134 ± 0.0009	-0.081 ± 0.10	-0.116 ± 0.001
5	-0.135 ± 0.027	-0.143 ± 0.0008	-0.117 ± 0.04	-0.111 ± 0.0009
10	-0.147 ± 0.030	-0.144 ± 0.001	-0.099 ± 0.02	-0.119 ± 0.002
15	-0.089 ± 0.033	-0.098 ± 0.001	-0.099 ± 0.02	-0.105 ± 0.002
18	-0.017 ± 0.047	-0.086 ± 0.002	-0.093 ± 0.02	-0.084 ± 0.003

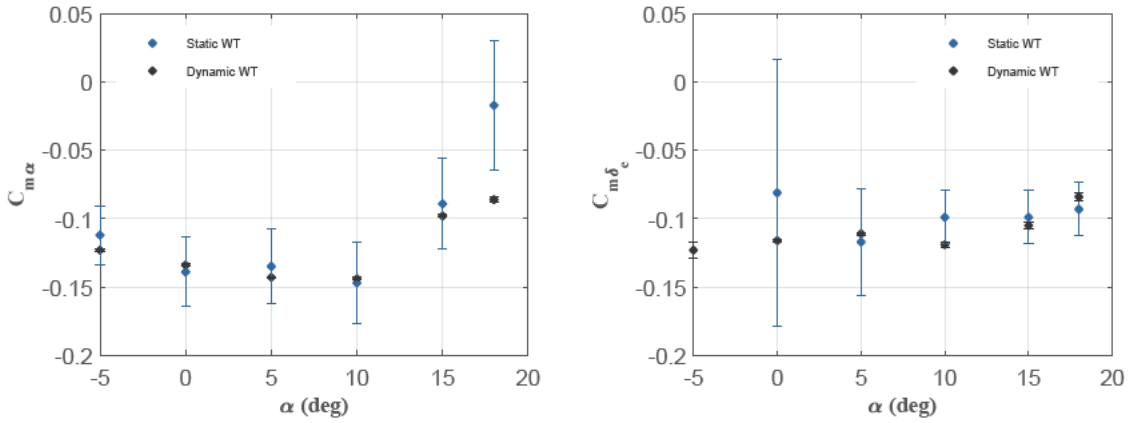

(a) Static and Dynamic Wind Tunnel C_{m_α} (b) Static and Dynamic Wind Tunnel $C_{m_{\delta_e}}$

Figure 5.24: Static and Dynamic wind tunnel test pitch stiffness and control authority results

5.8 Handling Qualities Assessment

To assess the handling qualities we focus on the short period mode performance based on the results from the dynamic wind tunnel tests. The short period mode tends to dominate the longitudinal handling qualities as the faster mode tends to affect the pilot workload to a greater degree than the slower phugoid motion. The short period mode is therefore a key part of longitudinal handling assessment. We assess the Hexafly vehicle using the Class II criteria for medium weight and low-to-medium maneuverability which

civilian transport aeroplanes such as the Boeing 737 or Airbus A320 would fall under in the MIL-F-8785C standard. Although the Hexafly is a civilian purpose design, we use the military specification, MIL-F-8785C to assess handling quality as suggested by Roskam in reference [88]. The speed will be the assumed landing speed of 80 m/s that was used in Chapters 3 and 4 and the mass and moment of inertia of the full vehicle outlined in Chapter 2. As the Hexafly EFTV is a scaled down version of the envisioned transport aircraft, the small scale may justify considering the Class I category for light aircraft as well. We focus on the Category C flight phase type, which includes take-off and landing phases.

The key parameters are defined in Eq. 5.11, the damping ratio, the natural frequency and the normal load factor per radian. The MIL-F-8785C standard uses these parameters to assess the handling quality level of the vehicle short period mode.

$$\begin{aligned} \omega_{n,SP} &= \sqrt{-\frac{\bar{q}Sc}{I_{yy}}C_{m_\alpha}} \quad (rad/s) \\ \zeta_{SP} &= -\frac{\frac{\bar{q}Sc^2}{2VI_{yy}}C'_{m_q}}{2\omega_n} \\ n/\alpha &= \frac{\bar{q_1}C_{L_\alpha}}{W/S_{ref}} \quad (g's/rad) \end{aligned} \tag{5.11}$$

Figure 5.25 shows the characteristics of the wind tunnel model and full scale vehicle within the MIL-F-8785C Category C defined envelope. To trim the aircraft at the landing speed of 80 m/s an AoA of around 12 degrees is required. However we do not have data at this exact AoA. The data point for 10 degrees AoA is marked for both scales in Figure 5.25 and the low spread of data from 5 to 15 degrees suggests that the 12 degree result would be in a similar region. The data for the wind tunnel scale model is calculated from the wind tunnel test condition of 20m/s. The full scale vehicle shows level 1 (flying qualities adequate for landing phase) characteristics. The dynamic model exhibits higher natural frequency and lower load factor per radian which is likely due to the insufficient mass and mass moment of inertia to achieve similar dynamic scaling with the full vehicle as discussed earlier. The short period response for the wind tunnel model is therefore faster than for the full scale vehicle and is considered level 2, flying qualities adequate but with excessive pilot workload or inadequate mission effectiveness.

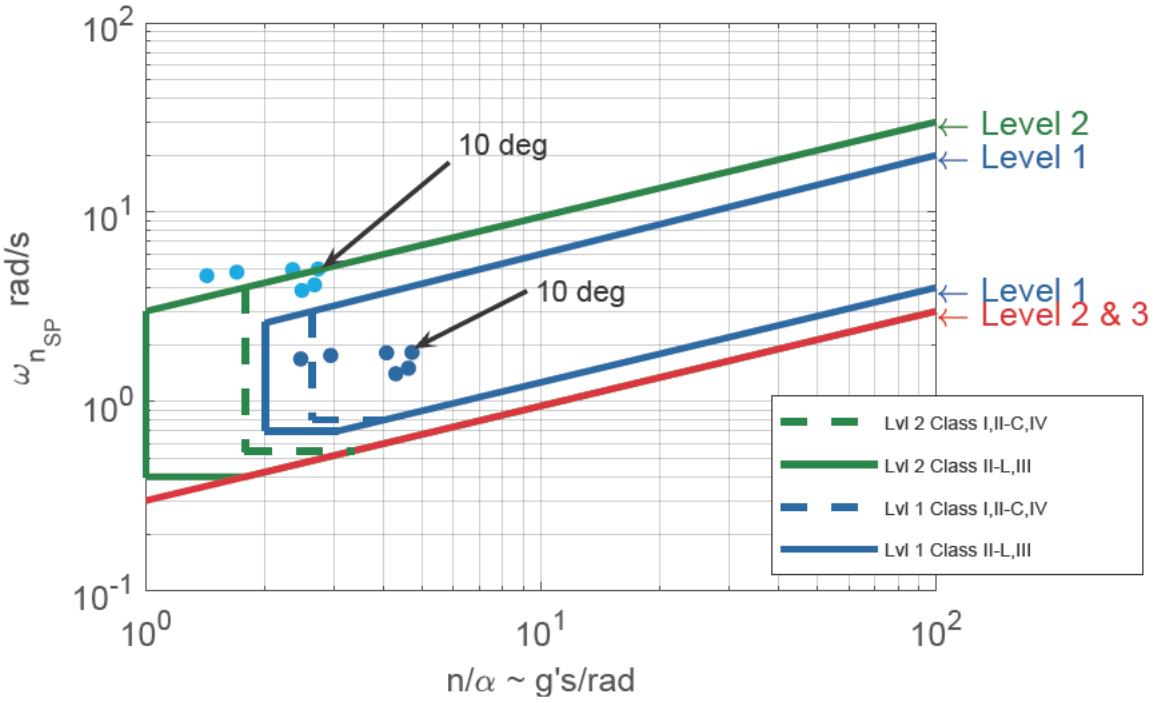

Figure 5.25: Short period handling qualities, MIL-F-8785C Category C ● - Wind tunnel scale, ● - Full scale

The required damping parameters according to MIL-F-8785C are shown in Table 5.9 for category C. The damping ratio at each AoA is shown in Table 5.10 for both the wind tunnel scale and the full scale vehicle. Level 1 is shown in blue, level 2 is shown in green, level 3 is shown in red.

Table 5.9: MIL-F-8785C Category C Short Period Damping Ratio Requirements [88]

Level	Minimum				Maximum
Level 1	0.35	⟵	ζ_{SP}	⟶	1.30
Level 2	0.25	⟵	ζ_{SP}	⟶	2.00
Level 3	0.15	⟵	ζ_{SP}	⟶	no maximum

Table 5.10: Damping ratio at wind tunnel and full scales from test results

	AoA (degrees)					
Scale	-5	0	5	10	15	18
Wind Tunnel	0.19	0.19	0.21	0.27	0.37	0.34
Full size	0.06	0.06	0.07	0.09	0.12	0.11

It is clear that the damping ratio at both scales is not adequate. Although the 'feel' of the wind tunnel model was good during dynamic testing, there is no requirement to maintain altitude during a constrained free-to-pitch test and the pilot workload cannot be properly assessed during this type of testing. The damping ratio at the full scale

is too low by a factor of 3 up to 6. The damping ratio is better at the higher AoA due to the lower pitch stiffness. The pitch stiffness can be lowered as far as needed by shifting the centre of gravity back towards the neutral point. However this would lower the AoA at which pitch instability is encountered. This in turn reduces the stable AoA envelop considerably and forces a higher landing speed to maintain lift. The original ESTEC Mach 8 waverider design, MR-2, of the LAPCAT project from which the Hexafly design was derived did feature a canard foreplane. This addition could improve the pitch damping characteristics and solve the pitch instability problem at the same time. The results here do suggest that such an addition might be necessary for a full scale civilian transport vehicle based off the Hexafly design and further investigation of this modification will be examined in future work.

There are no authority requirements for elevator control, applicable to civilian transport designs which have no requirement for high manoeuvrability. However, the stick force gradient is specified in MIL-F-8785C and is applicable to civilian aircraft with reversible control surfaces. As the Hexafly vehicle is designed to cruise at hypersonic speeds, an irreversible control system would be required and force feedback to the pilot could be tuned and scheduled to give the required force gradients at each flight condition.

5.9 Comparison of wind tunnel data and CFD data

One of the key aims of the wind tunnel test campaign has been to validate the dynamic and static CFD results. As covered in Chapter 3, the results of computational methods are difficult to assess in isolation. The C_{m_α} data collected from the static CFD simulations is compared to the dynamic testing data. All of the static longitudinal force and moment data is compared to the static wind tunnel test results. The dynamic CFD results are compared to the static and dynamic wind tunnel testing on the basis of the C_{m_α} and C'_{m_q} results. Again, it is noted that some wall effects in the wind tunnel testing will not have been fully accounted for. This is especially true with regards to the effect on the leading edge vortex system. As a result, the CFD simulations of freestream flight conditions will not match the wind tunnel results even in the ideal case where they are perfectly accurate to actual flight conditions.

5.9.1 Static CFD Comparison

The static CFD results compared to the static wind tunnel testing results are shown in Figure 5.26. The tolerances of the wind tunnel model geometry leave some uncertainty in determining the zero AoA setting during testing. To eliminate the resulting bias effect the wind tunnel data has been shifted such that the zero lift AoA matches with the CFD calculations. The same shift has been applied to the drag and moment data for consistency. The lift results shown in Figure 5.26(a) show excellent agreement. The increasing offset in drag (though still small) as AoA increases could be suggestive of over-accounting for wall effects in the correction of the wind tunnel dynamic pressure. The Shindo correction given in Chapter 4 is dependent on the lift and drag but may not be ideally suited for a vehicle where a large proportion of the lift is generated from vortex flow, rather than attached flow.

The moment curve shown in Figure 5.26(c) shows a larger difference between experiment and static CFD than the forces, with a maximum deviation at 5 degrees AoA. As there is no measure of the surface flow or pressure for the wind tunnel tests it is difficult to determine the reason for this difference at 10 degrees with certainty. It could be attributed to an effect of the wind tunnel mount. The pressure difference at the mount itself should not have a large impact on the moment as the wind tunnel model is mounted at the moment reference centre. In contrast, the effect of the wake of the mount reducing the surface pressure to the rear of the bottom surface will reduce the negative contribution to the pitch moment that this region of the vehicle would produce in freestream flow. This would have the effect of increasing the pitching moment across the range of AoA.

The results of the dynamic wind tunnel testing are also included in Figure 5.26(d) of C_{m_α} and show good agreement below 18 degrees. It is likely that the reduced effectiveness of the dynamic wind tunnel tests configuration approaches instability is the reason for this, and the agreement between the static CFD and static wind tunnel testing bears this out. The static CFD shows very good agreement with the wind tunnel testing with the exception of 10 degrees AoA. There is a reduction in the magnitude of C_{m_α} observed in the wind tunnel data between 10 and 15 degrees AoA. It is possible that the change in the flow that cause this is being delayed in the experiments due to wind tunnel effects from either the walls or the presence of the mount.

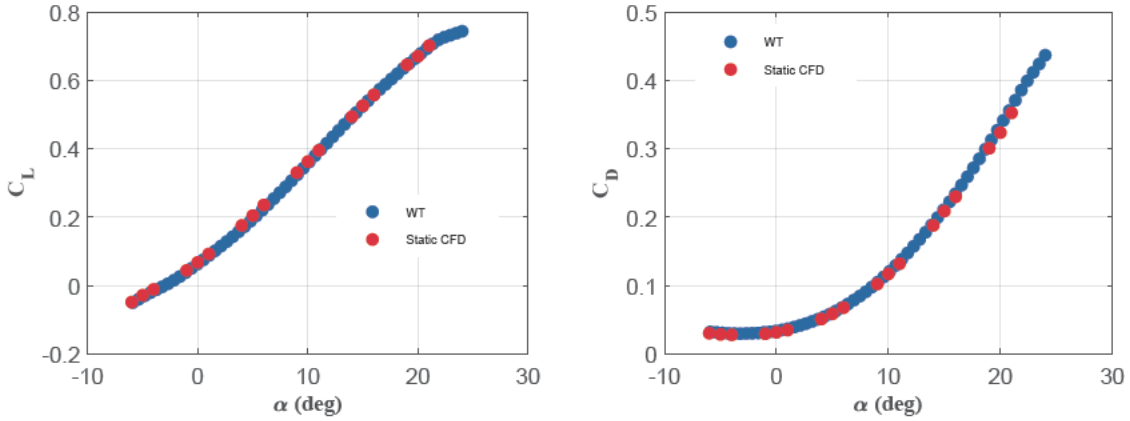

(a) Lift Coefficient

(b) Drag Coefficient

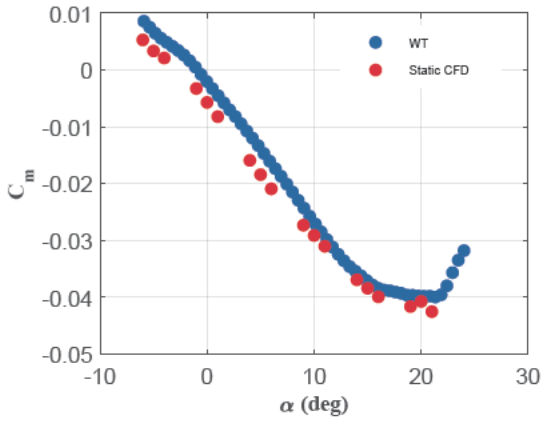

(c) Pitch Moment Coefficient

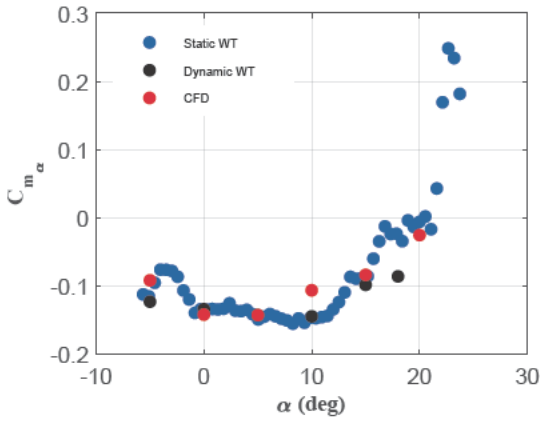

(d) Coefficient of Pitch Stiffness

Figure 5.26: Comparison of steady CFD simulation results with static wind tunnel testing

5.9.2 Dynamic CFD Comparison

Chapter 3 presented the C_{m_α} and C'_{m_q} results for the dynamic CFD testing of the pitching Hexafly vehicle for a number of different forcing amplitudes and frequencies. The results presented there show some variation in C_{m_α} with amplitude due to the single-point method used to extract the data. There was no appreciable effect of changing frequency on the resulting C_{m_α} and C'_{m_q} results. The dynamic pitch motion observed during the wind tunnel testing typically have an amplitude of between 3 and 5 degrees. The data from the 4 degree amplitude 1Hz, and 1 degree, 1 Hz dynamic CFD tests have been used for comparison with the wind tunnel data.

Figure 5.27(a) shows the pitch stiffness coefficient, C_{m_α}, from static CFD, static wind tunnel testing, dynamic wind tunnel testing and dynamic CFD. The results show good

correlation across the range, with the exception of 10 degrees AoA where both dynamic and static CFD results differ from the wind tunnel tests. Figure 5.27(b) shows good agreement for calculated pitch damping, C'_{m_q}, with around 6% deviation between the two methods except at 5 degrees and 18 degrees. As discussed previously, it is unlikely that the dynamic wind tunnel test results are reliable at the 18 degree AoA test point, however the larger 15% difference between the C'_{m_q} values at 5 deg AoA is more difficult to explain. This is in contrast to the very good agreement between the calculated C_{m_α} coefficient at 5 degrees AoA. In addition, the results for C'_{m_q} from CFD and wind tunnel overlap at 10 degree AoA where the C_{m_α} results showed the largest deviation.

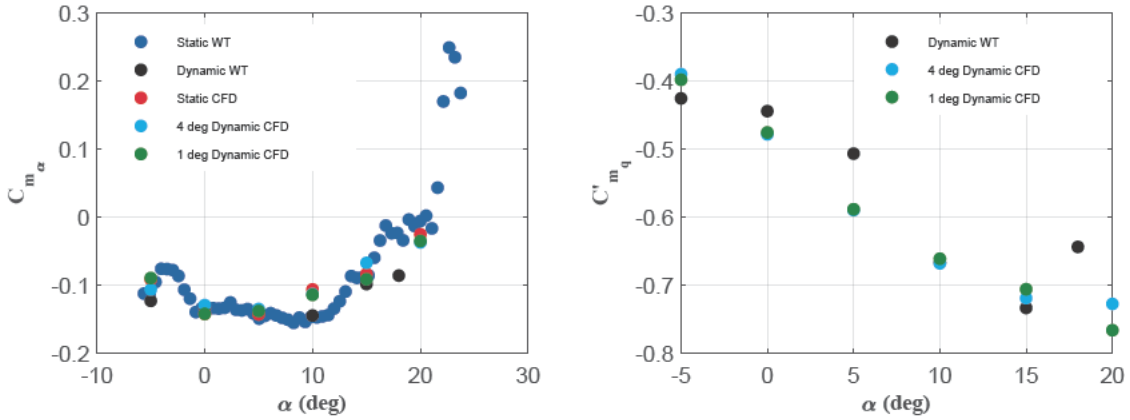

(a) Pitch Stiffness

(b) Pitch Damping

Figure 5.27: Comparison of dynamic CFD simulation results with dynamic wind tunnel testing

The comparison presented in Figure 5.27 show that overall, the dynamic CFD method produces results which match the dynamic wind tunnel testing well over the majority of the AoA range tested. Some deviation was always expected as the wind tunnel tests results suffer from the effects from the walls and the mount used. Therefore the low percentage difference in the CFD and wind tunnel pitch stability analysis increases the confidence that can be placed in the results of this computational method for the hypersonic cruise vehicle type investigated. In particular this validates the use of CFD to obtain dynamic derivatives for the class of dorsal engine waveriders, that the Hexafly-Int design belongs to, which show promising results for high aerodynamic efficiency hypersonic cruise.

5.10 Conclusions

Dynamic wind tunnel tests have been run which have obtained the longitudinal pitch damping derivatives for a hypersonic vehicle design at low speeds. Free-to-pitch testing has been used for the first time on this class of vehicle to obtain the results. They have been compared against the static wind tunnel results and show very good agreement for the comparable derivatives, C_{m_α} and $C_{m_{\delta_e}}$ over the majority of the AoA envelope. This agreement gives us confidence in the accuracy of the results. The calculated derivatives from the CFD studies of the Hexafly EFTV have been compared to the wind tunnel data and show good agreement, which increases confidence in the computational method used for this class of slender waverider vehicle under low speed flow conditions. The damping characteristics obtained from the dynamic wind tunnel tests have been used to evaluate the longitudinal handling qualities of the vehicle's short period mode, which is the most important mode of motion in the longitudinal plane [88]. The resulting ratings show deficiencies in the damping of the short period mode which when projected to the full scale EFTV suggest under-damped behaviour across the AoA range tested. The results are likely characteristic of this type of slender vehicle without a dedicated horizontal stabilising surface such as a canard foreplane or tail. Modifications to the base waverider shape or the addition of a canard would be necessary to alleviate this issue on a civilian transport based on the same design. The LAPCAT II MR2 vehicle on which the Hexafly EFTV is based does feature this canard surface for improved handling, stability and trim.

Chapter 6

Waverider Study

The preceding results from CFD and wind tunnel testing of the Hexafly EFTV have identified potential deficiencies in low speed stability that are characteristic of the waverider class of vehicle. The question which this chapter seeks to answer is whether or not the base waverider shape (from which a hypersonic vehicle such as the Hexafly EFTV is developed) can be improved with the objective of good low speed stability and handling qualities. A low fidelity numerical code has been created to generate osculating cone waverider shapes using power law curves to define the upper and lower surfaces. The resulting shapes are analysed using the Athena Vortex Lattice code [156] with corrections to account for vortex lift. The resulting aerodynamic performance is used to provide optimisation objectives to a standard genetic algorithm for improvement. The aim of this chapter is not to definitively find a best waverider shape for low speed stability. The outcome of the optimisation calculations is instead used to understand the qualities of the waverider shapes which improve the low speed handling qualities. The following sections will outline the optimisation objectives, the waverider design method used within the optimisation, low speed aerodynamic analysis method and the optimisation algorithm, NSGA-II.

6.1 Optimisation Problem

Before discussing the aerodynamic tools used for analysis it is important to be clear on what the objective of the optimisation loop will be. The analysis in the preceding

chapters has identified the pitch stiffness (C_{m_α}) at low speeds as a critical stability issue. The Hexafly-Int vehicle is statically unstable at its design centre of gravity as shown by the results of static wind tunnel tests in Chapter 4, Figure 4.10. This pitch stiffness deficiency which results in a low static margin (scaled distance from the centre of gravity to the unstable centre of gravity location) actually results in the aircraft requiring a centre of gravity which is further forward than would otherwise be necessary. Waverider shapes typically have a large volume distribution towards the rear of the vehicle with cross sectional areas which increase with chordwise distance. The ability to place the centre of gravity further to the rear due to increased static margin (pitch stiffness) will allow more of the waverider volume to be usable for payload, fuel or propulsion systems.

One objective will therefore be to improve the pitch stiffness of the landing phase trim condition. For the sake of comparison with Hexafly EFTV results, the waverider shapes will be generated with the same body length and span. In this case, the waverider shape will only be compared to the wing length of the Hexafly EFTV, the nose cone of the glider is considered part of the fuselage which will not be considered here. This will allow a comparison at the same assumed landing conditions. The mass of the generated waverider is set to 420kg, the same as the Hexafly EFTV and the trim lift coefficient is calculated for a speed of 80m/s, the assumed landing speed used in earlier chapters. The first optimisation objective will be to maximise the pitch stiffness at the AoA which produces the required trim lift coefficient during the landing phase. As the planform area of each waverider shape will be different, the trim lift coefficient will need to be recalculated for each one.

It is possible for pitch stiffness to be too large for a given aircraft causing the resulting dynamics to become too slow. However the goal of maximising the pitch stiffness at low speeds for a given centre of gravity actually translates to allowing the centre of gravity to be placed further to the rear. This will allow more scope to match the cruise centre of gravity requirements which are typically further to the rear than the low speed stability requirements will allow.

Improving the pitch stiffness at landing is a key goal of this chapter, however, this will ideally be achieved without compromising the aerodynamic efficiency at cruise conditions, which is the main appeal of the waverider. To that end, the second parallel objective will be defined as maximising the lift to drag ratio at the design Mach number, which

will also be set to that of the Hexafly EFTV at Mach 7.2.

The chosen centre of gravity for the optimisation loop is arbitrary in the absence of a detailed vehicle design with mass distributions. There are also a number of alterations to a pure waverider design which must be made in order to design a practical vehicle shape as shown by Eggers et al in reference [112] and outlined briefly in Chapter 2. These will all have an impact on the pitching moment which cannot be determined at this stage in the analysis.

6.2 Waverider Design

A variety of methods for waverider design were outlined in Chapter 2. For the purposes of an optimisation algorithm approach, it is best to use as versatile design method as possible to maximise the useful design space which the optimiser can explore. As the second objective, cruise lift to drag ratio, pertains to performance at cruise, a design method which allows for rapid aerodynamic performance estimation will allow the optimisation algorithm to run much faster. Waverider design methods which allow rapid calculation of design performance are those that use flow generating bodies with analytical flowfield solutions. The osculating cones design method satisfies both conditions. The ability to specify a shock and upper surface curve leads to a large design space and the use of conical shocks allows the flowfield to be solved by simple numerical integration of the Taylor-Maccoll equations. This is a computationally inexpensive process. The process and equations used in the osculating cones method are presented next.

6.2.1 Osculating Cones Design Method

The osculating cones method is an extension of the simple conical waverider design method. In the simple conical method a single shock generating cone is used to provide the flowfield from which the entire vehicle is designed. The osculating cones method extends this to multiple cones generating the lower surface in successive planes normal to the prescribed shock curve. The osculating procedure begins by defining an upper surface ($z_u = f_u(y)$) and shock surface curve ($z_s = f_s(y)$) in the Y-Z plane at the rear of the desired vehicle (referred to as YZ_{rear}).

For this work the curves have been defined as polynomials of degree six which define

the z axis position (height axis) as a function of y (span axis where $y : 0 \rightarrow b$, and b is vehicle semi-span). A sixth degree polynomial has been used as this produces sufficiently complex shapes for the resulting waveriders, and increases in the polynomial degree increase the design space members. Increasing the design space requires more optimisation iterations to arrive at a converged solution.

$$\begin{aligned} z_u = f_u(y) = a_u y^6 + b_u y^5 + c_u y^4 + d_u y^3 + e_u y^2 + f_u y + g_u \\ z_s = f_s(y) = a_s y^6 + b_s y^5 + c_s y^4 + d_s y^3 + e_s y^2 + f_s y + g_s \end{aligned} \tag{6.1}$$

The design Mach number, (M_∞), desired body length (L_{ref}) and span (b) are specified. The procedure begins by calculating the shock angle that will be used for every osculating cone. It is not actually necessary to define the cone apex angle itself, although this can be determined. The required shock angle is determined by assuming that the waverider maximum length will occur on the X-Z plane at $y = 0$. The radius of the conical shock, R_c, at YZ_{rear} is determined from the local radius of curvature of the shock curve at that point. This is defined in Eq. 6.2.

$$R_c = \frac{(1 + f_s^{'}(0))^{3/2}}{|f_s^{''}(0)|} \tag{6.2}$$

The angle of the shock emanating from the leading edge of the vehicle is the same as that of the generating cone. The equation of the line which intercepts the shock curve at $y = 0$ is determined from the gradient of the shock curve and the value of $z_s = f_s(0)$. The intercept of this normal line with the upper curve is then determined.

The curve definitions have been constrained such that the gradient at the X-Z plane is zero ($f_s^{'}(0) = 0$) as non zero gradients can cause unrealistic shapes where shocks generated from different points on the leading edge must cross to produce the desire shock curve. With this simplification, the intercept of the normal from the shock curve with the upper curve for $y = 0$ becomes $z_u = f_u(0)$. The height from the upper curve to the shock curve is the height from the leading edge at $y = 0$ to the shock curve at $y = 0$. The x axis length from the leading edge to the shock is the desired body length so the

shock angle θ_s can be determined.

This same shock angle is then applied at all points along the shock curve. The procedure at each point is to determine the equation of the line normal to the shock curve and use this to determine the intercept location with the upper curve. As the upper curve is a freestream surface, the y and z coordinates of the intercept with the upper curve in the YZ_{rear} plane is the same as the intercept point on the leading edge. The osculating plane is defined to contain the leading edge intercept, the upper curve intercept and the current point along the shock curve. A cone is defined such that its vertex lies on the osculating plane, defined such that the shock emanating with the angle θ_s will intercept both the leading edge and the current shock curve point with the same radius as the local radius of curvature of the shock curve.

This procedure is best illustrated by the diagram from reference [93] which was shown in Chapter 2 but is reproduced here for clarity in Figure 6.1. In Figure 6.1, the solid line at the bottom is the defined shock curve, the mesh is the bottom surface of the waverider and the top of the mesh is the upper surface of the vehicle which is aligned with the freestream and the viewpoint of the figure.

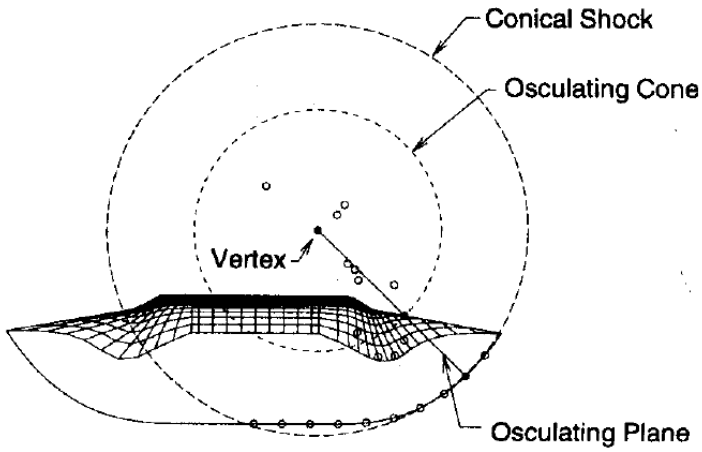

Figure 6.1: Osculating Cones waverider method [93]

Once the generating cone in the current osculating plane has been identified, the procedure is the same as that of the simple conical waverider. The streamline generated from the leading edge intercept point is determined using the procedure outlined by Bowcutt in reference [95]. This streamline is used to define the lower surface of the waverider in the osculating plane. Repeating this procedure from $y = 0 \rightarrow b/2$ defines the lower

surface and the upper surface is defined by lines parallel to the x axis from the leading edge intercept to the rear plane.

The streamlines of the flow behind the cone are determined by integrating the Taylor-Maccoll (T-M) equations (expressed in spherical coordinates in Eq. 6.3) which describe the inviscid flow behind a cone at zero inclination to a supersonic flow. Note in Eq. 6.3, r refers to the radial distance from the origin, and θ is the angular displacement from the cone axis ($\theta = 0$ represents all points along the centreline of the cone).

$$\begin{aligned} \frac{dV_\theta^{'}}{d\theta} &= \frac{V_r^{'}V_\theta^{'2} - \frac{\gamma-1}{2}[1 - V_r^{'2} - V_\theta^{'2}][2V_r^{'} + V_\theta^{'}\cot\theta]}{\frac{\gamma-1}{2}[1 - V_r^{'2} - V_\theta^{'2}] - V_\theta^{'2}} \\ \frac{dV_r^{'}}{d\theta} &= V_\theta^{'} \end{aligned} \tag{6.3}$$

To begin the integration the x-y-z coordinates of the leading edge point are converted into a spherical coordinate system with the origin located at the osculating cone vertex. The value of $V_\theta^{'}$ and $V_r^{'}$ are determined from the relation for the deflection angle δ behind an oblique shock given in Eq. 6.4. At the shock surface on the leading edge, the direction of the flow just behind the shock is given by Eq. 6.5.

$$\tan\delta = 2\cot\theta_s\left[\frac{M_{n1}^2 - 1}{M_\infty^2(\gamma + \cos 2\theta_s) + 2}\right] \tag{6.4}$$

$$\begin{aligned} \beta &= \theta_s - \delta \\ V_r^{'} &= V^{'}\cos\beta \\ V_\theta^{'} &= V^{'}\sin\beta \end{aligned} \tag{6.5}$$

$V^{'}$ is a non-dimensional velocity calculated from local Mach number M using Eq. 6.6. V_{max} is defined in Eq. 6.7.

$$
\begin{aligned}
V^{'} &= V/V_{max} \\
&= \frac{(V_r^2 + V_\theta^2)^{1/2}}{V_{max}} \\
&= (V_r^{'2} + V_\theta^{'2})^{1/2} \\
&= \left[\frac{2}{(\gamma-1)M^2} + 1\right]^{-1/2}
\end{aligned}
\tag{6.6}
$$

$$
\begin{aligned}
V_{max} &= \sqrt{2h_t} \\
&= [2c_pT_\infty + V_\infty^2]^{1/2}
\end{aligned}
\tag{6.7}
$$

And Mach number immediately after the shock is given by the oblique shock relation reproduced in Eq. 6.8:

$$
\begin{aligned}
M_{n1} &= M_\infty \sin\theta_s \\
M_{n2} &= \left[\frac{M_{n1}^2 + 2/(\gamma-1)}{[2\gamma/(\gamma-1)]M_{n1}^2 - 1}\right]^{1/2}
\end{aligned}
\tag{6.8}
$$

A numerical step length Δs is specified and the new position along the streamline is determined by a step along the calculated $V^{'}$ direction. The value of Δs is used to determine an equivalent step in θ, $\Delta\theta$. The values of $V_r^{'}$, $V_\theta^{'}$ and θ at this location are used in the next integration step of the T-M equations along with $\Delta\theta$. A fourth order Runge-Kutta integration scheme has been used to evaluate the next $V_r^{'}$ and $V_\theta^{'}$ values.

To calculate the lift, drag and pitching moment at cruise conditions, the pressure along the streamlines which define the lower surface are also calculated. The upper surface is a freestream surface and freestream static pressure conditions (p_∞) are assumed [95]. To calculate the pressure along the streamlines, the Mach number at each point is determined by inverting Eq. 6.6 to give Eq. 6.9.

$$M = \left[\frac{2}{\gamma - 1} \left(\frac{V'^2}{1 - V'^2} \right) \right]^{1/2} \tag{6.9}$$

This local Mach number M is used to determine the pressure using Eq. 6.10 where P_{t2}/P_∞ is given by Eq. 6.11 for M_2 and M_{n1} are given by Eq. 6.11 and Eq. 6.12 respectively.

$$\frac{P}{P_\infty} = \frac{P_{t2}}{P_\infty} \left(1 + \frac{\gamma - 1}{2} M^2 \right)^{-\gamma/(\gamma-1)} \tag{6.10}$$

$$\frac{P_{t2}}{P_\infty} = \left(1 + \frac{\gamma - 1}{2} M_2^2 \right)^{\gamma/(\gamma-1)} \left[1 + \frac{2\gamma}{\gamma + 1} (M_{n1}^2 - 1) \right] \tag{6.11}$$

$$M_2 = \frac{M_{n2}}{\sin(\theta_s - \delta)} \tag{6.12}$$

The pressure along the streamlines is integrated over the area of the bottom surface by dividing the bottom surface into a fine grid and using linear interpolation between the pressure values along streamlines to determine the pressure at each grid point. The resulting forces are split into lift and drag components based on the local angle of the surface grid element to the freestream. The moment is determined the grid element normal force multiplied by the x axis distance to the centre of gravity from each surface grid element.

One drawback that has been found when implementing this method is that the specification of shock angle based on the desired body length can lead to a large number of failed shapes. The waverider method relies on the initial flow after an oblique shock, which for a given Mach number has a minimum shock angle for a solution to exist [157]. The result is a highly discontinuous objective function output which a more efficient gradient based optimisation will not be suitable for. For this reason, the more computationally intensive evolutionary algorithm approach has been taken using the NSGA-II algorithm outlined in Section 6.4.

6.3 Low Speed Numerical Method

The second objective of the optimisation routine pertains to aerodynamic performance at the cruise condition and can be determined as part of the waverider generation process as described. The first objective is the pitch stiffness in the landing phase at low speeds (80m/s). To calculate this, a method is required which can determine the lift and moment curves of the waverider shape at landing speeds. The lift curve slope is necessary to determine the AoA at which the vehicle provides the required trim lift. The moment at this AoA and the adjacent AoA is then used to determine the gradient, C_{m_α}, which is the first optimisation objective. To calculate this within an optimisation loop, the calculation must be computationally efficient. The Hexafly-Int EFTV analysis conducted in Chapter 3 used high fidelity CFD methods which showed good agreement with the experimental results in Chapters 4 and 5. Each of these simulations took around 40 hours to complete on 48 CPUs. A quicker method will be needed for use in the optimisation loop.

The Athena Vortex Lattice (AVL) VLM software written by Drela and Youngren [156] has been used for the low speed aerodynamic performance estimates. This code provides a good estimate of the linear lift in attached flow conditions. As the waverider designs are very slender, the vortex lift, which has been a strong influence on the results of the Hexafly EFTV, must be accounted for. This has been done by implementing the Polhamus leading edge suction analogy [158] which provides a good estimate of the lift produced by the vortices shed from the leading edge. The implementation developed by Purvis in reference [159] has been used to determine the vortex lift distribution, which is used to calculate the vortex contribution to pitching moment.

6.3.1 Polhamus Suction Analogy

The Polhamus leading edge suction analogy uses the assumption that the centrifugal force required to maintain an attached flow by bending the airflow around the leading edge of the wing is instead applied by the vortex system to pull the flow down onto the wing surface. The reaction force on the vortex is treated as additional lift in the wing. This is illustrated in Figure 6.2 reproduced from reference [158]. As shown in Figure 6.2(a), the so-called thrust force itself is not dependent on the leading edge radius as the total force required to maintain flow attachment is the same. In a leading edge separated

flow the suction force is related to the thrust force as shown in Figure 6.2(b).

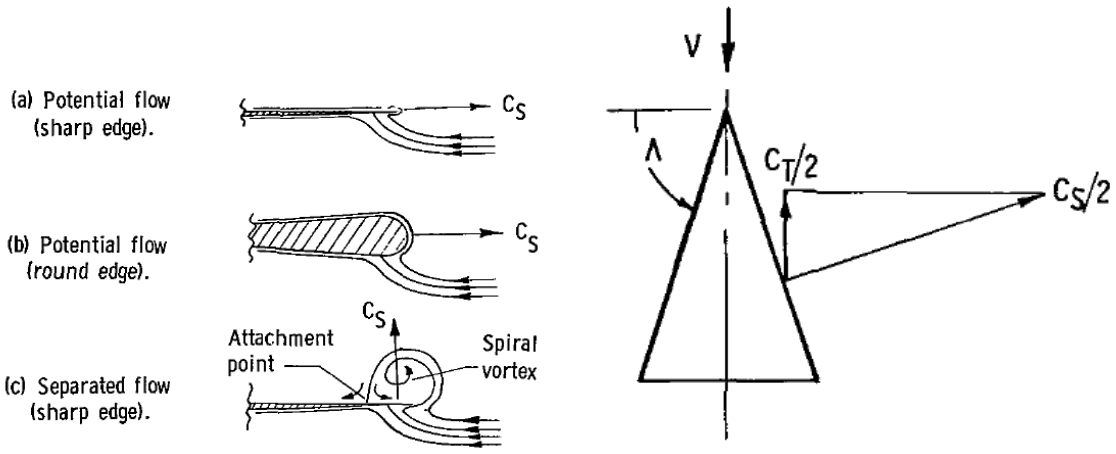

(a) Leading edge suction analogy

(b) Relation between leading edge thrust coefficient and suction coefficient

Figure 6.2: Polhamus leading edge suction analogy [158]

As previously mentioned, the Purvis implementation of the Polhamus vortex analogy has been used in the optimisation loop. The linear lift and drag coefficients are calculated in strips (cc_l and cc_d) along the span by AVL. The coefficient of suction at each strip (cc_s) is then calculated by Eq. 6.13 for span (b), proportionality constant $E_0 = \pi 1.106/b$ [159], AoA (α), non-dimensional spanwise coordinate $\eta = y/b$, and local sweep angle Λ.

$$cc_s = \frac{bE_0}{2cos(\Lambda)} \sum_{\eta=0}^{\eta} (cc_l \sin(\alpha) - cc_d \cos(\alpha)) \Delta\eta_0 \tag{6.13}$$

This is then integrated over the span to determine the total suction coefficient C_S (Eq. 6.14

$$C_S = \frac{2}{S_{ref}} \sum_{y=0}^{b/2} cc_s \Delta y \tag{6.14}$$

The vortex lift ($C_{L_{VLE}}$) is then determined by Eq. 6.15.

$$C_{L_{VLE}} = C_S \cos(\alpha) \tag{6.15}$$

This is added to the lift coefficient calculated from AVL to give the total lift, $C_{L_{tot}} = C_{L_{AVL}} + C_{L_{VLE}}$. The component of coefficient of pitching moment due to the leading edge vortices ($C_{m_{VLE}}$) is given by Eq. 6.16 for centre of gravity x coordinate X_{ref}, local leading edge x position X_{LE} and reference length L_{ref}.

$$C_{m_{VLE}} = \frac{-2}{S_{ref} L_{ref}} \sum_{y=0}^{b/2} cc_s (X_{LE} - X_{ref}) \Delta y \tag{6.16}$$

Total moment coefficient is then calculated by adding the moment coefficient from AVL, $C_{m_{tot}} = C_{m_{AVL}} + C_{m_{VLE}}$.

6.3.2 Validation

This method was validated against wind tunnel data for delta wings of aspect ratio 0.5 and 1.0 found in reference [160]. The results of the validation are shown in Figure 6.3. The lift coefficient results show very good correlation between the VLM method with Purvis implementation of the Polhamus correction while the moment coefficient shows good correlation for the wing with aspect ratio 0.5, but not as good for aspect ratio 1.0. As expected the correlation is better in the region from 0 to 20 degrees AoA as the method does not account for more complex phenomena such as vortex breakdown [71]. As the Hexafly-Int EFTV has an aspect ratio of 0.6, the waverider shapes that will be tested will have an aspect ratio closer to 0.5. This gives us good confidence that the low fidelity method chosen for the optimisation loop will yield physically reasonable results.

The AVL code used to provide the non-vortex components of lift and drag does not account for thickness of the vehicle. The panels for the AVL calculations are determined from an average of the upper surface and lower surface panels. The curvature of each spanwise section of the vehicle is accounted for in the AVL run file. Although the delta wings that are compared in Figure 6.3 show good correlation with wind tunnel tests, the

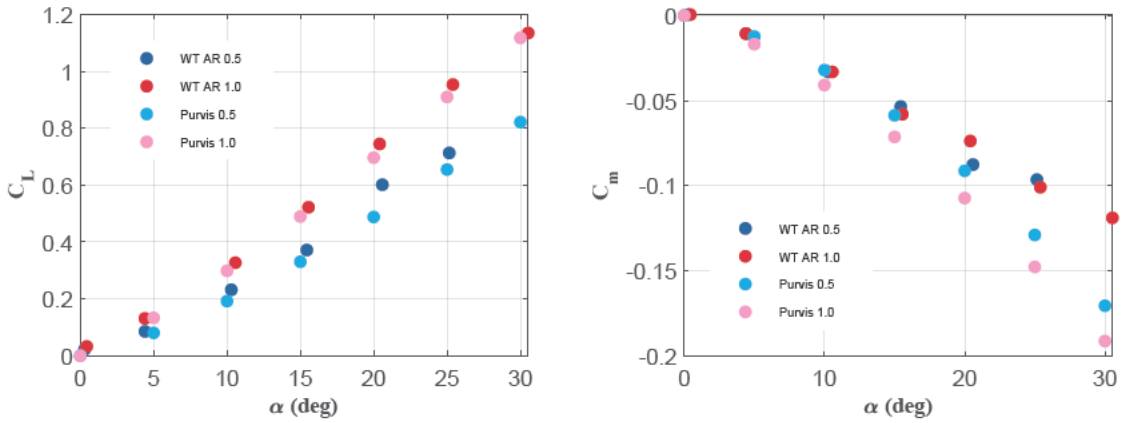

(a) Lift Coefficient Validation

(b) Moment Coefficient Validation

Figure 6.3: Validation of VLM with Purvis Correction for delta wings of aspect ratio 0.5 and 1.0

predictions for waverider shapes are expected to deviate more from the true aerodynamic performance at low speeds due to the unmodelled effects of thickness.

6.4 NSGA-II Algorithm

The optimisation algorithm used here is the NSGA-II (Nondominated Sorting Genetic Algorithm) developed by Deb et al [161]. It is a type of multi-objective evolutionary algorithm that is widely used for its excellent performance and well-distributed Pareto front. The method begins with a random spread of possible solutions distributed within the limits of the user defined parameter space. Each solution is evaluated by some cost function, in this case the waverider is generated and its cruise lift to drag and the low speed pitch stiffness are calculated. A cost is defined for each of these objectives which the goal is to minimise. The costs for each objective are also scaled so that their orders of magnitude are roughly equal. Once cost is determined the solutions are ranked to determine which will be used to form the next generation of test points within the parameter space.

The main ranking operators of the algorithm are the nondominated sorting process and the crowding distance calculation. These ensure that the algorithm progresses the solutions towards a Pareto-optimal front with a diverse spread. One solution dominates another if it represents an improvement in one of more objectives without deterioration in the remaining objectives. In NSGA-II the non-dominated sorting of solutions is achieved

by arranging them into fronts using a fast algorithm described in reference [161]. For each solution the number of solutions which dominate it (n_p) and the set of solutions which it dominates (S_p) are determined. The first non-dominated front is defined as all the solutions which have $n_p = 0$. The second front is determined by testing each of the sets S_p for every member of the first front. If the n_p value for any of these members is 1, then it is sorted into a new set which becomes the second front. This process continues to define all fronts and each solution is assigned an integer rank depending on which front it belongs to.

An estimation of the spread of solutions is obtained by analysing each solution within a front and defining a cuboid (box for 2 objectives, cube for 3 and so on) around it using its neighbours on each side along each objective within the same front as opposing vertices. The average side length of the resulting cuboid is used as the crowding distance. The selection of neighbouring points is achieved by sorting every solution along every objective. The solutions at the extremes of any objective are assigned an infinite crowding distance.

With all solutions assigned to fronts, and assigned a crowding distance, a comparison operator ranks them according to their front, and within fronts according to their crowding distance. A solution with a higher crowding distance outranks a solution of the same front with a lower crowding distance. This promotes a good spread of solutions along the front.

As stated, the algorithm begins with a random spread of possible solutions referred to by Deb et al as P_0 of size N, the user defined population size. This initial parent population is evaluated by the cost function (aerodynamic analysis tools) and then sorted into nondominated fronts, with the $n_p = 0$ front assigned rank 1, and the next rank 2 and so on. Processes of cross-over (where parameters from multiple parent solutions are mixed), and mutation (where parent parameters are randomly perturbed) are used to generate a child population Q_0. The parent and child populations are combined into set, R_0 of size $2N$ and the sorting and crowding functions are applied to select the best N solutions to form the next parent generation P_1. This is shown schematically in Figure 6.4 reproduced from reference [161]. Each subsequent step proceeds in the same fashion. If the population size at the ranking stage is less than N, all members of R become the next parent generation. If the population size of R is greater than N then each front

starting with rank 1 is passed through till the front which pushes the number over N is reached. This front is then split according to crowding distance.

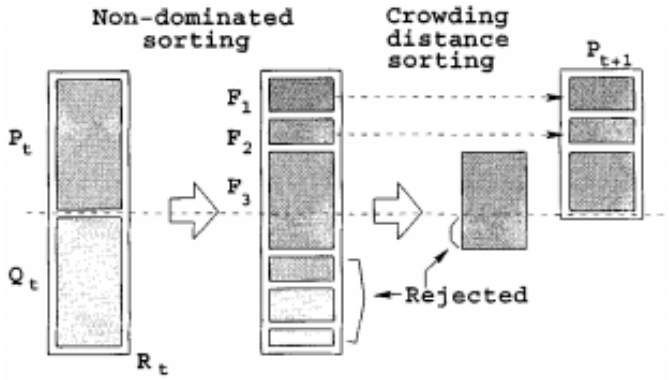

Figure 6.4: NSGA II sorting procedure [161]

The resulting algorithm will progress the solution towards a Pareto-optimal (optimal series of solutions which cannot be dominated) front where this convergence can be assessed by the magnitude of population changes between generations. The extremes of the resulting Pareto-optimal front within the objective space represent solutions which optimise on one objective more than the others, but optimise on the others to as great an extent as possible. The solutions that sit in the middle of the front represent compromise solutions. The overall flow of the optimisation routine is shown in Figure 6.5.

The Matlab implementation of the NSGA-II available at reference [162] has been used in this work with some minor modifications.

6.5 Optimisation Results

The optimisation algorithm has been run for three different wing span waveriders. The smallest is the same as the Hexafly wingspan, $b = 1.23$m. Spans of $b = 1.6$m and $b = 2.0$m have also been run to determine the effect of span on the resulting shapes. The two relations for maximum lift to drag at high Mach numbers given in Chapter 2, Kuchemann's Eq. 2.1 and Bowcutt's Eq. 2.2, are used for reference. Kuchemann's relation [91] predicts a maximum lift to drag ratio of 5.7 for a Mach number of 7.2 for non waverider type hypersonic vehicles. Bowcutt's relation [95] suggests a maximum lift to drag ratio of 7.7 for the viscous optimised class of waveriders which he developed at Mach 7.2. The C_{m_α} have all been calculated for a reference location of $x = 1.8$m

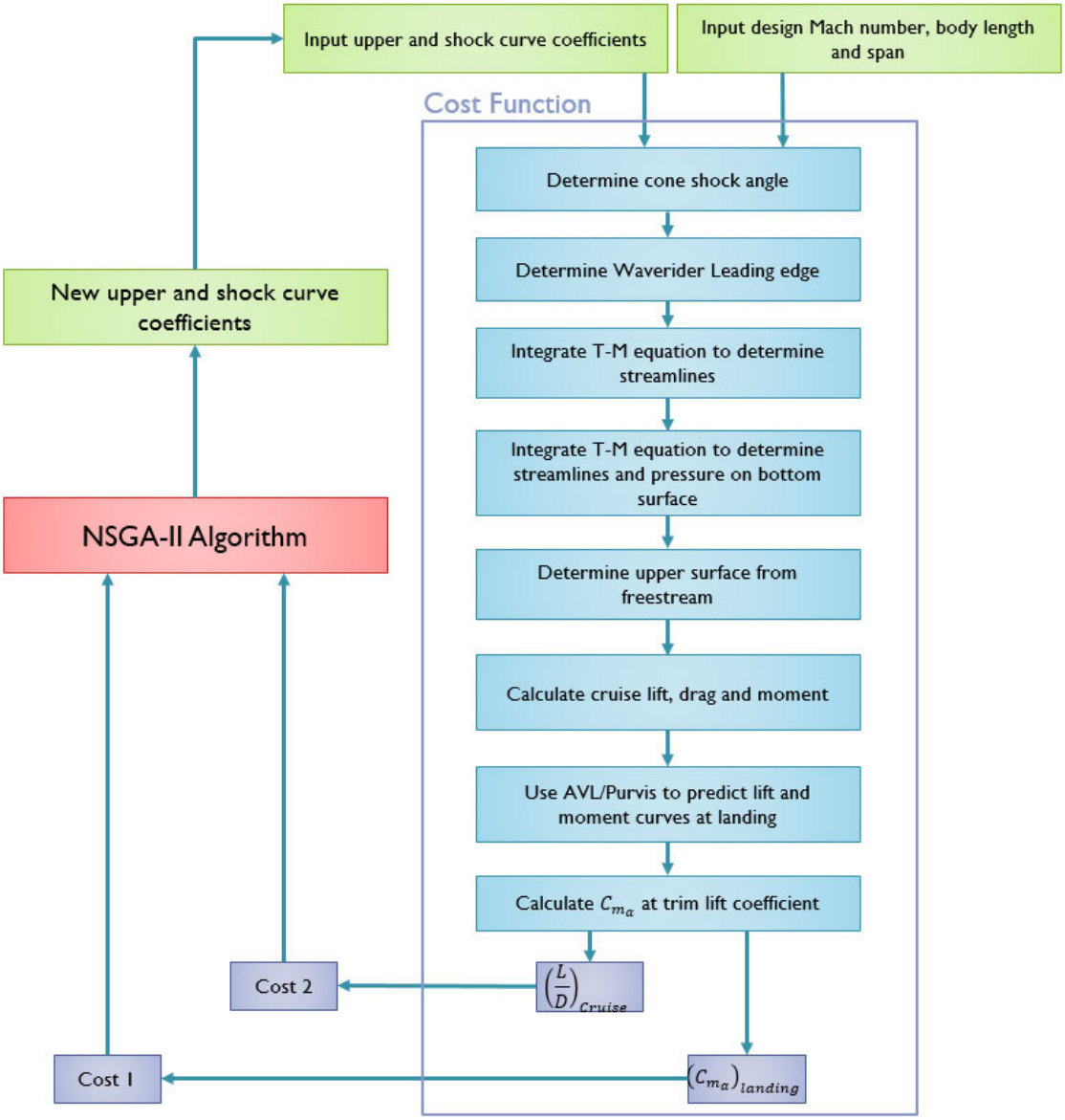

Figure 6.5: Waverider optimisation routine

$(x/L_{ref} = 0.6)$ from the leading edge tip of the waverider.

First we determine if the optimisation run has achieved convergence to the Pareto-optimal front by examining the non-dominated solutions at differing optimisation loop iteration numbers (generations). If the changes between generations become small between iterations then the algorithm is considered to have converged to the most optimal solution it can obtain. These fronts are shown in Figure 6.6 for all three spans plotted over the two objectives, C_{m_α} at low speed and cruise lift to drag ratio. For a span of 2.0m there is little change in the non-dominated solutions between 150 and 201 generations the optimisation routine is considered converged. This occurs between 196 and 228, and

199 and 215 for spans of 1.6m and 1.23m respectively.

The evolution of the non-dominated fronts for each span show significant differences. For a span of 2.0m the fronts shown in Figure 6.6(c) are smooth and continuous suggesting a gradual change in waverider shapes from the high lift to drag ratio, low pitch stiffness at the top right to the high pitch stiffness low lift to drag ratio at the bottom left. The non-dominated fronts show some discontinuity for a span of 1.6m with a sharp change in slope shown in Figure 6.6(b). This suggests that at least two distinct shapes have been found.

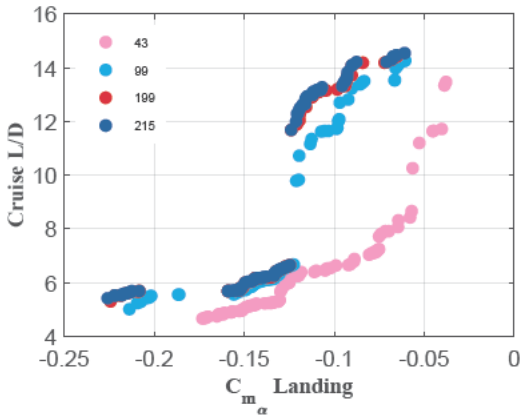

(a) Non-dominated fronts at 43rd, 99th, 199th and 215th generations, $b = 1.23$m

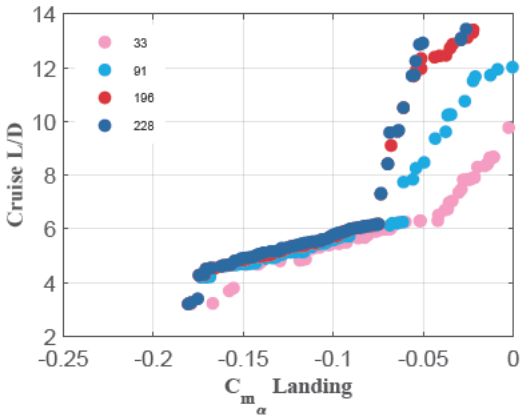

(b) Non-dominated fronts at 33rd, 91st, 196th and 228th generations, $b = 1.6$m

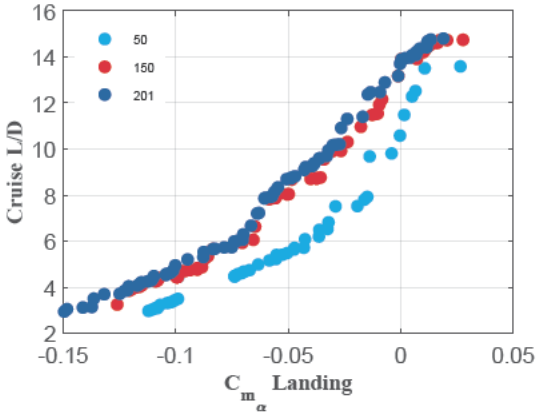

(c) Non-dominated fronts at 50th, 150th and 201st generations, $b = 2.0$m

Figure 6.6: Evolution of non-dominated fronts with generation for each span

The distinct waverider shapes of the non-dominated solutions for spans of 1.6m and 2.0m are shown in Figures 6.7 and 6.8. The range of shapes found for a span of 1.6m are very similar to those found for 1.23m. The high aerodynamic efficiency shape, waverider 1

on Figure 6.7 is very similar to the shape shown in Figure 6.10. Waverider 3 shows the largest departure from the solutions of 1.23m span with a fully positive dihedral wing shape. This suggests that the larger span has pushed the extent of this particular type of waverider shape in the objective space.

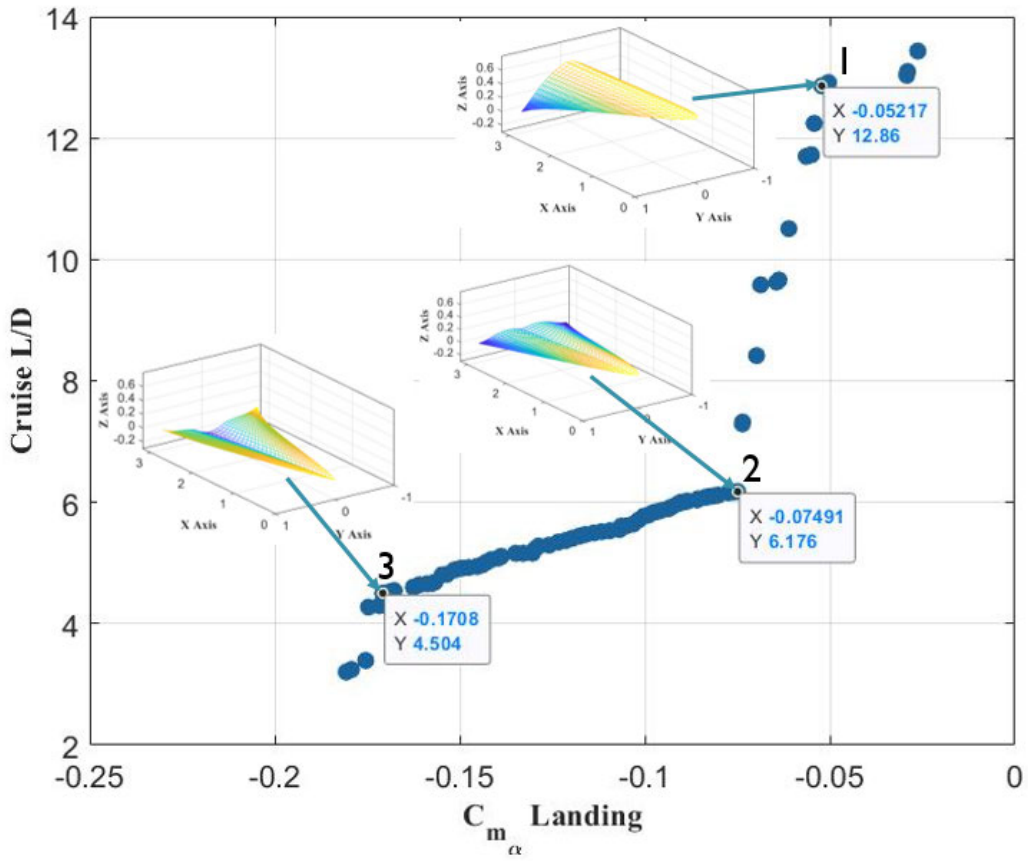

Figure 6.7: Distinct waverider shapes over the non-dominated front, span=1.6m

The optimal shapes found for a span of 2.0m show the smooth variation of a single waverider types that was expected from the shape of the Pareto front. The increased span has resulted in a series of solutions similar to the waverider shown in Figure 6.10. The increased span has allowed this shape to take on unrealistic proportions, especially that of waverider 4. The sharp tips which cause an increase in wave drag at cruise speeds shift the centre of pressure to the rear which increases the static margin. While it is clear that the optimal front is dominated by one type of waverider, again it is likely that the inclusion of viscous effects and volumetric efficiency could yield a wider variety of shapes which are currently dominated in the optimisation process.

For a span of 1.23m the non-dominated front shown in Figure 6.6(a) is highly discon-

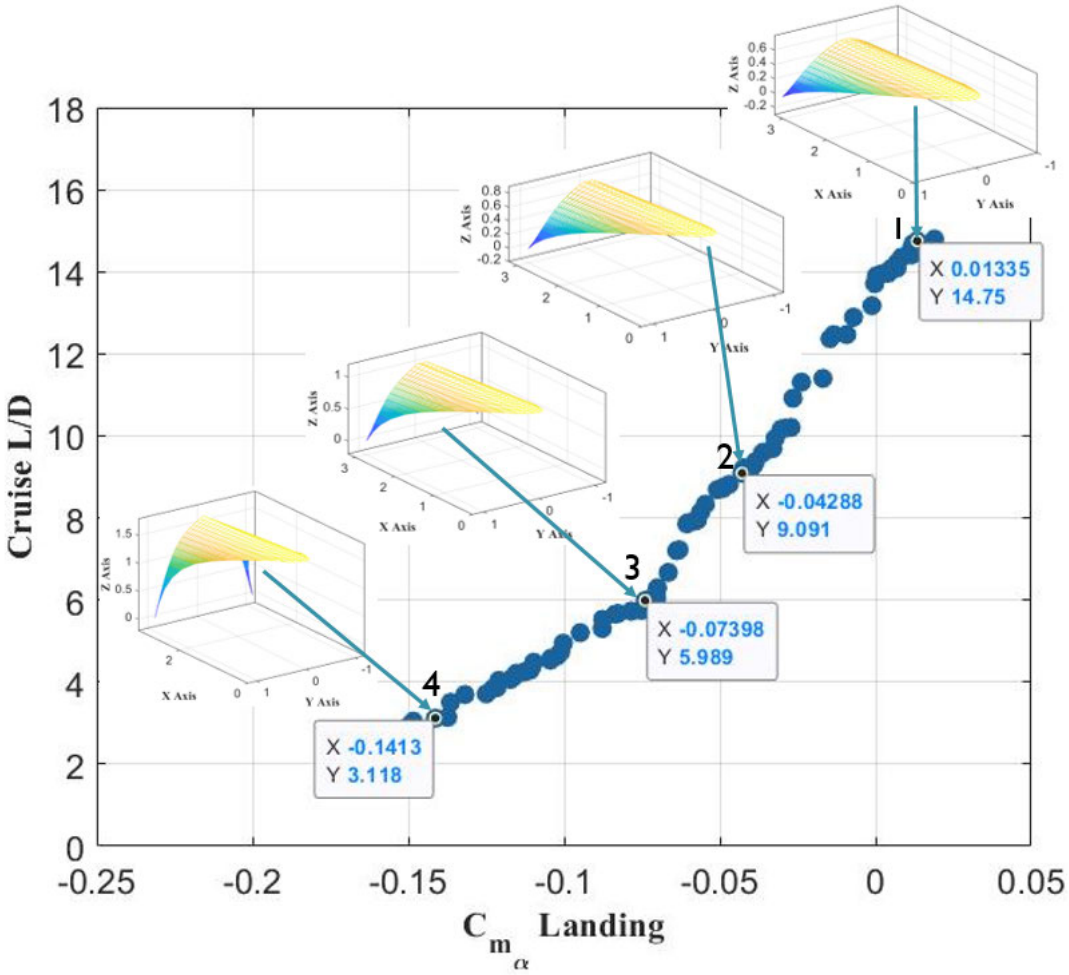

Figure 6.8: Distinct waverider shapes over the non-dominated front, span=2.0m

tinuous with distinct groupings and large gaps between them. This is likely due to the large number of potential shapes at this small span to length ratio which do not sufficiently deflect the flow for the oblique shock relations to yield a solution. The result is the distinct groupings which suggest isolated successful shapes over the objective space. Indicative shapes for each grouping of solutions have been shown in Figure 6.9. As the low speed analysis using AVL and the Purvis method is conducted on the average surface between the top and bottom of each waverider (thickness is not modelled) this averaged surface is the one which is shown on Figure 6.9.

The waverider shapes show two very distinct designs. The ones which exhibit the highest cruise lift to drag ratio show a large anhedral droop whereas the shapes with high low speed pitch stiffness show a much flatter profile with a dihedral upward turn at the wing tips. It can be inferred that the large anhedral droop has been found by the

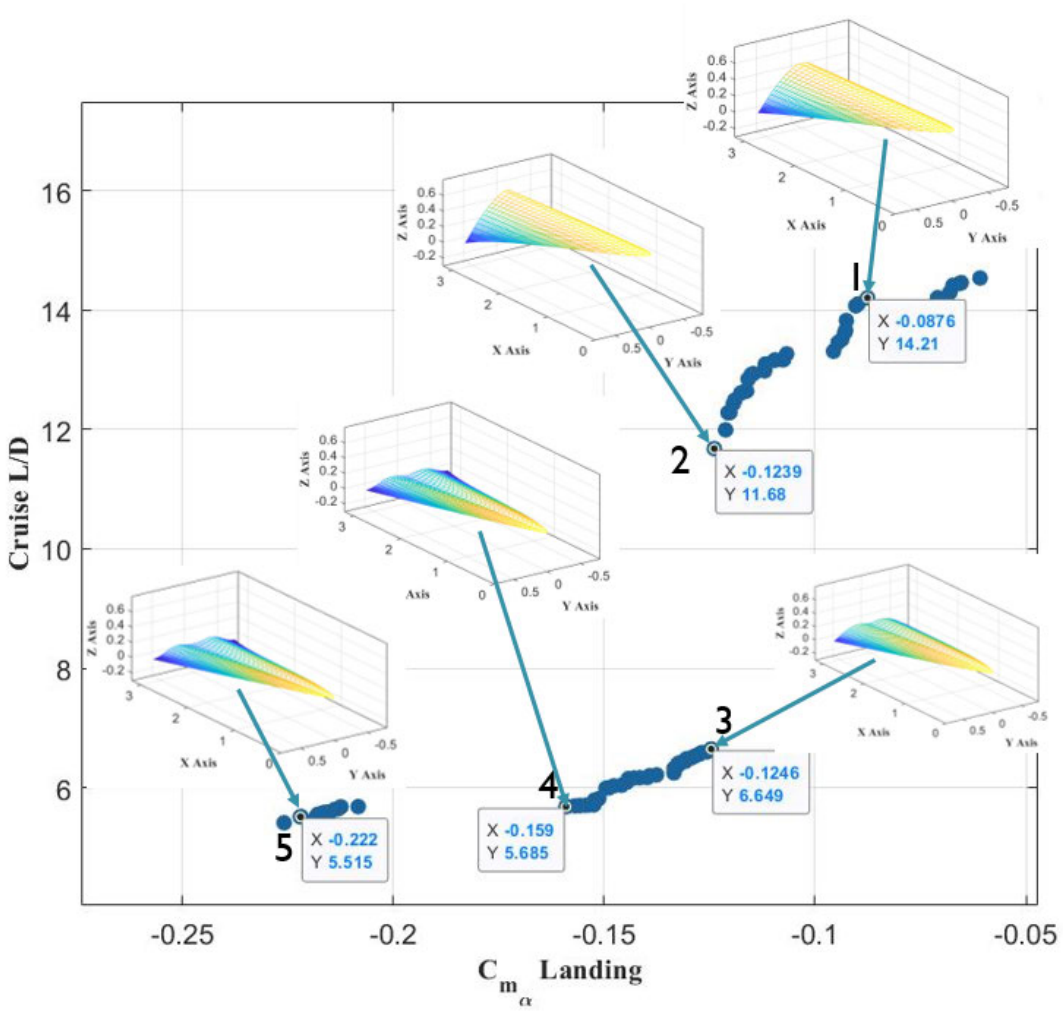

Figure 6.9: Distinct waverider shapes over the non-dominated front, span=1.23m

optimiser to allow a greater surface area at cruise conditions for obtaining lift. The analysis based on the osculating cones waverider method treats the upper surface as a freestream surface and the bottom as a high pressure surface behind the leading edge shock. As viscous effects are not modelled, there is no penalty in additional drag for increasing the high pressure surface area. It is likely that the anhedral droop would not be as highly pronounced if the viscous effects at cruise were calculated. This impacts both the top and bottom surface drag resulting in a large increase in drag for increased surface area. Although the lift still increases with increased area, the lift to drag ratio will decrease. This matches the trends observed in the optimised waverider shapes which Bowcutt found which did not show as large a anhedral droop. It is expected that the inclusion of the viscous effects will reduce the best lift to drag ratio designs to the 7.7 predicted by Bowcutt and will result in a number of solutions which were dominated

during the optimisation becoming optimal solutions.

The high pitch stiffness at low speed solutions appear to be pushing the centre of pressure as far to the rear as possible which results in a larger static margin and larger C_{m_α}. This is shown by the higher leading edge sweep at the front of the waverider shape than at the rear. The waverider shapes in Figure 6.9 are labelled with a number. The two most distinctly different shapes are numbers 1 and 5. Multiple views of these two waveriders are shown in Figures 6.10 to 6.11.

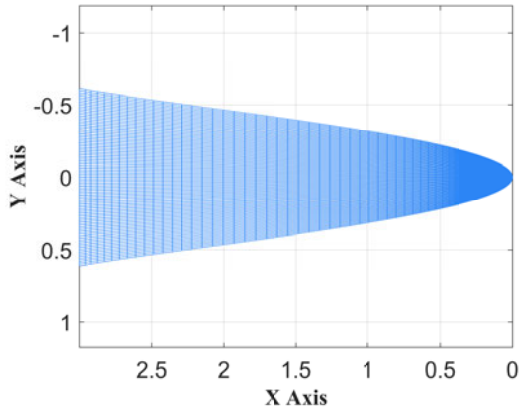

(a) Top view

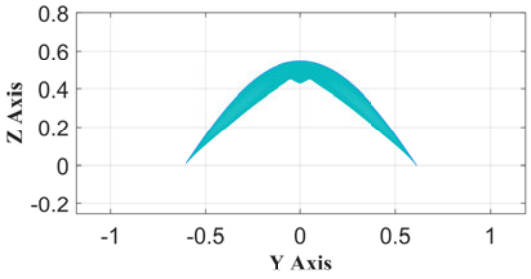

(b) Front View

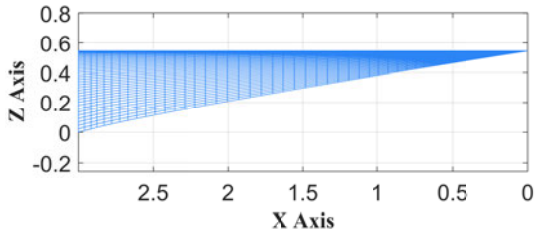

(c) Side View

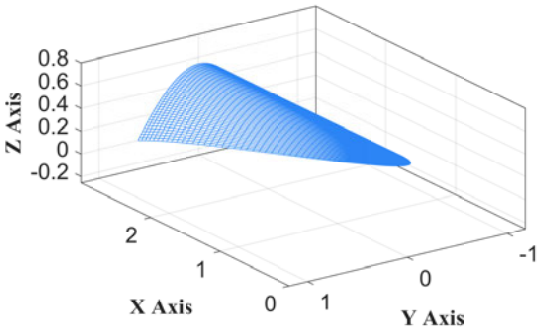

(d) Isometric View

Figure 6.10: Span = 1.23m Waverider 1 multiple views

In addition to the large anhedral droop of the waverider shown in Figure 6.10, there is very little useable volume in the design which renders it impractical. The fifth configuration shown in Figure 6.11 shows more potential for creating a practical waverider shape. This suggests that the optimisation could be improved by not only including viscous effects but also including volumetric efficiency to the objective function. The current

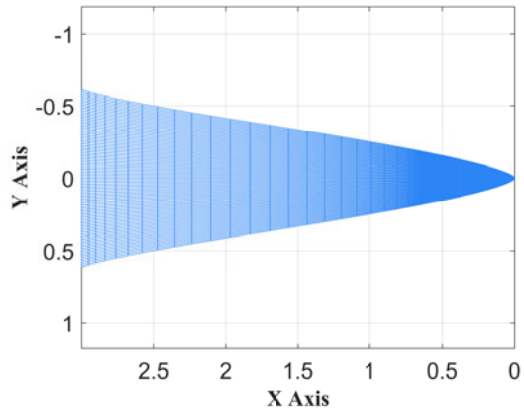

(a) Top view

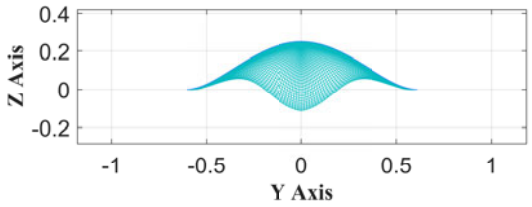

(b) Front View

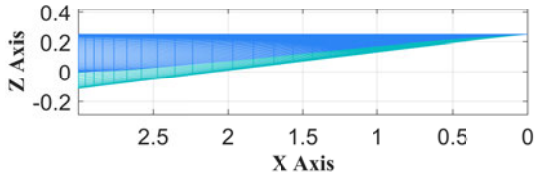

(c) Side View

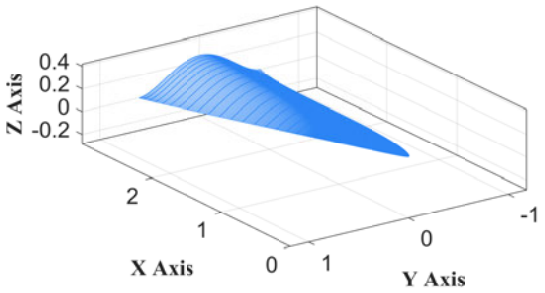

(d) Isometric View

Figure 6.11: Span = 1.23m Waverider 1 multiple views

routine appears to present a trade-off between high cruise aerodynamic efficiency and low speed pitch stiffness as two distinctly different shapes. However if these additional considerations of useable volume and viscous drag are accounted for, the gap between the shapes optimised for low speed stability and high speed performance will likely be smaller.

The Hexafly-Int Vehicle with the same span as these waveriders required a forward shift of 0.3m to obtain static pitch stability at low speed. Waverider 5 from the 1.23m span optimisation can have a rearward shift of 0.4m to suffer marginal stability ($C_{m_\alpha} = 0$) in the low speed condition. One of the most difficult problems of hypersonic waverider design identified by Keating and Mayne [73] was the rearward location of the centre of pressure at design speed. The centre of pressure at low speeds is further forward for typical slender wing designs and this presents a dilemma for selecting the appropriate

centre of gravity location to provide stability and performance over a wide operating range. The results for waverider 5 show promise for overcoming this by generating a waverider with a rearward centre of pressure at low speeds that can still provide good performance at high speed with the same centre of gravity location.

6.6 Conclusions

The optimisation routine that has been presented was able to efficiently obtain a series of waverider shapes at differing spans which accounted for both high speed aerodynamic performance and low speed stability. A clear trade-off between these two objectives has been observed however the large gap between between the optimal solutions on either end of the front would likely be reduced by the incorporation of viscous effects into the high speed performance calculations. In addition the inclusion of volumetric efficiency could also limit the dominance of impractical shapes and allow the optimisation routine to produce a wider variety of more useable waverider designs as done by Bowcutt [95]. The solutions which optimise for low speed stability show some promise for producing practical waverider shapes. The flatter shapes are closer to those designed by Bowcutt and Corda [97] and Eggers et al [112]. The results for the waveriders optimised primarily for low speed stability showed great promise for producing a design with a centre of gravity that can provide stability at low speed and low trim drag at the design speed.

Chapter 7

Conclusions and Further Work

The work presented here has characterised the low speed stability and handling of an innovative hypersonic vehicle design. A review of the literature on hypersonics has found that the low speed aerodynamics and, in particular, the low speed aerodynamic stability derivatives are often not studied in the process of designing or analysing hypersonic aircraft. While the challenges of hypersonic flight are significant, the low speed stability and handling must be considered to produce a civilian transport aircraft capable of hypersonic cruise. As FAA regulations require that civilian transport designs be statically stable, it is important for the practical implementation of a hypersonic cruise vehicle design to determine and include low speed stability as part of the design process. One of the goals of this research is to take steps towards understanding the stability issues encountered by typical hypersonic cruise aircraft designs and to validate the use of computational methods to evaluate dynamic damping characteristics for this class of aircraft. This will allow the use of these tools in the design process of hypersonic cruise vehicles in order to incorporate low speed stability considerations alongside the cruise performance. Finally, the incorporation of these considerations into the base design of waveriders is also considered to see what gains in low speed stability can be made from the outset of the design process and what the trade-offs with high speed performance are.

7.1 Completed Research Goals

The longitudinal low speed aerodynamics of a hypersonic vehicle design, the Hexafly-Int EFTV, have been studied using computational fluid dynamics and wind tunnel testing. The wind tunnel test data has been used to validate the computational methods for use on other hypersonic waverider based designs. Both static and dynamic testing has been conducted as the dynamic stability derivatives such as the pitch damping C_{m_q} have a significant influence on the handling qualities of the vehicle. There are definitive guidelines presented in flight vehicle standards such as MIL-F-8785C which provide objective measures of vehicle handling which can be assessed if the dynamic and static stability derivatives are known. These standards have been applied to the Hexafly-Int EFTV to understand the stability and handling limitations which a manned variant of the design, or other similar waverider type designs may face. This is the first time these landing/take-off phase, handling characteristic standards have been applied to a hypersonic vehicle design.

The data obtained from this study has provided a picture of the stability issues which waverider based hypersonic designs face. In particular this is the first study to experimentally obtain the dynamic pitch stability derivatives for a hypersonic vehicle. The Hexafly-Int EFTV is typical of waverider based shapes which are good candidates for high aerodynamic efficiency long range hypersonic flight. The defining characteristics of the vehicle, low span to length ratio and anhedral wing droop, are typical of these high cruise lift to drag ratio designs and present a departure from typical well-studied slender delta wing designs. Therefore the longitudinal stability characteristics of the Hexafly-Int EFTV expand our understanding of the issues which such designs encounter. The following research outcomes have been obtained.

- High fidelity computational fluid dynamics simulations of the Hexafly-Int EFTV under static conditions have been conducted that show good agreement with experimental data from wind tunnel static testing. The CFD results have also been used to visualise and understand the flowfield phenomena governing the aerodynamic forces and moments.

- Dynamic CFD simulations were conducted on a hypersonic type vehicle which were validated against experimental data. The vortex dynamics under oscillating motion

of this slender vehicle design were modelled accurately enough to provide good pitch damping information that was verified by matching dynamic wind tunnel test results.

- The building of a complex wind tunnel model using relatively low cost additive manufacturing methods that obtained relatively accurate static testing results and enables us to assess pitch instability issues for the Hexafly Vehicle. The lateral static derivatives were also obtained and lateral static stability was shown to be adequate over the normal AoA range.

- The use of a novel highly capable data acquisition system, UAVMainframe, to perform dynamic testing of the Hexafly Model. The model required detailed CAD designs and complex assembly to produce a wind tunnel test article capable of 'flying' test manoeuvres in the wind tunnel to obtain dynamic pitch data. This data has been used to examine the handling qualities of the Hexafly vehicle and deficiencies have been found in the damping, in addition to the static pitch instability at the design centre of gravity. This is the first time such dynamic wind tunnel testing has been conducted on a hypersonic vehicle and this data provides a validation case for the use of CFD on this class of vehicle in the terminal flight phase.

- A waverider design optimisation routine has been developed which accounts for both high speed aerodynamic performance and low speed aerodynamic stability and trim requirements. The resulting shapes highlight the gap between vehicles designs optimised for high speed performance and those designed for low speed stability.

It should be noted that, traditionally, wind tunnel testing has been viewed as a higher cost testing method over computational tools. During the course of this work the use of simple additive manufacturing techniques in the form of 3D printing allowed the construction of a complex model to be accomplished in a relatively short timeframe and for low cost. No hours of skilled labour in a workshop were required. Parts from a detailed CAD model were produced with minimal failed parts and tolerances which were sufficient to provide good data. The computational methods, on the other hand, required access to a highly capable computing cluster, and a large amount of hours of computing

time. The comparative cost of the 3D printing to the computing infrastructure suggests that, at least for static testing, if a wind tunnel is available, the cost of the production of models has reduced to the degree that wind tunnel testing may be the cheaper option.

7.2 Future Work

A number of areas of potential research have been identified during the course of this research as well as enhancements to the methods used here.

7.2.1 Computational Research

Simulations of the full model should be conducted under sideslip conditions to determine the lateral static coefficients for comparison with the static wind tunnel test lateral results. This thesis validated the ability of the dynamic CFD techniques to obtain good quality damping characteristics data for slender vehicles under separated flow conditions. If the static CFD lateral results match the wind tunnel results then the same dynamic techniques used to obtain pitch damping data can be used to obtain lateral dynamic damping data with a high degree of confidence.

In addition, vertical and lateral plunging motion can be implemented within the ANSYS Fluent CFD software that could independently assess the AoA rate ($C_{m_{\dot{\alpha}}}$) and AoS rate ($C_{n_{\dot{\beta}}}$, $C_{l_{\dot{\beta}}}$) derivatives. This would allow the separation of the damping derivatives into plunge and rotational components which was not possible in the CFD and wind tunnel testing conducted in this thesis. This would allow assessment of the full aircraft handling qualities.

Further work is also warranted on matching the wind tunnel test conditions in the CFD simulations. This includes the wind tunnel walls and the mount which the model is attached to. Where there has been deviation between the CFD results and the wind tunnel test results, it has been difficult to identify exactly where the discrepancy arises. CFD simulations of the wind tunnel mount and walls could clarify this.

More CFD computations of the full scale high Reynolds number case (3.3m vehicle at 80m/s) should be conducted around the 20 degree AoA region to identify if the region of instability which is observed in the smaller Reynolds number CFD is present in the

high Reynolds at all and just shifted or if it does not occur.

7.2.2 Wind Tunnel Experiments

While the work presented here consists of the first dynamic longitudinal wind tunnel tests of a hypersonic vehicle, the lateral dynamic stability must be evaluated in addition to the longitudinal data that was gathered in this thesis. While the static lateral data suggests good stability, the lateral damping characteristics will be important. This is especially true for slender vehicles with low mass moment of inertia about the roll axis which can be subject to inertial coupling [71]. A vehicle like the Hexafly EFTV and similar high lift to drag vehicles with low wing spans tend to have lower roll damping. The impact of this on the dynamic response of the aircraft can be examined by developing a 3 axis gimbal to test a wind tunnel model under longitudinal and lateral motion simultaneously.

A full 3 degree of freedom gimbal would also allow testing of novel flight control algorithms which may be necessary for the non-conventional layouts of hypersonic vehicles. The implementation of an Enhanced Kalman Filter would allow the gimbal and IMU data to be fused to obtain better and smoother data than was available during this thesis.

7.2.3 Waverider Optimisation

The work conducted in this thesis has identified potential waverider shapes which could have good low speed handling qualities and good high speed efficiency. Bowcutt showed the importance of viscosity in properly obtaining waverider shapes optimised for high speed performance [95]. The viscous models employed in that work could also be incorporated into the waverider optimisation routine to obtain shapes with more realistic performance that accounts for the contribution of viscous drag and not just wave drag.

Additional modifications can also be made to analyse more realistic vehicle shapes within the optimisation routine. The changes made by Eggers et al on the WRE 12 to create a more useful hypersonic vehicle shape could also be incorporated [112]. These changes create a vehicle with sharp trailing edges on the outer span of the wings to accommodate control surfaces. These modifications produce a vehicle with more distinct wings and fuselage similar to the Hexafly vehicle. An objective assessing the volumetric efficiency

should also be included to ensure that any resulting vehicle shapes can actually be used for a practical flight mission.

The resulting vehicle shapes should be analysed with high fidelity CFD tests to determine the validity of the low fidelity methods used within the optimisation loop.

THIS PAGE HAS BEEN INTENTIONALLY LEFT BLANK

Bibliography

[1] "X-15 #1 rocket-powered aircraft." `https://www.nasa.gov/centers/dryden/multimedia/imagegallery/X-15/E-5251.html`. Accessed: 2019-06-07.

[2] D. Jenkins, *X-15: Extending the Frontiers of Flight*. NASA, Washington DC, United States, 2007.

[3] D. Jenkins, *Hypersonics Before the Shuttle: A Concise History of the X-15 Research Airplane*. NASA, Washington DC, United States, 2000.

[4] J. E. Love and W. R. Young, "Survey of operation and cost experience of the X-15 airplane as a reusable space vehicle," NASA-TN-D-3732, NASA Flight Research Center, 1966.

[5] D. J. Garringer and E. J. Saltzman, "Summary of full-scale lift and drag characteristics of the X-15 airplane," NASA-TN-D-3343, NASA Flight Research Center, 1966.

[6] Staff of NASA Flight Research Center, "Experience with the X-15 Adaptive Flight Control System," NASA-TN-D-6208, NASA Flight Research Center, 1971.

[7] H. J. Walker and C. H. Wolowicz, "Stability and control derivative characteristics of the X-15 airplane," NASA-TM-X-714, NASA Flight Research Center, 1962.

[8] Staff of NASA Flight Research Center, "Aerodynamic and landing measurements obtained during the first powered flight of the North American X-15 research airplane," NASA-TM-X-269, NASA Flight Research Center, 1960.

[9] C. B. Hargis, "The X-20 (Dyna-Soar) Progress Report," in *NASA. Manned Spacecraft Center Proc. of the 2d Manned Space Flight Meeting*, pp. 17–48, NASA, 1964.

[10] J. S. Lesko, "Dyna-Soar aerodynamic performance," in *NASA. Langley Res. Center Joint Conf. on Lifting Manned Hypervelocity and Reentry Vehicles, part 2*, pp. 85–100, NASA, 1960.

[11] E. J. Saltzman, K. C. Wang, and K. W. Iliff, "Aerodynamic assessment of flight determined subsonic lift and drag characteristics of seven lifting-body and wing-body reentry vehicle configurations," NASA-TP-2002-209032, NASA Dryden Flight Research Centre, 2002.

[12] V. W. Horton, R. C. Eldredge, and R. E. Klein, "Flight determined low-speed lift and drag characteristics of the lightweight M2-F1 lifting body," NASA-TN-D-3021, NASA Flight Research Center, 1965.

[13] H. J. Smith, "Evaluation of the lateral-directional stability and control characteristics of the lightweight M2-F1 lifting body at low speeds," NASA-TN-D-3022, NASA Flight Research Center, 1965.

[14] "Aircraft Fleet 1960s." `https://www.nasa.gov/centers/dryden/multimedia/imagegallery/Fleet-1960s/ECN-1107.html`. Accessed: 2019-06-07.

[15] "HL-10 Lifting Body." `https://www.nasa.gov/centers/dryden/multimedia/imagegallery/HL-10/ECN-1289.html`. Accessed: 2019-06-07.

[16] J. S. Pyle and R. H. Swanson, "Lift and drag characteristics of the M2-F2 lifting body during subsonic gliding flight," NASA-TM-X-1431, NASA Flight Research Center, 1967.

[17] J. S. Pyle, "Lift and drag characteristics of the HL-10 lifting body during subsonic gliding flight," NASA-TN-D-6263, NASA Flight Research Center, 1971.

[18] S. M. Stubbs, "Landing characteristics of a dynamic model of the HL-10 manned lifting entry vehicle," NASA-TN-D-3570, NASA Langley Research Center, 1966.

[19] R. W. Kempel and R. C. Thompson, "Flight-determined aerodynamic stability and control derivatives of the M2-F2 lifting body vehicle at subsonic speeds," NASA-TM-X-2413, NASA Flight Research Center, 1971.

[20] L. G. Ash, "Flight test and wind tunnel performance characteristics of the X-24A

lifting body," FTC-TD-71-8, Air Force Flight Test Center, Edwards Air Force Base, Air Force Systems Command, United States Air Force, 1972.

[21] A. G. Sim, "A correlation between flight-determined derivatives and wind-tunnel data for the X-24B research aircraft," NASA TM 113084, NASA Dryden Flight Research Center, 1997.

[22] J. G. Armstrong, "Flight planning and conduct of the X-24B research aircraft flight test program," AFFTC-TR-76-11, Air Force Flight Test Center, Edwards Air Force Base, Air Force Systems Command, United States Air Force, 1977.

[23] C. J. Nagy and P. W. Kirsten, "Handling qualities and stability derivatives of the X-24B research aircraft," AFFTC-TR-76-8, Air Force Flight Test Center, Edwards Air Force Base, Air Force Systems Command, United States Air Force, 1976.

[24] "X-24A lifting body on the lakebed." `https://www.nasa.gov/centers/dryden/multimedia/imagegallery/X-24/ECN-2006.html`. Accessed: 2019-06-07.

[25] "X-24B lifting body on the lakebed." `https://www.nasa.gov/centers/dryden/multimedia/imagegallery/X-24/ECN-3764.html`. Accessed: 2019-06-07.

[26] R. J. Wilson and B. J. Love, "Evaluation of effects of high altitude turbulence encounters on the XB-70 airplane," NASA-TN-D-6457, NASA Flight Research Centre, 1971.

[27] T. P. Incrocci and J. R. Scoggins, "An investigation of the relationships between mountain wave conditions and clear air turbulence encountered by the XB-70 airplane in the stratosphere," NASA-CR-1878, NASA Flight Research Centre, 1971.

[28] D. J. Maglieri and H. R. Henderson, "Measured sonic boom signatures above and below the XB-70 airplane flying at mach 1.5 and 37000 feet," NASA-CR-2011-217077, NASA Langley Research Center, 2011.

[29] D. T. Berry and B. G. Powers, "Handling qualities of the XB-70 airplane in the landing approach," NASA-TN-D-5676, NASA Flight Research Center, 1970.

[30] T. J. Larson and W. G. Schweikhard, "Verification of takeoff performance predictions for the XB-70 airplane," NASA-TM-X-2215, NASA Flight Research Center, 1971.

[31] J. H. Wykes and R. E. Lawrence, "Estimated performance and stability and control data for correlation with XB-70-1 flight test data," NASA-CR-114335, NASA Ames Research Center, 1971.

[32] "XB-70 in cruise configuration." https://www.nasa.gov/centers/dryden/multimedia/imagegallery/XB-70/EC68-2131.html. Accessed: 2019-06-07.

[33] P. W. Merlin, "Design and development of the Blackbird: Challenges and lessons learned," in *Proceedings of the 47th Aerospace Sciences Meeting and Exhibit*, American Institute of Aeronautics and Astronautics, 2009.

[34] J. Anderson, *Hypersonic and High Temperature Gas Dynamics, Second Edition*. AIAA, Inc., Reston, Virginia, 2006.

[35] B. R. A. Burns, "HOTOL space transport for the twenty-first century," *Proceedings of the Institution of Mechanical Engineers, Part G: Journal of Aerospace Engineering*, vol. 204, no. 2, pp. 101–110, 1990.

[36] C. A. Lindley, "International aerospaceplane efforts," in *Rocket-Based Combined-Cycle (RBCC) Propulsion Technology Workshop*, NASA Lewis Research Center, 1992.

[37] "Reagan's impossible dream: The X-30 National Aerospace Plane." https://thehighfrontier.blog/2016/01/02/reagans-impossible-dream-the-x-30-national-aerospace-plane/. Accessed: 2019-06-07.

[38] "X-30 National Aerospace Plane (NASP)." https://www.globalsecurity.org/military/systems/aircraft/nasp.htm. Accessed: 2019-06-07.

[39] D. E. Koelle, "SANGER II, a hypersonic flight and space transportation system," in *Proceedings of the 16th Congress of the International Council of the Aeronautical Sciences*, American Institute of Aeronautics and Astronautics, 1988.

[40] R. P. Boyden, D. D. Dress, C. H. Fox, J. K. Huffman, and C. I. Cruz, "Subsonic static and dynamic stability characteristics of the test technique demonstrator NASP configuration," in *Proceedings of the 31st Aerospace Sciences Meeting and Exhibit*, American Institute of Aeronautics and Astronautics, 1993.

[41] "Report of the Defense Science Board task force on National Aero-Space Plane (NASP) Program," AD-A274530, Defense Science Board; Washington, DC, United States, 1992.

[42] B. N. Pamadi, G. J. Brauckmann, M. J. Ruth, and H. D. Fuhrmann, "Aerodynamic characteristics, database development and flight simulation of the X-34 vehicle," in *Proceedings of the 38th Aerospace Sciences Meeting and Exhibit*, American Institute of Aeronautics and Astronautics, 2000.

[43] D. C. Freeman, D. E. Reubush, C. R. McClinton, V. L. Rausch, and J. L. Crawford, "The NASA Hyper-X program," NASA/TM-1997-207243, NASA Langley Research Center, 1997.

[44] W. C. Engelund, S. D. Holland, C. E. Cockrell, and R. D. Bittner, "Aerodynamic database development for the Hyper-X airframe integrated scramjet propulsion experiments," in *Proceedings of the 18th Applied Aerodyanmics Conference*, American Institute of Aeronautics and Astronautics, 2000.

[45] R. T. Voland, L. D. Huebner, and C. R. McClinton, "X-43 hypersonic vehicle technology development," in *Proceedings of the 56th International Astronautical Congress*, International Astronautical Federation, 2005.

[46] E. A. Morelli, "Flight-test experiment design for characterizing stability and control of hypersonic vehicles," *Journal of Guidance, Control, and Dynamics*, vol. 32, no. 3, pp. 949–959, 2009.

[47] K. R. Jackson, M. R. Gruber, and T. F. Barhorst, "The HIFiRE Flight 2 experiment: An overview and status update," in *Proceedings of the 45th AIAA/ASME/SAE/ASEE Joint Propulsion Conference & Exhibit*, American Institute of Aeronautics and Astronautics, 2009.

[48] J. M. Schramm, S. Karl, K. Hannemann, and J. Steelant, "Ground testing of the HyShot II Scramjet Configuration in HEG," in *Proceedings of the 15th AIAA International Space Planes and Hypersonic Systems and Technologies Conference*, American Institute of Aeronautics and Astronautics, 2008.

[49] K. Barnstorff, "X-51A makes longest scramjet flight." `https://www.nasa.gov/topics/aeronautics/features/X-51A.html`. Accessed: 2019-06-29.

[50] H. Nakatani, N. Okamura, and S. Honami, "Evaluation of aerodynamic performance of a hypersonic experimental aircraft," in *Proceedings of the 17th AIAA International Space Planes and Hypersonic Systems and Technologies Conference*, American Institute of Aeronautics and Astronautics, 2011.

[51] H. Kobayashi, H. Taguchi, T. Kojima, and T. Sato, "Performance analysis of mach 5 hypersonic turbojet developed in JAXA," in *Proceedings of the 18th AIAA International Space Planes and Hypersonic Systems and Technologies Conference*, American Institute of Aeronautics and Astronautics, 2012.

[52] H. Taguchi, H. Kobayashi, T. Kojima, A. Ueno, S. Imamura, M. Hongoh, and K. Harada, "Research on hypersonic aircraft using pre-cooled turbojet engines," *Acta Astronautica*, vol. 73, pp. 164–172, 2012.

[53] S. Defoort, L. Serre, R. Grenon, J. Varnier, G. Carrier, D. Scherrer, and Narmada, "ZEHST: Environmental challenges for hypersonic passenger transport," in *Proceedings of the 18th AIAA International Space Planes and Hypersonic Systems and Technologies Conference*, American Institute of Aeronautics and Astronautics, 2012.

[54] J. Steelant, "Achievements obtained for sustained hypersonic flight within the LAPCAT project," in *Proceedings of the 15th AIAA International Space Planes and Hypersonic Systems and Technologies Conference*, American Institute of Aeronautics and Astronautics, 2008.

[55] J. Steelant, "Key technologies for hypersonic sustained flight assessed within LAPCAT and ATLLAS projects." `https://www.researchgate.net/publication/260450166_Key_Technologies_for_Hypersonic_Sustained_Flight_Assessed_within_LAPCAT_and_ATLLAS_Projects`. Accessed: 2019-06-29.

[56] J. Steelant, "European activities on high speed vehicles feasibility studies and technological challenges for hypersonic cruisers," in *Proceedings of the 7th European Symposium on Aerothermodynamics*, ESA Communications, 2011.

[57] J. Steelant, R. Varvill, S. Defoort, K. Hannemann, and M. Marini, "Achievements obtained for sustained hypersonic flight within the LAPCAT-II project," in

Proceedings of the 20th AIAA International Space Planes and Hypersonic Systems and Technologies Conference, American Institute of Aeronautics and Astronautics, 2015.

[58] L. Serre and S. Defoort, "LAPCAT II : Towards a mach 8 civil aircraft concept, using advanced Rocket/Dual-mode ramjet propulsion system," in *Proceedings of the 16th AIAA International Space Planes and Hypersonic Systems and Technologies Conference*, American Institute of Aeronautics and Astronautics, 2009.

[59] F. Falempin, M. Bouchez, and V. Perrillat, "LAPCAT 2 - Axisymmetric concept for a mach 8 cruiser preliminary design and performance assessment," in *Proceedings of the 16th AIAA International Space Planes and Hypersonic Systems and Technologies Conference*, American Institute of Aeronautics and Astronautics, 2009.

[60] J. Steelant and T. Langener, "The LAPCAT-MR2 hypersonic cruiser concept," in *Proceedings of the 29th Congress of the International Council of the Aeronautical Sciences*, American Institute of Aeronautics and Astronautics, 2014.

[61] T. Langener, J. Steelant, P. Roncioni, P. Natale, and M. Marini, "Preliminary performance analysis of the LAPCAT-MR2 by means of nose-to-tail computations," in *Proceedings of the 18th AIAA International Space Planes and Hypersonic Systems and Technologies Conference*, American Institute of Aeronautics and Astronautics, 2012.

[62] P. Gruhn and A. Gülhan, "Aerodynamic measurements of an air-breathing hypersonic vehicle at mach 3.5 to 8," *AIAA Journal*, vol. 56, no. 11, pp. 4282–4296, 2018.

[63] J. Steelant, "Achievements obtained on aero-thermal loaded materials for high-speed atmospheric vehicles within ATLLAS," in *Proceedings of the 16th AIAA International Space Planes and Hypersonic Systems and Technologies Conference*, American Institute of Aeronautics and Astronautics, 2009.

[64] J. Steelant, "Achievements obtained within ATLLAS-II on aero-thermal loaded material investigations for high-speed vehicles," in *Proceedings of the 21st AIAA International Space Planes and Hypersonic Systems and Technologies Conference*, American Institute of Aeronautics and Astronautics, 2017.

[65] J. Steelant, "ATLLAS: Aero-thermal loaded material investigations for high-speed vehicles," in *Proceedings of the 15th AIAA International Space Planes and Hypersonic Systems and Technologies Conference*, American Institute of Aeronautics and Astronautics, 2008.

[66] M. Bouchez, C. Davoine, B. Le Naour, and J. J. François, "ATLLAS: Aero-thermal loaded material investigations for high-speed vehicles," in *Proceedings of the 19th AIAA International Space Planes and Hypersonic Systems and Technologies Conference*, American Institute of Aeronautics and Astronautics, 2014.

[67] J. Steelant, T. Langener, F. Di Matteo, K. Hannemann, J. Riehmer, M. Kuhn, C. Dittert, F. Scheuerpflug, W. Jung, M. Marini, G. Pezzella, M. Cicala, and L. Serre, "Conceptual design of the high-speed propelled experimental flight test vehicle HEXAFLY," in *Proceedings of the 20th AIAA International Space Planes and Hypersonic Systems and Technologies Conference*, American Institute of Aeronautics and Astronautics, 2015.

[68] G. Pezzella, M. Marini, B. Reimann, and J. Steelant, "Aerodynamic design analysis of the HEXAFLY-INT hypersonic glider," in *Proceedings of the 20th AIAA International Space Planes and Hypersonic Systems and Technologies Conference*, American Institute of Aeronautics and Astronautics, 2015.

[69] N. Favaloro, A. Rispoli, L. Vecchione, G. Pezzella, V. Carandente, R. Scigliano, M. Cicala, G. Morani, and J. Steelant, "Design analysis of the high-speed experimental flight test vehicle HEXAFLY-International," in *Proceedings of the 20th AIAA International Space Planes and Hypersonic Systems and Technologies Conference*, American Institute of Aeronautics and Astronautics, 2015.

[70] J. S. Bowman Jr and W. D. Grantham, "Low-speed aerodynamic characteristics of a model of a hypersonic research airplane at angles of attack up to 90 ° for a range of reynolds numbers," NASA-TN-D-403, NASA Langley Research Center, 1960.

[71] R. C. Nelson and A. Pelletier, "The unsteady aerodynamics of slender wings and aircraft undergoing large amplitude maneuvers," *Progress in Aerospace Sciences*, vol. 39, pp. 185–248, 2003.

[72] D. C. Freeman Jr and R. S. Jones, "Low-speed static stability and control characteristics of two small-scale, hypersonic cruise configurations," NASA TM X-2021, NASA Langley Research Center, 1970.

[73] R. F. A. Keating and B. L. Mayne, "Low-speed characteristics of waverider wings," CP No. 1118, Ministry of Technology, Aeronautical Research Council, 1970.

[74] C. H. Fox Jr and J. E. Lamar, "Theoretical and experimental longitudinal aerodynamic characteristics of an aspect ratio 0.25 sharp-edge delta wing at subsonic, supersonic, and hypersonic speeds," NASA-TN-D-7651, NASA Langley Research Center, 1974.

[75] J. A. Penland and T. R. Creel Jr, "Low-speed aerodynamic characteristics of a lifting-body hypersonic research aircraft configuration," NASA-TN-D-7851, NASA Langley Research Center, 1975.

[76] E. B. Jackson and C. I. Cruz, "Preliminary subsonic aerodynamic model for simulation studies of the HL-20 lifting body," NASA TM-4302, NASA Langley Research Center, 1992.

[77] B. Spencer Jr, C. H. Fox Jr, and J. K. Huffman, "A study to determine methods of improving the subsonic performance of a proposed Personnel Launch System (PLS) concept," NASA/TM-110201, NASA Langley Research Center, 1995.

[78] G. M. Gatlin, "Low-speed, high-lift aerodynamic characteristics of slender, hypersonic accelerator type configurations," NASA Technical Paper 2945, NASA Langley Research Center, 1989.

[79] D. E. Hahne and P. L. Coe Jr, "The low-speed stability and control of three airbreathing transatmospheric vehicles," in *Proceedings of the 32nd Aerospace Sciences Meeting and Exhibit*, American Institute of Aeronautics and Astronautics, 1994.

[80] R. J. Pegg, D. E. Hahne, and C. E. Cockrell Jr, "Low-speed wind tunnel tests of two waverider configuration models," in *Proceedings of the 6th AIAA International Space Planes and Hypersonic Systems and Technologies Conference*, American Institute of Aeronautics and Astronautics, 1995.

[81] C. Lewis, C. Cox, R. Saeks, R. Pap, E. Wagner, and P. Hagseth, "Development of

the LoFLYTE vehicle," in *Proceedings of the 34th Aerospace Sciences Meeting and Exhibit*, American Institute of Aeronautics and Astronautics, 1996.

[82] D. E. Hahne, "Evaluation of the low-speed stability and control characteristics of a mach 5.5 waverider," NASA/TM-4756, NASA Langley Research Center, 1997.

[83] I. M. Blankson, M. Lewis, and R. Pap, "Subsonic experiments using the LoFLYTE hypersonic waverider vehicle," in *Proceedings of the 8th AIAA International Space Planes and Hypersonic Systems and Technologies Conference*, American Institute of Aeronautics and Astronautics, 1998.

[84] "Accurate automation LoFLYTE." `http://www.designation-systems.net/dusrm/app4/loflyte.html`. Accessed: 2019-06-07.

[85] C. S. Gibson, J. C. Neidhoefer, S. M. Cooper, L. Carlton, and C. J. Cox, "Development and flight test of the X-43A-LS hypersonic configuration UAV," in *Proceedings of the 1st Technical Conference and Workshop on Unmanned Aerospace Vehicles*, American Institute of Aeronautics and Astronautics, 2002.

[86] C. S. Gibson, R. J. Vess, and R. Pegg, "Low speed flight testing of a X-43A hypersonic lifting body configuration," in *Proceedings of the 12th AIAA International Space Planes and Hypersonic Systems and Technologies Conference*, American Institute of Aeronautics and Astronautics, 2003.

[87] K. G. Bowcutt, "Multidisciplinary optimization of airbreathing hypersonic vehicles," *Journal of Propulsion and Power*, vol. 17, no. 6, pp. 1184–1190, 2001.

[88] J. Roskam, *Airplane Flight Dynamics and Automatic Flight Controls*. Design, Analysis and Research Corporation (DARcorporation), 2007.

[89] E. H. Hirschel, *Basics of Aerothermodynamics*. AIAA/Springer-Verlag Berlin Heidelberg, 2005.

[90] E. H. Hirschel and C. Weiland, *Selected Aerothermodynamic Design Problems of Hypersonic Flight Vehicles*. Springer-Verlag Berlin Heidelberg, 2009.

[91] D. Küchemann, "Hypersonic aircraft and their aerodynamic problems," *Progress in Aerospace Sciences*, vol. 6, pp. 271–353, 12 1965.

[92] J. J. Bertin and R. M. Cummings, "Fifty years of hypersonics: where we've been and where we're going," *Progress in Aerospace Sciences*, vol. 39, pp. 511–536, 2003.

[93] N. Takashima and M. J. Lewis, "Optimization of waverider-based hypersonic cruise vehicles with off-design considerations," *Journal of Aircraft*, vol. 36, no. 1, pp. 235–245, 1999.

[94] D. Küchemann, *The Aerodynamic Design of Aircraft*. American Institute of Aeronautics and Astronautics, 2013.

[95] K. G. Bowcutt, *Optimization of Hypersonic Waveriders Derived from Cone Flows - Including Viscous Effects*. PhD Thesis, The University of Maryland, 1986.

[96] T. Nonweiler, "Delta wings of shapes amenable to exact shock-wave theory," *Journal of the Royal Aeronautical Society*, vol. 67, pp. 39–40, 1 1963.

[97] S. Corda and J. D. Anderson, "Viscous optimized hypersonic waveriders designed from axisymmetric flow fields," in *Proceedings of the 26th AIAA Aerospace Sciences Meeting*, American Institute of Aeronautics and Astronautics, 1988.

[98] T. Tsuchiya and Y. Takenaka, "Multidisciplinary design optimization for hypersonic experimental vehicle," *AIAA Journal*, vol. 45, no. 7, pp. 1655–1662, 2007.

[99] "Federal Aviation Administration Standard airworthiness certification regulations." `https://www.faa.gov/aircraft/air_cert/airworthiness_certification/std_awcert/std_awcert_regs/regs/`. Accessed: 2019-04-26.

[100] T. R. F. Nonweiler, "Aerodynamic problems of manned space vehicles," *Journal of the Royal Aeronautical Society*, vol. 63, pp. 521–528, 9 1959.

[101] C. E. Cockrell Jr, *Vehicle Integration Effects on Hypersonic Waveriders*. Masters Thesis, The George Washington University, 1990.

[102] B. Mangin, A. Chpoun, R. Benay, and B. Chanetz, "Comparison between methods of generation of waveriders derived from conical flows," *C. R. Mecanique*, vol. 334, pp. 117–122, 2006.

[103] T. Eggers and H. Sobieczky, "Design of advanced waveriders with high aerodynamic efficiency," in *Proceedings of the 5th AIAA International Aerospace Planes*

and Hypersonics Technologies Conference, American Institute of Aeronautics and Astronautics, 1993.

[104] J. G. Jones, K. C. Moore, and P. L. Roe, "A method for designing lifting configurations for high supersonic speeds, using axisymmetric flow fields," *Archive of Applied Mechanics*, vol. 37, pp. 56–72, 1968.

[105] M. L. Rasmussen, "Waverider configurations derived from inclined circular and elliptic cones," *Journal of Spacecraft and Rockets*, vol. 17, no. 6, pp. 537–545, 1980.

[106] H. Sobieczky, F. C. Dougherty, and K. Jones, "Hypersonic waverider design from given shock waves," in *Proceedings of the 1st International Hypersonic Waverider Symposium*, University of Maryland, 1990.

[107] M. Rasmussen and B. Duncan, "Hypersonic waveriders generated from power-law shocks," in *Proceedings of the 6th AIAA International Aerospace Planes and Hypersonics Technologies Conference*, American Institute of Aeronautics and Astronautics, 1995.

[108] B. Mangin, R. Benay, B. Chanetz, and A. Chpoun, "Optimization of viscous waveriders derived from axisymmetric power-law blunt body flows," *Journal of Spacecraft and Rockets*, vol. 43, no. 5, pp. 990–998, 2006.

[109] Y. P. Goonko, I. I. Muzhul, and G. N. Markelov, "Convergent-flow-derived waveriders," *Journal of Aircraft*, vol. 37, pp. 1178–1185, 2000.

[110] P. E. Rodi, "The osculating flowfield method of waverider geometry generation," in *Proceedings of the 43rd AIAA Aerospace Sciences Meeting and Exhibit*, American Institute of Aeronautics and Astronautics, 2005.

[111] P. E. Rodi, "Vortex lift waverider configurations," in *Proceedings of the 50th AIAA Aerospace Sciences Meeting*, American Institute of Aeronautics and Astronautics, 2012.

[112] T. Eggers, D. Strohmeyer, H. Nickel, and R. Radespiel, "Aerodynamic off-design behaviour of integrated waveriders from take-off up to hypersonic flight," in *Proceedings of the 2nd European Symposium on Aerothermodynamics*, ESA Communications, 1994.

[113] L. N. Long, "Off-design performance of hypersonic waveriders," *Journal of Aircraft*, vol. 27, no. 7, pp. 639–646, 1990.

[114] R. W. Miller and B. M. Argrow, "Subsonic aerodynamics of an osculating cones waverider," in *Proceedings of the 35th Aerospace Sciences Meeting and Exhibit*, American Institute of Aeronautics and Astronautics, 1997.

[115] T. Langener, S. Erb, and J. Steelant, "Trajectory simulation and optimization of the lapcat-mr2 hypersonic cruiser concept," in *Proceedings of the 29th Congress of the International Council of the Aeronautical Sciences*, American Institute of Aeronautics and Astronautics, 2014.

[116] J. Steelant, V. Villace, A. Kallenbach, A. Wagner, J. Y. Andro, S. di Benedetto, B. Saracoglu, S. L. Chernyshev, A. A. Gubanov, V. A. Talyzin, N. V. Voevodenko, N. V. Kukshinov, A. N. Prokhorov, N. V. Grigoriev, A. J. Neely, D. Verstraete, and D. Buttsworth, "Flight testing designs in HEXAFLY-INT for high-speed transportation," in *Proceedings of the International Conference on High-Speed Vehicle Science and Technology*, TsAGI, 2018.

[117] C. J. Schueler, L. K. Ward, and A. E. Hodapp Jr, "Techniques for measurement of dynamic stability derivatives in ground test facilities," AGARDograph-121, Adivosory Group for Aerospace Research and Development, 1967.

[118] E. H. Hirschel, "Vortex flows - some general properties, and modelling, configurational and manipulation aspects," in *Proceedings of the 14th AIAA Applied Aerodynamics Conference*, American Institute of Aeronautics and Astronautics, 1996.

[119] M. Lee and C. Ho, *Frontiers in Experimental Fluid Mechanics*, ch. Vortex Dynamics of Delta Wings, pp. 365–427. Springer-Verlag Berlin, 01 1989.

[120] J. H. B. Smith, "Technical evaluation report on the fluid dynamics panel symposium on vortex flow aerodynamics," AGARD-AR-299, Adivosory Group for Aerospace Research and Development, 1992.

[121] ANSYS, "Ansys fluent 15.0 theory guide," 2013.

[122] F. R. Menter, "Two-equation eddy-viscosity turbulence models for engineering applications," *AIAA Journal*, vol. 32, no. 8, pp. 1598–1605, 1994.

[123] J. Tu, G. Yeoh, and C. Liu, "Computational fluid dynamics: A practical approach," in *Computational Fluid Dynamics (Second Edition)*, pp. 177 – 217, Butterworth-Heinemann, second ed., 2013.

[124] aerospaceweb.org, "Atmospheric properties calculator version 2.2.0." `http://www.aerospaceweb.org/design/scripts/atmosphere/`, 2016. Accessed: 2019-04-08.

[125] United States Committee on Extension to the Standard Atmosphere, "US Standard Atmosphere 1976," ada035728, National Oceanic and Atmospheric Administration, NASA, US Air Force, 1976.

[126] Airservices Australia, "Standard terminal area arrival speeds." `http://www.airservicesaustralia.com/wp-content/uploads/Standard-Terminal-Area-Arrival-Speeds-final.pdf`, 2015. Last accessed: 2019-05-29.

[127] T. Bykerk, D. Verstraete, S. Wolf, V. F. Villace, and J. Steelant, "Performance and stability analysis of a hypersonic vehicle for a low speed flight test program," in *Proceedings of the HiSST: International Conference on High-Speed Vehicle Science Technology*, 2018.

[128] "High Performance Computing, The University of Sydney." `https://sydney.edu.au/research_support/hpc/index.shtml`. Accessed: 2019-04-26.

[129] G. Haller, "An objective definition of a vortex," *Journal of Fluid Mechanics*, vol. 525, pp. 1–26, 2005.

[130] J. Jeong and F. Hussain, "On the identification of a vortex," *Journal of Fluid Mechanics*, vol. 285, pp. 69–94, 1995.

[131] D. Pagan and J. L. Solignac, "Experimental study of the breakdown of a vortex generated by a delta wing," *La Recherche Aerospatiale (English Edition)*, vol. 3, pp. 29–51, 01 1986.

[132] G. Hoe, D. B. Owens, and C. Denham, "Forced oscillation wind tunnel testing for FASER flight research aircraft," in *AIAA Atmospheric Flight Mechanics Conference*, 08 2012.

[133] X. Liu, W. Liu, and Y. Zhao, "Navier-Stokes predictions of dynamic stabil-

ity derivatives for air-breathing hypersonic vehicle," *Acta Astronautica*, vol. 118, pp. 262–285, 2016.

[134] A. Da Ronch, D. Vallespin, M. Ghoreyshi, and K. J. Badcock, "Evaluation of dynamic derivatives using computational fluid dynamics," *AIAA Journal*, vol. 50, no. 2, pp. 470–484, 2012.

[135] M. J. L. Anderson, *A Methodology for Aerodynamic Parameter Estimation of Tail-Sitting Multi-Rotors*. PhD Thesis, The University of Sydney, 2018.

[136] K. Lehmküler, *Direct Comparison of Small Aircraft Dynamics between Wind Tunnel and Flight Tests*. PhD Thesis, The University of Sydney, 2016.

[137] J. C. Daugherty, "NASA Ames Unitary Plan Wind Tunnel blockage recommendations." `https://www.nasa.gov/sites/default/files/643649main_UPWT_Blockage_Recommendations_Rev0.pdf`, 1984. Accessed: 2019-04-08.

[138] J. Barlow, W. Rae, and A. Pope, *Low-Speed Wind Tunnel Testing*. John Wiley & sons, 1999.

[139] "Anytime Inc, Digital Magnetic Angle Cube." `https://www.igagingstore.com/Digital-Magnetic-Angle-Cube-Gage-Gauge-Level-Table-p/203922.htm`. Accessed: 2019-04-08.

[140] S. Shindo, "Simplified tunnel correction method," *Journal of Aircraft*, vol. 32, no. 1, pp. 210–213, 1994.

[141] S. J. Kline and F. A. McClintock, "Describing uncertainties in single sample experiments," *Mechanical Engineering*, pp. 3–8, 1953.

[142] "ATI Industrial Automation Inc, F/T Sensor: Mini45." `https://www.ati-ia.com/products/ft/ft_models.aspx?id=Mini45`. Accessed: 2019-04-08.

[143] A. J. Steer and M. V. Cook, "Control and handling qualities considerations for an advanced supersonic transport aircraft," *The Aeronautical Journal*, pp. 265–272, 06 1999.

[144] J. M. Delery, "Aspects of vortex breakdown," *Progress in Aerospace Sciences*, vol. 30, pp. 1–59, 01 1994.

[145] P. Hamel and R. Jategaonkar, "Evolution of flight vehicle system identification.," *Journal of Aircraft*, vol. 33, pp. 10–28, 01 1996.

[146] D. B. Owens, J. M. Brandon, M. A. Croom, C. M. Fremaux, E. H. Heim, and D. D. Vicroy, "Overview of dynamic test techniques for flight dynamics research at NASA LaRC," in *25th AIAA Aerodynamic Measurement Technology and Ground Testing Conference*, AIAA, NASA, 2006.

[147] H. Subke, "Test installations to investigate the dynamic behaviour of aircraft with scaled models in wind tunnels," *Transactions of the Institute of Measurement and Control*, vol. 1, no. 3, pp. 135–140, 1979.

[148] B. Owens, D. Cox, and E. Morelli, "Development of a low-cost sub-scale aircraft for flight research: The FASER project," in *25th AIAA Aerodynamic Measurement Technology and Ground Testing Conference*, 06 2006.

[149] V. Klein, P. C. Murphy, and N. M. Szyba, "Analysis of wind tunnel lateral oscillatory data of the F-16XL aircraft," NASA/TM-2004-213246, National Aeronautics and Space Administration, 2004.

[150] D. Rohlf, S. Schmidt, and J. Irving, "Stability and control analysis for an unmanned aircraft configuration using system-identification techniques," *Journal of Aircraft*, vol. 49, pp. 1597–1609, 11 2012.

[151] S. D. Carnduff, S. D. Erbsloeh, A. K. Cooke, and M. V. Cook, "Characterizing stability and control of subscale aircraft from wind-tunnel dynamic motion," *Journal of Aircraft - J AIRCRAFT*, vol. 46, pp. 137–147, 01 2009.

[152] V. Klein and E. Morelli, *Aircraft System Identification: Theory And Practice*. AIAA, 08 2006.

[153] R. Jategaonkar, *Flight Vehicle System Identification: A Time Domain Methodology*, vol. 216. 08 2006.

[154] "AMT20 datasheet." `https://www.cui.com/product/motion/rotary-encoders/absolute/modular/amt20-series`. Accessed: 2019-04-26.

[155] "MA3 Miniature Absolute Magnetic Shaft Encoder." `https://cdn.usdigital.`

com/assets/datasheets/MA3_datasheet.pdf?k=636956481101539862. Accessed: 2019-04-26.

[156] M. Drela and H. Youngren, "AVL Overview." http://web.mit.edu/drela/Public/web/avl/. Accessed: 2019-04-26.

[157] NASA Ames Research Staff, "Equations, tables, and charts for compressible flow," NACA TR 1135, National Advisory Committee for Aeronautics, 1953.

[158] E. C. Polhamus, "A concept of the vortex lift of sharp-edge delta wings based on a leading-edge-suction analogy," NASA TN D-3767, National Aeronautics and Space Administration, 1966.

[159] J. W. Purvis, "Analytical prediction of vortex lift," *Journal of Aircraft*, vol. 18, pp. 225–230, 04 1981.

[160] L. P. Tosti, "Low-speed static stability and damping-in-roll characteristics of some swept and unswept low-aspect-ratio wings," NACA TN 1468, National Advisory Committee for Aeronautics, 1947.

[161] K. Deb, A. Pratap, S. Agarwal, and M. T., "A fast and elitist multiobjective genetic algorithm: NSGA-II," *IEEE Transactions on Evolutionary Computation*, vol. 6, pp. 182–197, 04 2002.

[162] Yarpiz, "NSGA-II in MATLAB." http://yarpiz.com/56/ypea120-nsga2. Accessed: 2019-06-27.

[163] J. J. Jeyaratnam and D. Verstraete, "Analysis of low speed stability derivatives of a hypersonic test vehicle," in *7th Asia-Pacific International Symposium on Aerospace Technology*, Engineers Australia, 2015.

[164] E. Seckel and J. J. Morris, "The stability derivatives of the navion aircraft estimated by various methods and derived from the flight test data," Report No. FAA-RD-71-6, Department of Transportation Federal Aviation Administration, 1971.

[165] J. Jeyaratnam, T. Bykerk, and D. Verstraete, "Low speed stability analysis of a hypersonic vehicle design using CFD and wind tunnel testing," in *21st AIAA International Space Planes and Hypersonics Technologies Conference*, AIAA, 2017.

Appendix A

Tranair Simulations

The work presented in this appendix has in part been previously presented in reference [163].

A.1 Software Description and Operation

Tranair is a non-linear full potential 3D flow solver with pseudo-3D boundary layer coupling. Tranair uses a second order transpiration method to emulate control surface deflections and flow angles. Unsteady solutions are provided by imposing time harmonic oscillations on top of the steady state solution giving the static and dynamic stability derivatives. Tranair accepts a surface mesh and a definition of the bounding volume of the problem. The input file also defines the flow Mach number, AoA, AoS and various volume discretisation controls. Aero Grid and Panelling System (AGPS) is used to generate accurate surface meshes. The tool features a highly flexible scripting language with GUI to view the resulting mesh. The surface mesh of the hexafly vehicle is shown in Figure A.1. Boundary conditions such as Kutta condition at the trailing edges of wings is applied using wake surfaces, which are shown in Figure A.1(b). Division of the computational volume is handled within Tranair by extrapolating prism elements from the input surface mesh.

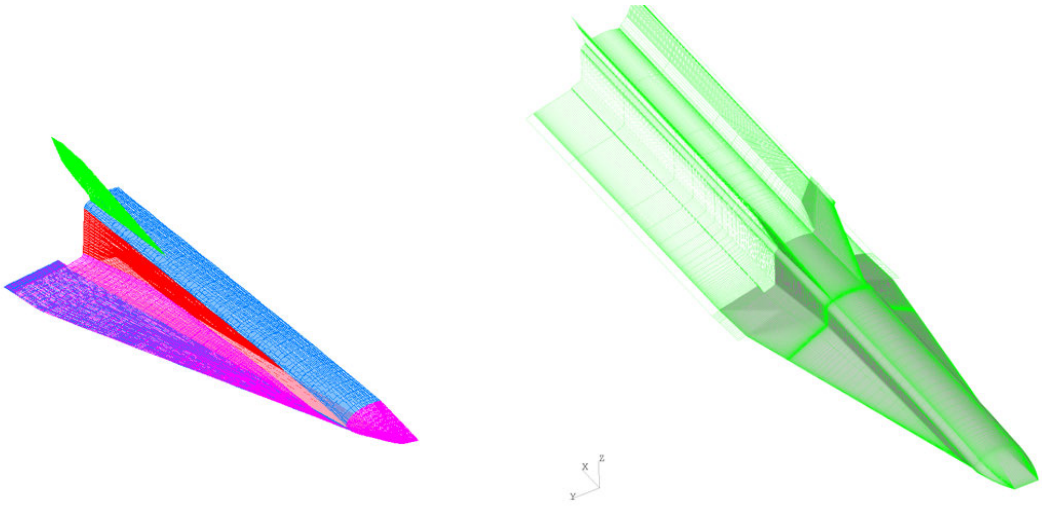

(a) Hexafly surface mesh (b) Hexafly surface mesh with wakes

Figure A.1: Hexafly AGPS mesh

A.2 Validation

The dynamic stability results of Tranair were validated using flight test data found in reference [164] for the Ryan Navion aircraft. These are tabulated in Table A.1. The results show good agreement although the Ryan Navion is a conventional subsonic general aviation aircraft.

Table A.1: Ryan Navion Tranair Validation

	Tranair	Flight Test Data	USAF Datcom
C_{l_r}	0.070	0.069	0.130
C_{l_p}	-0.463	-0.46	-0.3
C_{n_r}	-0.125	-0.088	-0.12
C_{n_p}	-0.067	-0.038	-0.03
$C_{m_{\dot{\alpha}}}$	-7.233		-6.58
$C_{m_{\dot{\alpha}+q}}$	-17.64	-18.3	-19.8

A.3 Results

The viscous results with boundary layer coupling show little difference to the inviscid results with no boundary layer coupling. As the inviscid computations converged over larger range of AoA and AoS, both sets of results are presented. The results for lift coefficient, C_L, and moment coefficient, C_m are shown in figure A.2. The results for lift

coefficient (Fig. A.2(a)) show a linear trend, in contrast to the results of CFD and wind tunnel testing. The vortex lift component has not been accounted for. The moment coefficient (Fig. A.2(b)) shows a stable linear trend over the range of AoA. Again this is in contrast to the non-linear moment distribution obtained from CFD and wind tunnel testing.

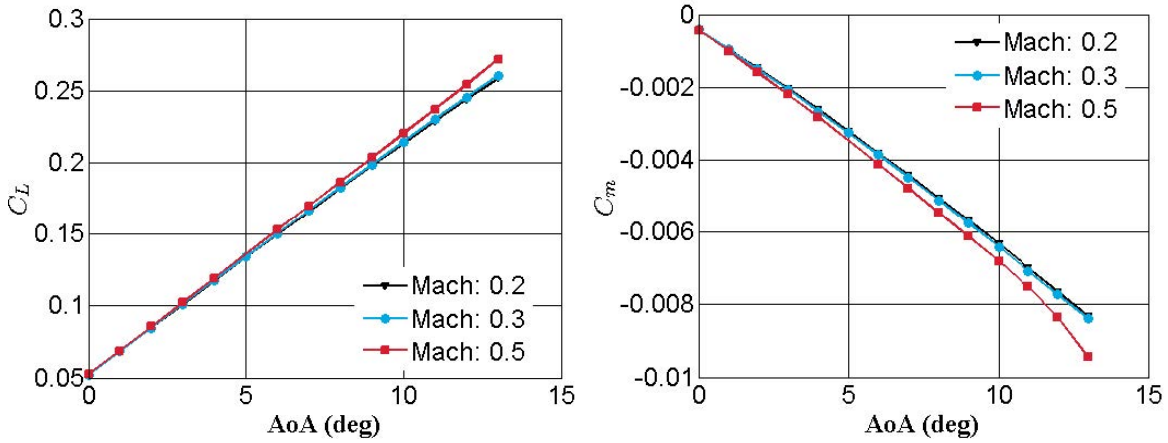

(a) Lift Coefficient (b) Moment Coefficient

Figure A.2: Static longitudinal coefficients

The dynamic longitudinal results are shown in Figure A.3 while the main dynamic lateral coefficients are shown in Figure A.4.

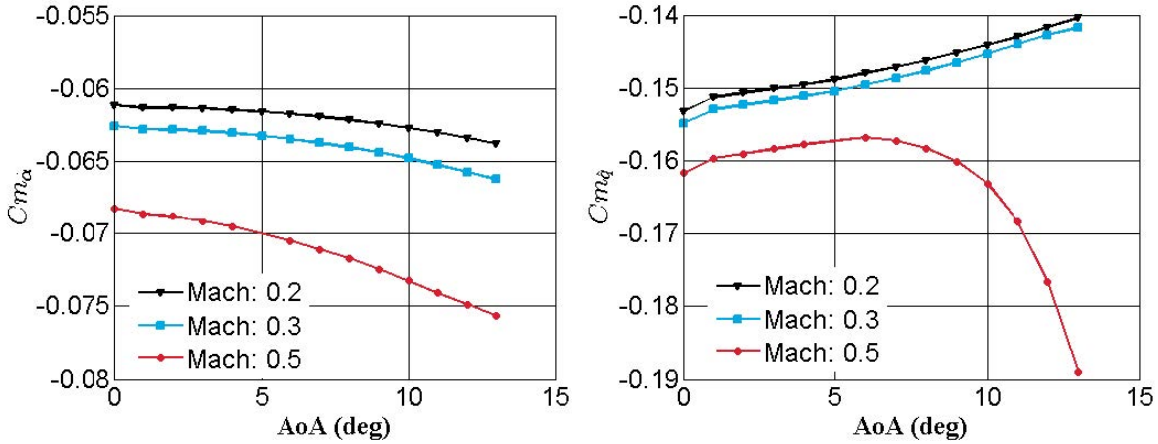

(a) C_{m_α} (b) C_{m_q}

Figure A.3: Dynamic pitching moment coefficient derivatives

The Tranair results indicated stability by all criteria. However the importance of modelling the vortex lift distribution to both aerodynamic performance and to static and dynamic stability was highlighted by the large differences with the CFD and wind tun-

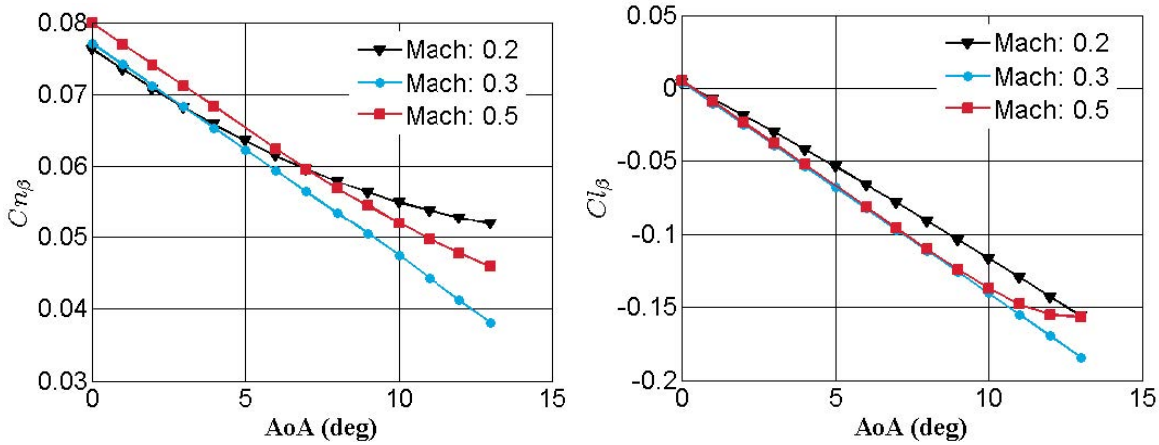

(a) C_{n_β} (b) C_{l_β}

Figure A.4: Static lateral stability gradients

nel test results. Although Tranair is effective for general aviation vehicles and for slender vehicles with low AoA, it was found to be inadequate for the Hexafly-Int and similar vehicles at low-speeds and high AoA.

Appendix B

Small Model Wind Tunnel Tests

The work presented in this appendix has in part been previously presented in reference [165].

B.1 Model Details

A scale model of the Hexafly-Int vehicle of length 0.56m has been constructed. The length and centre of gravity information is presented in Table B.1. The centre of gravity is the equivalent of the full scale vehicle.

Table B.1: Small wind tunnel model Hexafly-Int glider vehicle details

	Full scale	Small WT model
$L_{ref}(m)$	3.29	0.561
$S_{ref}(m^2)$	2.52	0.073
$B_{ref}(m)$	1.23	0.211
CoG [m] (LRF x,y,z)	(1.555,0.0,0.0)	(0.2652,0.0,0.0)

The model was constructed out of layers of Jelutong wood cut using a 3 degree of freedom computer controlled milling machine. The nose piece, and elevons were 3D printed from ABS plastic. The resulting model is shown unpainted in Figure B.1(a) and mounted for testing in Figure B.1(b).

(a) Wooden Hexafly model

(b) Wooden Hexafly model mounted in wind tunnel

Figure B.1: 0.56m Hexafly model

B.2 Results

The model was tested for a range of AoA from -5 to 28 degrees in The University of Sydney 3x4ft wind tunnel. The speed was set to 20m/s with a resulting Reynolds number of 7.7×10^5. The resulting lift and pitching moment data is shown in Figure B.2.

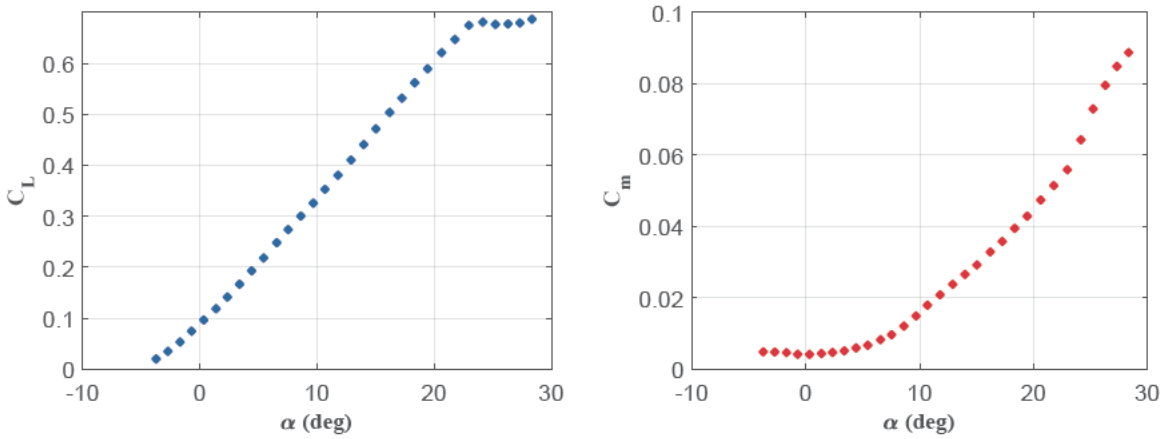

(a) C_L

(b) C_m at CG_{des}

Figure B.2: Lift and pitching moment at CG_{des}

The pitching moment coefficient shown in Figure B.2(b) showed an unstable trend across the AoA range. For dynamic stability testing a stable centre of gravity was required. The centre of gravity was shifted forward until a stable pitching moment trend was obtained across the majority of the AoA. A forward shift of 52mm resulted in the stable pitch moment shown in Figure B.3. This was the basis of the centre of gravity selected for

dynamic testing in Chapter 5.

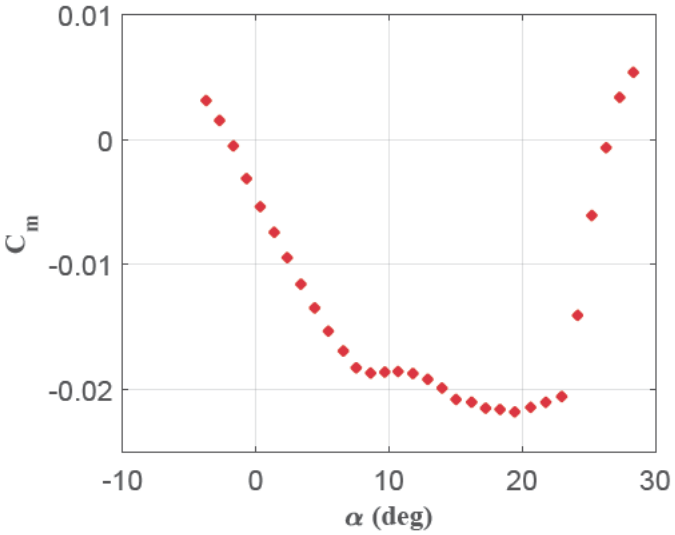

Figure B.3: Pitch moment coefficient for shifted centre of gravity